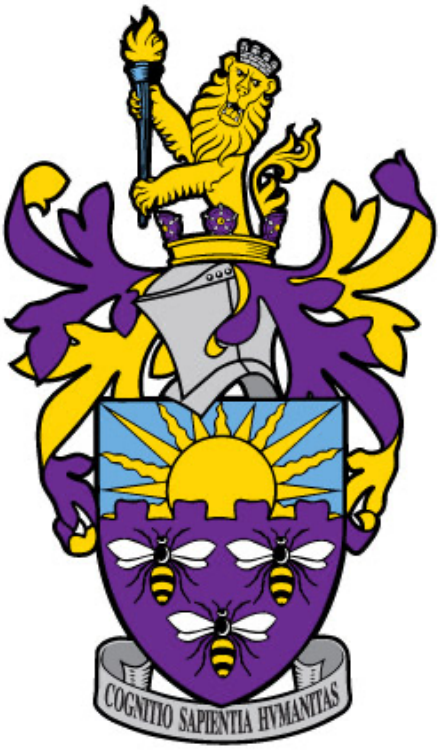

Exploring the Subcomponent Self-Assembly of Three-Dimensional Architectures from Transition Metals and Heteroditopic Ligands

A thesis submitted to The University of Manchester for the degree of Doctor of Philosophy in the Faculty of Science and Engineering.

2021

Lauren L. K. Taylor

The Department of Chemistry

Table of Contents

1. Abbreviations

Å	Ångstrom (10^{-10} m)
acac	Acetylacetonate anion
B	Applied magnetic field
BVS	Bond valence sum
CD_3CN	Deuterated acetonitrile
$CDCl_3$	Deuterated chloroform
CH_3CN	Acetonitrile
$CHCl_3$	Chloroform
cm	Centimetre (10^{-2} m)
COSY	Correlation spectroscopy
CSD	Crystal structure database
DFT	Density functional theory
DL	Dynamic library
DMF	Dimethylformamide
DMSO	Dimethyl sulfoxide
DNA	Deoxyribonucleic acid
DOSY	Diffusion-ordered spectroscopy
dppp	1,3-Bis(diphenylphosphino)propane
EPR	Electron Paramagnetic Resonance
equiv	Equivalent
ESI	Electronic supplementary information
fac	*Facial*
g	Isotopic *g*-factor
g	Gram
GHz	Gigahertz
H	Magnetic field strength
H_2O	Water
HMBC	Heteronuclear Multiple Bond Correlation
hr	Hour
HR-MS	High resolution mass spectrometry
HS	High-spin
HSQC	Heteronuclear Single Quantum Coherence
Hz	Hertz
i	Cation
j	Anion

J, $_zJ$, J_1, J_2	Coupling constants
K	Kelvin
LS	Low-spin
M	Molar magnetisation
m s^{-1}	Metres per second
m/z	Mass / charge
MeCN	Acetonitrile
MeOD	Deuterated methanol
MeOH	Methanol
mer	*Meridional*
mg	Milligram (10^{-3} g)
MHz	Megahertz (10^{6} Hz)
mL	Millilitre (10^{-3} L)
MLCT	Metal to ligand charge transfer
mmol	Millimole (10^{-3} mol)
Mol^{-1}	Per mole
NMR	Nuclear magnetic resonance
NOESY	Nuclear Overhauser effect spectroscopy
^{o}C	Degrees celsius
Oe	Oersted
p-	Para-
Ph	Phenyl
ppm	Parts per million
p-TsOH	*p*-Toluenesulfonic acid
r_{ij}	Bond length
SCO	Spin crossover
S_{ij}	Bond valence
SQUID	Superconducting quantum interference device
T	Temperature
TAME	1,1,1-Tris(aminoethyl)ethane
THF	Tetrahydrofuran
TREN	Tris(2-aminoethyl)amine
TRPN	Tris(3-aminopropyl)amine
μ_B	Bohr-Magneton, magnetic moment
µL	Microlitre (10^{-6} L)
µmol	Micromole (10^{-6} mol)

UV-Vis	Ultraviolet-visible
ZFS	Zero-field splitting
Δ	Delta
Λ	Lambda
χ'_M	In-phase magnetic susceptibility
χ''_M	Out-of-phase magnetic susceptibility

2. Abstract

Exploring the Subcomponent Self-Assembly of Three-Dimensional Architectures from Transition Metals and Heteroditopic Ligands. A thesis submitted to the University of Manchester for the degree of Doctor of Philosophy in the Faculty of Science and Engineering.

Subcomponent self-assembly has become an attractive design strategy for the formation of functional three-dimensional container molecules, many of which have been employed for a wide variety of applications. The subcomponent syntheses described in this thesis utilise heteroditopic ligands and a range of transition metal salts to prepare a series of novel metal-organic complexes.

Chapter one presents an introduction into supramolecular chemistry and the relevant inorganic principles utilised within the area for the formation of functional architectures. The chapter provides a review of the literature surrounding subcomponent self-assembly with a variety of ligands, highlighting the site-specific binding of different metal ions, as well as the stabilisation of metals in different spin-states.

Chapter two reports the synthesis of a trigonal bipyramidal complex formed from a heteroditopic ligand, where iron was bound within the construct as low-spin iron(II), high-spin iron(II) and high-spin iron(III). This complex was the first literature example of a fluoride-bridged mixed-valence iron star, with six fluoride ions being abstracted from the tetrafluoroborate counterions.

Chapter three highlights a series of analogous iron(II) and silver(I) trigonal bipyramidal complexes with different anions bound within the central cavity. The complex was also formed with copper(I) in place of silver for potential catalytic applications.

In Chapter four, anion-induced self-sorting phenomena were explored to facilitate the formation of a heteroleptic tetrahedral iron(II) cage. Control over the sorting within the system was obtained through the choice of anion in the starting metal salt, with iron(II) perchlorate supporting integrative self-sorting.

Chapter five contains results relevant to the work described in the preceding chapters. This work highlights a number of polynuclear architectures formed from both hetero- and homoditopic ligands in the presence of transition metal ions. The experimental procedures and characterisation for each compound are given.

Lauren L. K. Taylor

September 2021

2.1. Publication List

1. Lauren L. K. Taylor, Imogen A. Riddell, Maarten M. J. Smulders, Self-Assembly of Functional Discrete Three-Dimensional Architectures in Water, *Angew. Chem. Int. Ed.,* 2019, **58**(5), 1280-1307.
2. Lauren L. K. Taylor, Iñigo J. Vitorica-Yrezabal, Ivana Borilović, Floriana Tuna, Imogen A. Riddell, Self-assembly of a trigonal bipyramidal architecture with stabilisation of iron in three spin states, *Chem. Commun.,* 2021, **57**, 11252–11255.

3. Declaration

The work in this thesis was carried out at The University of Manchester between September 2017 and September 2021 under the supervision of Dr Imogen A. Riddell. All the work is my own, with contributions from collaborators acknowledged throughout. No portion of this work has been submitted for another degree or qualification at this, or any other university.

Lauren L. K. Taylor

4. Copyright Statement

5. Acknowledgements

I would first like to say a huge thank you to my supervisor Dr Imogen Riddell for giving me the opportunity to be the first PhD student in her research group. Imogen has supported me throughout my time at Manchester and has been the best supervisor I could have ever asked for. Her continuous encouragement and reassurance has helped me develop as a scientist, and her own experience as a successful chemist and a mother has inspired me. I would also like to thank Prof. Dave Mills for being my co-supervisor, and the EPSRC for financial support.

I want to say thank you to the ever-expanding Riddell group who have always been there for me throughout my time as a PhD student. Thank you Jonathan for all your help within the lab and for being emotionally supportive when I purified triphenyl phosphine instead of my ligand. Thank you to Dan and Becky who have also helped me during my time in the lab, and have made being in the office so enjoyable. I will miss all the funny TikToks and the baffling news headlines.

I am so grateful to both the Natrajan and the Mills groups for making me feel so welcome when I first started the PhD. You all treated me as though I was in your group and made me feel so comfortable in the office. I want to say a HUGE thank you to Hannah Nicholas who literally made my first two years here incredible- thank you for all the food, the laughs, the sleepovers and the nights out! Thank you to Hannah Wilson who started her PhD at the same time as me and was one of the first people I met here. Hannah Wilson has been so supportive as a colleague and as a friend, thank you for all the fun times we've had (usually you cooking and me eating!). I also want to say a huge thank you to Dr. Louise Natrajan for always being a supportive and positive figure, and for being there when I've needed someone to talk to.

I want to say a massive thank you to Ciaran, Matt, Laura and Lowra for making these last few (kind of) post-pandemic months SO enjoyable. Huge thanks to Ciaran for always being supportive during the last few months of my PhD, and for always coming to my house for Sunday dinner. Thank you for being both a shoulder to cry on and the (second) main character. I also want to thank Matt for his continued support during the hardest months of my PhD, for helping me stay positive even when I've felt overwhelmed and for always being my biggest cheerleader.

Finally I want express how eternally grateful I am to my mum Kerry for being my rock during all my time in higher education. We have been through the highest highs and the lowest lows and have always managed to come out strong. Thank you SO much for everything you have done for me, and even if this thesis makes no sense, I hope the pretty pictures make you proud! Thank you to my grandparents Kath and Bill, my brother Joseph and to Jason for being absolutely amazing, so supportive and always loving throughout not only my PhD but my whole life!

I also want to say thank you to my cats, love you.

6. Preface

6.1. Rationale for Alternative Format Submission

The research undertaken in this PhD have resulted in a number of results which fall into distinct publishable categories. As such, the results have been written up as papers in the format of journal articles. Paper one is published in Chemical Communications, 2021. Paper two is unpublished and paper three is ready for submission.

Below is a summary of each paper presented in this thesis, followed by an explanation of the contributions of each author.

6.2. Brief of Included Works and Roles of Authors

Paper One: Self-Assembly of a Trigonal Bipyramidal Architecture with Stabilisation of Iron in Three Spin States

Lauren L. K. Taylor, Iñigo J. Vitorica-Yrezabal, Ivana Borilović, Floriana Tuna, and Imogen A. Riddell, *Chem. Commun.,* 2021, **57**, 11252–11255.

Paper one reports the synthesis and characterisation of a mixed spin-state trigonal bipyramidal architecture formed from a heteroditopic ligand, TREN and iron(II) tetrafluoroborate. The complex was fully characterised by NMR, mass spectrometry, elemental analysis, X-ray crystallography, bond valence sum analysis and magnetic studies. This compound is the first literature example of a complex containing a six fluoride-bridged mixed-valence iron star motif.

LLKT and IAR designed the experiments. IAR wrote the initial draft of the manuscript and LLKT wrote the initial draft of the supplementary information. LLKT was responsible for the characterisation of all complexes, as well as preparation of all NMR and MS samples. IAR supervised the work and edited the final draft of the manuscript. IVY solved and refined all the crystallographic data. IB and FT collected the magnetic measurements.

Paper Two: The Development of Self-Assembled Bimetallic Trigonal Bipyramidal Complexes for Supramolecular Catalysis

Lauren L. K. Taylor, April C. Y. Sung, Iñigo J. Vitorica-Yrezabal, and Imogen A. Riddell.

Paper two highlights the synthesis and characterisation of a series of heterometallic trigonal bipyramidal architectures formed from a heteroditopic ligand. The complexes formed were either mixed iron(II)-silver(I) or iron(II)-copper(I) architectures with the formula $[Fe_2Ag_3L_6T_2]^{7+}$ and $[Fe_2Cu_3L_6T_2]^{7+}$, respectively. The complexes were characterised by NMR, mass spectrometry and X-ray crystallography. The crystallographic data highlighted the anion encapsulation abilities and the subsequent flexibility of the architecture.

LLKT and IAR designed the experiments. LLKT wrote the initial draft of the manuscript and the initial draft of the supplementary information. LLKT was responsible for the characterisation of all complexes, as well as preparation of all NMR and MS samples. ACYS was responsible for the synthesis of the novel ligand used in the paper. IAR supervised the work and edited the final draft of the manuscript. IVY solved and refined all the crystallographic data.

Paper Three: Factors Governing Integrative Self-Sorting of an $[Fe_4L_6]^{8+}$ Tetrahedron with One Unique Vertex

Lauren L. K. Taylor, April C. Y. Sung, Iñigo J. Vitorica-Yrezabal, and Imogen A. Riddell.

Paper three presents the formation of a heteroleptic tetrahedral iron(II) cage from a mixture of a heteroditopic ligand, a homoditopic ligand, TREN and iron(II) perchlorate. Access to the desired mixed-ligand tetrahedron was achieved through anion-induced integrative self-sorting. In the presence of other ions such as BF_4^-, OTf^- and NTf_2^-, a mixture of products were obtained. The complexes were characterised by NMR, mass spectrometry and X-ray crystallography.

LLKT and IAR designed the experiments. LLKT wrote the initial draft of the manuscript and the initial draft of the supplementary information. LLKT was responsible for the characterisation of all complexes, as well as preparation of all NMR and MS samples. ACYS was responsible for the synthesis of the novel ligand used in the paper. IAR supervised the work and edited the final draft of the manuscript. IVY solved and refined all the crystallographic data.

7. Chapter One: Introduction

7.1. Supramolecular Chemistry

Supramolecular chemistry is often described as '*the chemistry of the intermolecular bond',* a term expressed by Jean-Marie Lehn who, along with Donald J. Cram and Charles J. Pedersen, won the Nobel Prize in 1987 for their work in the area.[1] Whilst more traditional chemistry focuses on covalent bonding, supramolecular chemistry utilises weaker and reversible intermolecular non-covalent interactions such as hydrogen bonding, van der Waals interactions and π-effects.

Supramolecular chemistry is heavily influenced by concepts found in biological systems and as a discipline can generally be divided into two categories: host-guest recognition and self-assembly. Host-guest binding in supramolecular chemistry is comparable to the enzyme 'lock and key' model proposed by Emil Fischer in 1894, which explains how two complementary shapes can fit within one another.[2] This theory was elaborated on by Daniel Koshland and the 'induced fit model' for substrate binding was proposed which takes into account the flexibility of enzymes and thus the capability of a host to adapt and reshape to fit a particular substrate.[3] Supramolecular chemistry has utilised these biological concepts to form synthetic host-guest complexes, with the first examples including the binding of cationic molecules and metals within crown ethers[4] and hydrogen-bonded complexation reactions between arylurea molecules and sulfonates, phosphates and carboxylates.[5] Host-guest chemistry within the supramolecular field has come a long way since the formation of simple two-dimensional complexes, and has now been used to form larger three-dimensional structures. Prominent examples include tetrahedral architectures capable of encapsulating and stabilising reactive guests such as white phosphorus,[6] and the encapsulation of proteins such as ubiquitin within large synthetic architectures.[7]

Self-assembly is the process by which a disordered system undergoes spontaneous and reversible organisation to form ordered structures stabilised by non-covalent interactions.[8] In supramolecular chemistry, subcomponent self-assembly is a coordination driven design strategy whereby reversible covalent and coordination bonds are formed between simple ligand building blocks and metal ion templates, respectively. This approach has been used to form functional three-dimensional architectures which often contain internal void space.[9] This feature gives many constructs unique capabilities leading to applications including the encapsulation and stabilisation of reactive guest molecules,[6,10] drug delivery[11] and catalysis.[12,13] In more recent years, three-dimensional supramolecular constructs have increased in both complexity[14] and size,[15] expanding the scope even further for functional purposes.

7.2. Inorganic Principles

7.2.1. Geometric Preferences

Transition metals are often incorporated within supramolecular structures due to their well-understood coordination geometries and intrinsic properties such as individual redox potentials and fluorescence.[16,17] Knowledge of these features has allowed chemist to propose and synthesize a range of architectures.[18,19] Three common geometries adopted by transition metal ions in coordination compounds are square planar, tetrahedral and octahedral (figure 1). These geometric preferences arise from the *d*-orbital splitting of the individual metal ions caused by the introduction of ligands into the system.

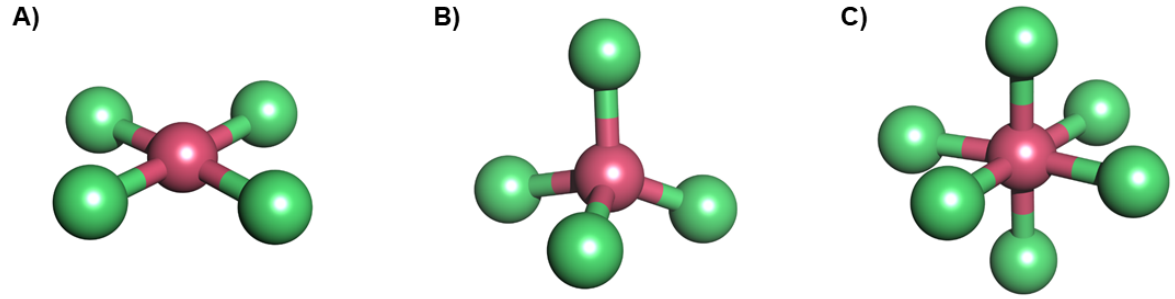

Figure 1. Three commonly observed metal coordination geometries: A) square planar, B) tetrahedral and C) octahedral. Pink spheres represent metal ions, whilst the green spheres represent the donor atoms of organic ligands.

7.2.2. Crystal Field Theory

As transition metal ions carry positive charges, coordination chemistry considers ligands to be negatively charged. A metal ion surrounded by six ligands can be visualised as a sphere containing a central metal cation surrounded by six equally distributed negative charges. The average orbital energy of this sphere complex would be much higher than the metal cation alone, making its formation unfavourable. In reality, as ligands approach the cationic metal centre the *d*-orbitals experience different levels of electrostatic repulsion which causes splitting of the *d*-orbital energy levels (figure 3). Depending on the number of ligands approaching the metal centre and the shape adopted by the resulting complex, the level of splitting differs. If the metal *d*-orbitals are full, the resulting geometry is no longer directed by electronics and, as presented in Chapter three, sterics govern the arrangement.

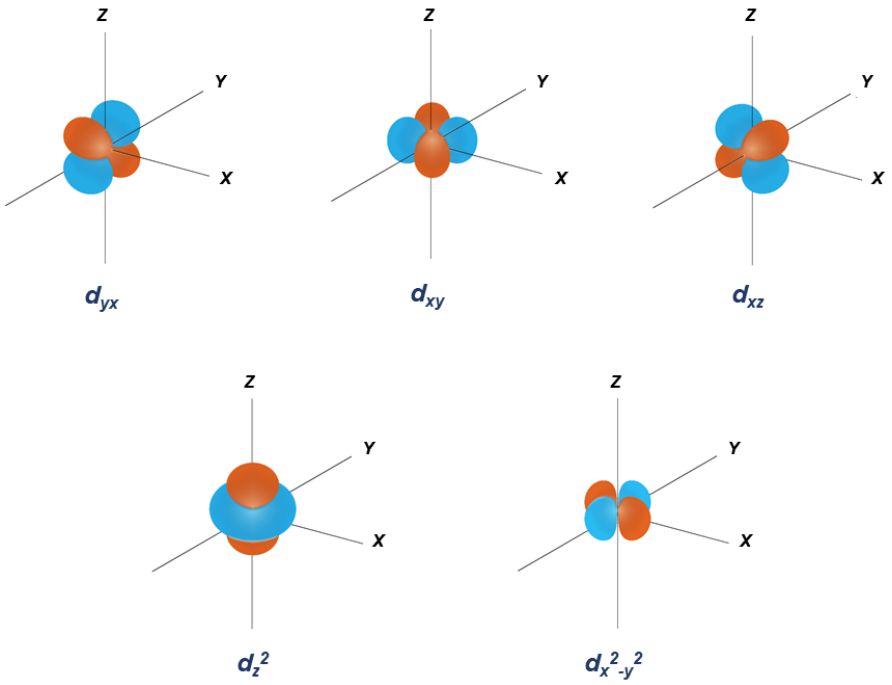

Figure 2. Figures representing the five *d*-orbitals and where they lie on the *x*, *y* and *z* axes. The subscript letters after d in d_{yx}, d_{xy} and d_{xz} indicate the planes in which the lobes of the orbitals exist. In the case of $d_{x^2-y^2}$, the lobes lie on the *x* and *y* axes, whilst lying along the *z* axis in d_{z^2}.

Iron(II) is a metal with an intrinsic preference for adopting an octahedral geometry.[20] Introduction of ligands around an iron(II) centre results in the five degenerate *d*-orbitals (figure 2) splitting into two groups with differing energies: the doubly degenerate e_g orbitals, and the triply degenerate t_{2g}. The e_g orbitals, $d_{x^2-y^2}$ and d_{z^2}, interact directly with the incoming ligands and therefore experience electrostatic repulsion that increases their energy with respect to the spherical crystal field. In contrast, the d_{yx}, d_{xy} and d_{xz} orbitals in the t_{2g} group are oriented between the ligands, which consequently decreases their energy with respect to the metal-ligand sphere, giving rise to an octahedral splitting pattern (figure 3).

Similarly, the crystal field splitting in tetrahedral complexes results in the *d*-orbitals separating into two groups: t_2 and e (figure 3). Electrostatic repulsions between the four coordinating ligands and the d_{yx}, d_{xy} and d_{xz} orbitals are high, whilst the ligands lie between the $d_{x^2-y^2}$ and d_{z^2} axes and so are lower in energy.

The square planar geometry is also four-coordinate and has a structure analogous to that of the octahedral arrangement following removal of the two ligands on the *z* axis. The absence of these ligands results in the stabilisation of the d_{z^2}, d_{yz} and d_{xz} energy levels and thus decreases their energy (figure 3). Complexation with second and third row transition metals results in more significant splitting of the *d*-orbitals compared with the first row,[21] and palladium(II) and platinum(II) are both d^8 metals with a bias for square planar geometries. This preference can be put down to significant splitting of the *d*-orbitals caused by incoming ligands, meaning the spin pairing energy is much less than the energy penalty for populating the $d_{x^2-y^2}$ energy level. Both octahedral and four-coordinate geometries are adopted by metals described in this thesis.

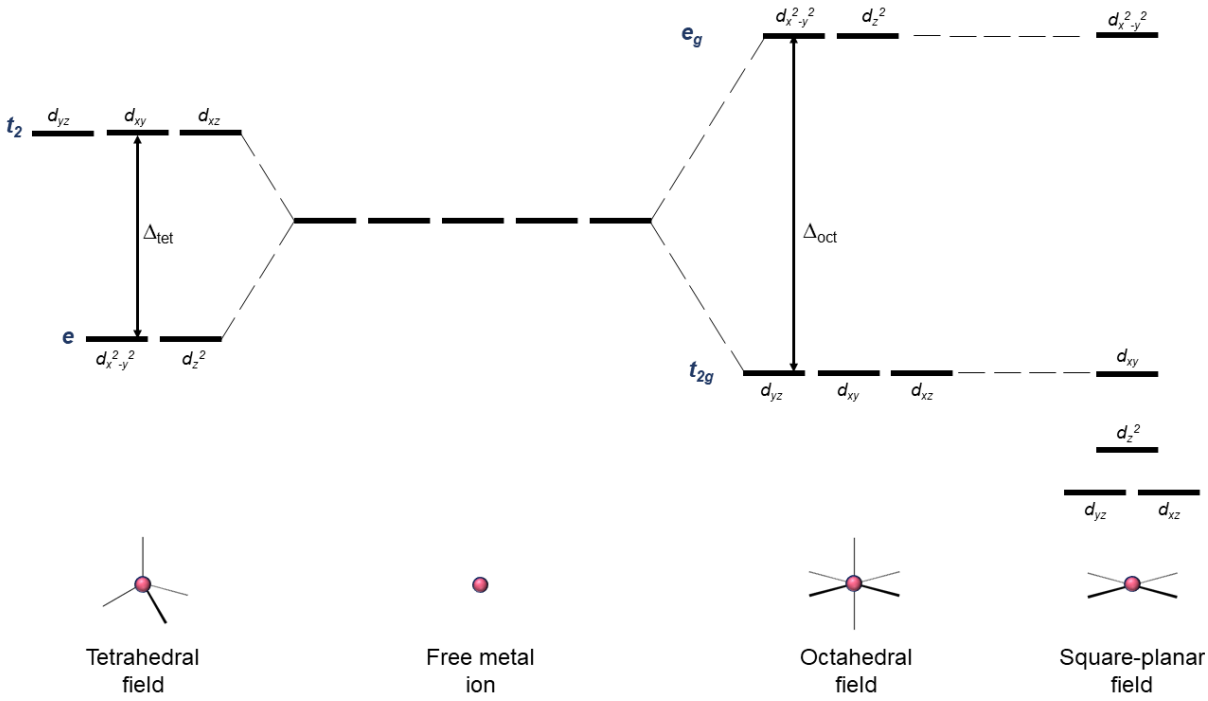

Figure 3. Crystal field splitting diagram for the tetrahedral, octahedral and square-planar coordination environments in relation to a free metal ion. The tetrahedral crystal field splitting energy is denoted Δ_{tet}, and the octahedral crystal field splitting energy is denoted Δ_{oct}.

7.2.3. Paramagnetism

The degree to which the *d*-orbital energy levels are split depends on the field strength of the ligand that is approaching the metal centre. In supramolecular self-assembly, a commonly employed binding motif is the *bis*bidentate imino-pyridyl ligand scaffold (figure 4), of which three can bind to an octahedral metal centre, saturating its coordination sphere. Octahedrally coordinating metal ions such as iron(II)[22] and ruthenium(II)[23] usually form low-spin complexes in the presence of *bis*bidentate imino-pyridyl ligands as the spin-pairing energy is much less than that of $\Delta_{oct,}$ making it more favourable for all six *d*-electrons to pair up in a low-spin arrangement rather than populating the higher energy e_g orbitals. Weaker field ligands such as those containing imidazole-imine[24] and benzimidazole[25,26] binding motifs are capable of binding iron(II) in its high-spin configuration as Δ_{oct} < spin-pairing energy, allowing electrons to populate the e_g orbital and subsequently form a paramagnetic d^6 iron(II) complex (figure 4). Studying high-spin iron(II) complexes by means of NMR can be more complicated relative to diamagnetic compounds, as the unpaired electrons influence and increase spin relaxation rates, resulting in broad NMR spectra with high chemical shifts.

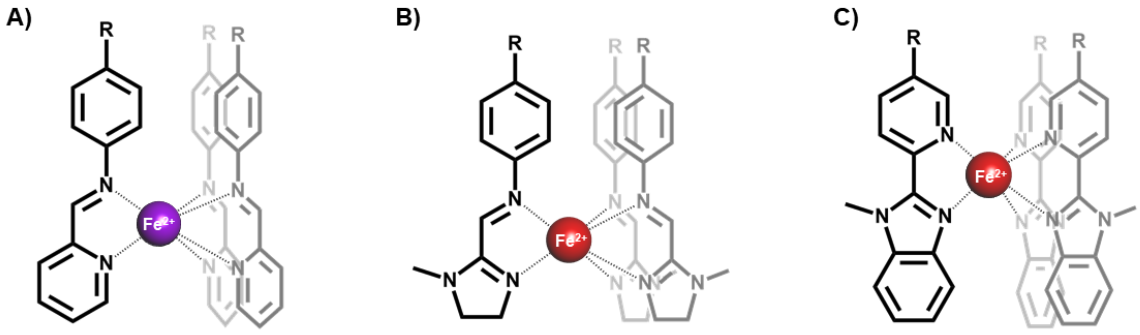

Figure 4. Iron(II) coordinated to three bidentate ligands in A: a low-spin iron(II) configuration (purple) bound by three imino-pyridyl ligands, B: a high-spin iron(II) configuration (red) bound by three imidazole-imine ligands and C: a high-spin iron(II) configuration (red) with three benzimidazole ligands bound.

In comparison to first-row octahedral metal complexes, tetrahedral complexes only have four ligands bound to the central metal atom. The splitting caused by these ligands tends to be less than that for octahedral complexes, resulting in Δ_{tet} being not only smaller than Δ_{oct}, but also smaller than the spin-pairing energy, favouring a high spin electron arrangement.

7.3. Subcomponent Self-Assembly

7.3.1. Imine-Bond Formation

Dynamic imine bond formation is prevalent throughout supramolecular self-assembly systems, where the reversible reaction between an amine and an aldehyde proceeds under thermodynamic control to give a C=N imine bond (scheme 1).[27]

Scheme 1. Imine condensation reaction mechanism between an aldehyde and a primary amine resulting in the loss of a water molecule and formation of an imine bond.

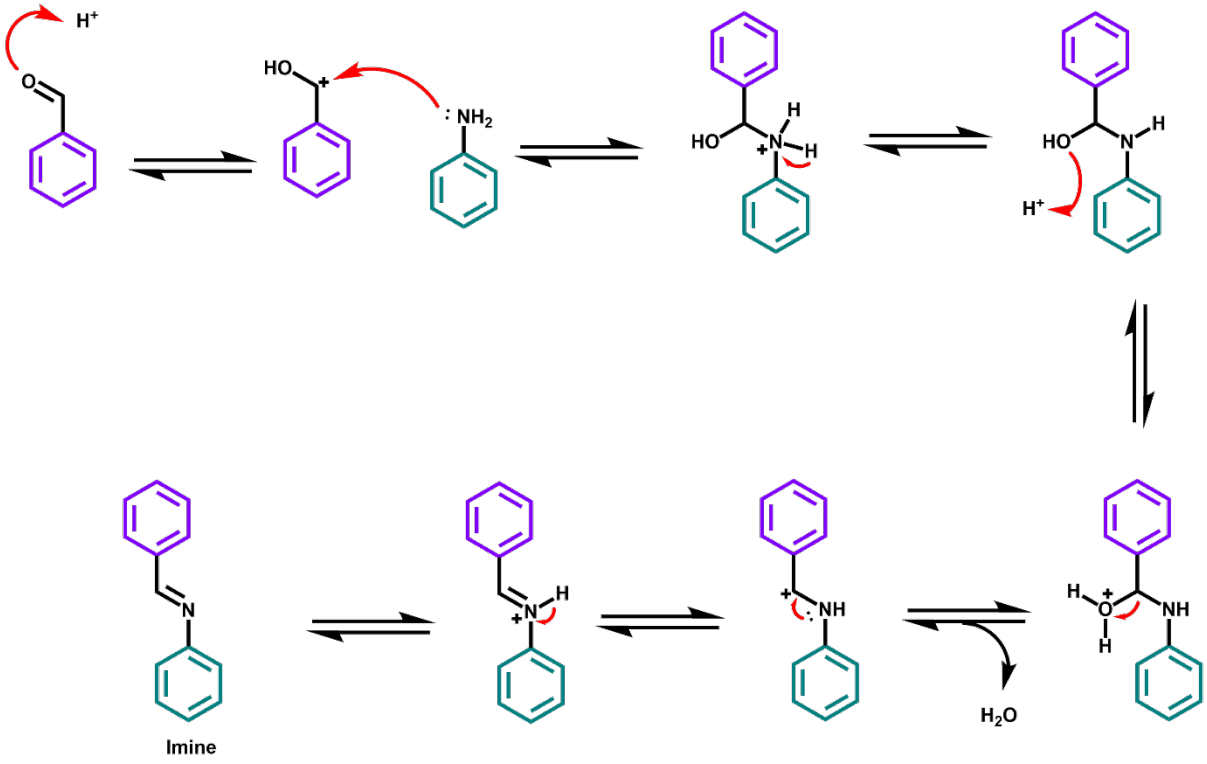

The imine is dynamic in nature and exists in equilibrium with the starting aldehyde and amine. It is possible to influence the position of this equilibrium to favour the imine, for example by introduction of suitable metal ions into the system to template the formation of metal-organic complexes. This strategy was demonstrated in 1964 by D. H. Busch,[28] and was elaborated on in 1969 by L. F. Lindoy, where the reaction between an amine and a dialdehyde gave the anticipated diimino ligand **2** (scheme 2) as the minor product, and undesired molecule **1** (scheme 2) as the major species. Upon introduction of nickel(II) ions into the system, interconversion of **1** into **2** occurred, and the nickel(II) was bound through molecule **2**'s tetradentate binding motif, resulting in formation of the desired product, nickel(II) complex **3** (scheme 2).[29]

Scheme 2. Condensation of 2-aminoethanethiol and a dialdehyde, forming major product: *bis*-thiozolidine **1**, and minor product **2**. Addition of nickel(II) templates the schiff-base **2**, resulting in the formation of the tetracoordinated complex **3** solely.

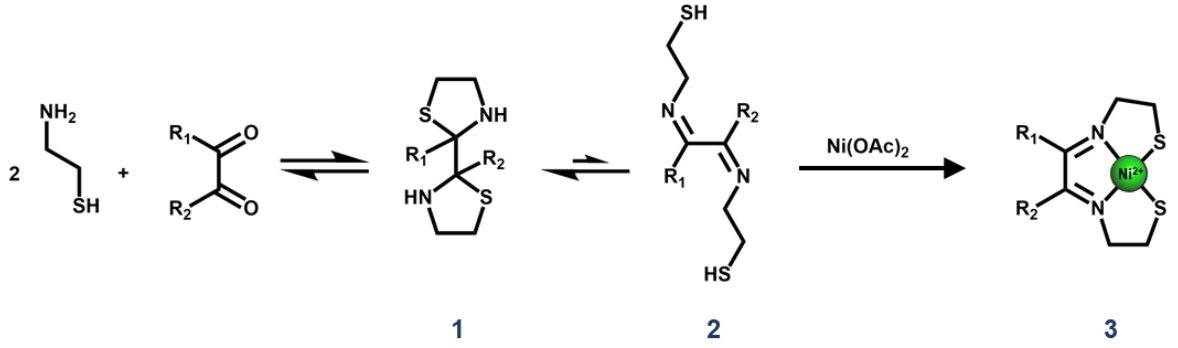

1 2 3

The metal template effect is key for the stabilisation of the imino-ligand, but the reverse has also been demonstrated in aqueous solution. In 2014, an example of mutual stabilisation was reported within a copper(I) system (scheme 3) where, in the absence of a metal, a mixture of the aldehyde and amine precursors were shown to exist in equilibrium, with the imine ligand **4** being disfavoured (scheme 3).[30] The combination of Cu(II) and metallic Cu(0) in an aqueous solution resulted in comproportionation and the formation of Cu(I) salt in small amounts. When combined, the system showed a preference for both minor species, Cu(I) and ligand **4**, resulting in the formation of Cu(I) complex **5** solely (scheme 3).

Scheme 3. Condensation of 2-aminoethanesulfonate and 2-formylpyridine, forming small amounts of the higher energy imine species **4**. Addition of a copper mixture prompts comproportionation and the resulting copper(I) species templates the formation of **5**.

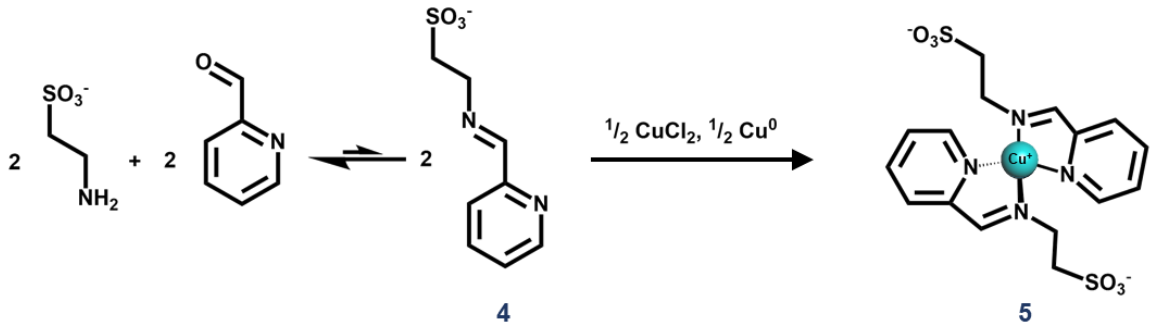

4 5

7.3.2. Triamine Molecules

In self-assembly reactions, imine condensation is often achieved using aldehydes and monoamines, where the aldehyde:amine ratio is 1:1. Imine condensation has also been accomplished using triamine molecules (figure 5) where, in combination with pyridyl-aldehyde molecules, *tris*pyridylimine binding sites ideal for octahedral coordination environments are formed.[31–34] Three commonly employed triamines include tris(2-aminoethyl)amine (TREN), tris(3-aminopropyl)amine (TRPN) and 1,1,1-tris(aminomethyl)ethane (TAME), all of which have been used in subcomponent self-assembly reactions to form three-dimensional architectures.[31,32,35]

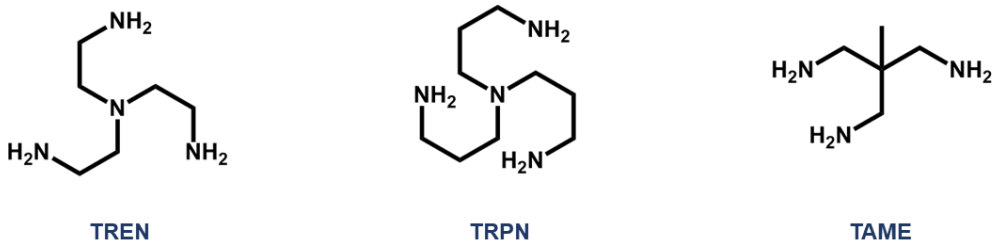

Figure 5. Triamines TREN, TRPN and TAME and their corresponding chemical structures.

Much of the research conducted into self-assembly with triamines utilises TREN,[34,36–38] and numerous examples of TREN-based functional complexes have been reported.[38–41] Tetrahedral architectures are one of the most reported three-dimensional architectures in supramolecular chemistry and in 2015 TREN was used in combination with zinc(II) and a perylene *bis*imide ligand for the formation of a fluorescent tetrahedral construct capable of encapsulating large aromatic guests.[34] Another TREN-based tetrahedral cage was reported to encapsulate a tetrameric mixed phosphate cluster within its internal cavity, with stabilisation of the host-guest complex achieved through hydrogen bonding.[36] More recently the formation of larger constructs which incorporate TREN, such as bimetallic cubic and trigonal bipyramidal architectures, have been reported with palladium(II) and iron(II) ions.[31]

7.4. Polynuclear Architectures

Three-dimensional container molecules are highly sought after due to their unique sizes, shapes and chemical properties.[42,43] Container molecules possess well-defined void space and often have a different internal environment compared with the surrounding bulk solvent. This feature gives many architectures the ability to encapsulate smaller guest molecules, forming host-guest complexes that are often stabilised by non-covalent interactions. The unique capabilities of this class of compound have been utilised for the stabilisation of reactive guests,[6,44,45] photoreactions[46–48] and catalysis.[12,13,49] As the supramolecular field continues to develop, the search for more intricate complexes with different cage geometries has become more appealing.

7.4.1. Helical Complexes

Metal-organic helicates do not have a fixed formula, but can be described as metal containing helices,[50] and are often double[51] or triple-stranded[52], although examples of single stranded helicates do exist (figure 6).[53] Careful design has allowed increasingly complex helical structures to be formed through subcomponent self-assembly,[44,45] but their restricted void space limits their potential applications in host-guest chemistry. Helicates have, however, shown promise in bioinorganic settings, where they have been shown to induce the formation of DNA junctions[56] and act as cytolytic peptide mimics.[57]

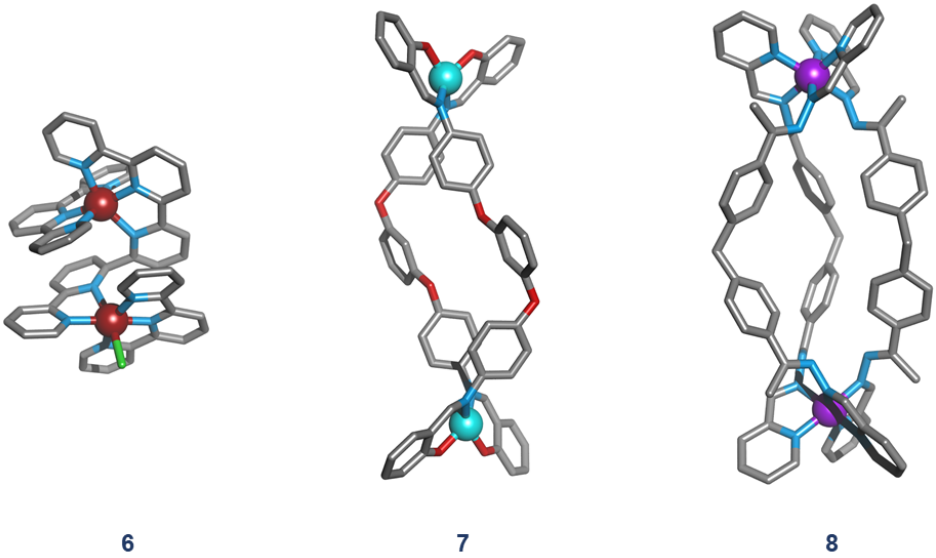

Figure 6. Single-crystal X-ray structures of ruthenium(II) single-stranded helicate **6**, copper(II) double-stranded helicate **7** and iron(II) triple-stranded helicate **8**.

Complex **6** is an unsymmetrical single stranded diruthenium(II) helicate that was shown to be electrochemically active.[53] One ruthenium centre is bound in an N_6 environment, whilst the other is bound to five nitrogen atoms and one chloride anion. Dinuclear double stranded helicate **7** is a copper(II) based helical structure that binds each copper in a $[CuO_2N_2]$ arrangement.[58] Due to the flat nature of the structure it was determined that the helicate was incapable of guest binding. Helicate **8** is a triple stranded dinuclear iron(II) complex formed by three flexible ligands, and has shown promise in biomolecular DNA recognition.[59]

7.4.2. Tetrahedral Complexes

Due to their inherently charged nature, the formation of either helical or tetrahedral metal-organic constructs within a subcomponent system is often influenced by the potential templation of ions.[60] Metal-organic tetrahedra formed with neutral ligands are often inherently cationic due to the positive metal ions, making encapsulation of anionic guests highly favourable. These type of cages have been shown to encapsulate counterions already present in the system from the metal salt,[61] or anions that have been added into the system externally.[62,63] Negatively charged tetrahedra formed from metal salts and negatively charged ligands are also capable of encapsulating guest molecules and have been shown to bind externally added cationic species such as diazonium ions[64] and alkyl ammonium ions.[65,66]

The dynamic nature of self-assembled structures also allows for interconversion between different architectures in solution, and ion templation and encapsulation can act as a driving force for these types of transformations. This concept was initially reported by Raymond and co-workers who reported the interconversion between a $[Ti_2L_3]^{4-}$ helical structure **9** and a $[Ti_4L_6]^{8-}$ tetrahedron **10** through inclusion of an alkylammonium cation which was subsequently bound within the tetrahedral cavity (figure 7).[67] The reaction was successful when both $[TiO(acac)_2]$ and $[Ga(acac)_2]$ were used as the metal salts, and in both cases the tetrahedral structure was entropically unfavourable when Me_4N^+ was not present in solution.

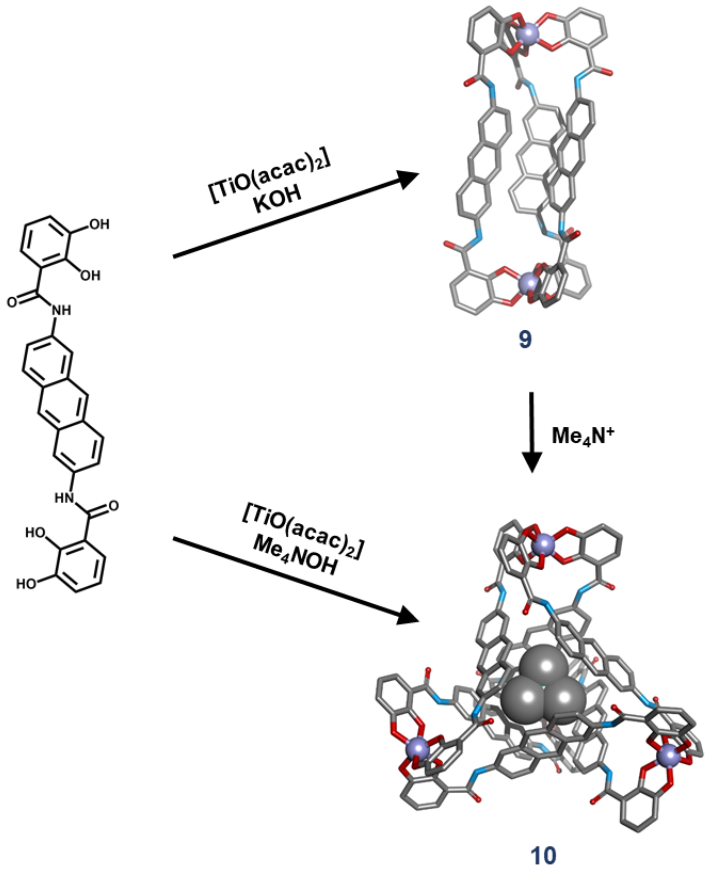

Figure 7. Self-assembly of a $[Ti_2L_3]^{4-}$ helicate from an anthracene-based ligand and titanium salt, and subsequent conversion of the helicate to a $[Ti_4L_6]^{8-}$ tetrahedron upon introduction and encapsulation of a Me_4N^+ cation.

Structural interconversion between self-assembled complexes based on ion-templation has also been reported between anion triple helicates and tetrahedra which contain no metal ions,[68] tetrahedra and larger constructs such as square-prisms,[69] and between octa- and dodeca-metallic six stranded helicates.[70]

Cationic tetrahedra formed from metal salts and bidentate ligands containing nitrogen-donor groups have been extensively explored by supramolecular chemists. Tetrahedron **11** (figure 8) was self-assembled from an aminobenzyl urea based ligand and nickel(II) sulfate, where the SO_4^{2-} anion templated the formation of a $[Ni_4L_6]^{8+}$ tetrahedron and was bound within the central cavity of the construct.[71] The host-guest complex was stabilised by hydrogen bonds formed between the oxygens of the sulfate anion and the N-H urea protons in the ligand. Similarly, tetrahedron **12** was formed through self-assembly of cobalt(II) tetrafluroborate and a napthyl containing pyrazolyl-pyridine ligand to form a $[Co_4L_6]^{8+}$ tetrahedron with a BF_4^- anion bound in the internal void space.[72] The host-guest complex was also stabilised by hydrogen bonding, forming favourable interactions between the fluorides of BF_4^- and the methylene protons of the ligands.

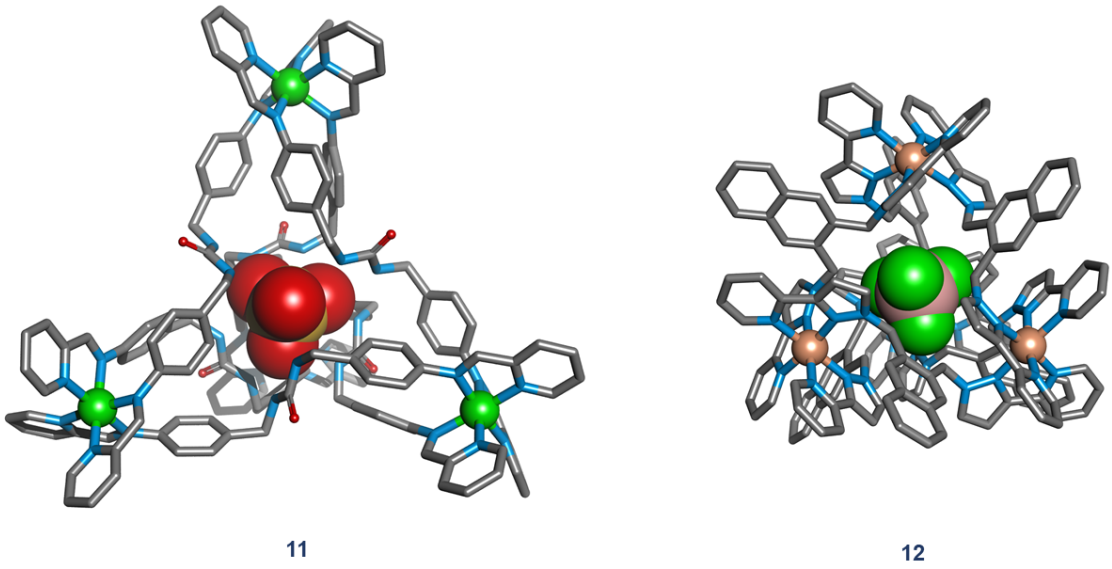

Figure 8. Single-crystal X-ray structures of $[Ni_4L_6]^{8+}$ tetrahedron **11** which encapsulates a sulfate anion, and $[Co_4L_6]^{8+}$ tetrahedron **12** which contains a tetrafluoroborate anion within its central cavity.

Binding neutral guest molecules within the internal cavities of three-dimensional tetrahedra has also been investigated.[6,73,74] Solvophobic effects often dictate the binding of neutral guests, for example iron(II) tetrahedra have been shown to bind a range of neutral organic molecules in water, whilst only a subset of these guests were encapsulated when the solvent was acetonitrile.[75] Similarly, a bimetallic porphyrin-edged tetrahedron was shown to bind up to three C_{60} molecules in nitromethane, whilst in acetonitrile the construct transformed into a cone-like shaped complex and could only encapsulate one C_{60} molecule.[76]

7.4.3. Cubic Structures

As self-assembled architectures begin to increase in size, their potential applications involving guest encapsulation also broaden. Cubic architectures often possess increased internal void space compared with smaller tetrahedra and helicates, and recently functional cubic architectures have been subject of investigation. Homometallic cubic architectures with the formula $[M_8L_{12}]^{16+}$ have been reported with a variety of symmetric ligands and first-row transition metals (figure 9, **13**),[77–80] and have been shown to bind anions[78] and ferrocene[77] within the internal cavity.

Cubic cages containing more than one type of metal ion have also been reported, for example an $[Fe_8Pd_6L_{24}T_8]^{28+}$ heterobimetallic cube was synthesized in 2018 by Lützen and co-workers, where the iron(II) ions were bound at the vertices, and the palladium(II) centres were on each face of the construct.[31] Other examples of bimetallic cubes exist where one metal is bound in a symmetric porphyrin moiety on the face of the cube, and a second metal is bound at the vertices of the structure (figure 9, **14**).[31,81–83] In 2011, the bimetallic cubic architecture **14** incorporating iron(II) and nickel(II), was reported to bind multiple equivalents of coronene, as well as fullerenes C_{60} and C_{70} within its 1340 $Å^3$ cavity. The encapsulation of polypeptides and drug molecules has also been demonstrated by a large bimetallic cubic cage containing iron(II) and zinc(II).[82] This cage was highly flexible, with a volume estimated between 3000-10,000 $Å^3$, and was able to protect the peptide guest molecules from enzymatic degradation by trypsin.

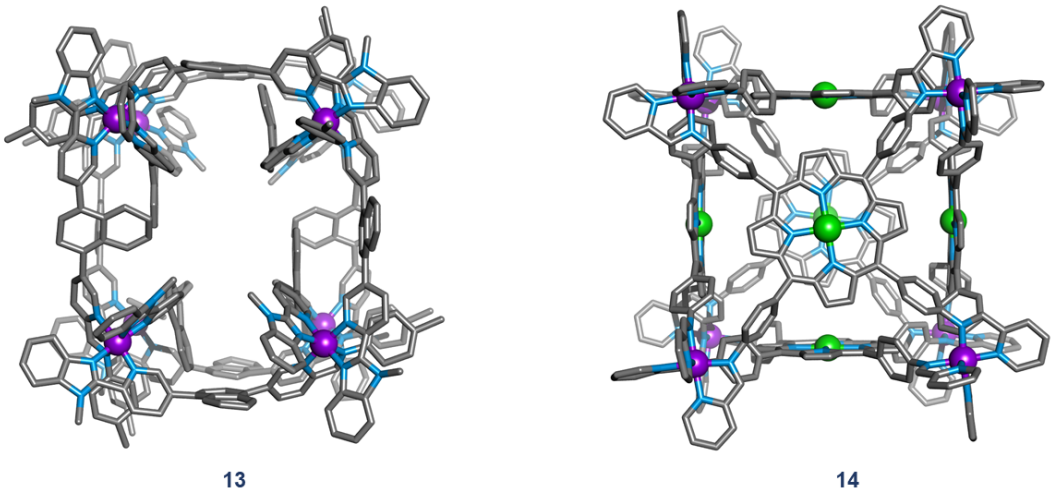

Figure 9. Single-crystal X-ray structures of cubic construct **13** formed with iron(II) and a naphthalene-based ligand, and bimetallic nickel(II) and iron(II) cube **14,** with a large internal cavity capable of fullerene encapsulation.

7.4.4. Trigonal Bipyramidal Complexes

Trigonal bipyramidal constructs like those reported in Chapters two and three, have been reported less frequently than tetrahedral and cubic architectures. These cages have previously been described with the general formula $[M_2L_3]$, where two tritopic ligands self-assemble with metal ions to form a three-dimensional supramolecular system.[84,85] Although such systems have been shown to encapsulate C_{60}[86] and to act as photophysically active complexes,[87] the rigidity of tritopic ligands limits the flexibility of the cages and thus restricts potential host-guest applications. Increasing the flexibility of trigonal bipyramidal cages can be achieved through introduction of three additional metal centres in the equatorial positions of the construct (figure 10). Bimetallic cages have been constructed using a variety of metals in the axial and equatorial positions of the trigonal bipyramid (figure 10), highlighting the versatility and hence the flexibility of this class of compound.[88] The inclusion of more than one type of metal centre also allows the functionality of each ion to be incorporated simultaneously into the same structure, as well as the possibility for interactions between the metal centres themselves which may have relevance in the field of molecular magnetism.[26]

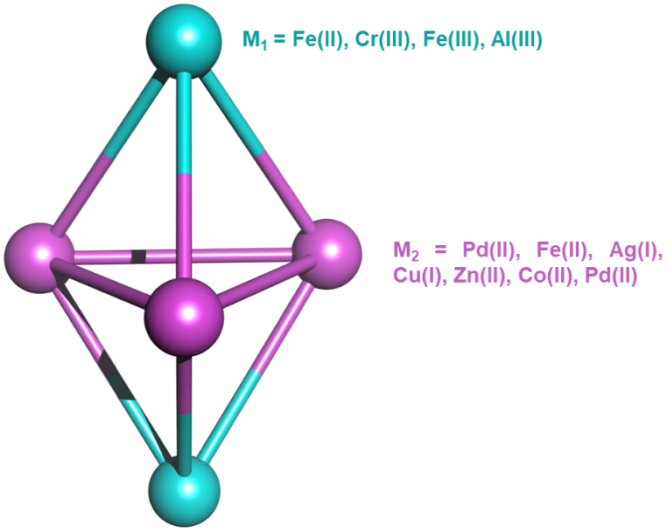

Figure 10. General structure of an $[(M_1)_2(M_2)_3L_6]$ trigonal bipyramidal structure where M_1 (aqua): axial metal centres and M_2 (pink): equatorial metal centres.

Increasing the length of the organic ligand allows larger trigonal bipyramidal architectures with increased void space to be formed (figure 11). Complex **15** incorporates six equivalents of a 1-(4-pyridyl)butane-1,3-dione ligand bound to two aluminium(III) ions in the axial positions and three *cis*-protected palladium(II) ions in the equatorial positions.[88] Similarly, construct **16** also incorporates three equatorial *cis*-protected palladium(II) ions, as well as two axial iron(II) ions and six equivalents of [3,4'-bipyridine]-6-carbaldehyde in combination with TREN.[31] Although both constructs are bimetallic $[M_5L_6]$ trigonal bipyramids, their metal-metal distances vary significantly. The distance between the two axial aluminium(III) centres of **15** was 11.11 Å, whilst the distance between the two axial iron(II) centres of **16** was considerably longer at 14.34 Å. Likewise, the average Pd-Pd distance in **15** was 11.86 Å, which was 0.27 Å shorter than the average Pd-Pd distances of **16** at 12.13 Å. Compound **16** possessed a larger internal cavity compared with **15** due to the increased length of the organic ligand used, highlighting the flexibility of this collection of complexes.

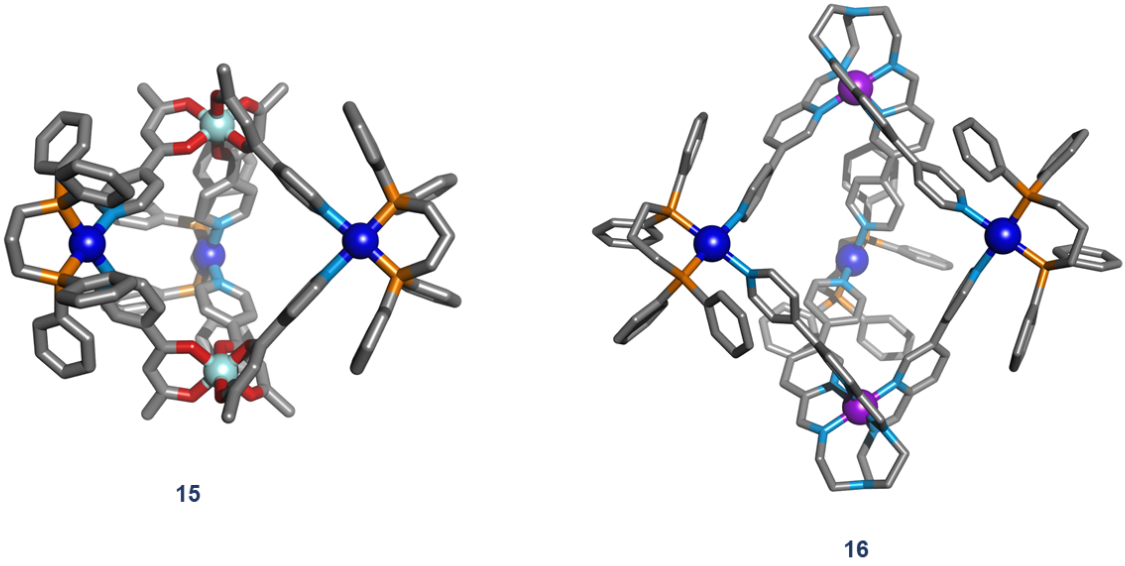

Figure 11. Single-crystal X-ray structures of bimetallic Pd(II)/Al(III) trigonal bipyramid **15** and bimetallic Pd(II)/Fe(II) trigonal bipyramid.

Although traditional design of self-assembled container molecules has focussed on the use of symmetric ligands, trigonal bipyramidal complexes often employ unsymmetrical ligands in order to accommodate the different binding preferences of the axial and equatorial metal ions within the structure. Homometallic trigonal bipyramidal architectures have also been reported, where an unsymmetrical ligand was able to bind iron(II) octahedrally in both the axial and equatorial positions of the structure in *tris*bidentate and *bis*tetradentate binding sites respectively (figure 12).[89] This complex was characterised by mass spectrometry and ^{1}H NMR spectroscopy, and DFT calculations estimated the construct had a cavity size of 415 Å^{3}.

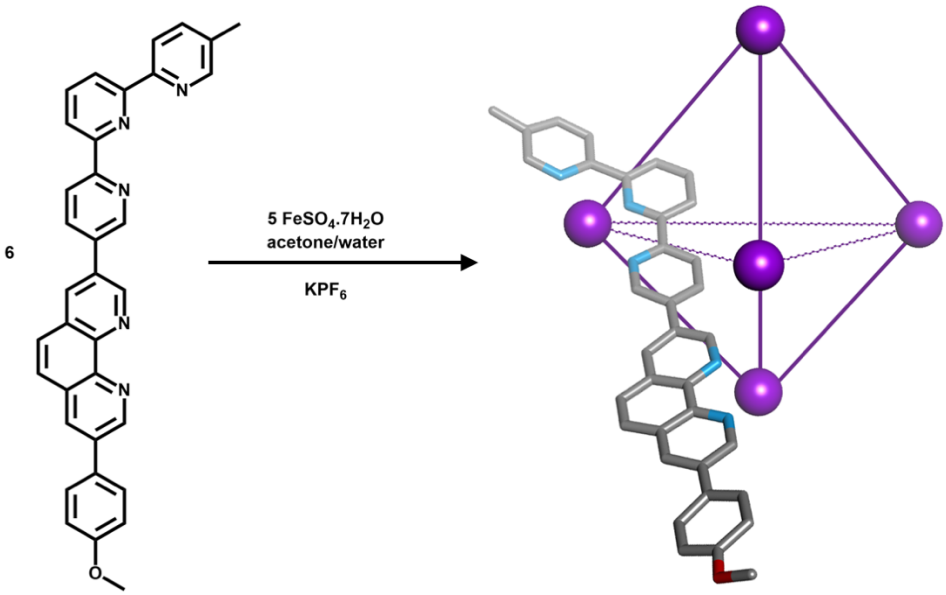

Figure 12. Formation of a homometallic $[Fe_5L_6]^{10+}$ trigonal bipyramidal cage from an unsymmetrical ligand and iron(II) sulfate.

Functional homometallic trigonal bipyramidal constructs capable of carbon dioxide fixation and sulfate sequestration have also been reported (figure 13).[90] An extended naphthalene-based dialdehyde ligand underwent subcomponent self-assembly in the presence of *p*-anisidine and cadmium(II) triflate to form $[Cd_5L_6]^{10+}$ trigonal bipyramid **17** with two OTf^- anions bound in the pockets of the architecture. One OTf^- anion was bound to the three equatorial cadmium atoms, and a CO_3^{2-} anion was also found to bind three-coordinate to the equatorial cadmium centres. Under a nitrogen atmosphere, the carbonate anion was not found within the structure, highlighting the cages ability to fix carbon dioxide from the air as carbonate within the construct.

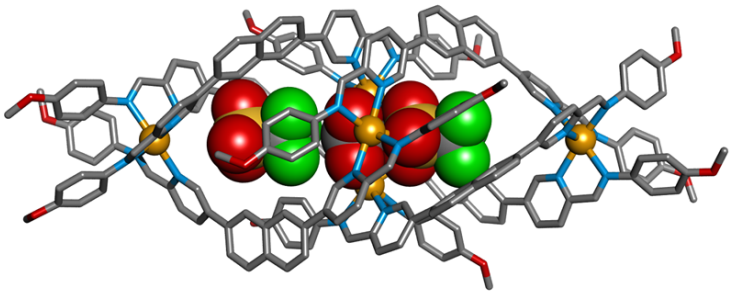

17

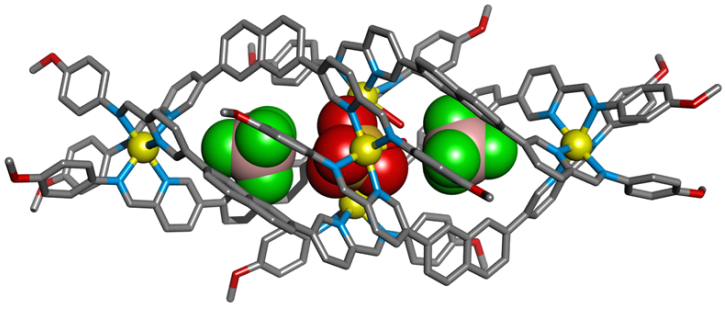

18

Figure 13. Single-crystal X-ray structures of $[Cd_5L_6]^{10+}$ trigonal bipyramid **17** containing two triflate anions and one carbonate anion within the structures internal space, and $[Zn_5L_6]^{10+}$ trigonal bipyramid **18** which contains two encapsulated tetrafluoroborate anions and a sulfate anion within its cavity.

Under the same conditions zinc(II) tetrafluoroborate formed a $[Zn_5L_6]^{10+}$ trigonal bipyramid with two BF_4^- anions bound in the pockets of the structure, as well as a central BF_4^- anion that bridged the three equatorial zinc(II) ions with three of the fluoride atoms. When sulfur dioxide was added to a solution of the zinc subcomponent mixture, trigonal bipyramidal complex **18** formed. The cage was characterised by X-ray crystallography, which highlighted the inclusion of an SO_4^{2-} anion between the equatorial zinc(II) centres.[90]

7.4.5. Larger Complexes

Supramolecular chemists strive to design and synthesize larger, more complex self-assembled architectures with increased functionality. Nature accomplishes self-assembly effortlessly[91,92] on a scale almost unimaginable by supramolecular chemists, and so research into systems which self-assemble from high numbers of components is highly attractive. The Fujita group have worked on the formation of large multicomponent systems for the past decade, using symmetric ligands and palladium(II) to form a family of large, spherical architectures with void space in excess of 100,000 Å^3 (figure 14). In 2010, the large $[Pd_{24}L_{48}]^{48+}$ rhombicuboctahedron **19** was reported by the group,[93] and just two years later they reported the first example of a synthetic cage capable of encapsulating a protein. The self-assembled $[Pd_{12}L_{24}]^{24+}$ supramolecular cage encapsulated the protein ubiquitin within its central cavity when tethered to one of the subcomponents.[7] Since then, the group have synthesized larger structures including a $[Pd_{30}L_{60}]^{60+}$ icosidodecahedra **20**, and the largest synthetic supramolecular cage to date the $[Pd_{48}L_{96}]^{96+}$ polyhedron **21**.[15]

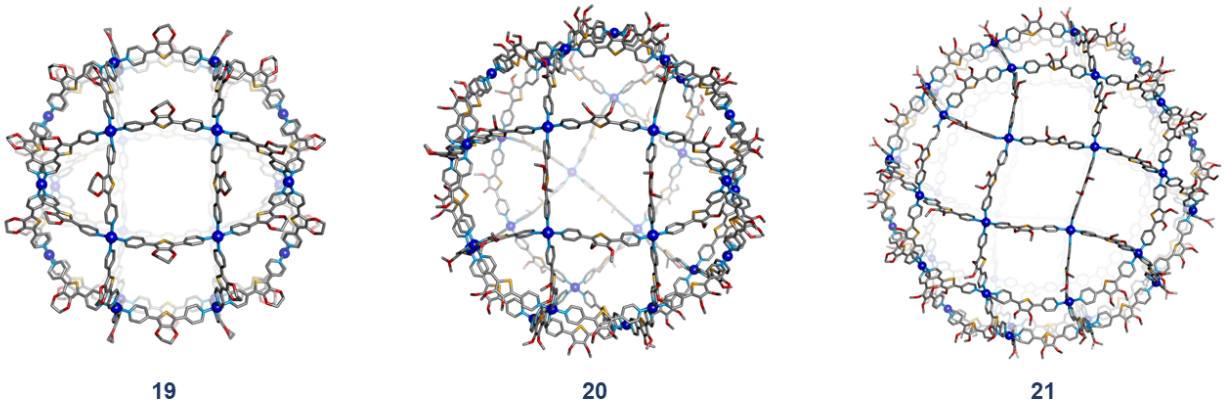

Figure 14. Single-crystal X-ray structures of the $[Pd_{24}L_{48}]^{48+}$ rhombicuboctahedron **19**, $[Pd_{30}L_{60}]^{60+}$ icosidodecahedra **20**, and $[Pd_{48}L_{96}]^{96+}$ polyhedron **21**.

Complexes with void volumes large enough to enclose biological molecules such as proteins could offer chemists an insight into the mechanisms utilised by biological systems. The magnitude of void space within such structures creates possibilities for a category of biological molecule encapsulation that has not been yet been possible to explore.

7.4.6. Increasing Complexity

Traditional design of self-assembled container molecules has relied heavily on the use of symmetric multitopic organic ligands in combination with metals to form products with high-symmetry[22] that can be readily characterised spectroscopically.[18] More recently, supramolecular architectures containing more than one type of ligand have been investigated due to their unique and increased complexity.[94–98] The functionality associated with each ligand incorporated is integrated within the final structure, with many intricate examples being reported. It can however be difficult to control the sorting within these heteroleptic systems and it's often found that multiple structures exist in equilibrium with each other,[99–101] making the formation of a singular discrete architecture objectively difficult.

One way to mitigate the issues associated with unfavourable system-sorting is the formation of low symmetry heterotopic ligands.[89,102–104] Interestingly, systems containing heterotopic ligands have been shown to favour a single defined species even when a pool of potential isomeric structures are theoretically able to form.[102,104]

7.5. Ligand Design

The following sections discuss different types of ligands used in self-assembly reactions for the formation of discrete three-dimensional architectures. We focus herein on how ligand design facilitates site-specific binding and the formation of increasingly complex structures, as well as stabilisation of metal ions in different oxidation and spin states.

7.5.1. Homotopic Ligands

The generation of *bis*bidentate ligands incorporating well-documented *mono*bidentate binding motifs[105–107] has facilitated the formation of larger, three-dimensional structures. The Nitschke group have extensively reported the use of *bis*bidentate ligand: 3,3'-bipyridine-6,6'-dicarboxaldehyde (figure 15, **L′**) in subcomponent self-assembly reactions.[22,33,63,108] Depending on the amine and metal salt involved in the self-assembly reaction, as well as any additional templating anions introduced into the system, a variety of multinuclear complexes have been observed and characterised (figure 15). In the presence of aniline and iron(II) tetrafluoroborate, **L′** self-assembles to form $[Fe_4\mathbf{L'}_6]^{8+}$ tetrahedron **22**, which was capable of encapsulating BF_4^-, OTf^- and PF_6^- anions within its cavity.[108]

Iron(II) tetrahedral cage **26** which contained a OTf⁻ anion encapsulated within the cage, was also formed with **L′** in the presence of (*S*)-1-phenylethylamine (***S*A**) and iron(II) triflate (figure 15).[109] In solution, cages often exist as a racemic mixture based on the configuration (Λ or Δ) at each metal centre present within the structure. The introduction of chiral amine ***S*A** resulted in the formation of enantiopure ΔΔΔΔ-tetrahedron **26**, where all four Fe(II) centres adopted a Δ configuration. X-ray crystallographic data of the construct highlighted the *fac*-arrangement at each Fe(II) centre, and π-stacking between the ligand pyridyl rings and the phenyl rings of ***S*A**, which had been observed previously for mononuclear iron(II) complexes formed with ***S*A.**[110]

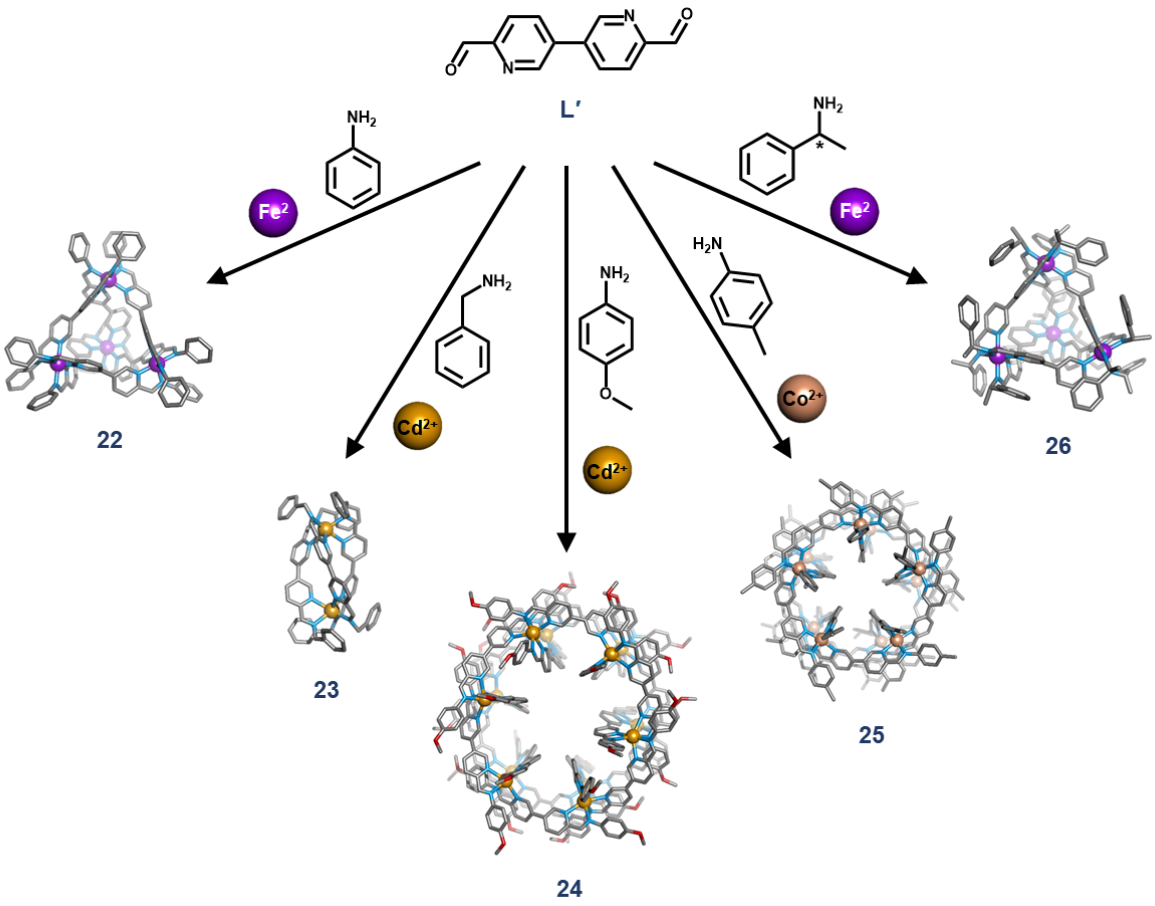

Figure 15. Self-assembly of homoditopic ligand **L′** with a range of anilines and transition metal ions resulting in the formation of multimetallic structures. Tetrahedra **22** and **26** were formed from **L′** in the presence of iron(II) and either aniline or (*S*)-1-phenylethylamine (***SA***), respectively (* denotes chiral centre). Small helicate **23** formed with **L′**, benzylamine and cadmium(II), whilst cadmium(II) formed hexagonal prism **24** in the presence of **L′** and *p*-anisidine. Ligand **L′** formed pentagonal prism **25** in the presence of *p*-toluidine and cobalt(II) that was able to encapsulate small anionic guests.

Subtle differences in the subcomponent mixture, for example differing the amine molecule slightly,[111] can have a drastic influence on the resulting self-assembled product. Smaller helical assemblies like **23** can be formed with **L′** when the metal salt is cadmium(II) triflate and the amine is benzylamine,[32] however, when the amine employed was instead *p*-anisidine, a large $[Cd_{12}L_{18}]^{24+}$ hexagonal prism **24** was formed, which contained six peripheral pockets with an average volume of 141 Å^3.[32] Analysis of the single-crystal X-ray structure of **23** revealed favourable π–π stacking interactions between the phenyl rings of benzylamine and the pyridylimine rings of the ligand, stabilising the resulting helical structure.

When the amine used was *p*-toluidine, cobalt(II) perchlorate self-assembled with **L′** to form $[Co_{10}\mathbf{L'}_{15}]^{20+}$ pentagonal prism **25**, capable of binding halide anions, as well as N_3^-, OCN^- and SCN^-, within its central cavity.[112] The formation of $[M_{10}\mathbf{L'}_{15}]^{20+}$ pentagonal prisms has also been observed with nickel(II), zinc(II) and cadmium(II) salts in the presence of *p*-toluidine.[22,63]

7.5.2. Heterotopic Ligands

Utilising *bis*bidentate homotopic ligands in self-assembly is well documented and has become highly attractive due to the predictability of the resulting architectures formed. Symmetrical starting materials often allow for greater control over a system than lower symmetry elements, allowing products to be more readily anticipated and characterised. In contrast, the use of heterotopic ligands in self-assembly reactions remains relatively sparse, despite the potential for the supramolecules generated to display applications yet to be observed for this class of compound.[113] The more synthetically challenging procedures involved in the generation of heterotopic ligands, as well as the complexity arising from characterisation of lower symmetry species is often presumed to lead to difficulties in both predicting and interpreting the outcome of self-assembly reactions that use heterotopic ligands.[113]

Examples of three-dimensional architectures formed with heterotopic ligands have been reported but so far remain limited. In 2013, cobalt(II) pentanuclear trigonal bipyramidal cage **27** was formed from an heterotopic pyridine-pyrazole based ligand (figure 16).[114] This cage was calculated to have an internal volume of 15,028 Å^3, making it highly attractive for potential host-guest applications. The same ligand was also shown to form a mononuclear one-dimensional helical polymer species with manganese(II), and a magnetically active tetranuclear grid with copper(II).[114]

Subcomponent systems containing heterotopic ligands have also been shown to form cubic constructs in the presence of nickel(II).[115] A methoxy pyridyl ligand underwent imine condensation with an imidazole based aldehyde in the presence of nickel bromide, forming $[Ni_8L_{12}Br_4]$ cubic cage **28** with a volume of 227 $Å^3$. The addition of methylamine into a THF solution of **28** resulted in displacement of the methyoxy pyridyl ligand and formation of rhombic dodecahedral cage **29** which contained fourteen nickel(II) ions and an internal volume of around 1000 $Å^3$.

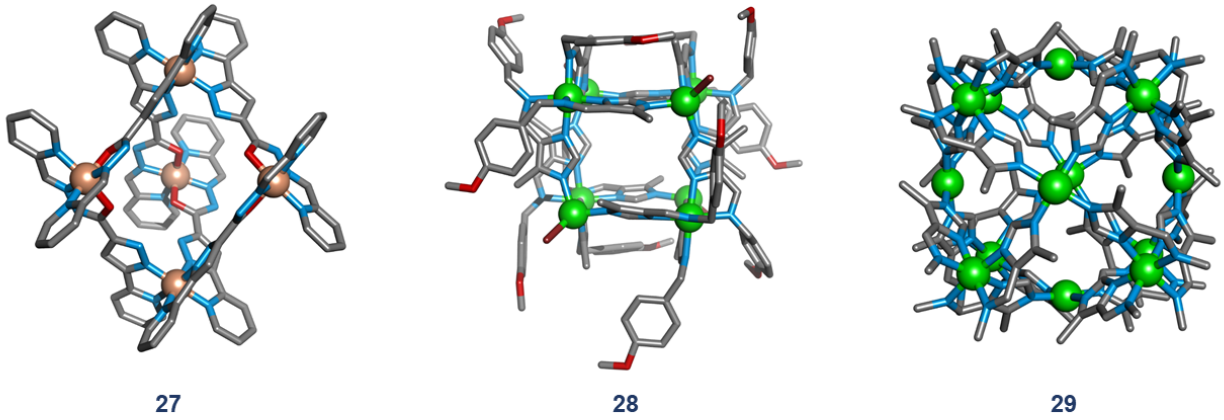

Figure 16. Single-crystal X-ray structures of cobalt(II) trigonal bipyramidal cage **27**, nickel(II) cubic cage **28** and nickel(II) rhombic dodecahedral cage **29**, all formed using heterotopic ligands.

As well as the potential to form highly complex architectures, heterotopic ligands can also contain different types of binding sites to complex metals with different coordination geometries and spin states.

7.5.3. Spin-State Stabilisation of Iron(II)

The field strength of ligands employed in subcomponent self-assembly reactions can affect the spin-configuration of the metals they bind. For octahedral coordination centres, nitrogen atoms in unsubstituted pyridyl rings often split the t_{2g} and e_g energy levels significantly enough for $\Delta E >$ spin-pairing energy. For iron(II), this means the pyridyl imine binding site often binds iron in its low-spin configuration.[116] Benzimidazole[25,26] and imidazole-imine[24] groups exhibit weaker field strengths than that of pyridyl-imines and often $\Delta_{oct} <$ spin-pairing energy, allowing iron(II) to be stabilised in its high-spin state.[116]

Functional self-assembled low-spin iron(II) architectures built with pyridylimine ligands have been investigated extensively by the Nitschke group.[74,77,81,117–119] Cubic construct **30** was assembled from a dialdehyde-based ligand, *p*-toluidine and iron(II) triflimide and was shown to encapsulate a ferrocene complex within its >1000 Å^3 cavity.[77] The binding of larger ferrocenyl complexes such as methylferrocene and acetylferrocene was also investigated but the compounds did not interact with cage **30**, highlighting the significance steric bulk has on potential encapsulation attempts.

In the presence of 2-formylpyridine and iron(II) sulfate, a bipyridine-based ligand containing two hydroxyl groups was shown to bind iron(II), forming $[Fe_{10}L_{15}]^{20+}$ prism **31** in a 90:10 MeOH:H_2O solution. This interesting construct remained intact for >2 months in solution at room temperature, but dissolution of the complex in H_2O at 50°C resulted in the interconversion into an $[Fe_4L_6]^{8+}$ tetrahedron.[118]

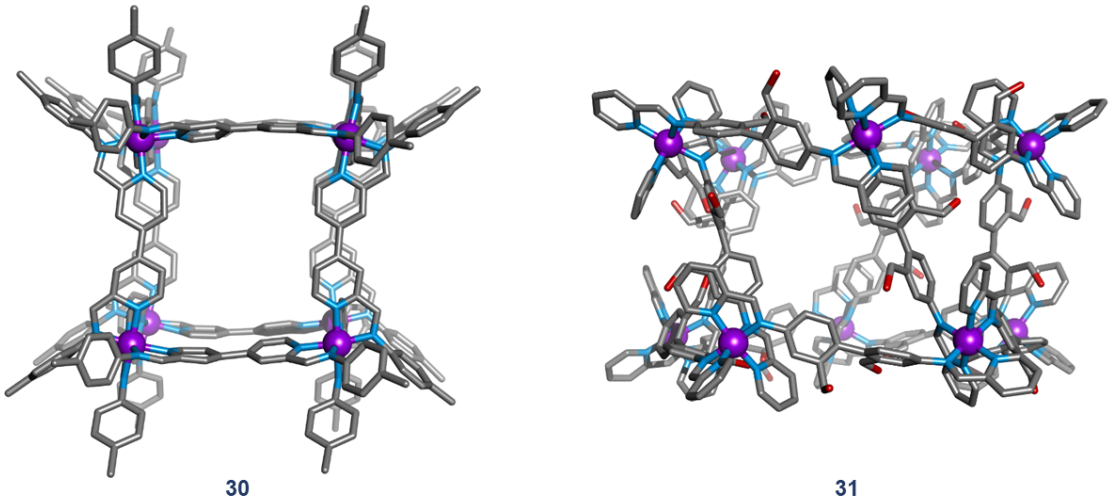

Figure 17. Single-crystal X-ray structures of iron(II) cubic architecture **30** and iron(II) prism **31**.

Both **30** and **31** are examples of self-assembled cages containing dialdehyde-based ligands that bind and stabilise iron(II) in the low-spin state, and examples of self-assembled structures containing HS Fe(II) are less common.

Several examples of three-dimensional multimetallic architectures with high-spin iron(II) bound in benzimidazole sites have been reported (figure 18).[120] Complex **32** is a mixed lanthanide/transition metal complex that contains both europium(III) and iron(II) metal centres.[121] When the ligand employed contained a methyl in the ortho-position of the pyridyl ring, the iron(II) centre was found to be strictly high-spin. This was due to significant interstrand constraints found between the ligands which prevented the Fe-N bond lengths from being compressed enough to bind the

iron(II) in a low-spin configuration. When the methyl group was in the meta-position relative to the nitrogen, the resulting heterometallic complex was reported to undergo thermal spin crossover.

Similarly, due to the strained arrangements of the benzimidazole ligands, tetranuclear grid complex **33** binds iron(II) in the high-spin state solely.[122] The tauto-conformer of this structure is a low-spin iron(II) complex which is capable of undergoing spin crossover due to the reduced strain within the structure.

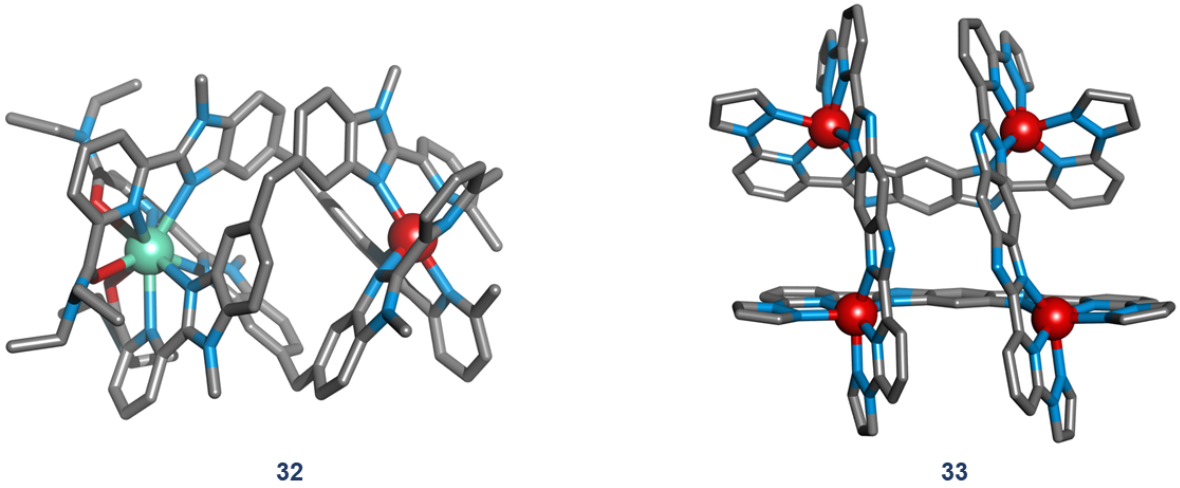

Figure 18. Single-crystal X-ray structures of mixed europium(III)/high-spin iron(II) complex **32** and high-spin iron(II) tetranuclear grid **33**.

Although examples of self-assembled iron(II) structures capable of undergoing thermal spin-crossover are reported,[123–126] three-dimensional constructs containing both high-spin and low-spin iron(II) within the same architecture at room temperature are sparse.[26] The discovery of this class of compound and the potential applications associated remains in its infancy.

7.5.4. Metalloligands

When forming complex three-dimensional architectures, a common design strategy is to carry out the synthesis in a stepwise manner. This allows improved control over the system and increases the predictability of the final structure(s). This is often achieved by using a metalloligand, a conformationally rigid metal complex which contains secondary binding sites capable of complexation with additional metal ions added to the system.[127] Metalloligands are often unsymmetrical in nature to allow specific binding of the primary metal ion, and examples of both cubes[4,31,128] and trigonal bipyramidal structures[26,31,88] formed stepwise from metalloligands have been reported.

Metalloligand **34** was formed in acetonitrile from three equivalents of [3,4'-bipyridine]-6-carbaldehyde, one equivalent of TREN and one equivalent of iron(II) tetrafluoroborate (figure 19).[31] In a second synthetic step, **34** reacted with 1.5 equivalents of [Pd(dppp)$(OTf)_2$] to form trigonal bipyramid **16** (figure 11), which contains three palladium(II) centres in the equatorial plane and two low-spin iron(II) centres in the axial positions.

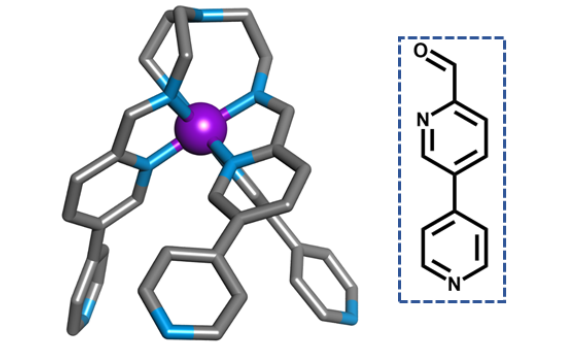

34

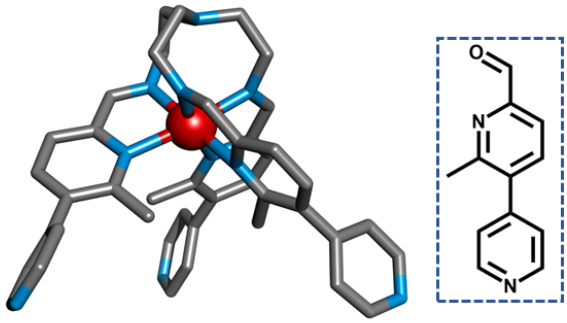

35

Figure 19. Single-crystal X-ray structures of metalloligands **34** and **35**, and their corresponding ligand structures in blue dashed boxes.

Modification of the ligand to include an ortho substituted pyridyl ring imparted significant steric strain on resulting metalloligand **35**, resulting in stabilisation of high-spin iron(II) within the complex (figure 19).[129] The steric repulsion caused by the inclusion of three methyl groups resulted in longer iron(II)-nitrogen bonds, altering the spin-state of the iron(II) centre compared with **34**. Similarly to **34**, metalloligand **35** was capable of undergoing self-assembly with 1.5 equivalents of $[Pd(dppp)(OTf)_2]$ to form a trigonal bipyramidal structure with two high-spin iron(II) centres in the axial positions, and three palladium(II) ions in the equatorial positions. Complex **35** could also self-assemble with 0.75 equivalents of $[Pd(MeCN)_4](BF_4)_2$ in acetonitrile to form a $[Fe_8Pd_6L_{24}T_8]^{28+}$ cube where, again, the iron(II) centres were bound in a high-spin configuration.

7.5.5. Inorganic Bridging Ligands

In a given system, if the organic ligands present are incapable of saturating the coordination sphere of a metal ion, smaller atoms or molecules such as hydroxides,[130] halides[131,132] or hydrides,[133] can coordinate to the centres and fulfil the preferred coordination number. Many complexes achieve this by utilising bridging ligands between metal centres within the compound, and the resulting structures have shown promise for a number of different applications.

Bridging ligands have the ability to couple metal centres, allowing communication between the ions and often granting the complex interesting properties. Transition metal complexes containing bridging ligands have been used for the reduction of protons and CO_2,[134] electron transfer between metal centres,[135] and for investigations into bridging-ligand-mediated metal-metal communication.[136,137]

7.5.6. Bridged Iron(II) Complexes

Complexes containing iron(II) centres bridged by μ_2 ligands have been reported, with ferromagnetic coupling observed between the two cationic metals in three bimetallic complexes containing either bridging fluoride or chloride ligands.[132] A *mono*(μ-F)diiron(II) complex with a linear bridging fluoride ligand that displays weak antiferromagnetic coupling between the iron(II) centres has previously been reported and characterised by ^{1}H NMR, mass spectrometry and EPR spectroscopy.[138] The system could not support sterically the inclusion of two bridging fluoride atoms, although this has been observed for other compounds. A *bis*(μ-F)diiron(II) complex was also reported and acted as a pre-catalyst for the hydrodefluorination of perfluoroolefins, and reacted with silyl compounds.[131]

7.5.7. Bridged Iron(II) / Iron(III) Complexes

Examples of mixed-valence proteins that contain both iron(II) and iron(III) centres, such as hemerythrin,[139] ribonucleotide reductase[140] and methane monooxygenase,[141] can be found throughout biology. The majority of natural examples contain bridging atoms that allow communication between metal centres, and there are now many reports of synthetic mixed-valence iron complexes where the metal centres are bridged by hydroxy,[142–144] cyano,[145] or halide[132,146] atoms. As of present, there is only one example of a fluoride-bridged mixed iron(II)/iron(III) complex where one bridging fluoride atom connects the two metals (figure 20).[146]

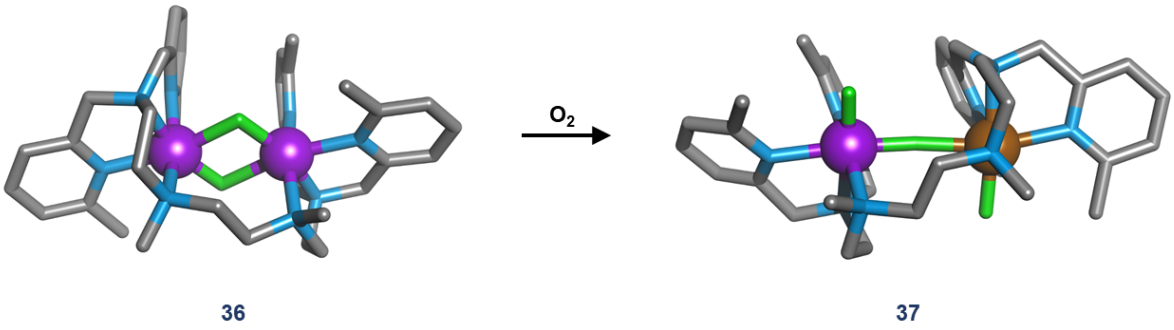

Figure 20. Single-crystal X-ray structures of homovalent *bis*(μ-F)diiron(II) complex **36**. Upon the introduction of oxygen, the complex converts to mixed-valence *mono*(μ-F)iron(II)/iron(III) complex **37**.

The reaction between dinucleating ligand: 6-methylpyridine-2-carboxaldehyde, iron(II) tetrafluoroborate and a base resulted in the formation of homovalent *bis*(μ-F)diiron(II) complex **36**, where both iron centres were characterised as iron(II) by ^{1}H NMR, X-ray crystallography, magnetic measurements and Mössbauer spectroscopy.[146] Upon introduction of air into the system, brown crystals of complex **37** were formed and analysed. Compound **37** was a mono-fluoride-bridged mixed-valence structure with both metal centres bound in an [N_4F_2] environment. As the metal oxidation number increases, the average metal-fluoride bond length decreases due to stronger electrostatic interactions between the positive metal ion and the negative fluoride ligand. This was evident from the crystal structure as the Fe(II)-F bond length was 2.162 Å, whist the Fe(III)-F bond length was significantly shorter at 1.870 Å. Each metal had an addition fluoride atom bound to their centre, as well as four nitrogen atoms from the ligand.

The fluoride atoms within these complexes are thought to have been abstracted from the BF_4^- counterions in the system and so far, the maximum number of bridging fluorides found in a mixed-valence Fe(II)/Fe(III) complex has been one. Since this discovery, there had been no more reports for

compounds of this class until the trigonal bipyramidal complex discussed in Chapter two was formed.[26] The structure presents the first literature example of a fluoride-bridged mixed-valence iron complex with more than one bridging-fluoride atom. The central $[Fe^{III}(\mu_2\text{-}F)_6(Fe^{II})_3]^{3+}$ star motif contains six fluoride atoms abstracted from BF_4^- counterions which connect one central iron(III) centre to three high-spin iron(II) ions.

7.6. Aims and Objectives

The introduction to this thesis highlighted the fundamentals of self-assembly and how the formation of functional polynuclear architectures can be achieved from ligands and transition metal ions, with a specific focus on heteroditopic ligands. The following chapters report the use of heteroditopic ligands to generate highly symmetrical three-dimensional architectures, the structures reported make a significant contribution to scarce literature in this area.

Chapter two discusses the formation of a homometallic trigonal bipyramidal architecture from a heteroditopic ligand and iron. The ligand contains a pyridyl-aldehyde unit that undergoes imine condensation with TREN, and a benzimidazole moiety capable of binding high-spin iron(II). The trigonal bipyramidal structure contains two axially bound low-spin iron(II) centres, three high-spin iron(II) centres bound within the equatorial plane, and a high-spin Fe(III) ion at the centre of the structure. The core of the structure contains an $[Fe^{III}(\mu_2\text{-}F)_6(Fe^{II})_3]^{3+}$ star motif, where the three high-spin iron(II) ions are bridged to the central iron(III) centre through six fluoride atoms that were abstracted from the BF_4^- counterions. This complex was the first literature example of a fluoride-bridged mixed-valence iron star and is notably due to the controlled incorporation of iron in three distinct spin states.[26]

Chapter three reports the formation of a flexible heterometallic trigonal bipyramid from a heteroditopic ligand, TREN and iron(II) and silver(I) salts. The ligand contains both a pyridyl-aldehyde unit and a bipyridine moiety capable of binding metal ions in their low-spin state. The resulting construct binds two iron(II) ions in the axial positions and three silver(I) ions in the equatorial plane. A series of structurally related trigonal bipyramidal architectures with different anionic guests encapsulated within the central cavity (BF_4^-, PF_6^- and SbF_6^-) are reported. When a chloride ion is bound within the central cavity of the trigonal bipyramid direct coordination of the halide anion with the equatorial metal centres is observed. This increases the coordination number of the silver ions from four to five and indicates the potential opportunities for this architecture as a supramolecular catalyst. The final sections of this chapter details the replacement of the equatorial silver(I) ions with copper (I) and characterisation of the mixed metal $[Fe_2Cu_3\mathbf{L}_6T_2]^{7+}$ trigonal bipyramidal structure. Preliminary investigations into the effects of anions and phosphine at the copper(I) centres are also reported.[62]

The integrative sorting of an M_4L_6 tetrahedral iron(II) cage is reported in Chapter four. The heteroleptic cage, which incorporates one unique vertex, is formed through self-assembly of the heteroditopic ligand described in Chapter three alongside a symmetric *bis*bipyridine ligand in combination with TREN and iron(II) ions. When iron(II) perchlorate is used as the metal salt the integratively sorted cage is formed exclusively. In contrast, when other iron(II) salts are used (BF_4^-, OTf^- and NTf_2^-), a mixture of a homoleptic cage formed with the symmetric *bis*bipyridine ligand, the heteroleptic cage and the mononuclear species $[Fe\mathbf{L}_3T]^{2+}$ were found to co-exist in solution.[101]

The final chapter contains a number of miscellaneous polynuclear architectures formed from subcomponent self-assembly reactions. All the work is unpublished and all the complexes are either fully or partially characterised. These fundamental results have relevance to the work described in the preceding chapters, and may form the basis of future work.

7.7. References

1 J. Lehn, *Angew. Chem. Int. Ed.*, 1988, **27**, 89–112.

2 E. Fischer, *Ber. Dtsch. Chem. Ges.*, 1894, **27**, 2985–2993.

3 D. E. Koshland, *Angew. Chem. Int. Ed.*, 1995, **33**, 2375–2378.

4 S. Sanz, H. M. O'Connor, E. M. Pineda, K. S. Pedersen, G. S. Nichol, O. Mønsted, H. Weihe, S. Piligkos, E. J. L. McInnes, P. J. Lusby and E. K. Brechin, *Angew. Chem. Int. Ed.*, 2015, **54**, 6761–6764.

5 P. J. Smith, M. V Reddington and C. S. Wilcox, *Tetrahedron Lett.*, 1992, **33**, 6085–6088.

6 P. Mal, B. Breiner, K. Rissanen and J. R. Nitschke, *Science*, 2009, **324**, 1697–1699.

7 D. Fujita, K. Suzuki, S. Sato, M. Yagi-Utsumi, Y. Yamaguchi, N. Mizuno, T. Kumasaka, M. Takata, M. Noda, S. Uchiyama, K. Kato and M. Fujita, *Nat. Commun.*, 2012, **3**, 2–8.

8 D. W. Hobson, *Compr. Biotechnol. Second Ed.*, 2011, **3**, 683–697.

9 L. L. K. Taylor, I. A. Riddell and M. M. J. Smulders, *Angew. Chem. Int. Ed.*, 2019, **58**, 1280–1307.

10 A. Galan and P. Ballester, *Chem. Soc. Rev.*, 2016, **45**, 1720–1737.

11 M. J. Webber and R. Langer, *Chem. Soc. Rev.*, 2017, **46**, 6600–6620.

12 D. H. Leung, R. G. Bergman and K. N. Raymond, *J. Am. Chem. Soc.*, 2007, **129**, 2746–2747.

13 C. J. Brown, R. G. Bergman and K. N. Raymond, *J. Am. Chem. Soc.*, 2009, **131**, 17530–17531.

14 L. Li, Y. Zhang, M. Avdeev, L. F. Lindoy, D. G. Harman, R. Zheng, Z. Cheng, J. R. Aldrich-Wright and F. Li, *Dalt. Trans.*, 2016, **45**, 9407–9411.

15 D. Fujita, Y. Ueda, S. Sato, N. Mizuno, T. Kumasaka and M. Fujita, *Nature*, 2016, **540**, 563–566.

16 Y. Y. Chia and M. G. Tay, *Dalt. Trans.*, 2014, **43**, 13159–13168.

17 H. L. M. V. A. N. Gaal and J. G. M. V. A. N. D. E. R. Linden, *Coord. Chem. Rev.*, 1982, **47**, 41–54.

18 D. L. Caulder and K. N. Raymond, *Acc. Chem. Res.*, 1999, **32**, 975–982.

19 R. Chakrabarty, P. S. Mukherjee and P. J. Stang, *Chem. Rev.*, 2011, **111**, 6810–6918.

20 D. Venkataraman, Y. Du, S. R. Wilson, K. A. Hirsch, P. Zhang and J. S. Moore, *J. Chem. Educ.*,

1997, **74**, 915–918.

21 A. Greenwood, N. N. & Earnshaw, *Chemistry of the Elements*, 1997, chapter 27.

22 I. A. Riddell, Y. R. Hristova, J. K. Clegg, C. S. Wood, B. Breiner and J. R. Nitschke, *J. Am. Chem. Soc.*, 2013, **135**, 2723–2733.

23 S. Choudhury, A. K. Deb and S. Goswami, *J. Chem. Soc. Dalt. Trans.*, 1994, 1305–1310.

24 L. Li, N. Saigo, Y. Zhang, D. J. Fanna, N. D. Shepherd, J. K. Clegg, R. Zheng, S. Hayami, L. F. Lindoy, J. R. Aldrich-Wright, C. G. Li, J. K. Reynolds, D. G. Harman and F. Li, *J. Mater. Chem. C*, 2015, **3**, 7878–7882.

25 B. Brachňaková, J. A. Kožíšková, J. Kožíšek, E. Melníková, M. Gál, R. Herchel, T. Dubaj and I. Šalitroš, *Dalt. Trans.*, 2020, **49**, 17786–17795.

26 L. L. K. Taylor, I. J. Vitorica-Yrezabal, I. Borilovic, F. Tuna and I. A. Riddell, *Chem. Commun.,* 2021, **57**, 11252–11255.

27 M. E. Belowich and J. F. Stoddart, *Chem. Soc. Rev.*, 2012, **41**, 2003–2024.

28 Busch, D. H. *Record Chem. Prog.* 1964, 25, 107-126.

29 L. F. Lindoy, *Coord. Chem. Rev.*, 1969, **4**, 41.

30 J. R. Nitschke, *Angew. Chem. Int. Ed.*, 2004, **43**, 3073–3075.

31 M. Hardy, N. Struch, F. Topić, G. Schnakenburg, K. Rissanen and A. Lützen, *Inorg. Chem.*, 2018, **57**, 3507–3515.

32 W. Meng, T. K. Ronson, J. K. Clegg and J. R. Nitschke, *Angew. Chem. Int. Ed.*, 2013, **52**, 1017–1021.

33 J. Mosquera, S. Zarra and J. R. Nitschke, *Angew. Chem. Int. Ed.*, 2014, **53**, 1556–1559.

34 P. D. Frischmann, V. Kunz and F. Würthner, *Angew. Chem. Int. Ed.*, 2015, **54**, 7285–7289.

35 M. Seredyuk, A. B. Gaspar, V. Ksenofontov, Y. Galyametdinov, J. Kusz and P. Gütlich, *Adv. Funct. Mater.*, 2008, **18**, 2089–2101.

36 R. Chutia, S. K. Dey and G. Das, *Cryst. Growth Des.*, 2015, **15**, 4993–5001.

37 A. M. Castilla, N. Ousaka, R. A. Bilbeisi, E. Valeri, T. K. Ronson and J. R. Nitschke, *J. Am. Chem. Soc.*, 2013, **135**, 17999–18006.

38 A. J. Plajer, E. G. Percástegui, M. Santella, F. J. Rizzuto, Q. Gan, B. W. Laursen and J. R. Nitschke, *Angew. Chem.*, 2019, **131**, 4244–4248.

39 P. Zhao, M. Grillaud, L. Salmon, J. Ruiz and D. Astruc, *Adv. Synth. Catal.*, 2012, **354**, 1001–1011.

40 Z. W. Mao, L. Günter and R. Van Eldik, *J. Chem. Soc. Dalt. Trans.*, 2001, 1593–1600.

41 A. M. Castilla, T. K. Ronson and J. R. Nitschke, *J. Am. Chem. Soc.*, 2016, **138**, 2342–2351.

42 B. Breiner, J. K. Clegg and J. R. Nitschke, *Chem. Sci.*, 2011, **2**, 51–56.

43 T. K. Ronson, S. Zarra, S. P. Black and J. R. Nitschke, *Chem. Commun.*, 2013, **49**, 2476–2490.

44 M. Yoshizawa, J. K. Klosterman and M. Fujita, *Angew. Chem. Int. Ed.*, 2009, **48**, 3418–3438.

45 S. Horiuchi, T. Murase and M. Fujita, *J. Am. Chem. Soc.*, 2011, **133**, 12445–12447.

46 M. Yoshizawa, S. Miyagi, M. Kawano, K. Ishiguro and M. Fujita, *J. Am. Chem. Soc.*, 2004, **126**, 9172–9173.

47 M. Yoshizawa, Y. Takeyama, T. Okano and M. Fujita, *J. Am. Chem. Soc.*, 2003, **125**, 3243–3247.

48 X. Jing, C. He, L. Zhao and C. Duan, *Acc. Chem. Res.*, 2019, **52**, 100–109.

49 C. J. Hastings, M. D. Pluth, R. G. Bergman and K. N. Raymond, *J. Am. Chem. Soc.*, 2010, **132**, 6938–6940.

50 C. Piguet, G. Bernardinelli and G. Hopfgartner, *Chem. Rev.*, 1997, **97**, 2005–2062.

51 M. Boiocchi and L. Fabbrizzi, *Chem. Soc. Rev.*, 2014, **43**, 1835–1847.

52 C. Uerpmann, J. Malina, M. Pascu, G. J. Clarkson, V. Moreno, A. Rodger, A. Grandas and M. J. Hannon, *Chem. Eur. J.*, 2005, **11**, 1750–1756.

53 C. J. Cathey, E. C. Constable, M. J. Hannon, D. A. Tohcer and M. D. Ward, *J. Chem. Soc. Chem. Commun.*, 1990, 621–622.

54 V. E. Campbell, X. De Hatten, N. Delsuc, B. Kauffmann, I. Huc and J. R. Nitschke, *Nat. Chem.*, 2010, **2**, 684–687.

55 M. Hutin, R. Frantz and J. R. Nitschke, *Chem. Eur. J.*, 2006, **12**, 4077–4082.

56 L. Cerasino, M. J. Hannon and E. Sletten, *Inorg. Chem.*, 2007, **46**, 6245–6251.

57 S. M. Mcneill, N. M. Giles, D. Preston, P. P. Jones, J. D. Crowley and G. I. Giles, *Chem. Res. Toxicol.*, 2020, **33**, 1822–1834.

58 N. Kelly, F. Taube, K. Gloe, T. Doert, W. Seichter, A. Heine, J. J. Weigand and K. Gloe, *Crystals*, 2016, **6**, 1–15.

59 A. Oleksi, A. G. Blanco, R. Boer, I. Usón, J. Aymamí, A. Rodger, M. J. Hannon and M. Coll, *Angew. Chem. Int. Ed.*, 2006, **45**, 1227–1231.

60 N. Gimeno and R. Vilar, *Coord. Chem. Rev.*, 2006, **250**, 3161–3189.

61 C. R. K. Glasson, G. V. Meehan, J. K. Clegg, L. F. Lindoy, P. Turner, M. B. Duriska and R. Willis, *Chem. Commun.*, 2008, 1190–1192.

62 L. L. K. Taylor, I. J. Vitorica-Yrezabal and I. A. Riddell, *Unpublished*, 2021

63 I. A. Riddell, T. K. Ronson, J. K. Clegg, C. S. Wood, R. A. Bilbeisi and J. R. Nitschke, *J. Am. Chem. Soc.*, 2014, **136**, 9491–9498.

64 J. L. Brumaghim, M. Michels, D. Pagliero and K. N. Raymond, *Eur. J. Org. Chem.*, 2004, 5115–5118.

65 T. N. Parac, M. Scherer and K. N. Raymond, *Angew. Chem. Int. Ed.*, 2000, **39**, 1239–1242.

66 B. Li, W. Zhang, S. Lu, B. Zheng, D. Zhang, A. Li, X. Li, X. J. Yang and B. Wu, *J. Am. Chem. Soc.*, 2020, **142**, 21160–21168.

67 M. Scherer, D. L. Caulder, D. W. Johnson and K. N. Raymond, *Angew. Chem. Int. Ed.,* 1999, 1587–1592.

68 X. Bai, C. Jia, Y. Zhao, D. Yang, S. C. Wang, A. Li, Y. T. Chan, Y. Y. Wang, X. J. Yang and B. Wu, *Angew. Chem. Int. Ed.*, 2018, **57**, 1851–1855.

69 D. A. Roberts, B. S. Pilgrim, G. Sirvinskaite, T. K. Ronson and J. R. Nitschke, *J. Am. Chem. Soc.*, 2018, **140**, 9616–9623.

70 C. T. McTernan, T. K. Ronson and J. R. Nitschke, *J. Am. Chem. Soc.*, 2021, **143**, 664–670.

71 S. Yi, V. Brega, B. Captain and A. E. Kaifer, *Chem. Commun.*, 2012, **48**, 10295–10297.

72 R. L. Paul, Z. R. Bell, J. C. Jeffery, J. A. McCleverty and M. D. Ward, *Proc. Natl. Acad. Sci.,* 2002, **99**, 4883–4888.

73 D. Zhang, T. K. Ronson and J. R. Nitschke, *Acc. Chem. Res.*, 2018, **51**, 2423–2436.

74 T. K. Ronson, A. B. League, L. Gagliardi, C. J. Cramer and J. R. Nitschke, *J. Am. Chem. Soc.,* **136**, 15615-15624.

75 J. L. Bolliger, T. K. Ronson, M. Ogawa and J. R. Nitschke, *J. Am. Chem. Soc.*, 2014, **136**, 14545–14553.

76 D. M. Wood, W. Meng, T. K. Ronson, A. R. Stefankiewicz, J. K. M. Sanders and J. R. Nitschke,

Angew. Chem. Int. Ed., 2015, **54**, 3988–3992.

77 C. Browne, S. Brenet, J. K. Clegg and J. R. Nitschke, *Angew. Chemie*, 2013, **125**, 1998–2002.

78 I. S. Tidmarsh, T. B. Faust, H. Adams, L. P. Harding, L. Russo, W. Clegg and M. D. Ward, *J. Am. Chem. Soc.*, 2008, **130**, 15167–15175.

79 J. Yang, X. Y. Chang, K. C. Sham, S. M. Yiu, H. L. Kwong and C. M. Che, *Chem. Commun.*, 2016, **52**, 5981–5984.

80 J. A. Robson and I. A. Riddell, *Unpublished*.

81 M. M. J. Smulders, A. Jiménez and J. R. Nitschke, *Angew. Chem. Int. Ed.*, 2012, **51**, 6681–6685.

82 J. Mosquera, B. Szyszko, S. K. Y. Ho and J. R. Nitschke, *Nat. Commun.*, 2017, **8**, 6–11.

83 W. Meng, B. Breiner, K. Rissanen, J. D. Thoburn, J. K. Clegg and J. R. Nitschke, *Angew. Chem. Int. Ed.*, 2011, **50**, 3479–3483.

84 H. B. Yang, K. Ghosh, A. M. Arif and P. J. Stang, *J. Org. Chem.*, 2006, **71**, 9464–9469.

85 U. Radhakrishnan, M. Schweiger and P. J. Stang, *Org. Lett.,* 2001, **3**, 3141–3143.

86 A. Ikeda, M. Yoshimura, H. Udzu, C. Fukuhara, S. Shinkai, *J. Am. Chem. Soc.,* 1999, **2**, 4296–4297.

87 M. Wang, V. Vajpayee, S. Shanmugaraju, Y. R. Zheng, Z. Zhao, H. Kim, P. S. Mukherjee, K. W. Chi and P. J. Stang, *Inorg. Chem.*, 2011, **50**, 1506–1512.

88 S. Sanz, H. M. O'Connor, V. Martí-Centelles, P. Comar, M. B. Pitak, S. J. Coles, G. Lorusso, E. Palacios, M. Evangelisti, A. Baldansuren, N. F. Chilton, H. Weihe, E. J. L. McInnes, P. J. Lusby, S. Piligkos and E. K. Brechin, *Chem. Sci.*, 2017, **8**, 5526–5535.

89 S. Cardona-Serra, E. Coronado, P. Gaviña, J. Ponce and S. Tatay, *Chem. Commun.*, 2011, **47**, 8235–8237.

90 C. Browne, W. J. Ramsay, T. K. Ronson, J. Medley-Hallam and J. R. Nitschke, *Angew. Chem. Int. Ed.*, 2015, **54**, 11122–11127.

91 Z. Wang, L. P. Zhou, T. H. Zhao, L. X. Cai, X. Q. Guo, P. F. Duan and Q. F. Sun, *Inorg. Chem.*, 2018, **57**, 7982–7992.

92 A. R. Naik, E. R. Kuhn, K. T. Lewis, K. M. Kokotovich, K. R. Maddipati, X. Chen, J. H. K. Hörber, D. J. Taatjes, J. J. Potoff and B. P. Jena, *J. Phys. Chem. B*, 2019, **123**, 6997–7005.

93 Q. F. Sun, J. Iwasa, D. Ogawa, Y. Ishido, S. Sato, T. Ozeki, Y. Sei, K. Yamaguchi and M. Fujita,

Science, 2010, **328**, 1144–1147.

94 T. K. Ronson, D. A. Roberts, S. P. Black and J. R. Nitschke, *J. Am. Chem. Soc.*, 2015, **137**, 14502–14512.

95 W. M. Bloch, Y. Abe, J. J. Holstein, C. M. Wandtke, B. Dittrich and G. H. Clever, *J. Am. Chem. Soc.*, 2016, **138**, 13750–13755.

96 M. Wang, Y. R. Zheng, K. Ghosh and P. J. Stang, *J. Am. Chem. Soc.*, 2010, **132**, 6282–6283.

97 D. Preston, J. E. Barnsley, K. C. Gordon and J. D. Crowley, *J. Am. Chem. Soc.*, 2016, **138**, 10578–10585.

98 L. He, S. C. Wang, L. T. Lin, J. Y. Cai, L. Li, T. H. Tu and Y. T. Chan, *J. Am. Chem. Soc.*, 2020, **142**, 7134–7144.

99 S. Sudan, R. J. Li, S. M. Jansze, A. Platzek, R. Rudolf, G. H. Clever, F. Fadaei-Tirani, R. Scopelliti and K. Severin, *J. Am. Chem. Soc.*, 2021, **143**, 1773–1778.

100 H. I. A. Phillips, A. V. Chernikov, N. C. Fletcher, A. E. Ashcroft, J. R. Ault, M. H. Filby and A. J. Wilson, *Chem. Eur. J.*, 2012, **18**, 13733–13742.

101 L. L. K. Taylor, A. Sung, I. J. Vitorica-Yrezabal and I. A. Riddell, *Unpublished*, 2021.

102 J. E. M. Lewis, A. Tarzia, A. J. P. White and K. E. Jelfs, *Chem. Sci.*, 2020, **11**, 677–683.

103 A. D. Faulkner, R. A. Kaner, Q. M. A. Abdallah, G. Clarkson, D. J. Fox, P. Gurnani, S. E. Howson, R. M. Phillips, D. I. Roper, D. H. Simpson and P. Scott, *Nat. Chem.*, 2014, **6**, 797–803.

104 R.-J. Li, A. Marcus, F. Fadaei-Tirani and K. Severin, *Chem. Commun.*, 2021, 6–9.

105 S. J. Lee and S. W. Lee, *Polyhedron*, 2019, **159**, 259–264.

106 M. Wałęsa-Chorab, A. Gorczyński, M. Kubicki, Z. Hnatejko and V. Patroniak, *Polyhedron*, 2012, **31**, 51–57.

107 J. Zhang, D. Campolo, F. Dumur, P. Xiao, J. P. Fouassier, D. Gigmes and J. Lalevee, *J. Polym. Sci. Part A: Polym. Chem.*, 2015, **53**, 42–49.

108 Y. R. Hristova, M. M. J. Smulders, J. K. Clegg, B. Breiner and J. R. Nitschke, *Chem. Sci.*, 2011, **2**, 638–641.

109 N. Ousaka, J. K. Clegg and J. R. Nitschke, *Angew. Chem. Int. Ed.*, 2012, **51**, 1464–1468.

110 S. E. Howson, L. E. N. Allan, N. P. Chmel, G. J. Clarkson, R. J. Deeth, A. D. Faulkner, D. H.

Simpson and P. Scott, *Dalt. Trans.*, 2011, **40**, 10416–10433.

111 D. Schultz and J. R. Nitschke, *J. Am. Chem. Soc.*, 2006, **128**, 9887–9892.

112 I. A. Riddell, M. M. J. Smulders, J. K. Clegg, Y. R. Hristova, B. Breiner, J. D. Thoburn and J. R. Nitschke, *Nat. Chem.*, 2012, **4**, 751–756.

113 M. M. J. Smulders, I. A. Riddell, C. Browne and J. R. Nitschke, *Chem. Soc. Rev.*, 2013, **42**, 1728–1754.

114 S. Bala, A. Goswami, S. Sengupta, S. Ganguly, S. Bhattacharya, S. Khanra and R. Mondal, *Cryst. Growth Des.*, 2013, **13**, 5068–5075.

115 X. P. Zhou, Y. Wu and D. Li, *J. Am. Chem. Soc.*, 2013, **135**, 16062–16065.

116 Y. Sunatsuki, R. Kawamoto, K. Fujita, H. Maruyama, T. Suzuki, H. Ishida, M. Kojima, S. Iijima and N. Matsumoto, *Coord. Chem. Rev.*, 2010, **254**, 1871–1881.

117 W. Meng, J. K. Clegg, J. D. Thoburn and J. R. Nitschke, *J. Am. Chem. Soc.*, 2011, **133**, 13652–13660.

118 S. Zarra, J. K. Clegg and J. R. Nitschke, *Angew. Chem. Int. Ed.*, 2013, **52**, 4837–4840.

119 R. A. Bilbeisi, T. K. Ronson and J. R. Nitschke, *Angew. Chem. Int. Ed.*, 2013, **52**, 9027–9030.

120 A. W. Addison, S. Burman, C. G. Wahlgren, O. A. Rajan, T. M. Rowe and E. Sinn, *Dalt. Trans.*, 1987, 2621–2630.

121 T. Lathion, A. Fürstenberg, C. Besnard, A. Hauser, A. Bousseksou and C. Piguet, *Inorg. Chem.*, 2020, **59**, 1091–1103.

122 B. Schäfer, J. F. Greisch, I. Faus, T. Bodenstein, I. Šalitroš, O. Fuhr, K. Fink, V. Schünemann, M. M. Kappes and M. Ruben, *Angew. Chem. Int. Ed.*, 2016, **55**, 10881–10885.

123 R. A. Bilbeisi, S. Zarra, H. L. C. Feltham, G. N. L. Jameson, J. K. Clegg, S. Brooker and J. R. Nitschke, *Chem. Eur. J.*, 2013, **19**, 8058–8062.

124 A. Ferguson, M. A. Squire, D. Siretanu, D. Mitcov, C. Mathonière, R. Clérac and P. E. Kruger, *Chem. Commun.*, 2013, **49**, 1597–1599.

125 D. H. Ren, D. Qiu, C. Y. Pang, Z. Li and Z. G. Gu, *Chem. Commun.*, 2015, **51**, 788–791.

126 R. W. Hogue, S. Singh and S. Brooker, *Chem. Soc. Rev.*, 2018, **47**, 7303–7338.

127 S. Srivastava and R. Gupta, *Cryst. Eng. Comm.*, 2016, **18**, 9185–9208.

128 L. Li, Y. Zhang, M. Avdeev, L. F. Lindoy, D. G. Harman, R. Zheng, Z. Cheng, J. R. Aldrich-

Wright and F. Li, *Dalt. Trans.*, 2016, **45**, 9407–9411.

129 M. Hardy, N. Struch, J. J. Holstein, G. Schnakenburg, N. Wagner, M. Engeser, J. Beck, G. H. Clever and A. Lützen, *Angew. Chem. Int. Ed.*, 2020, **59**, 3195–3200.

130 W. R. Scheidt, B. Cheng, M. K. Safo, F. Cukiernik, J. C. Marchon and P. G. Debrunner, *J. Am. Chem. Soc*., **114**, 1992, 4420–4421.

131 J. Vela, J. M. Smith, Y. Yu, N. A. Ketterer, C. J. Flaschenriem, R. J. Lachicotte and P. L. Holland, *J. Am. Chem. Soc.*, 2005, **127**, 7857–7870.

132 Yan Zang, H. G. Jang, Y. M. Chiou, M. P. Hendrich and L. Que, 1993, *Inorganica Chim. Acta*, **213**, 41-48

133 N. M. Hein, F. S. Pick and M. D. Fryzuk, *Inorg. Chem.*, 2017, **56**, 14513–14523.

134 M. Schulz, M. Karnahl, M. Schwalbe and J. G. Vos, *Coord. Chem. Rev.*, 2012, **256**, 1682–1705.

135 H. Taube, *Ber. Bunsenges. Phys. Chem.*, 1972, **76**, 964–973.

136 M. Leschke, H. Lang and R. Holze, *J. Solid State Electrochem.*, 2003, **7**, 518–524.

137 P. Srinivasan, R. H. Mason, J. R. G. MacNeil and B. J. MacLean, *Inorganica Chim. Acta*, 2011, **366**, 116–121.

138 D. L. Reger, A. E. Pascui, M. D. Smith, J. Jezierska and A. Ozarowski, *Inorg. Chem.*, 2012, **51**, 11820–11836.

139 P. C. Wilkins and R. G. Wilkins, *Coord. Chem. Rev.*, 1987, **79**, 195–214.

140 M. Atta, K. K. Andersson, R. Ingemarson, L. Thelander and A. Gräslund, *J. Am. Chem. Soc.,* 1994, **116**, 6429–6430.

141 A. C. Rosenzweig, *Nature*, 1993, **366**, 537–543.

142 U. Bossek, H. Hummel, T. Weyhermüller, E. Bill and K. Wieghardt, *Angew. Chem. Int. Ed.,* 1996, **34**, 2642–2645.

143 Y. Sano, A. C. Weitz, J. W. Ziller, M. P. Hendrich and A. S. Borovik, *Inorg. Chem.*, 2013, **52**, 1–8.

144 R. K. Egdal, A. Hazell, F. B. Larsen, C. J. McKenzie and R. C. Scarrow, *J. Am. Chem. Soc.*, 2003, **125**, 32–33.

145 A. Mondal, Y. Li, P. Herson, M. Seuleiman, M. L. Boillot, E. Rivière, M. Julve, L. Rechignat, A. Bousseksou and R. Lescouëzec, *Chem. Commun.*, 2012, **48**, 5653–5655.

146 S. Dammers, T. P. Zimmermann, S. Walleck, A. Stammler, H. Bögge, E. Bill and T. Glaser, *Inorg. Chem.*, 2017, **56**, 1779–1782.

8. Chapter Two: Paper One - Self-Assembly of a Trigonal Bipyramidal Architecture with Stabilisation of Iron in Three Spin States

Lauren L. K. Taylor, Iñigo J. Vitorica-Yrezabal, Ivana Borilović, Floriana Tuna, and Imogen A. Riddell, 2021, **57**, 11252–11255.

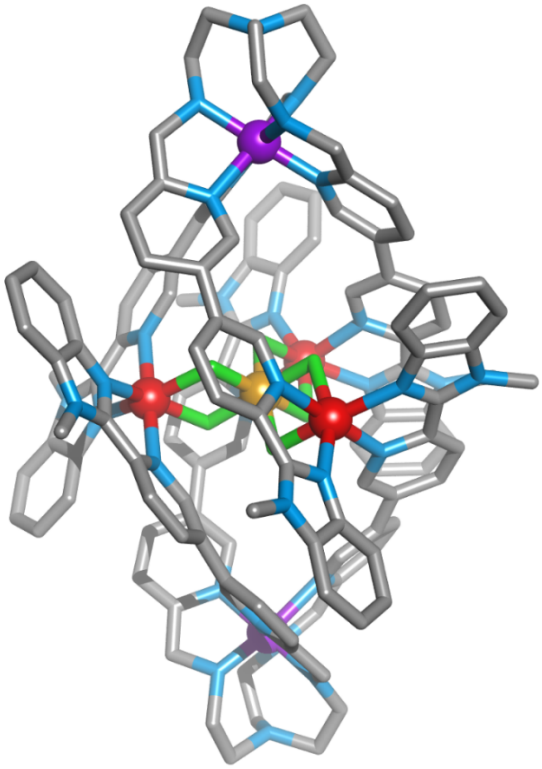

ChemComm

COMMUNICATION

Self-assembly of a trigonal bipyramidal architecture with stabilisation of iron in three spin states

Received 00th January 20xx,
Accepted 00th January 20xx

DOI: 10.1039/x0xx00000x

Lauren L. K. Taylor,[a] Iñigo J. Vitorica-Yrezabal,[a] Ivana Borilović,[a,b] Floriana Tuna,[a,b*] and Imogen A. Riddell[a*]

Self-assembly and characterisation of a supramolecular trigonal bipyramidal iron cage containing an $[Fe^{III}(\mu_2\text{-}F)_6(Fe^{II})_3]^{3+}$ star motif at its core is reported. The complex can be formed in a one step reaction using an heterotopic ligand that supports site-specific incorporation of iron in three distinct electronic configurations: low-spin Fe^{II}, high-spin Fe^{II} and high-spin Fe^{III}, with iron(II) tetrafluoroborate as the source of the bridging fluorides. Formation of a μ_2-F bridged mixed-valence Fe^{II}-Fe^{III} star is unprecedented. The peripheral high-spin Fe^{II} centres of the mixed-valence tetranuclear star incorporated in the iron cage are highly anisotropic and engage in F-mediated antiferromagnetic exchange with the central Fe^{III} ion.

Design approaches for the synthesis of self-assembled complexes have grown increasingly elaborate in recent years in a bid to diversify the structures generated and thus the applications of these molecular constructs.[1, 2] Initial approaches to metal-organic cage formation focused on the construction of capsules using symmetric, multitopic ligands in combination with a single metal ion.[3, 4] More recently heteroleptic[5] and heterometallic[6, 7] systems incorporating more than one type of ligand or metal ion have gained interest as viable routes to synthesise novel architectures displaying properties not observed in their simpler analogues.[2, 8] To date however, examples of discrete three-dimensional structures generated from heterotopic ligands and a single metal precursor remain scarce,[9] as do reports of complexes that incorporate one metal ion in a variety of spin or oxidation states.[10-12] We hypothesized that ligand **L** (Scheme 1) that features both a pyridyl benzimidazole binding unit and a pyridine aldehyde moiety, that undergoes self-assembly reactions[13] in the presence of amine and metal ion subcomponents, could give rise to novel metal-organic architectures not accessible when only one of these binding sites was incorporated. Furthermore, including pyridyl benzimidazole moieties, which favour binding of high-spin (HS) iron(II),[14, 15] alongside pyridyl imine coordination sites, which generally support complexation of low-spin (LS) iron(II),[13, 16] provided the opportunity for spin-state selective binding.

Herein we describe the design and synthesis of a heteroditopic ligand that, in combination with iron(II) tetrafluoroborate salt, generates a metal-organic cage in which the metal ions outline a trigonal bipyramidal structure of approximate D_3 symmetry. The complex incorporates six iron atoms in a mixture of spin and oxidation states and includes an $[Fe^{III}(\mu_2\text{-}F)_6(Fe^{II})_3]^{3+}$ star motif[17, 18, 19] at its core.

Reaction of one equivalent of iron(II) tetrafluoroborate salt with three equivalents of **L** resulted in the formation of a dynamic mixture containing the mononuclear $[FeL_3]^{2+}$ complex **1** (Figure *S*6). This complex undergoes a gradual and incomplete thermally induced spin crossover (SCO), which is reversible (Figure *S*30) and consistent with an Fe^{II} centre in a pseudo-octahedral $Fe^{II}N_6$ crystal field of moderate strength.[20,21] Subsequent addition of one equivalent of *tris*(2-aminoethyl)amine (TREN) to the reaction mixture resulted in a dramatic change in the ^{1}H NMR resonances consistent with formation of the LS iron(II) *tris*pyridylimine complex **2**. In the presence of TREN, iron(II) is preferentially accommodated at the pyridyl imine binding site, rather than the pyridyl benzimidazole site, due to the higher level of preorganisation afforded by the multidentate *tris*pyridylimine. The decreased bond length and reduced lability of the LS Fe^{II}–N bonds relative to their HS analogues, also promotes formation of complex **2**. The single-crystal X-ray structure of **2** (Figure *S*20) confirms a facial arrangement of the pyridyl imine ligands which is consistent with the single set of resonances per ligand proton observed in the ^{1}H NMR spectrum.[7]

Following characterisation of mononuclear complex **2**, additional equivalents of iron(II) were added to the reaction mixture as we hypothesised the C_3-metalloligands (**2**) could be brought together using their uncoordinated pyridyl benzimidazole binding sites.

[a] *Department of Chemistry, University of Manchester, Oxford Road, Manchester, M13 9PL (UK). E-mail: imogen.riddell@manchester.ac.uk*
[b] *Photon Science Institute, University of Manchester, Oxford Road, Manchester, M13 9PL (UK).*

† Electronic Supplementary Information (ESI) available: Full experimental details, NMR, ESI-MS and UV-vis spectra, SQUID data and analysis, and CIFS. Crystallographic have been deposited with the CCDC (numbers (CCDC 1952397 – 1952402). See DOI: 10.1039/x0xx00000x

ChemComm

COMMUNICATION

Scheme 1. Stepwise self-assembly of the trigonal bipyramidal complex **3**, from ligand **L** *via* the C_3-symmetric metalloligand **2**. For clarity only two of the six ligand arms forming complex **3** are shown explicitly. Iron spin and oxidation states are depicted by coloured spheres: high-spin iron(II) red, low-spin iron(II) purple and iron(III) orange.

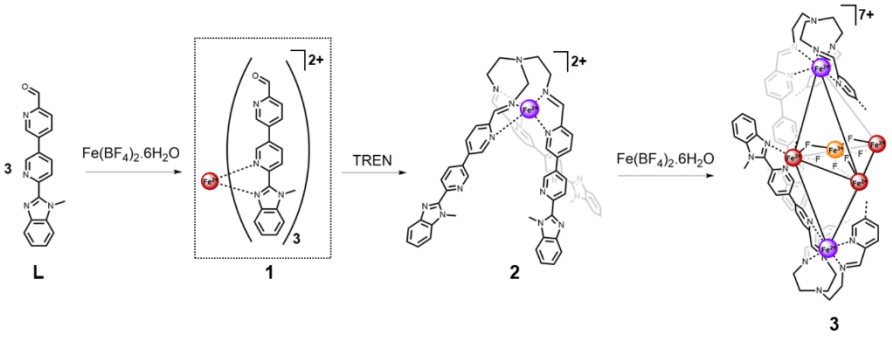

Analysis of crystals grown through diffusion of diethyl ether into an acetonitrile mixture of $Fe(BF_4)_2$ and **2** revealed the structure of the multinuclear species (**3**) to be a mixed oxidation iron complex incorporating an $[Fe_4F_6]^{3+}$ star motif at its centre (Figure 1). High-resolution mass spectral analysis (Figure *S*14) was consistent with a complex cation containing two equivalents of metalloligand **2** and a mixed valent $Fe(II)_3Fe(III)$ core bridged by six fluoride ligands.

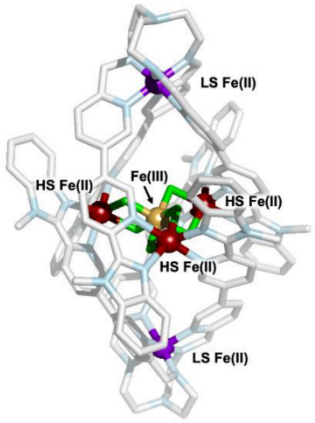

Figure 1. Single-crystal X-ray structure of the cationic portion of complex **3**. The different spin and oxidation states of the iron atoms are highlighted; purple: low-spin (LS) iron(II); red: high-spin(HS) iron(II); yellow: high-spin iron(III); green: fluoride ions; pale-blue: nitrogen; light-grey: carbon.

Bond valence sum (BVS) analysis (Supporting Information S3) supports assignment of the apical irons in **3** as LS iron(II), while those bound by two bridging fluorides and two pyridyl benzimidazoles moieties were assigned as HS iron(II) sites. The latter connect to the central Fe^{III} ion via two μ_2-F^- ligands (Fe^{II}-F bond lengths 2.089(8)-2.112(6) Å; Fe^{III}-F bond lengths 1.898(8)-1.932(5) Å; average Fe^{II}-F-Fe^{III} bridging angle 102.53(3)°). This is the first literature example of a F-bridged mixed valence iron star. The average Fe^{II}...Fe^{III} and Fe^{II}...Fe^{II} distances of 3.121(4) and 5.407(14) Å, respectively, are shorter than those observed in oxo-bridged iron stars.[18] Comparison of the *tris*pyridylimine iron bonds in complexes **2** and **3** confirmed both were LS Fe^{II} ions, and no significant change in the Fe^{II}-N bond lengths are required to generate the higher nuclearity structure.

^{1}H NMR analysis of the intense purple solution of **3** revealed resonances spanning chemical shift values from −2 to 136 ppm (Figure *S*11). Diffusion ordered spectroscopy (DOSY) NMR (Figure *S*12) confirmed that resonances at 23 and 28 ppm were consistent with formation of a structure with a diffusion coefficient of 6.32×10^{-10} m^2 s^{-1}, corresponding to a structure with a hydrodynamic radius of 12.6 Å. This value is in agreement with the solid state data which indicates that **3** is 22.4 Å along its maximum dimension. Variable temperature ^{1}H NMR studies (Figure *S*13) provided no evidence of SCO for complex **3** within the solution state accessible temperature range (−38 to 70°C).

Formation of **3** could not have been predicted based on previous results and established design criteria.[3] In combination with transition metals, linear homotopic *bis*bidentate ligands featuring either two pyridyl benzimidazoles[22] or two pyridyl imine moieties generated with TREN[23] generate M_4L_6 tetrahedra and M_2L_3 helicates. Furthermore, analysis of self-

assembly reactions with six equivalents of *p*-toluidine and **L** alongside four equivalents of metal supported formation of a $[Fe_4\mathbf{L}_6]^{8+}$ tetrahedron (Supporting Information S1.3.4).

Central to the formation of **3** are the fluoride bridges which connect the Fe^{III} ion with the three surrounding HS Fe^{II} centres. Since no traditional fluorinating agent was added, the tetrafluoroborate counterions are proposed as the source of fluoride. Generation of fluoride from tetrafluoroborate has previously been attributed to Lewis acid assisted abstraction, hydrolysis or the presence of a base,[24] all of which are present under the conditions of our reaction. Formation of a $M_4(\mu_2\text{-}F)_6$ coordination motif has only previously been reported with a family of complexes with the outer metal atoms being supplied through titanocenes.[25]

In addition to fluoride generation, we also report *in situ* oxidation of iron(II).[11,21,26] Following formation of **3** no further oxidation was observed and the complex was stable in air, in the solid state over a period of weeks, and in acetonitrile which had a stream of air blown through it for a day. Attempts to synthesize **3** via *in situ* reduction of iron(III) with DMF, following a recent report,[10] were unsuccessful and yielded an orange solution of unknown composition.

SQUID measurements for **3** gave $\chi_M T = 12.85$ cm^3 K mol^{-1} (χ_M = molar magnetic susceptibility) at room temperature in agreement with the presence of a magnetic $Fe^{II}_3Fe^{III}$ entity (Figure 2; $\chi_M T = 13.37$ cm^3 K mol^{-1} for three $S = 2$ and one $S = 5/2$ non-interacting centres, assuming g = 2), along with two non-magnetic ($S = 0$) LS Fe^{II} centres. Upon cooling, $\chi_M T$ decreases slowly until 50 K and then more rapidly to reach 3.67 cm^3 K mol^{-1} at 2 K (Figure 2B), indicative of weak antiferromagnetic interactions between metal centres coupled with zero-field splitting (ZFS) effects at the lowest temperature. In agreement with this, the *M* vs. *H* curves (*M* = molar magnetization) at 2 and 4 K show no sign of saturation under the 0-7 T applied magnetic fields (inset Figure 2B), indicative of large magnetic anisotropy. Consistent with the solution state data, no evidence for temperature dependant SCO was observed for **3**. Simultaneous fitting of $\chi_M T$ vs. *T* and *M* vs. *H* was performed using PHI.[27] The spin Hamiltonian used[28] includes the exchange between the peripheral HS Fe^{II} with the central HS Fe^{III} (J_1) and with its nearest neighbouring HS Fe^{II} (J_2) (Figure 2A), and gave $g = 1.98(01)$, $D = 9.06(13)$ cm^{-1}, $J_1 =$ −1.58(03) cm^{-1} and $J_2 =$ −0.19(02) cm^{-1}, where *g* is the *g*-factor of individual Fe centres and *D* is the axial ZFS term for HS Fe^{II} ions (Supporting Information *S*5). Attempts to model the experimental magnetic data with $J_2 = 0$ gave unsatisfactory results, but further inclusion of an intermolecular interaction term of $zJ = -0.011$ cm^{-1} enabled a good fit (Figure *S*31 and Table *S*10). Nevertheless, both models give the exchange interaction through μ_2-F bridges as weakly antiferromagnetic ($J_2^{FeII\text{-}FeIII} \cong$ -1.6 cm^{-1}). As **3** is the first molecular mixed-valence $Fe^{II}_3Fe^{III}$ system with μ_2-F bridges comparison of our coupling constants with precedent is not straightforward. Structurally related $[Fe^{III}_4(\mu\text{-}O)_6]^{6+}$ compounds were reported to display antiferromagnetic coupling.[19, 29] In contrast, the $[Fe^{III}(\mu\text{-}O)_6Fe^{II}_3]^{3+}$ homologue displays weak ferromagnetic exchange via μ_2-O ($J = 2.77$ cm^{-1}),[18] though the peripheral Fe^{II} centres still couple antiferromagnetically. The Fe^{II}-F and Fe^{III}-F bond lengths in **3** are shortened by 0.048 and 0.084 Å, respectively, compared to the equivalent ones in the oxo-bridged homologue, while the Fe^{II}...Fe^{III} distance is reduced by 0.104 Å. These differences are sufficient to cause variation in magnetic behaviour. Diiron(II) complexes with an $[Fe^{II}(\mu_2\text{-}F)_2Fe^{II}]^{2+}$ core were found to be either weakly antiferromagnetic (J = -0.26 cm^{-1})[30] or weakly ferromagnetic ($J = 0.6$ cm^{-1}).[31] A triple fluoride-bridged complex $[F_3Fe^{III}(\mu_2\text{-}F)_3Fe^{III}F_3]^{3-}$ whose Fe-F-Fe bridging angles average to 90.6° also shows weak ferromagnetism ($J = 0.24$ cm^{-1}).[32] While, diiron complexes with a single μ_2-F bridging unit manifest a stronger antiferromagnetic exchange (16 < -J < 36 cm^{-1})[33] due to a better magnetic orbital overlap enabled by a wider (151-180°) Fe-F-Fe bridging angle. In agreement with this, the $[FFe^{II}(\mu_2\text{-}F)Fe^{III}F]^{2+}$ complex (Fe-F-Fe 166.1°) exhibits stronger antiferromagnetic exchange (J = -10.1 cm^{-1})[30] than **3**. Ac susceptibility measurements on **3** detected frequency-dependent tails above 1.8 K that could indicate weak slow magnetic relaxation.

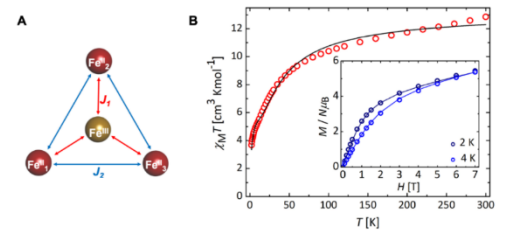

Figure 2. A: Coupling scheme depicting the magnetic $Fe^{II}_3Fe^{III}$ unit present in **3**, where J_1 and J_2 represent the magnetic coupling constants; **B**: $\chi_M T$ (*T*) and *M* (*H*) (inset) for **3** with the best fit (solid line).

In conclusion, we report a novel one-step synthesis that generates an air-stable complex containing site-specifically incorporated metal ions in three electronic configurations. Isolation of **3** represents a significant advance in construction of multi-metallic architectures, where the goal is to emulate biological systems that control metal spin and oxidation states to direct a myriad of chemical processes. Magnetic measurements support F-mediated antiferromagnetic exchange between the peripheral Fe^{II} ions and the central Fe^{III} of the star motif. Future work will focus on identifying reaction conditions that give rise to structurally related complexes and evaluating their magnetic and physical properties. Analysis of mixed oxidation state iron star complexes containing halogens other than fluoride will be invaluable in determining the role of the bridging ligand on the exchange interactions between the peripheral and central metal ions.

This research was supported by a University of Manchester Dame Kathleen Ollerenshaw Fellowship and a Royal Society University Research Fellowship (IAR), the Engineering and Physical Sciences Research Council (grants EP/K039547/1 and EP/R00482X/1), the Leverhulme Trust (RF/2018-545/4), the National EPSRC UK EPR Facility, and Diamond Light Source (beamline I19; cy23480). The authors thank Dr. R. W. Adams, C.

Bawn, G. Smith, D. Bell and Profs D. Collison and S. Liddle for helpful discussions.

Conflicts of interest

There are no conflicts to declare.

Notes and references

(1) M. C. O'Sullivan, J. K. Sprafke, D. V. Kondratuk, C. Rinfray, T. D. W. Claridge, A. Saywell, M. O. Blunt, J. N. O'Shea, P. H. Beton, M. Malfois and H. L. Anderson, *Nature*, 2011, **469**, 72; S. M. Jansze and K. Severin, *Acc. Chem. Res.*, 2018, **51**, 2139-2147; A. J. Metherell and M. D. Ward, *Chem. Sci.*, 2016, **7**, 910-915.
(2) M. L. Saha, S. Neogi and M. Schmittel, *Dalton Trans.*, 2014, **43**, 3815-3834.
(3) D. L. Caulder and K. N. Raymond, *Acc. Chem. Res.*, 1999, **32**, 975-982.
(4) P. J. Steel, *Acc. Chem. Res.*, 2005, **38**, 243-250; P. J. Stang, *Chem. Eur. J.*, 1998, **4**, 19-27.
(5) S. P. Argent, H. Adams, T. Riis-Johannessen, J. C. Jeffery, L. P. Harding and M. D. Ward, *J. Am. Chem. Soc.*, 2006, **128**, 72-73; W. M. Bloch, Y. Abe, J. J. Holstein, C. M. Wandtke, B. Dittrich and G. H. Clever, *J. Am. Chem. Soc.*, 2016, **138**, 13750-13755; M. Wang, Y.-R. Zheng, K. Ghosh and P. J. Stang, *J. Am. Chem. Soc.*, 2010, **132**, 6282-6283; Q. Sun, S. Sato and M. Fujita, *Angew. Chem. Int. Ed.*, 2014, **126**, 13728-13731; D. Preston, J. E. Barnsley, K. C. Gordon and J. D. Crowley, *J. Am. Chem. Soc.*, 2016, **138**, 10578-10585.
(6) M. M. J. Smulders, A. Jiménez and J. R. Nitschke, *Angew. Chem. Int. Ed.*, 2012, **51**, 6681-6685; F. Reichel, J. K. Clegg, K. Gloe, K. Gloe, J. J. Weigand, J. K. Reynolds, C.-G. Li, J. R. Aldrich-Wright, C. J. Kepert, L. F. Lindoy, H. Yao and F. Li, *Inorg. Chem.*, 2014, **53**, 688-690; S. Sanz, H. M. O'Connor, P. Comar, A. Baldansuren, M. B. Pitak, S. J. Coles, H. Weihe, N. F. Chilton, E. J. L. McInnes, P. J. Lusby, S. Piligkos and E. K. Brechin, *Inorg. Chem.*, 2018, **57**, 3500-3506; S. Sanz, H. M. O'Connor, V. Martí-Centelles, P. Comar, M. B. Pitak, S. J. Coles, G. Lorusso, E. Palacios, M. Evangelisti, A. Baldansuren, N. F. Chilton, H. Weihe, E. J. L. McInnes, P. J. Lusby, S. Piligkos and E. K. Brechin, *Chem. Sci.*, 2017, **8**, 5526-5535; M. Schmittel, V. Kalsani and J. W. Bats, *Inorg. Chem.*, 2005, **44**, 4115-4117.
(7) M. Hardy, N. Struch, F. Topić, G. Schnakenburg, K. Rissanen and A. Lützen, *Inorg. Chem.*, 2018, **57**, 3507-3515.
(8) M. Otte, P. F. Kuijpers, O. Troeppner, I. Ivanović-Burmazović, J. N. H. Reek and B. de Bruin, *Chem. Eur. J.*, 2013, **19**, 10170-10178; E. T. Luis, H. Iranmanesh, K. S. A. Arachchige, W. A. Donald, G. Quach, E. G. Moore and J. E. Beves, *Inorg. Chem.*, 2018, **57**, 8476-8486.
(9) S. Cardona-Serra, E. Coronado, P. Gaviña, J. Ponce and S. Tatay, *Chem. Commun.*, 2011, **47**, 8235-8237; A. D. Faulkner, R. A. Kaner, Q. M. A. Abdallah, G. Clarkson, D. J. Fox, P. Gurnani, S. E. Howson, R. M. Phillips, D. I. Roper, D. H. Simpson, P. Scott, *Nat. Chem.*, 2014, **6**, 797.
(10) A. S. Rathnayake, H. W. L. Fraser, E. K. Brechin, S. J. Dalgarno, J. E. Baumeister, J. White, P. Rungthanaphatsophon, J. R. Walensky, S. P. Kelley, C. L. Barnes and J. L. Atwood, *J. Am. Chem. Soc.*, 2018, **140**, 15611-15615.
(11) A. S. Rathnayake, H. W. L. Fraser, E. K. Brechin, S. J. Dalgarno, J. E. Baumeister, J. White, P. Rungthanaphatsophon, J. R. Walensky, C. L. Barnes, S. J. Teat and J. L. Atwood, *Nat. Commun.*, 2018, **9**, 2119.
(12) I. C. Berdiell, T. Hochdörffer, C. Desplanches, R. Kulmaczewski, N. Shahid, J. A. Wolny, S. L. Warriner, O. Cespedes, V. Schünemann, G. Chastanet and M. A. Halcrow, *J. Am. Chem. Soc.*, 2019, **47**, 18759-18770.
(13) T. K. Ronson, S. Zarra, S. P. Black and J. R. Nitschke, *Chem. Commun.*, 2013, **49**, 2476-2490.
(14) C. Brewer, G. Brewer, C. Luckett, G. S. Marbury, C. Viragh, A. M. Beatty and W. R. Scheidt, *Inorg. Chem.*, 2004, **43**, 2402-2415; R. W. Hogue, S. Singh and S. Brooker, *Chem. Soc. Rev.*, 2018, **47**, 7303-7338.
(15) T. Lathion, L. Guénée, C. Besnard, A. Bousseksou and C. Piguet, *Chem. Eur. J.*, 2018, **24**, 16873-16888.
(16) P. Mal, D. Schultz, K. Beyeh, K. Rissanen and J. R. Nitschke, *Angew. Chem. Int. Ed.*, 2008, **47**, 8297-8301; J.-F. Ayme, J. E. Beves, D. A. Leigh, R. T. McBurney, K. Rissanen and D. Schultz, *Nat. Chem.*, 2011, **4**, 15.
(17) E. Tancini, M. J. Rodriguez-Douton, L. Sorace, A. Barra, R. Sessoli and A. Cornia, *Chem. Eur. J.*, 2010, **16**, 10482-10493; Y. Zhu, T. Yin, S. Jiang, A. Barra, W. Wernsdorfer, P. Neugebauer, R. Marx, M. Dörfel, B. Wang, Z. Wu, J. van Slageren and S. Gao, *Chem. Commun.*, 2014, **50**, 15090-15093; T. Matsumoto, G. N. Newton, T. Shiga, S. Hayami, Y. Matsui, H. Okamoto, R. Kumai, Y. Murakami and H. Oshio, *Nat. Commun.*, 2014, **5**, 3865.
(18) D. Sertphon, P. Harding, K. S. Murray, B. Moubaraki, N. F. Chilton, S. Hill, J. Marbey, H. Adams, C. G. Davies, G. N. L. Jameson and D. J. Harding, *Dalton Trans.*, 2018, **47**, 7118-7122.
(19) A. Cornia, M. Mannini, R. Sessoli and D. Gatteschi, *Eur. J. Inorg. Chem.*, 2019, **2019**, 552-568; J. Mayans, M. Font-Bardia and A. Escuer, *Dalton Trans.*, 2018, **47**, 8392-8401.
(20) B. Brachňková, J. Adamko Kožíšková, J. Kožíšek, E. Melníková, M. Gál, R. Herchel, T. Dubaj and I. Šalitroš, *Dalton. Trans.*, 2020, **49**, 17786-17795.
(21) F. Tuna, M. R. Lees, G. J. Clarkson and M. J. Hannon, *Chem. Eur. J.* 2004, **10**, 5737-5750.
(22) M. J. Burke, G. S. Nichol and P. J. Lusby, *J. Am. Chem. Soc.*, 2016, **138**, 9308-9315.
(23) W. Meng, T. K. Ronson, J. K. Clegg and J. R. Nitschke, *Angew. Chem. Int. Ed.*, 2013, **52**, 1017-1021; J. Mosquera, S. Zarra and J. R. Nitschke, *Angew. Chem. Int. Ed.*, 2014, **53**, 1556-1559.
(24) Y. I. Cho, M. L. Ward and M. J. Rose, *Dalton Trans.*, 2016, **45**, 13466-13476; E. Tomat, L. Cuesta, V. M. Lynch and J. L. Sessler, *Inorg. Chem.*, 2007, **46**, 6224-6226; F. Jiang, M. A. Siegler and E. Bouwman, *Inorg. Chem. Commun.*, 2018, **94**, 53-56; D. L. Reger, R. P. Watson, J. R. Gardinier, M. D. Smith and P. J. Pellechia, *Inorg. Chem.*, 2006, **45**, 10088-10097.
(25) F. Liu, A. Künzel, A. Herzog, H. W. Roesky, M. Noltemeyer, R. Fleischer and D. Stalke, *Polyhedron*, 1997, **16**, 61-65; F. Liu, H. Gornitzka, D. Stalke and H. W. Roesky, *Angew. Chem. Int. Ed.*, 1993, **32**, 442-444.
(26) A. S. Rathnayake, H. W. L. Fraser, E. K. Brechin, S. J. Dalgarno, J. E. Baumeister, P. Rungthanaphatsophon, J. R. Walensky, C. L. Barnes and J. L. Atwood, *J. Am. Chem. Soc.*, 2018, **140**, 13022-13027.
(27) N. F. Chilton, R. P. Anderson, L. D. Turner, A. Soncini and K. S. Murray, *J. Comp. Chem.*, 2013, **34**, 1164-1175.
(28) $\hat{H} = \mu_B B \sum_i g_i \hat{S}_i \text{-} 2J_1(\hat{S}_{Fe^{III}}\hat{S}_{Fe^{II}_1} + \hat{S}_{Fe^{III}}\hat{S}_{Fe^{II}_2} + \hat{S}_{Fe^{III}}\hat{S}_{Fe^{II}_3}) \text{-} 2J_2(\hat{S}_{Fe^{II}_1}\hat{S}_{Fe^{II}_2} + \hat{S}_{Fe^{II}_2}\hat{S}_{Fe^{II}_3} + \hat{S}_{Fe^{II}_3}\hat{S}_{Fe^{II}_1}) + D_{Fe^{II}} \sum_i \left(\hat{S}^2_{z_{Fe^{II}}} - \frac{\hat{S}^2_{Fe^{II}}}{3}\right)$
(29) C. Schlegel, E. Burzurí, F. Luis, F. Moro, M. Manoli, E. K. Brechin, M. Murrie and J. van Slageren, *Chem. Eur. J.*, 2010, **16**, 10178-10185.
(30) S. Dammers, T. P. Zimmermann, S. Walleck, A. Stammler, H. Bögge, E. Bill and T. Glaser, *Inorg. Chem.*, 2017, **56**, 1779-1782.
(31) Z. Yan, H. G. Jang, Y. Chiou, M. P. Hendrich and L. Que, *Inorg. Chim. Acta*, 1993, **213**, 41-48.
(32) J. M. Dance, J. Mur, J. Darriet, P. Hagenmuller, W. Massa, S. Kummer and D. Babel, *J. Solid State Chem.*, 1986, **63**, 446-451.
(33) D. Sil, A. Kumar and S. P. Rath, *Chem. Eur. J.*, 2016, **22**, 11214-11223; D. L. Reger, A. E. Pascui, M. D. Smith, J. Jezierska, A. Ozarowski, *Inorg. Chem*., 2012, **51**, 11820-1183.

Supporting Information for

Self-assembly of a trigonal bipyramidal architecture with stabilisation of iron in three spin states

Lauren L. K. Taylor,[a] Iñigo J. Vitorica-Yrezabal,[a] Ivana Borilović,[a,b] Floriana Tuna,[a,b*] Imogen A. Riddell*[a]

[a] Department of Chemistry, University of Manchester, Oxford Road, Manchester, M13 9PL (UK)

[b] Photon Science Institute, University of Manchester, Oxford Road, Manchester, M13 9PL (UK)

*Email: imogen.riddell@manchester.ac.uk; floriana.tuna@manchester.ac.uk

Table of Contents

S1 Synthesis and Characterization

S1.1 General Experimental Details

Unless stated otherwise, all chemicals were supplied from Sigma-Aldrich, Fluorochem, Fisher Scientific, Alfa Aesar or Scientific Laboratory Supplies Ltd and used without further purification. Deuterated NMR solvents were supplied from Sigma-Aldrich and NMR spectra were recorded on a B500 Bruker Advance II+ 500 MHz spectrometer. Chemical shifts are reported in parts per million (ppm). Coupling constants (*J*) are reported in hertz (Hz). Standard abbreviations indicating multiplicity were used as follows: s = singlet, d = doublet, t = triplet, dd = doublet of doublets, m = multiplet. ^{1}H and ^{13}C assignments were made using 2D NMR methods (COSY, NOESY, HSQC, HMBC). High resolution mass spectra were obtained using a Thermo Orbitrap Exactive Plus Extended Mass Range mass spectrometer. Elemental analyses were performed by the microanalytical services of The University of Manchester with a CFlash 2000 elemental analyser for the analyses of carbon, hydrogen and nitrogen. The DOSY experiment was performed using a stimulated echo sequence with bipolar gradients (Bruker standard sequence ledbpgp2s). The experiment was performed using 10 gradient steps with a minimum nominal gradient of 75 G/cm and a maximum 300 G/cm, incremented in steps of gradient squared. Smoothed-square gradients with a duration of 0.5 ms were used. Gradient recovery delay was 20 μs and diffusion time was 4 ms. The dataset was processed using GNAT[1] and hydrodynamic radii were calculated using the Stokes-Einstein-Gierer-Wirtz approach.[2,3] Experiments were acquired at 298 K using a Bruker 500 NEO NMR spectrometer equipped with 5 mm diffusion probe.

S1.2 Ligand Synthesis

Scheme S1: Synthesis of asymmetric ligand **L** via a convergent synthesis strategy starting from 5-bromo-2-pyridinecarboxaldehyde. i) *p*-TsOH, ii) $Pd(dppf)Cl_2.CH_2Cl_2$, KOAc, iii) $Na_2S_2O_5$, iv) $Pd(PPh_3)_4$, Na_2CO_3, v) HCl (2 M).

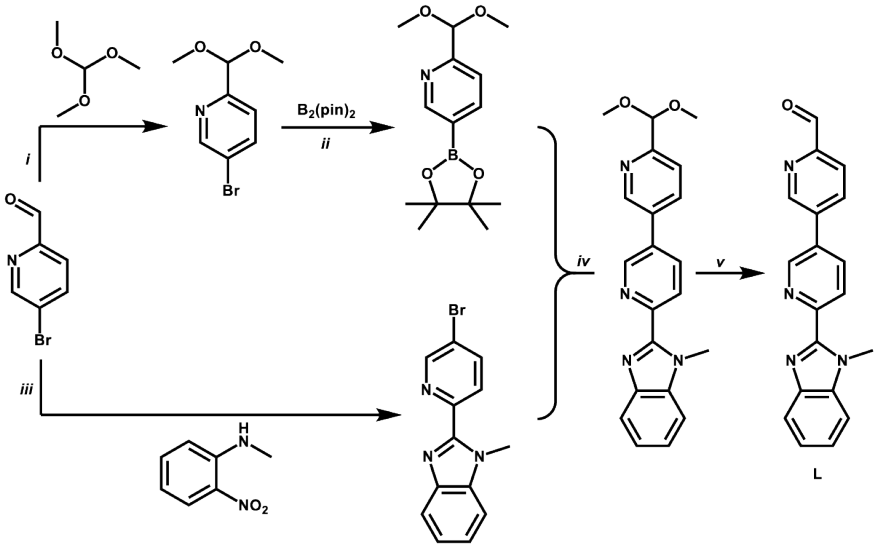

5-Bromo-2-(dimethoxymethyl)pyridine: 5-Bromo-2-pyridinecarboxaldehyde (1.6 g, 8.6 mmol) and *p*-toluenesulfonic acid monohydrate (34 mg, 0.18 mmol) were dissolved in dry methanol (32 mL). Trimethyl orthoformate (4.7 mL, 43.0 mmol) was added and the brown solution was refluxed under N_2 (100°C, 24 hr). The solvent was removed *in vacuo* giving an orange oil that was dissolved in dichloromethane and neutralised with $NaHCO_3$. The product was extracted with dichloromethane (3 x 20 mL) and dried over $MgSO_4$. After filtering, the solvent was removed under reduced pressure to give the product as a brown oil (1.56 g, 6.75 mmol, 79%).[1]H (500 MHz, 298 K, $CDCl_3$): δ = 8.60 (d, 1H, *J* = 2.30 Hz, H_e), 7.78 (dd, 1H, *J* = 2.33, 8.38 Hz, H_d), 7.39 (d, 1H, *J* = 8.35 Hz, H_c), 5.27 (s, 1H, H_b), 3.32 (s, 6H, H_a). ^{13}C (125.8 MHz, 300 K, $CDCl_3$): 155.9, 150.3, 139.3, 122.7, 120.6, 103.3, 53.6. [Accurate mass]: expected = 230.9895, found = 231.9960 $[M + H]^+$.

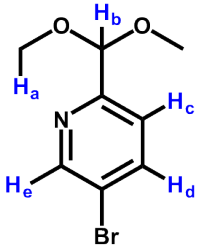

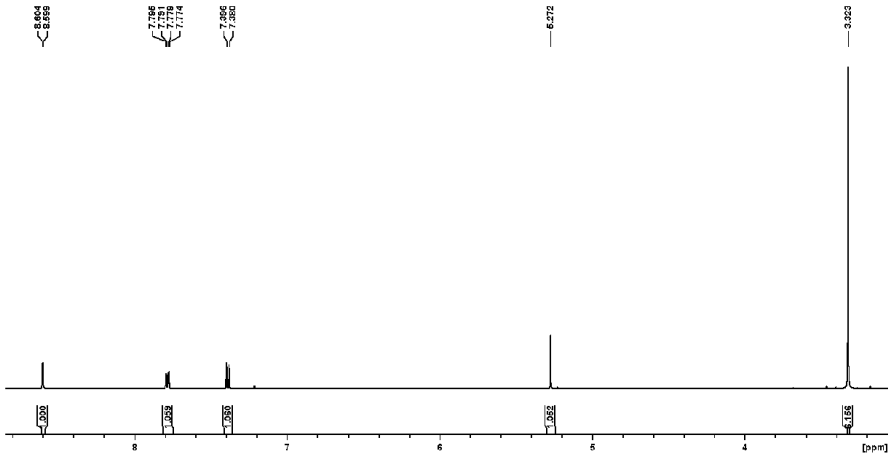

Figure S1: ^{1}H NMR (500 MHz, $CDCl_3$, 298 K) spectrum of protected aldehyde 5-bromo-2-(dimethoxymethyl)pyridine.

2-(Dimethoxymethyl)-5-(4,4,5,5-tetramethyl-1,3,2-dioxaborolan-2-yl)pyridine:

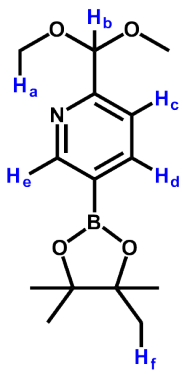

5-Bromo-2-(dimethoxymethyl)pyridine (0.84 g, 3.64 mmol), bis(pinacolato)diboron (1.1 g, 4.37 mmol), potassium acetate (1.1 g, 10.9 mmol) and $Pd(dppf)Cl_2.CH_2Cl_2$ (0.15 g, 0.18 mmol) were dissolved in DMF (22 mL) and the orange solution was heated under N_2 (50°C, 24 hr). The solvent was removed *in vacuo* and the resulting brown solid was dissolved in diisopropyl ether. The suspended brown solid was filtered off, and the solvent was removed *in vacuo* to give a green oil that was then dissolved in hexane. The insoluble material was filtered off and the solvent was removed to yield the final product as a green oil (0.65 g, 2.34 mmol, 64%). ^{1}H (500 MHz, 298 K, $CDCl_3$): δ = 8.87 (s, 1H, H_e), 8.03 (d, 1H, J = 7.61 Hz, H_d), 7.47 (d, 1H, J = 7.69 Hz, H_c), 5.33 (s, 1H, H_b), 3.32 (s, 6H, H_a), 1.28 (s, 12H, H_f). ^{13}C (125.7 MHz, 300 K, $CDCl_3$): 159.3, 154.9, 143.1, 135.1, 120.6, 103.8, 84.3, 53.5, 24.9, 24.8. [Accurate mass]: expected = 279.1642, found = 279.1743 $[M]^+$, 280.1705 $[M + H]^+$.

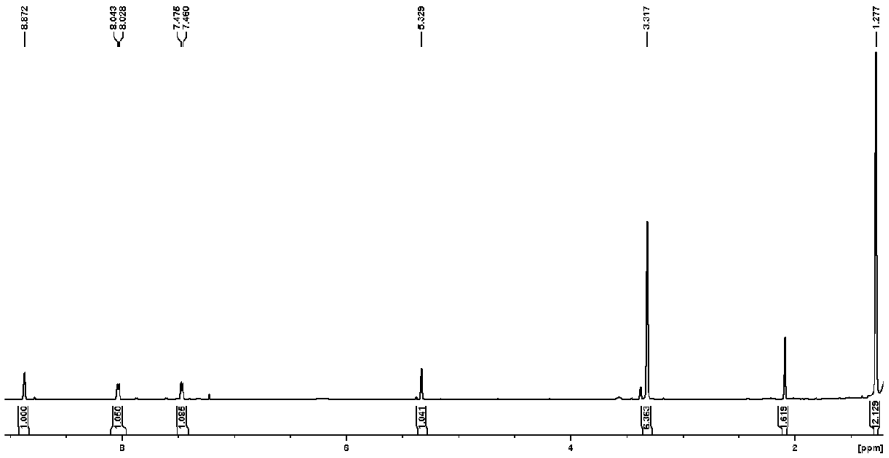

Figure S2: ^{1}H NMR (500 MHz, $CDCl_3$, 298 K) spectrum of 2-(dimethoxymethyl)-5-(4,4,5,5-tetramethyl-1,3,2-dioxaborolan-2-yl)pyridine.

2-(5-Bromopyridin-2-yl)-1-methyl-1*H*-benzo[*d*]imidazole:

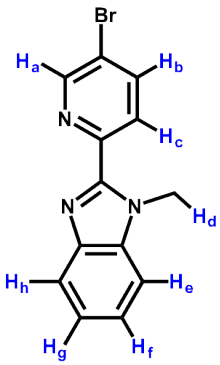

5-Bromo-2-pyridinecarboxaldehyde (2 g, 10.7 mmol) and *N*-methyl-2-nitroaniline (1.6 g, 10.7 mmol) were dissolved in a 4:1 mixture of DMF:H_2O (72 mL). The resulting orange solution was degassed by three vacuum/N_2 fill cycles before $Na_2S_2O_5$ (6.1 g, 32 mmol) was added. The solution was stirred under reflux (24 hr) which turned the solution green then eventually gave a cloudy yellow solution that was added to an ethyl acetate/water mixture. The aqueous layer was washed with ethyl acetate (3 x 30 mL) and the organic layers were combined and dried over $MgSO_4$. Filtration and removal of the solvent *in vacuo* yielded a yellow crystalline solid (2.4 g, 8.5 mmol, 79%). Crystals suitable for X-ray diffraction were obtained through slow evaporation of $CHCl_3$. ^{1}H (500 MHz, 298 K, $CDCl_3$): δ = 8.68 (s, 1H, H_a), 8.25 (d, 1H, J = 8.50 Hz, H_c), 7.90 (d, 1H, J = 8.50 Hz, H_b), 7.75 (d, 1H, J = 7.85 Hz, H*h*), 7.37 (d, 1H, J = 7.90 Hz, H_e), 7.29 (t, 1H, J = 7.49 Hz, H_g), 7.25 (t, 1H, J = 7.45 Hz, H_f), 4.19 (s, 3H, H_d). ^{13}C (126 MHz, 300 K, $CDCl_3$): 149.65, 149.27, 149.06, 142.51, 139.52, 137.35, 125.85, 123.62, 122.81, 121.25, 120.09, 109.98, 30.91. [Accurate mass]: expected = 287.0058, found = 288.0121 $[M + H]^+$.

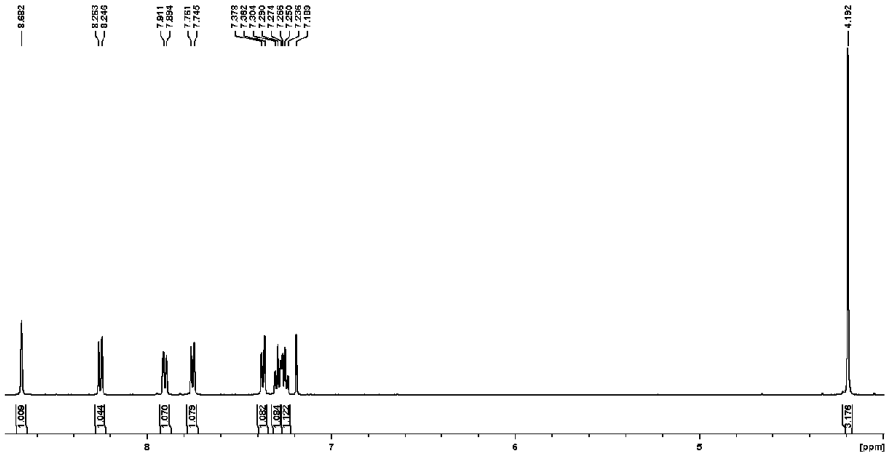

Figure S3: ^{1}H NMR (500 MHz, $CDCl_3$, 298 K) spectrum of 2-(5-bromopyridin-2-yl)-1-methyl-1*H*-benzo[*d*]imidazole.

Protected Ligand, L': Protected borate (0.43 g, 1.55 mmol), imidazole fragment (0.29 g, 1.03 mmol), Na_2CO_3 (0.33 g, 3.09 mmol) and $Pd(PPh_3)_4$ (0.12 g, 0.10 mmol) were dissolved in a 10:1 mixture of DMF:H_2O (8 mL). The yellow solution was degassed by three vacuum/N_2 fill cycles before being stirred under a flow of N_2 (70ºC, 24 hr). The resulting brown solution was cooled and diluted in water before being extracted with dichloromethane (3 x 10 mL). The combined organic layers were then washed with water (3 x 10 mL) and dried over Na_2SO_4 before the solvent was removed to give the product as a brown solid (0.17 g, 0.46 mmol, 45%). Crystals suitable for X-ray diffraction were obtained through slow evaporation of $CHCl_3$. ^{1}H (500 MHz, 298 K, $CDCl_3$): δ = 8.88 (s, 1H, H_f), 8.87 (s, 1H, H_e), 8.48 (d, 1H, J = 8.23 Hz, H_g), 7.99 (d, 1H, J = 8.27 Hz, H_h), 7.95 (d, 1H, J = 8.02 Hz, H_d), 7.78 (d, 1H, J = 7.71 Hz, H_m), 7.64 (d, 1H, J = 8.17 Hz, H_c), 7.40 (d, 1H, J = 7.85 Hz, H_j), 7.30 (t, 1H, J = 7.64 Hz, H_l), 7.27 (t, 1H, J = 7.42 Hz, H_k), 5.40 (s, 1, H_b), 4.28 (s, 3H, H_i), 3.40 (s, 5H, H_a). ^{13}C (126 MHz, 300 K, $CDCl_3$): 32.89, 53.79, 103.72, 109.99, 120.13, 121.55, 122.79, 123.57, 124.81, 128.46, 131.92, 132.07, 132.15, 132.94, 135.08, 135.14, 146.85, 147.46, 149.72, 157.26. [ESI+]: $[M + Na]^+$ = 383.10, $[M + K]^+$ = 399.10.

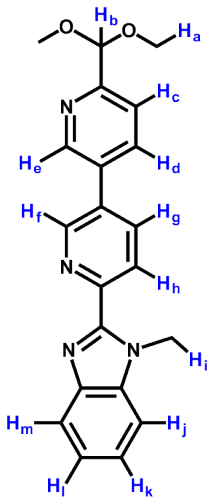

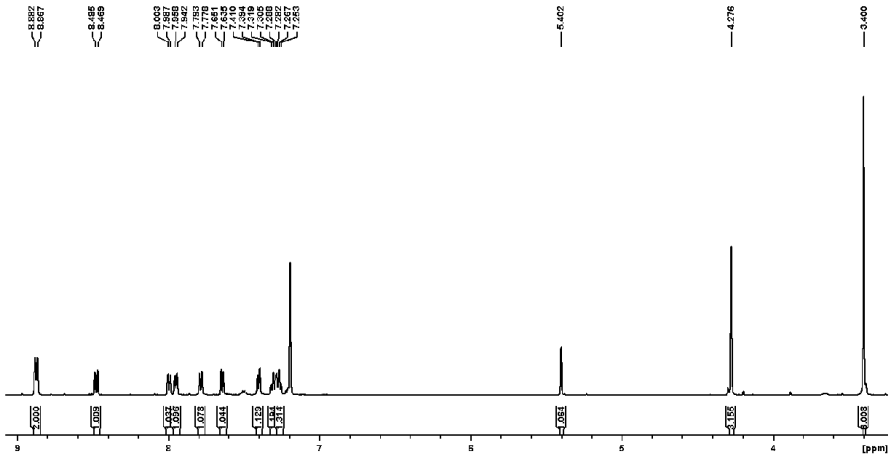

Figure S4: ^{1}H NMR (500 MHz, CD_3CN, 298 K) spectrum of the protected ligand.

Target Ligand, L: Protected ligand, **L'** (99 mg, 0.27 mmol) was dissolved in THF (1.5 mL) and HCl (2 M, 2.9 mL) was added. The yellow solution was sealed under N_2 and heated (40°C, 22 hr) before being neutralised by the addition of saturated $NaHCO_3$, resulting in the formation of a white precipitate. The white solid was dissolved in a 3:1 mixture of $CHCl_3$:2-propanol and the aqueous layer was washed with $CHCl_3$ (3 x 5 mL) before being dried over $MgSO_4$ and filtered to give a yellow solid (62 mg, 0.20 mmol, 73%). ^{1}H (500 MHz, 298 K, CD_3CN): δ = 10.01 (s, 1H, H_a), 9.11 (s, 1H, H_d), 9.02 (s, 1H, H_e), 8.43 (d, 1H, J = 8.26 Hz, H_f), 8.25 (d, 1H, J = 7.93 Hz, H_c), 8.21 (d, 1H, J = 8.34 Hz, H_g), 8.00 (d, 1H, J = 8.11 Hz, H_b), 7.67 (d, 1H, J = 7.94 Hz, H_l), 7.50 (d, 1H, J = 8.11 Hz, H_i), 7.30 (t, 1H, J = 7.51 Hz, H_j), 7.24 (t, 1H, J = 7.51 Hz, H_k), 4.24 (s, 3H, H_h). ^{13}C (126 MHz, 300 K, $CDCl_3$): 32.97, 110.08, 120.24, 122.02, 122.97, 123.79, 124.91, 131.97, 135.34, 137.09, 137.49, 142.67, 147.05, 148.49, 149.40, 151 .18, 152.29, 192.84. [Accurate mass]: expected = 314.1168, found = 315.1228 $[M + H]^+$.

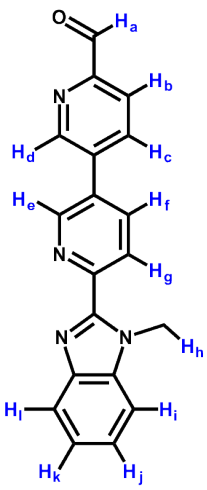

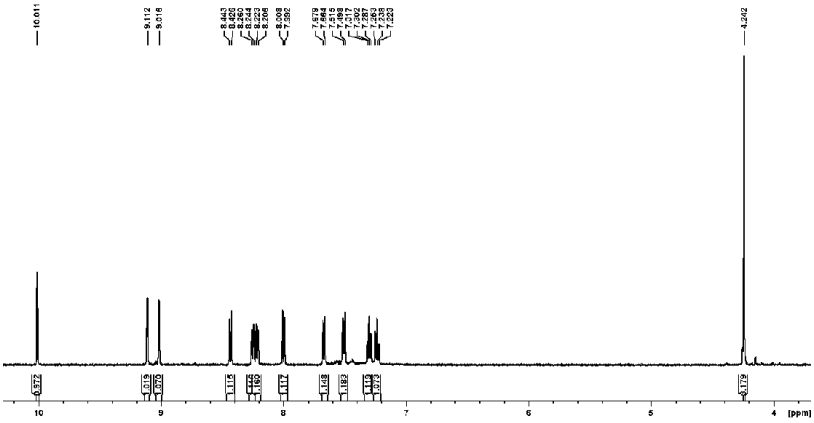

Figure S5: ^{1}H NMR (500 MHz, CD_3CN, 298 K) spectrum of the final ligand, **L**, following deprotection with HCl.

S1.3 Iron Self-Assembly Reactions

Scheme S2: Stepwise formation of **3** proceeds through iron(II) intermediates **1** and **2**.

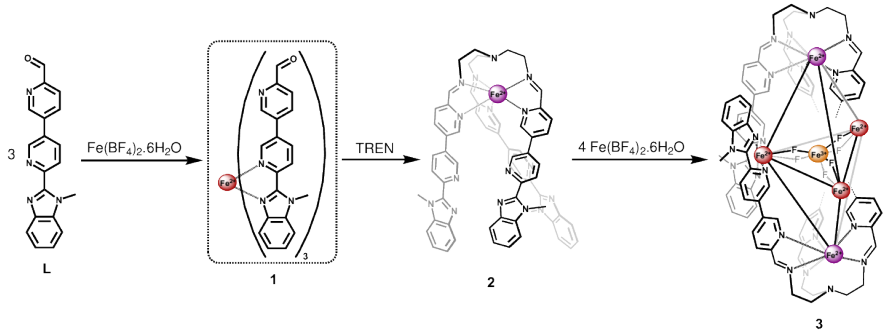

S1.3.1 Complex 1; $[Fe^{II}L_3](BF_4)_2$

Ligand **L** (10 mg, 31.81 μmol, 3 equiv) and $Fe(BF_4)_2.6H_2O$ (3.58 mg, 10.60 μmol, 1 equiv) were dissolved in deuterated acetonitrile (0.5 mL) and the resulting red solution was added to a J-Young NMR tube. The tube was sealed, and the solution was degassed by three vacuum/N_2 fill cycles before being heated (50°C, 24 hr). Diethyl ether was added to the red solution, causing precipitation of the product which was washed with chloroform to give a red solid (4.3 mg, 3.94 μmol, 37%) [Accurate mass, *m/z*]: $\{FeL_3\}^{2+}$ = 499.1435, $\{FeL_3\}(BF_4)^{+}$ = 1085.2915. Elemental analysis (%) calculated for $C_{63}H_{54}B_2F_8FeN_{16}\cdot 3.65\ CHCl_3$: C 53.69, H 3.93, N 12.39; found: C 53.69, H 3.93, N 12.11.

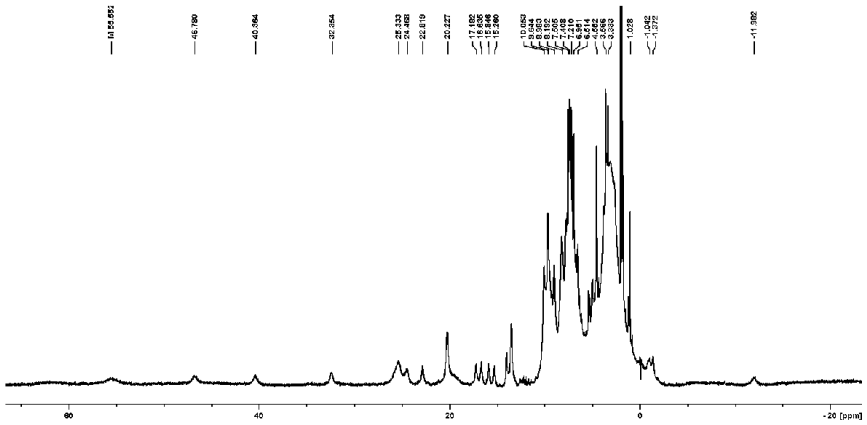

Figure S6: ^{1}H NMR (500 MHz, CD_3CN, 298 K) spectrum of the dynamic mixture containing complex **1**.

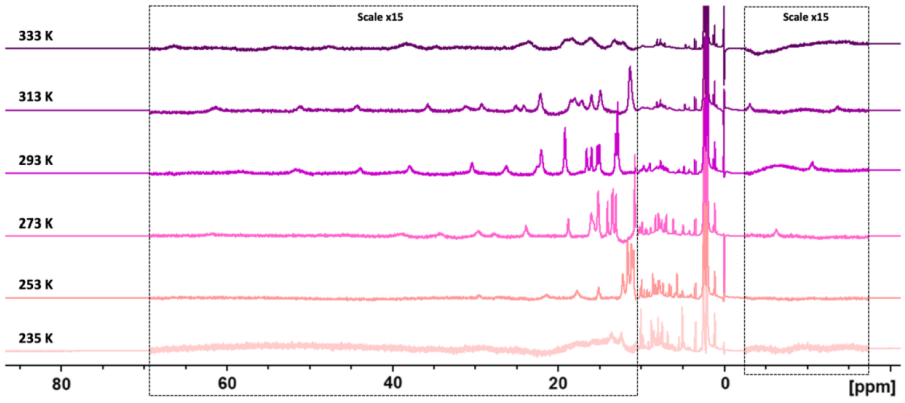

Figure S7: ^{1}H NMR (500 MHz, CD_3CN) spectra of dynamic mixture containing complex 1 recorded at temperatures from 235 K (bottom) to 333 K (top) in five steps of 20 K. At room temperature, the ^{1}H NMR spectrum of complex 1 contains peaks between 20 – 60 ppm indicating a significant fraction of the sample exists as HS Fe(II).

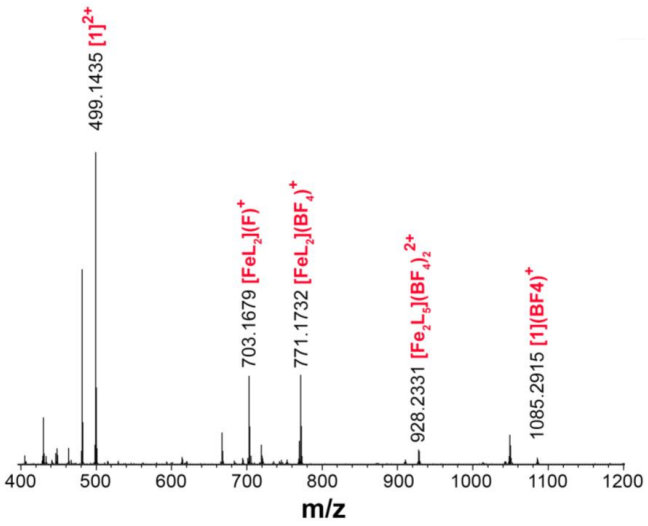

Figure S8: High-resolution mass spectrum for an acetonitrile solution of complex **1**, annotating additional isotopic patterns that were also present.

S1.3.2 Complex 2; $[FeL_3T](BF_4)_2$

To a solution of complex **1** in a J-Young NMR tube, *tris*(2-aminoethyl)amine (TREN, T) (1.94 µL, 12.94 µmol, 1 equiv) was added. The tube was sealed, and the resulting blue solution was degassed by three vacuum/N_2 fill cycles before being heated (50°C, 24 hr). Diethyl ether was added to the resulting purple solution, causing precipitation of the product which was washed with chloroform to give a purple solid. ^{1}H (500 MHz, 298 K, CD_3CN): δ = 9.28 (s, 1H, H_c), 8.71 (s, 1H, H_f), 8.46 (broad s, 1H, H_g) 8.38 (broad s, 1H, H_h), 8.30 (d, 1H, J = 7.86 Hz, H_e), 7.86 (d, 1H, J = 7.79 Hz, H_d), 7.61 (d, 1H, J = 7.45 Hz, H_k), 7.45 (d, 2H, J = 7.99 Hz, H_n/H_i), 7.27 (t, 1H, J = 7.47 Hz, H_m), 7.20 (t, 1H, J = 7.49 Hz, H_l), 4.12 (s, 3H, H_j), 3.73 (m, 1H, H_b), 3.58 (m, 1H, H_a), 3.19 (broad t, 1H, H_b), 3.09 (broad t, 1H, H_a). [Accurate mass, *m/z*]: $\{FeL_3T\}^{2+}$ = 545.2005, $\{FeL_3T\}(BF_4)^+$ = 1177.4044. Elemental analysis (%) calculated for $C_{63}H_{54}B_2F_8FeN_{16}\cdot 1.15\ CHCl_3\cdot 1.8\ C_2H_3N$: C 55.12, H 4.13, N 16.89; found: C 55.20, H 4.46, N 16.57.

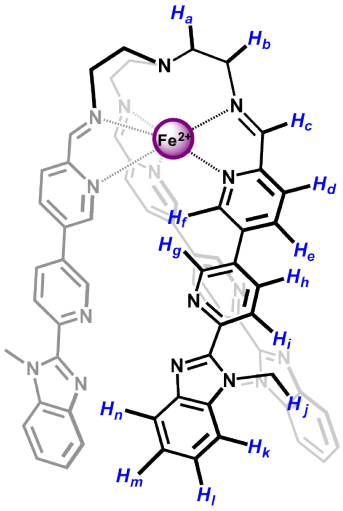

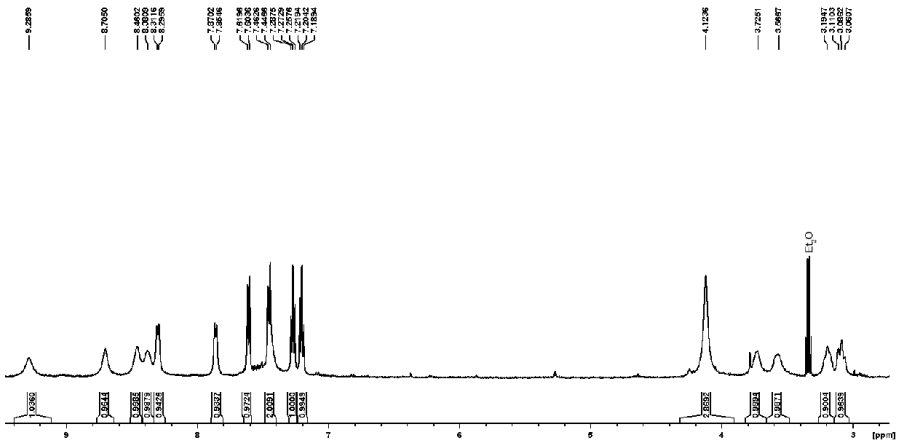

Figure S9: ^{1}H NMR (500 MHz, CD_3CN, 298 K) spectrum of diamagnetic complex **2**. Peak broadening is attributed to the chemical exchange of CH_2 protons of TREN as previously reported.[4]

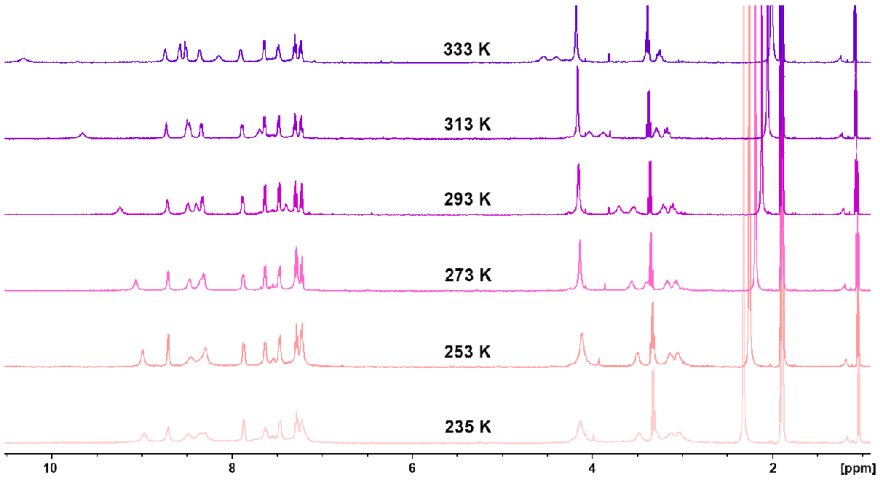

Figure S10: ^{1}H NMR (500 MHz, CD_3CN) spectra for complex **2** recorded at temperatures from 235 K (bottom) to 333 K (top) in five steps of 20 K.

S1.3.3 Complex 3: $[Fe_6F_6L_6T_2](BF_4)_7$

Ligand **L** (30.3 mg, 96.5 μmol, 6 equiv), $Fe(BF_4)_2.6H_2O$ (32.6 mg, 96.5 μmol, 6 equiv) and tris-2(aminoethyl)amine (4.8 μL, 32.16 μmol, 2 equiv) were dissolved in acetonitrile (3 mL) giving a bright blue solution. This was heated (50°C, 24 hr) and the purple solution was layered with diethyl ether. The resulting purple solid was filtered and washed with chloroform to give a purple crystalline solid (38.2 mg, 12.2 μmol, 38%). DOSY diffusion coefficient: 6.32 x 10^{-10} m^2 s^{-1}. [Accurate mass, *m/z*]: $\{Fe_6\mathbf{L}_6F_6T_2\}^{7+}$ = 359.93 $\{Fe_6\mathbf{L}_6F_6T_2(BF_4)\}^{6+}$ = 434.42, $\{Fe_6\mathbf{L}_6F_6T_2(BF_4)_2\}^{5+}$ = 538.71, $\{Fe_6\mathbf{L}_6F_6T_2(BF_4)_3\}^{4+}$ = 694.89, $\{Fe_6\mathbf{L}_6F_6T_2(BF_4)_4\}^{3+}$ = 955.52, $\{Fe_6\mathbf{L}_6F_6T_2(BF_4)_5\}^{2+}$ = 1476.78. Elemental analysis (%) calculated for $C_{126}H_{108}B_7F_{34}Fe_6N_{32}.1.75\ CHCl_3$: C 47.71, H 3.55, N 13.94; found: C 47.20, H 3.73, N 14.45.

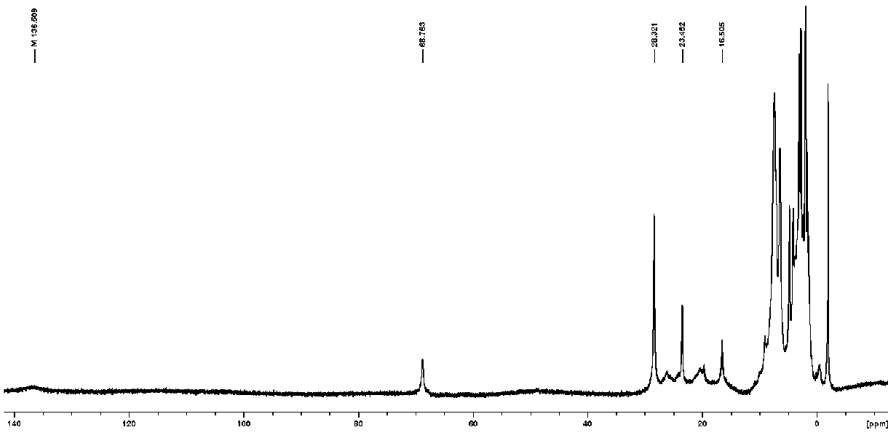

Figure S11: ^1H NMR (500 MHz, CD_3CN, 298 K) spectrum of complex **3**.

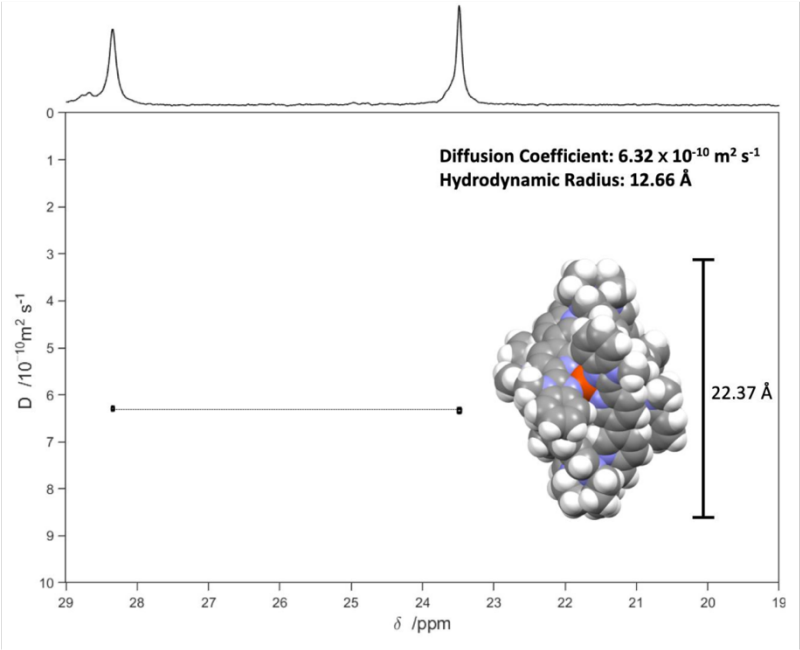

Figure S12: ^{1}H DOSY NMR (500 MHz, CD_3CN, 298 K) spectrum of complex **3**, highlighting two distinct peaks between 19 and 29 ppm.

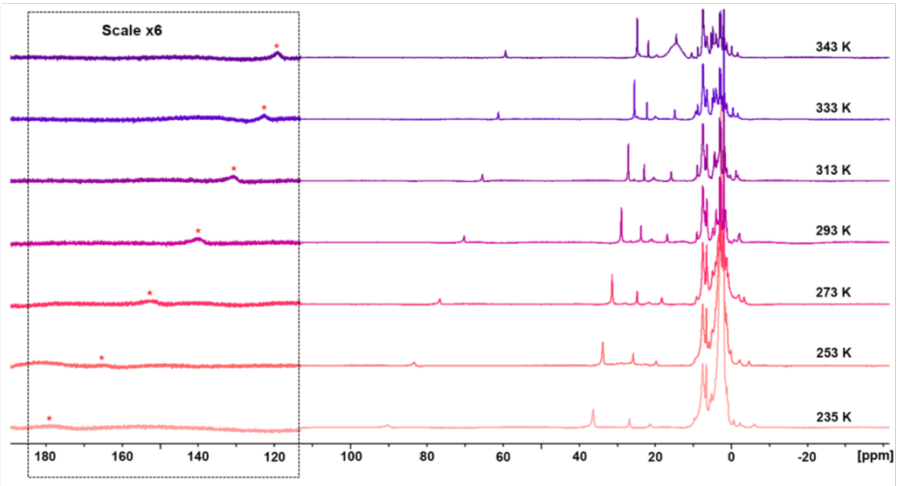

Figure S13: ^{1}H NMR (500 MHz, CD_3CN) spectra for complex **3** recorded at temperatures from 235 K (bottom) to 343 K (top) in five steps of 20 K and one of 10 K.

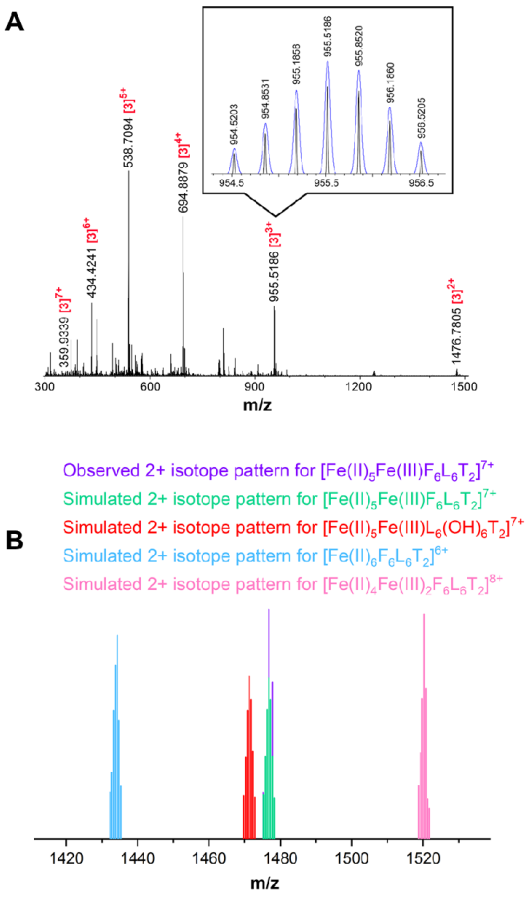

Figure S14: **A:** High-resolution mass spectrum for an acetonitrile solution of **3**. Inset the isotopic pattern for the $[\mathbf{3}]^{3+}$ peak, with the simulated isotopic pattern overlaid in blue. **B**: Isotopic distribution pattern for $[\mathbf{3}]^{2+}$; experimentally observed values are shown in purple alongside simulated values for complex **3** (green). Simulated values are also given for a complex in which all six fluoride ions are replaced with bridging hydroxides (red), where all six iron centres are found in the Fe(II) oxidation state (blue), and where the complex contains four irons as Fe(II) and two irons as Fe(III) (pink). The simulated isotope patterns in red, blue and pink all deviate significantly from the experimentally observed value. Variable numbers of tetrafluoroborate counterions balance the charge with the metal centres, sequential loss of these counterions gives rise to the series of peaks observed in Figure *S*14A. For all patterns observed in the mass spectrum of complex **3**, model values were calculated with enviPat Web 2.4.[5]

S1.3.4 Fe_4L_6 Tetrahedron with *p*-Toluidine

Ligand **L** (2.8 mg, 8.9 μmol, 6 equiv), *p*-toluidine (0.96 mg, 8.9 μmol, 6 equiv) and $Fe(OTf)_2.6H_2O$ (2.2 mg, 5.9 μmol, 4 equiv) were dissolved in acetonitrile (0.5 mL) and the resulting purple solution was added to a J-Young NMR tube. The tube was sealed, and the solution was degassed by three vacuum/N_2 fill cycles before being heated (50°C, 24 hr). [Accurate mass, *m/z*]: $\{Fe_4\mathbf{L}_6(p\text{-Tol})_6(BF_4)\}^{7+}$ = 398.89, $\{Fe_4\mathbf{L}_6(p\text{-Tol})_6(BF_4)_2\}^{6+}$ = 490.45, $\{Fe_4\mathbf{L}_6(p\text{-Tol})_6(BF_4)_3\}^{5+}$ = 618.13, $\{Fe_4\mathbf{L}_6(p\text{-Tol})_6(BF_4)_4\}^{4+}$ = 819.15, $\{Fe_4\mathbf{L}_6(p\text{-Tol})_6(BF_4)_5\}^{3+}$ = 1129.86, $\{Fe_4\mathbf{L}_6(p\text{-Tol})_6(BF_4)_6\}^{2+}$ = 1769.26.

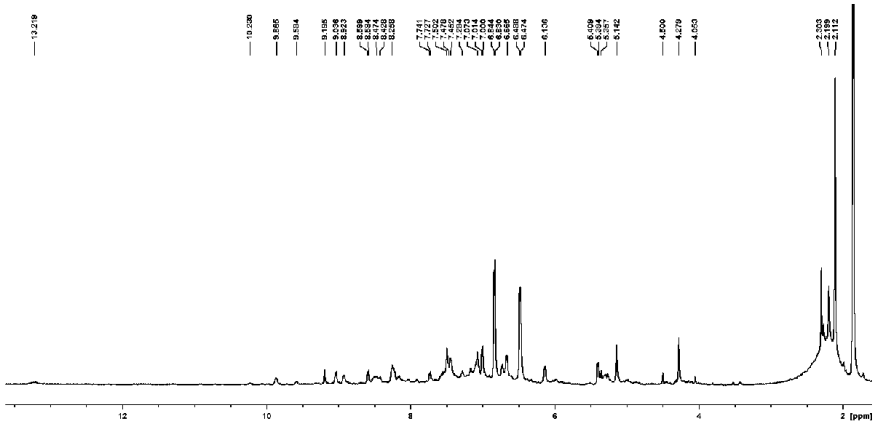

Figure S15: ^{1}H NMR (500 MHz, CD_3CN, 298 K) spectrum of the Fe_4L_6 tetrahedron formed with ligand **L**, *p*-toluidine and $Fe(OTf)_2$. The complicated ^{1}H NMR spectrum is attributed to the asymmetric ligand, which generates three isomers when arrange in a tetrahedral structure (Figure *S*15) giving rise to seven distinct imine environments before consideration of diastereoisomers.

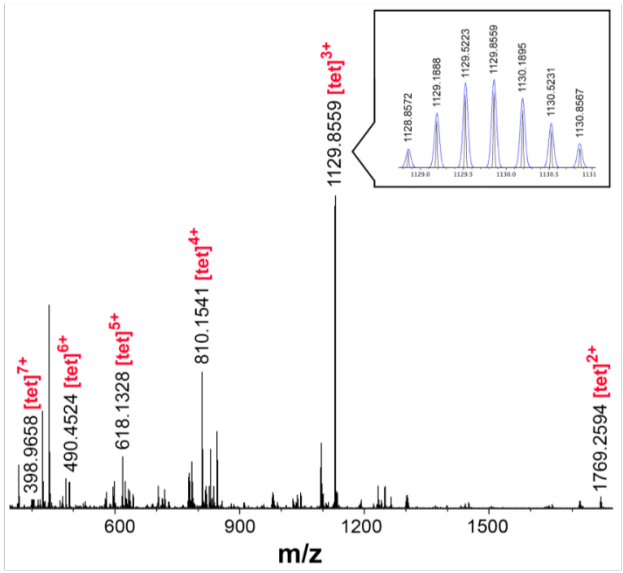

Figure S16: High-resolution mass spectrum for an acetonitrile solution of the Fe_4L_6 tetrahedron [tet]. Insert shows a zoom of the $[tet]^{3+}$ isotopic pattern, with the simulated isotopic pattern overlaid in blue.

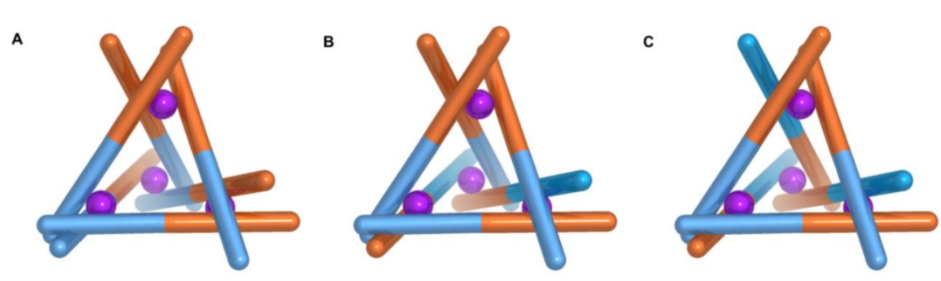

Figure S17: Models of the three possible isomeric structures formed with ligand **L,** *p*-toluidine and $Fe(OTf)_2$. Orange and blue represent the different bidentate binding sites on the asymmetric ligand.

S2 X-Ray Crystallography

Data Collection. Single crystals of 2-(5-bromopyridin-2-yl)-1-methyl-1*H*-benzo[*d*]imidazole and protected ligand **L'** were obtained through the slow evaporation of chloroform to yield colourless crystals. X-ray data for 2-(5-bromopyridin-2-yl)-1-methyl-1*H*-benzo[*d*]imidazole were collected at 150(2) K using an Oxford Diffraction XCalibur II four circle diffractometer with an Atlas CCD detector and an enhance graphite-monochromated Mo K_α radiation source (λ = 0.71073 Å). X-ray data for **L'** was collected at 150(2) K using an Agilent SuperNova four circle diffractometer with an Eos CCD detector and SuperNova microfocused Mo K_α radiation source (λ = 0.71073 Å). X-ray data for complex **1** was collected at 150(2) K using a Rigaku FR-X four circle diffractometer with a Hypix-6000HE HPC detector and FR-X microfocused rotating anode Cu K_α radiation source (λ = 1.54146). X-ray data for ligand **L** and compounds **2** and **3** were collected at a temperature of 100 K using a synchrotron radiation at the single crystal X-ray diffraction beamline I19 in Diamond Light Source,[6] equipped with a Pilatus 2M detector and an Oxford Cryosystems nitrogen flow gas system. Data were measured using GDA suite of programs.

Crystal Structure Determinations and Refinements. X-ray data were processed and reduced using CrysAlisPro.[7] Absorption correction was performed using empirical methods (SCALE3 ABSPACK) based upon symmetry-equivalent reflections combined with measurements at different azimuthal angles. The crystal structure was solved and refined against all F^2 values using the SHELX and Olex2 suite of programmes.[8, 9, 10] All atoms were refined anisotropically. Hydrogen atoms were placed in calculated positions and refined using idealised geometries and assigned fixed isotropic displacement parameters.

Protected ligand **L'** co-crystallised with 5% starting material 2-(5-bromopyridin-2-yl)-1-methyl-1*H*-benzo[*d*]imidazole. Atomic displacement parameters of the molecule were restrained using SIMU SHELX commands. For complex **1**, atomic displacement parameters were restrained using a rigid body approach by applying SHELX RIGU commands and to be similar using SHELX SIMU commands. For complex **2**, the BF_4^- anions were modelled to have ideal geometry, and the occupancy of the BF_4^- anions were refined and constrained to be 2. The B-F distances were restrained to be similar using SHELX SADI commands. Atomic displacement parameters were restrained using a rigid body approach by applying SHELX RIGU commands and to be similar using SHELX SIMU commands.

For complex **3**, BF_4 anions were constrained to have idealized BF_4 structure and were placed on tetrahedral electron density regions as shown in Figure *S*22. One BF_4 anion was found to be disordered over two positions with a 50/50 occupancy. The overall occupancies of the BF_4 anions were refined, obtaining three fully occupied BF_4 positions and one BF_4 with a 50% occupancy in the asymmetric unit. Then, the occupancies were set to be 100 and 50%, respectively. Atomic displacement parameters were restrained using a rigid body approach by applying SHELX RIGU commands and to be similar using SHELX SIMU commands.

Packing of large molecules as proteins,[11] molecular knots,[12] cages,[13] rotaxanes[14] and metal-organic frameworks[15] present large voids filled with ill-shaped electron density, corresponding to highly disordered solvent molecules. The Solvent Mask protocol implemented in OLEX 2 was applied to account for the poorly defined electron density remaining in the voids of crystal structures of **2** and **3** (figure *S*22)**.** 220.2 electrons were found in two different voids in compound **2**. which could correspond to three diethyl ether molecules and two acetonitrile molecules in void 1, and two acetonitrile molecules in void 2. 902 electrons were found in one void for compound **3**, which could correspond to either 42 acetonitrile, 21 diethyl ether or 8 chloroform molecules. Mercury, Discovery Studio and PovRay were used for molecular graphics.[16, 17, 18]

Crystallographic data have been deposited with the CCDC (CCDC 1952397 – 1952402, 2101118).

Table S1: Crystallographic data for molecules 2-(5-bromopyridin-2-yl)-1-methyl-1*H*-benzo[*d*]imidazole, L' and L.

	2-(5-bromopyridin-2-yl)-1-methyl-1*H*-benzo[*d*]imidazole	**L'**	**L**
Formula	$C_{13}H_{10}BrN_3$	$C_{20.62}H_{19.53}Br_{0.05}N_{3.96}O_{1.90}$	$C_{19}H_{14}N_4O$
Fw	288.15	356.88	314.34
Cryst size, mm	0.2 x 0.2 x 0.08	0.2 x 0.2 x 0.2	0.2 x 0.2 x 0.1
Cryst syst	monoclinic	triclinic	triclinic
Space group	$P12_1/n1$	P-1	P-1
a, Å	11.4679 (11)	8.3959(14)	7.2185(6)
b, Å	3.8858 (4)	10.4913(17)	8.4349(7)
c, Å	24.8130 (3)	10.5635(18)	13.3131(7)
α, °	90	75	73
β, °	96	86	88
γ, °	90	80	68
V, Å^3	1099.8(2)	886.0(3)	718.6(11)
Z	4	2	2
ρ_{calcd}, g cm^{-3}	1.740	1.338	1.453
μ, mm^{-1}	3.715	0.201	0.089
No. of reflections made	7336	4679	15467
No. of unique reflns, R_{int}	2657, 0.0768	3224, 0.0449	6580, 0.0649
No. of reflns with $F^2>2\sigma(F^2)$	1786	2028	4030
Transmn coeff range	0.860-1.000	0.730-1.000	0.367-1.000
R, R_w[a] ($F^2 > 2\sigma(F^2)$)	0.0696, 0.1151	0.0797, 0.1992	0.0735, 0.1884
R, R_w[a] (all data)	0.1171, 0.1324	0.1154, 0.2417	0.1111, 0.2089
S[a]	1.063	1.070	0.976
Parameters	155, 0	245, 6	218, 0
Max, min, diff map, e Å^{-3}	1.148, -0.564	0.600, -0.751	0.669, -0.462

[a] Conventional $R = \Sigma||F_o| - |F_c||/\Sigma|F_o|$; $R_w = [\Sigma w(F_o^2 - F_c^2)^2/ \Sigma w(F_o^2)^2]^{1/2}$; $\Sigma = [\Sigma w(F_o^2 - F_c^2)^2/\text{no. data} - \text{no. params})]^{1/2}$ for all data.

Table S2: Crystallographic data for complexes **1**, **2** and **3**.

	1	**2**	**3**
Formula	$C_{61.62}H_{49.07}B_2F_{7.84}FeN_{14.07}O_3$	$C_{63}H_{54}B_2F_8FeN_{16}$	$C_{126}H_{108}B_7F_{34}Fe_6N_{32}$
Fw	1261.14	1264.69	3127.21
Cryst size, mm	0.1 x 0.1 x 0.1	0.03 x 0.02 x 0.01	0.26 × 0.17 × 0.15
Cryst syst	triclinic	triclinic	trigonal
Space group	*P*-1	*P*-1	$P3_121$
a, Å	10.5589(7)	15.105(3)	26.679(3)
b, Å	14.5471(9)	15.136(2)	26.679(3)
c, Å	21.5140(12)	19.131(3)	21.8284(11)
α, °	72	74	90
β, °	82	70	90
γ, °	70	61	120
V, Å^3	2953.7(4)	3562.6(12)	13455(3)
Z	2	2	3
ρ_{calcd}, g cm^{-3}	1.418	1.179	1.158
μ, mm^{-1}	0.340	2.276	0.506
No. of reflections made	24792	40026	84019
No. of unique reflns, R_{int}	13157, 0.0426	14501, 0.1226	16361, 0.1039
No. of reflns with $F^2>2\sigma(F^2)$	8895	6112	7658
Transmn coeff range	0.922-1.000	0.897-1.000	0.691-1.000
R, R_w[a] ($F^2 > 2\sigma(F^2)$)	0.0896, 0.2300	0.0955, 0.2538	0.0789, 0.2135
R, R_w[a] (all data)	0.1325, 0.2558	0.1780, 0.3085	0.1572, 0.2678
S[a]	1.052	0.952	0.969
Parameters	877, 448	766, 152	1155, 960
Max, min, diff map, e Å^{-3}	1.262, -0.599	1.166, -0.532	0.63, -0.38

[a] Conventional $R = \Sigma||F_o| - |F_c||/\Sigma|F_o|$; $R_w = [\Sigma w(F_o^2 - F_c^2)^2/ \Sigma w(F_o^2)^2]^{1/2}$; $\Sigma = [\Sigma w(F_o^2 - F_c^2)^2/\text{no. data} - \text{no. params})]^{1/2}$ for all data.

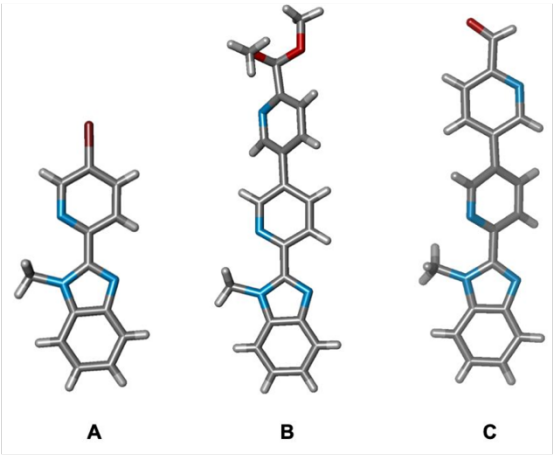

Figure S18: Single-crystal X-ray structures of **A**: starting material 2-(5-bromopyridin-2-yl)-1-methyl-1*H*-benzo[*d*]imidazole; **B**: protected ligand **L'** and **C**: target ligand **L**.

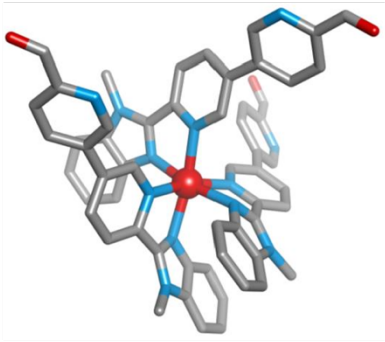

Figure S19: Single-crystal X-ray structure of structure of complex **1**. The counterions and hydrogen atoms are omitted for clarity.

The crystal structure obtained for complex **1** does not necessarily represent the major structure in solution. Although the *mer* isomer was characterised in figure *S*19, there is evidence in the ^{1}H NMR spectrum for the presence of both the *mer* and *fac* isomers in the solution state. In the mass spectrum there is evidence of substochiometric complexes such as $[Fe\mathbf{L}_2]^{2+}$, which could also exist in solution alongside complex **1**.

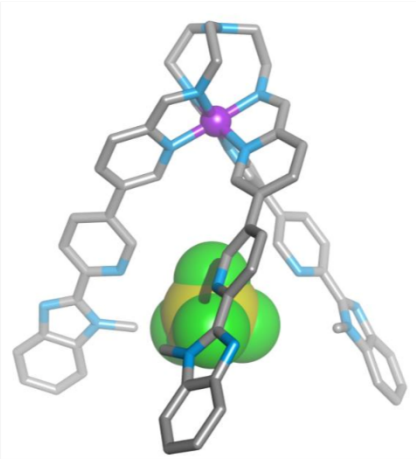

Figure S20: Single-crystal X-ray structure of complex **2**. BF_4^- counterions were distributed across three positions in the crystal lattice, one of which was on the three-fold rotation axis of the complex (occupancy ~75%). The occupancy of the BF_4^- counterions were refined and constrained to be two. The additional counterion and hydrogen atoms are omitted for clarity.

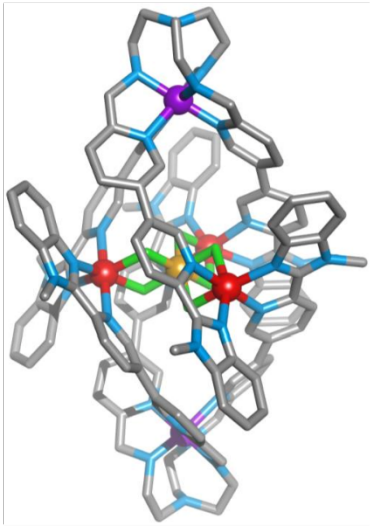

Figure S21: Single-crystal X-ray structure of complex **3**, where purple: low-spin iron(II); red: high-spin iron(II), yellow: iron(III), green: fluoride ions; blue: nitrogen; grey: carbon. The counterions and hydrogen atoms are omitted for clarity.

Table S3: Crystallographically characterised bond angles between the central Fe^5 ion and the connected Fe^3 and Fe^4 ions through the bridging fluoride atoms in complex **3**.

Atoms	Bond Angle (°)
$Fe^3 – F^1 – Fe^5$	103.5(3)
$Fe^4 – F^2 – Fe^5$	101.9(3)
$Fe^4 – F^3 – Fe^5$	102.2(3)

Table S4: Crystallographically characterised bond lengths between the central Fe^5 ion and the six bonded fluoride atoms in complex **3**.

Atoms	Bond Length (Å)
$Fe^5 – F^1$	1.922(8)
$Fe^5 – F^1$	1.922(8)
$Fe^5 – F^2$	1.932(5)
$Fe^5 – F^2$	1.932(5)
$Fe^5 – F^3$	1.898(8)
$Fe^5 – F^3$	1.898(8)

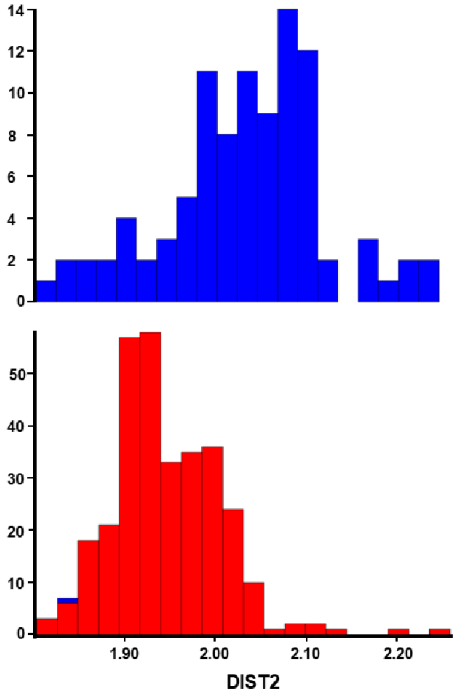

Figure S22: Top (blue): Histogram for Fe(II)-F bond distances excluding μ_3-F-Fe structures. Bottom (red): Histogram for Fe(III)-F bond distances excluding μ_3-F-Fe structures. Based on the CCDC data on crystal structures containing Fe(II)-F and Fe(III)-F bonds (excluding μ_3-F-Fe), data for complex **3** is entirely consistent with our assignment of the Fe^5 atom as an Fe(III) ion.

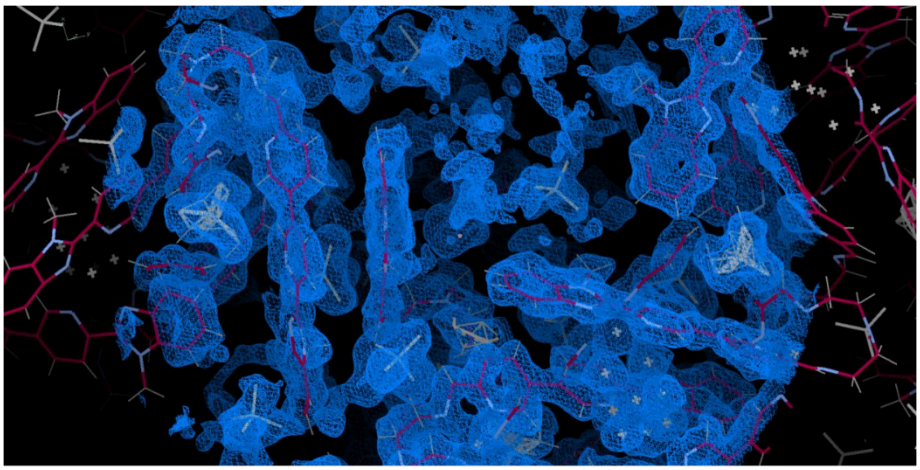

Figure S23: 2Fo-Fc electron density map representation of compound **3**. Electron density map pictures (4 msd) is represented in blue, carbon atoms are represented in red, nitrogen in light blue, BF_4 in grey and iron in white crosses. 2Fo-Fc electron density maps were obtained using Phenix software. Initially, the reflections file (.mtz) obtained from CrysAlisPro were edited to include the map coefficients. Then, the maps were calculated from the edited reflections file and the model (pdb file) obtained from structure solution software (OLEX 2) using phenix.maps software.

S3 Bond Valence Sum (BVS) Analysis

Bond valence sum analysis is a method widely used throughout coordination chemistry to support assignment of oxidation states at metal centres. Bond valence parameters are established from structural data, often obtained from the Cambridge Structural Database (CSD).[19]

Equation 1 describes the relationship between bond valence (S_{ij}) and bond length (r_{ij}) based on cation i and anion j.[20] Both r_0 and B are parameters of empirical origin, where r_0 is specific to a particular ionic pair, and B is a constant assigned the value 0.37 Å.[19]

$$S_{ij} = \exp\left(\frac{(r_0 - r_{ij})}{B}\right) \quad (1)$$

The Fe^{II}-N bond distances are indicative of the spin-state of iron(II) metal centres. In 2017, Zheng and co-workers examined the literature and refined r_0 values for Fe^{II}-N bonds, enabling distinct values for both low-spin (LS) and high-spin (HS) centres to be tabulated. The appropriate r_0 values are reported in table *S*5.

Table S5: Calculated r_0 values for both low-spin and high-spin iron(II) centres.[19]

Fe^{II} Spin State	**r_0 (Å)**
Low spin	1.57
High spin	1.76

S3.1 Complex 1

For complex **1**, the spin state of the iron(II) centre bound at the benzimidazole binding site was investigated using the BVS analysis method.

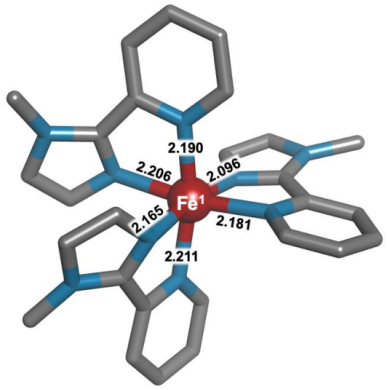

Figure S24: Image of the Fe^{1} centre in **1** obtained from the single-crystal X-ray structure where red: high-spin iron(II); blue: nitrogen; grey: carbon. Atoms above the pyridyl-imine ring were omitted for clarity. All Fe-N bond lengths are reported in Å.

As seen in figure *S*19, the iron(II) centre is bound octahedrally to six nitrogen atoms. Using the crystallographically obtained bond lengths for **1**, S_{ij} values were calculated for the iron(II) centre in both the HS and LS state (Table *S*6).

S_{ij} values were calculated using equation 1, and the valence (V_i), which corresponds to the oxidation state of the metal centre, was calculated using equation 2.

$$V_i = \sum_j S_{ij} \quad (2)$$

Table S6: Crystallographically characterised bond lengths between the Fe^{1} ion and nitrogen donors in complex **1**.

Fe^{1}-N (Å)	**S_{ij} Fe^{II}-N (LS)**	**S_{ij} Fe^{II}-N (HS)**
2.190(17)	0.187	0.313
2.096(4)	0.241	0.403
2.181(4)	0.192	0.321
2.211(3)	0.177	0.296
2.165(4)	0.200	0.335
2.206(4)	0.179	0.300
Average = 2.17	**V_i = 1.18**	**V_i = 1.97**

Based on the crystallographically characterised bond lengths listed in table *S*6, the BVS analysis data supports that the iron(II) centre in complex **1** is high-spin.

S3.2 Complex 2

The spin state of the iron(II) centre bound in the pyridyl-imine binding site of complex **2** was also investigated using the BVS analysis method.

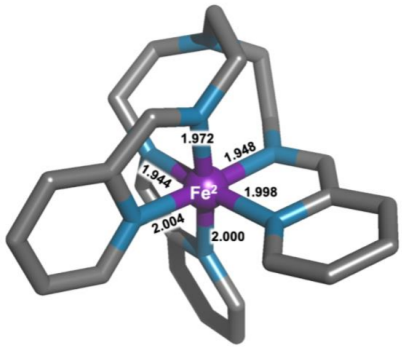

***Figure S25*:** Image of the Fe^{2} centre in **2** obtained from the single-crystal X-ray structure where purple: low-spin iron(II); blue: nitrogen; grey: carbon. Atoms below the pyridyl-imine ring were omitted for clarity. All Fe-N bond lengths are reported in Å.

Table S7: Crystallographically characterised bond lengths between the Fe^2 ion and nitrogen donors in complex **2**.

Fe^2-N (Å)	**S_{ij} Fe^{II}-N (LS)**	**S_{ij} Fe^{II}-N (HS)**
1.972(5)	0.337	0.564
1.948(5)	0.360	0.602
1.998(2)	0.315	0.526
2.000(3)	0.313	0.523
2.004(3)	0.309	0.517
1.944(5)	0.364	0.608
Average = 1.98	**V_i = 2.00**	**V_i = 3.34**

Based on the crystallographically characterised bond lengths listed in table *S*7, the BVS analysis data supports that the iron(II) centre in complex **2** is low-spin.

S3.3 Complex 3

For complex **3** four separate iron environments were observed crystallographically, we have assigned them Fe^2, Fe^3, Fe^4, and Fe^5.

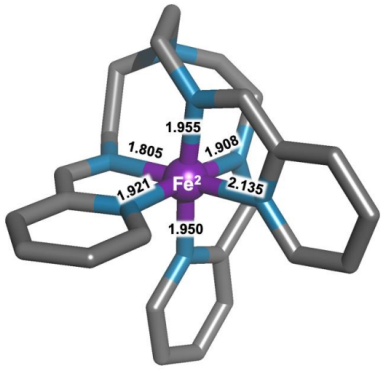

Figure S26: Image of the Fe^2 centre in **3** obtained from the single-crystal X-ray structure purple: low-spin iron(II); blue: nitrogen; grey: carbon. Atoms below the pyridyl-imine ring were omitted for clarity. All Fe-N bond lengths are reported in Å.

Table S8: Crystallographically characterised bond lengths between the Fe^2 ion and nitrogen donors in the pyridyl-imine binding sites in complex **3**.

Fe^2-N (Å)	**S_{ij} Fe^{II}-N (LS)**	**S_{ij} Fe^{II}-N (HS)**
1.963(13)	0.347	0.579
1.960(12)	0.349	0.582
1.981(11)	0.329	0.550
1.932(14)	0.376	0.628
1.951(13)	0.357	0.597
1.935(10)	0.373	0.623
Average = 1.95 Å	**V_i = 2.13**	**V_i = 3.56**

Based on the crystallographically characterised bond lengths listed in table *S*8, the BVS analysis data supports that the iron(II) centres bound in the pyridyl-imine binding sites in complex **3** are low-spin.

S3.3.1 High-Spin Fe(II)/Fe(III) Core

Since the electronic configuration of the iron ions is linked with the length of the Fe-N bonds (Table *S*5), the Fe-F bond lengths are similarly expected to vary based on their oxidation and spin-states. However, due to the limited number of reported Fe-F bonded structures the CSD contains insufficient data to generate reliable r_0 estimations for Fe-F bonds.[19] The r_0 values for Fe^{II}-F bonds that are available are therefore undifferentiated in terms of spin-state and are assigned as r_0 = 1.67 Å, a value calculated by Zheng and co-workers based on all homo- and heteroleptic iron(II) sites found on the CSD.[19]

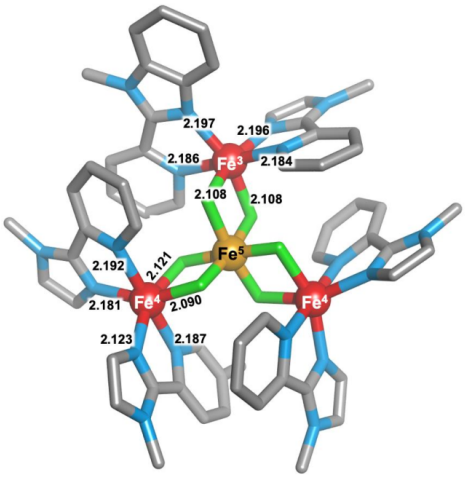

Figure S27: Image of the $[Fe^{III}(\mu\text{-}F)_6(Fe^{II})_3]^{3+}$ core obtained from the single-crystal X-ray structure where red: high-spin iron(II), yellow: iron(III), green: fluoride ions; blue: nitrogen. All Fe-N/F bond lengths are reported in Å.

Table S9: Crystallographically characterised bond lengths between Fe^3 and Fe^4 ions and nitrogen donors/fluoride ions in the $[Fe^{III}(\mu\text{-}F)_6(Fe^{II})_3]^{3+}$ core.

Fe^3 bond lengths (Å)		**S_{ij} Fe^3 (LS)**		**S_{ij} Fe^3 (HS)**		**Fe^4 bond lengths (Å)**		**S_{ij} Fe^4 (LS)**		**S_{ij} Fe^4 (HS)**	
N	F	N	F	N	F	N	F	N	F	N	F
2.202(11)	2.048(7)	0.181	0.360	0.303	0.306	2.123(12)	2.089(8)	0.224	0.322	0.375	0.322
2.202(11)	2.048(7)	0.181	0.360	0.303	0.306	2.136(9)	2.112(6)	0.217	0.360	0.362	0.360
2.104(12)		0.236		0.395		2.189(15)		0.188		0.314	
2.104(12)		0.236		0.395		2.109(15)		0.233		0.389	
		V_i = 1.55		**V_i = 2.11**				**V_i = 1.54**		**V_i = 2.12**	

Based on the crystallographically characterised bond lengths listed in table *S*9, the BVS analysis data supports that the three iron(II) centres (Fe^3, Fe^4) in the core of complex **3** are high-spin.

S4 UV-Vis Spectroscopy

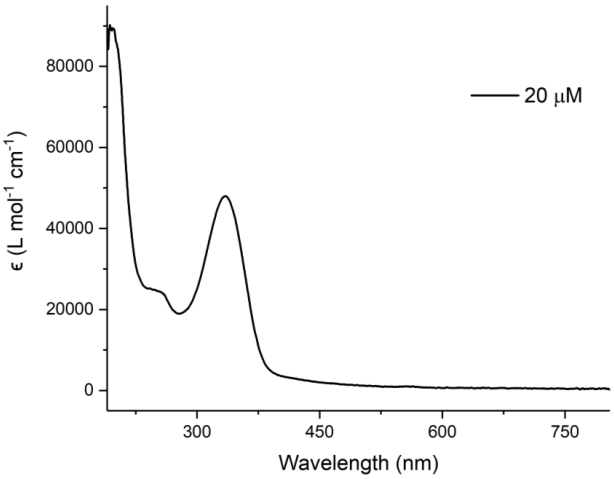

Figure S28: UV-Vis absorption spectrum of ligand **L** in acetonitrile (20 μM).

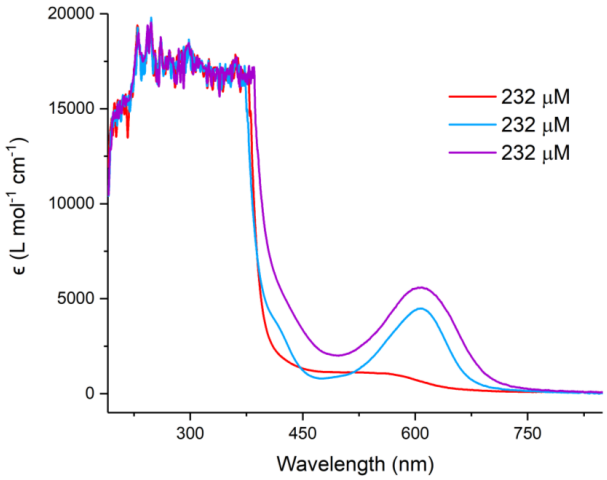

Figure S29: UV-Vis absorption spectrum of red: complex **1**, blue: complex **2** and purple: complex **3** in acetonitrile (232 μM). A characteristic MLCT transition for the Fe(II) *tris*pyridylimine site can be seen at around 607 nm.[21, 22]

S5 SQUID Magnetometry

Magnetic measurements were performed on powdered samples of **1** and **3** using a Quantum Design MPMS-XL7 SQUID magnetometer equipped with a 7 T magnet. Magnetic susceptibility data were recorded under applied fields of 1, 5 or 10 kG, over the temperature range 2-300 K. Prior to measurement, the finely ground crystalline samples were restrained in eicosane to avoid the reorientation of the sample in applied magnetic field. Experimental data were corrected for the diamagnetism of the compound by using tabulated Pascal constants and for the diamagnetism of the sample holder and eicosane by measurement.

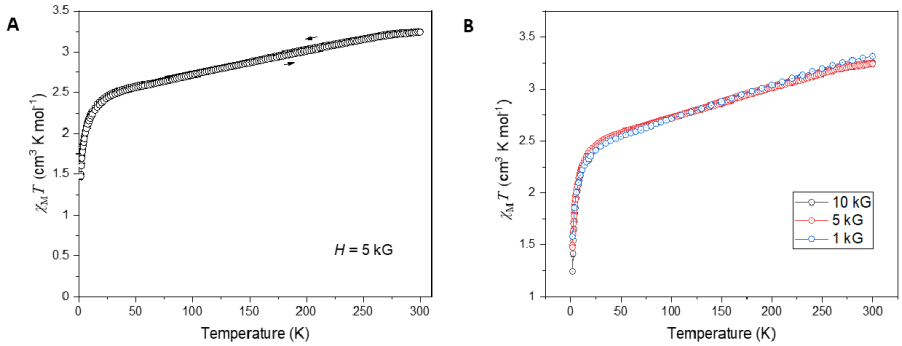

Figure S30: Plots of $\chi_M T$ vs T for **1** measured under cooling and warming regimes, at the temperature sweeping rate of 2 K/min and under applied fields of 1, 5 and 10 kG, and showing: A) the reversible nature of the spin-crossover (SCO) behavior, and B) the effect of field strength. Only a small fraction of the Fe(II) molecules (ca. 16%) undergo thermally induced spin crossover, while the large majority remains high-spin over the 2-300 K range.

Field dependent magnetization data for complex **3** were recorded at 2 and 4 K, by varying the magnetic field from 0 to 7 T. Possible slow relaxation of magnetization of **3** was investigated through measurements of the alternate-current (ac) magnetic susceptibility. Frequency dependence (1-1400 Hz) of the in-phase (χ'_M) and out-of-phase (χ''_M) ac susceptibilities were recorded at fixed temperatures between 1.85 and 6.2 K, under applied dc fields of either 0 or 1000 Oe, and an ac field of 1.55 Oe varying at frequencies between 1 and 1400 Hz. The resulting $\chi_M T$ vs. T and M vs. H curves were fitted simultaneously using the program PHI[23]

(version 3.1.1) by matrix diagonalisation of the (perturbative) anisotropic spin Hamiltonian defined in either equation (3) or (4):

$$\widehat{H} = \mu_B B \sum_i g_i \hat{S}_i - 2J_1 \left(\hat{S}_{\mathrm{Fe}^{III}} \hat{S}_{\mathrm{Fe}_1^{II}} + \hat{S}_{\mathrm{Fe}^{III}} \hat{S}_{\mathrm{Fe}_2^{II}} + \hat{S}_{\mathrm{Fe}^{III}} \hat{S}_{\mathrm{Fe}_3^{II}} \right)$$

$$-2J_2 \left(\hat{S}_{Fe_1^{II}} \hat{S}_{\mathrm{Fe}_2^{II}} + \hat{S}_{Fe_2^{II}} \hat{S}_{\mathrm{Fe}_3^{II}} + \hat{S}_{Fe_3^{II}} \hat{S}_{\mathrm{Fe}_1^{II}} \right) + D_{\mathrm{Fe}_i^{II}} \sum_i \left(\hat{S}^2_{z_{\mathrm{Fe}_i^{II}}} - \frac{\hat{S}^2_{Fe_i^{II}}}{3} \right) \quad (3)$$

$$\widehat{H} = \mu_B B \sum_i g_i \hat{S}_i - 2J_1 \left(\hat{S}_{\mathrm{Fe}^{III}} \hat{S}_{\mathrm{Fe}_1^{II}} + \hat{S}_{\mathrm{Fe}^{III}} \hat{S}_{\mathrm{Fe}_2^{II}} + \hat{S}_{\mathrm{Fe}^{III}} \hat{S}_{\mathrm{Fe}_3^{II}} \right) - 2\, zJ \left(\hat{S}_i \hat{S}_j \right) +$$

$$D_{\mathrm{Fe}_i^{II}} \sum_i \left(\hat{S}^2_{z_{\mathrm{Fe}_i^{II}}} - \frac{\hat{S}^2_{Fe_i^{II}}}{3} \right) \quad (4)$$

where $\hat{S}_{Fe^N}$ (S = 2 for N = *II* or S = 5/2 for N = *III*) represents the total spin operator of the individual iron ions within the cluster, B is the applied magnetic field, μ_B is the Bohr magneton, g is the isotropic g-factor of the compound, $D_{\mathrm{Fe}_i^{II}}$ is the axial zero-field splitting term for high-spin iron(II) ions, while J_1, J_2 and zJ are coupling constants measuring interactions between Fe(II) and Fe(III) ions (J_1), between neighbouring Fe(II) sites (J_2), and long-distance inter-cluster interactions (zJ), respectively. To avoid the overparameterization of the spin Hamiltonian, the anisotropy term of the Fe(III) site was assumed to be negligible, due to $3d^5$ (high-spin) configuration, and the g factor was fixed.

Scheme S3: Coupling scheme used for the modelling of magnetic data (Spin Hamiltonian eq. 3 and 4).

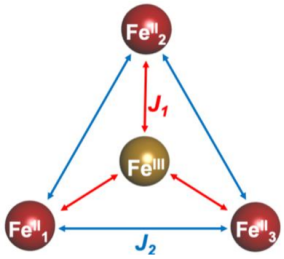

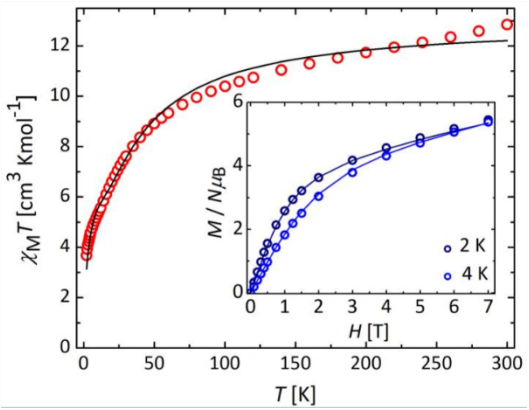

Figure S31: $\chi_M T$ vs T and M vs H (inset) curves of compound **3** with the best fit (solid line) employing the spin Hamiltonian defined in equation 4, and magnetic parameters listed in table *S*10 (Fit 2).

Table S10: Comparison of parameters and quality of four best fits ($\chi_M T$ vs T and $M/N_{\mu B}$ vs H) for the **3**.

Fit	**Fitted parameters**					
	g	J_1 (cm^{-1})	J_2 (cm^{-1})	zJ (cm^{-1})	D (cm^{-1})	Residual
1	1.97	−1.55	−0.17	-	8.93	0.101
2	1.97	−1.54	-	−0.011	9.94	0.157
3	1.99	−1.61	−0.21	-	9.19	0.123
4	1.99	−1.60	-	−0.014	10.46	0.200

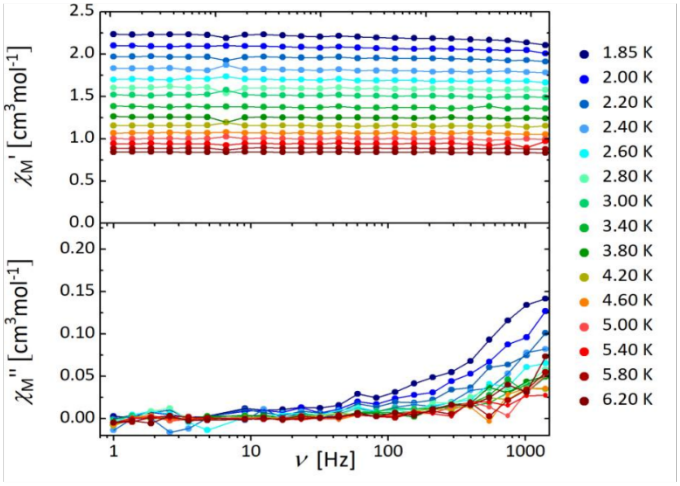

Figure S32: Frequency dependence of the in-phase ($\chi_M^{'}$) and out-of-phase ($\chi_M^{''}$) ac susceptibility for **3** under an applied dc field of 1000 Oe. The solid lines are guides for the eye.

S6 EPR spectroscopy

EPR spectra were collected on a Bruker EMX 300 EPR spectrometer operated at 34 GHz (Q-band) microwave frequency and at variable temperatures.

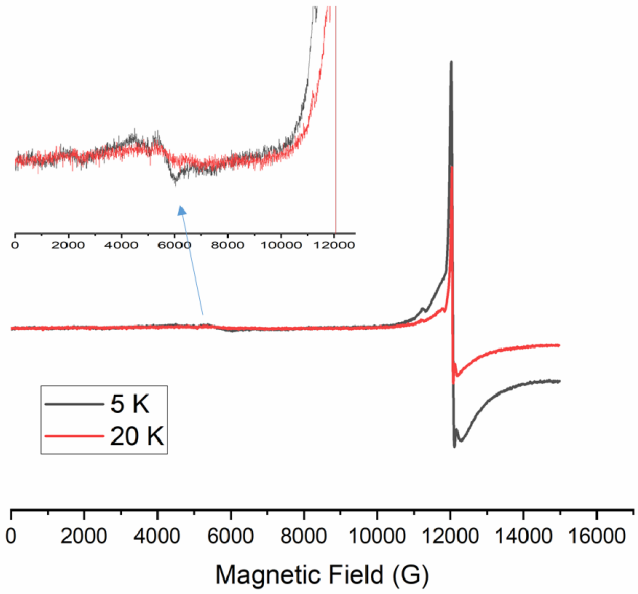

Figure S33: Q-band (34 GHz) EPR spectra at 5 and 20 K for a polycrystalline sample of **3**.

S7 References

1. L. Castañar, G. Dal Poggetto, A. A. Colbourne, G. A. Morris, M. Nilsson, *Magn. Reson. Chem.,* 2018, **56**(6), 546-558
2. R. Evans, Z. Deng, A. K. Rogerson, A. S. McLachlan, J. J. Richards, M. Nilsson, G. A. Morris, *Angew. Chem.,* 2013, **125**(11), 3199-3202
3. R. Evans, G. Dal Poggetto, M. Nilsson, G. A. Morris, *Anal. Chem.,* 2018, **90**(6), 3987-3994
4. H. He, K. R. Rodgers, A. M. Arif, *J. Inorg. Biochem.,* 2004, **98**, 667-676
5. M. Loos, C. Gerber, F. Corona, J. Hollender and H. Singer, *Anal. Chem.,* 2015, **87**(11), 5738-5744
6. H. Nowell, S. A. Barnett, K. E. Christensen, S. J. Teat and D. R. Allan, *J. Synchrotron Radiat.,* 2012, **19**, 435-441.
7. CrysAlisPRO, Oxford Diffractions /Agilent Technologies UK Ltd, Tarnton, England.
8. G. M. Sheldrick, *Acta. Cryst.,* 2015, A**71**, 3-8.
9. G. M. Sheldrick, *Acta. Cryst.,* 2015, C**71**, 3-8.
10. O. V. Dolomanov, L. J. Bourhis, R. J. Gildea, J. A. K. Howard and H. Puschmann, *J. Appl. Cryst.,* 2009, **42**, 339-341.
11. P. V. Afonine, R. W. Grosse-Kunstleve, P. D. Adams and A. Urzhumtsev, *Acta. Cryst.*, **D69**, 2013, 625-634
12. J. J. Danon, A. Krüger, D. A. Leigh, J-F. Lemonnier, A. J. Stephens, I. J. Vitorica-Yrezabal and S. L. Woltering, *Science*, 2017, **355**, 159-162.
13. I. A. Riddell, M. M. J. Smulders, J. K. Clegg, Y. R. Hristova, B. Breiner, J. D. Thoburn, Jonathan R. Nitschke, *Nat. Chem.*, **4**, 2012, 751–756.
14. J. Ferrando-Soria, E. Moreno Pineda, A Chiesa, A. Fernandez, S. A. Magee, S. Carretta, P. Santini, I. J. Vitorica-Yrezabal, F. Tuna, G. A Timco, E. J.L. McInnes, R. E. P. Winpenny, *Nat. Commun*, 2016, **7**, 11377.
15. M. Souto, J. Romero, J. Calbo, I. J. Vitórica-Yrezábal, J. L. Zafra, J. Casado, E. Ortí, A. Walsh, G. Mínguez Espallargas, *J. Am. Soc. Chem.*, **140**, 2018, 10562-10569
16. C. F. Macrae, I. J. Bruno, J. A. Chisholm, P. R. Edgington, P. McCabe, E. Pidcock, L. Rodriguez-Monge, R. Taylor, J. van de Streek and P. A. Wood, *J. Appl. Cryst.,* 2008, **41**, 466-470.
17. Dassault Systèmes BIOVIA, *Discovery Studio Visualizer,* [v17.2.0.16349], San Diego: Dassault Systèmes, [2016].

18. Persistence of Vision Pty. Ltd., 2004, Persistence of Vision Raytracer (Version 3.6), [Computer software]. Retrieved from http://www.povray.org/download/.
19. H. Zheng, K. M. Langner, G. P. Shields, J. Hou, M. Kowiel, F. H. Allen, G. Murshudov and W. Minor, *Acta. Cryst.,* 2017, D**73**, 316-325.
20. E. Pidcock, 1995, 'Structural Considerations of d-Transition Metal Compounds', PhD thesis, The University of Manchester, Manchester.
21. N. Huse, T. K. Kim, L. Jamula, J. K. McCusker, F. M. F. de Groot and R. W. Schoenlein, *J. Am. Chem. Soc.,* 2010, **132**, 6809-6816
22. M. Hardy, N. Struch, F. Topić, G. Schnakenburg, K. Rissanen and A. Lützen, *Inorg. Chem.*, 2018, **57**, 3507-3515.
23. N. F. Chilton, R. P. Anderson, L. D. Turner, A. Soncini and K. S. Murray, *J. Comp. Chem.*, 2013, **34**, 1164-1175.

9. Chapter Three: Paper Two - Mixed Metal Trigonal Bipyramidal Metal-Organic Cages with Adaptable Metal Coordination Centres

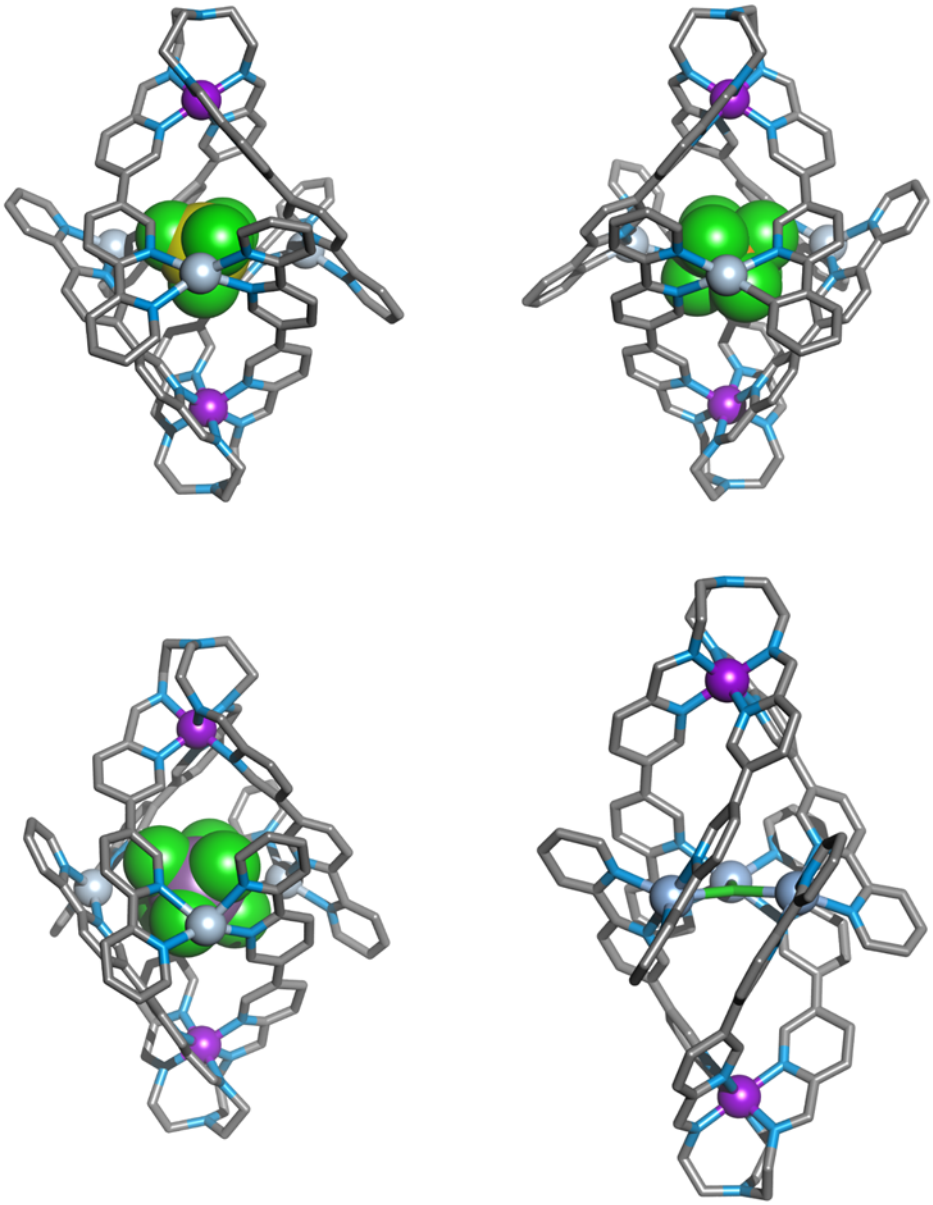

Chemical Science

EDGE ARTICLE

Mixed Metal Trigonal Bipyramidal Metal-Organic Cages with Adaptable Metal Coordination Centres

Received 00th January 20xx,
Accepted 00th January 20xx

DOI: 10.1039/x0xx00000x

Lauren L. K. Taylor,[a] April C. Y. Sung, Iñigo J. Vitorica-Yrezabal,[a] and Imogen A. Riddell[a*]

Heterometallic architectures formed from heteroditopic ligands are of great interest within the field of supramolecular chemistry, but examples remain sparse due to the increased complexity related to the synthesis and characterisation of such compounds. A series of heterometallic iron/silver and iron/copper trigonal bipyramidal architectures with unique structural adaptability are reported herein. Three crystallographically characterised iron(II) and silver(I) trigonal bipyramidal cages with formula $[Fe_2Ag_3L_6T_2]^{7+}$ are shown to encapsulate polyatomic anions, with minor changes to the overall dimensions of the host. In contrast, a $[Fe_2Ag_3L_6T_2(Cl)]^{6+}$ trigonal bipyramidal complex with a central μ_3-Cl ion bound to the three Ag(I) ions is shown to vary significantly in its dimensions. The elongated structure is significantly narrower than comparable structures encapsulating non-covalently bound counterions. Dynamic binding of the central Cl^- anion revealed the ability of each silver ion within the structure to exist in a five-coordinate configuration, prompting us to explore the incorporation of copper ions which may both increase in coordination number and oxidation state. A mixed-valence $[Fe_2Cu^{I}_2Cu^{II}L_6T_2(Cl)]^{7+}$ architecture is characterised by X-ray crystallography and mass spectrometry following oxidation at one of the Cu(I) centres upon chloride ion binding. This complex is an attractive starting point for the formation of heterometallic supramolecular catalysts with redox active metal ions incorporated within the framework.

The design and synthesis of 3D self-assembled architectures has become a popular area of research due to their impressive capabilities in a number of areas including catalysis,[1–3] gas storage[4–6] and stabilisation of reactive guest molecules.[7,8] The construction of structurally flexible self-assembled container molecules capable of adapting their shape to fit specific guests is particularly attractive for host-guest applications. Cages with the ability to adapt their shape to accommodate guests of different sizes[9,10] have previously been utilised as anion receptors,[11] drug delivery vehicles,[12] and for the separation and purification of fullerenes.[13,14] To date a limited number of architectures demonstrating structural flexibility have been reported, but the majority of these examples are homometallic cages.[14,15]

In general, heterometallic architectures still represent a substantial challenge in the supramolecular field due to the increased complexity associated with their synthesis and characterisation.[16–18] Smaller, two-dimensional heterometallic complexes have shown promise as enzyme mimics[19] and antibiotic sensors,[20] whilst examples of larger three-dimensional structures are still in their infancy. Heterometallic architectures containing mixtures of *d*- and *f*-block metal ions have previously been shown to exploit the paramagnetic properties associated with lanthanide ions to act as single-molecule magnets,[21] whilst purely transition metal cages have exhibited large cavities with guest encapsulation capabilities.[22,23]

Self-assembled heterometallic tetrahedra with internal void space[24,25] have been reported, however their flexibility remains somewhat limited. This restricts the range of guest molecules that a single tetrahedron can encapsulate,[26] or forces molecules to change their conformation in order to fit within the tetrahedral cavity.[10]

Larger constructs, such as trigonal bipyramids are less investigated than tetrahedra but have the potential to exist in much less restrictive configurations due to their shape.[27] Moreoever, the requirement for two different binding sites in this architecture allows the incorporation of additional functionality through variation of the metal centre. Although homometallic trigonal bipyramidal architectures exist,[12,28,29] bimetallic trigonal bipyramids are more common.[30–32] The extent of functionality associated with trigonal bipyramidal architectures remains relatively unexplored however, examples have so far demonstrated the fixation of carbon dioxide and sulfur dioxide,[33] and encapsulation of metal cations.[32]

Within metal-organic architectures the metal ions act primarily as structural building blocks, and their intrinsic properties are under-utilised. Incorporation of more than one type of metal centre within a construct provides additional intricacy,[30] and we propose that utilising the redox properties and adaptable coordination sphere of transition metals incorporated within coordination cages will allow access to an exciting new class of supramolecular catalysts.[34,35]

Herein we report the design and synthesis of a series of bimetallic trigonal bipyramidal architectures. The complexes can be generated with a mixture of iron(II) and either silver(I) or copper metal salts, and can encapsulate polyatomic anions including tetrafluoroborate, and hexafluoroantimonate. The ligand employed, **L1**, was previously

[a] *Department of Chemistry, University of Manchester, Oxford Road, Manchester, M13 9PL (UK). E-mail: Imogen.riddell@manchester.ac.uk*

reported to undergo integrative sorting to generate a M_4L_6 tetrahedral complex in the presence of a *bis*bipyridine ligand.[36] In contrast to the previous report, the trigonal bipyramidal architectures featured in this report utilise one asymmetric ligand alongside two different metal ions. The ligand incorporates a non-dynamic bipyridyl binding site at one end, and a dynamic pyridine aldehyde unit at the other which can undergo subcomponent self-assembly in the presence of an appropriate amine and metal ions.[29] The inclusion of two binding sites within the same ligand allows for the formation of novel metal-organic complexes with distinct metal coordination sites (scheme 1). Differentiation of the metal binding sites introduces potential functionality within metal-organic structures, which we propose may be relevant for catalytic applications.

Commonly, trigonal bipyramidal architectures employ heteroditopic ligands[30,31] to form bimetallic complexes in a predictable manner. Within these structures the metal centres may be defined as axial, where metal ions are bound in the apex of the pyramid, and equatorial where metal ions generate the trigonal base of the pyramid. Axial metal ions are commonly bound within octahedral coordination environments, while equatorial metals are bound four-coordinate.[31]

Scheme 1. Stepwise self-assembly of a bimetallic $[M^1_2M^2_3\mathbf{L}_6T_2]^{7+}$ trigonal bipyramidal cage following the initial formation of a mononuclear $[Fe\mathbf{L}_3T]^{2+}$ complex, **ML.**

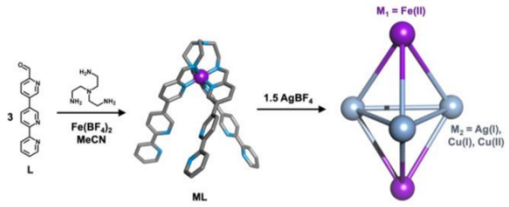

Bimetallic Trigonal Bipyramid Formation with Silver(I)

Ligand **L** has previously been shown to form mononuclear $[M\mathbf{L}_3T]^{2+}$ and helical $[M_2\mathbf{L}_3T]^{4+}$ structures in combination with *tris*(2-aminoethyl)amine and octahedrally coordinating metal ions.[36,37] The mononuclear metalloligand $[Fe\mathbf{L}_3T](BF_4)_2$ (**ML**) contains three terminal bipyridine binding sites which we hypothesised could be combined pairwise with silver(I) metal ions.

Initial reactions indicated that following the addition of $AgBF_4$ (1.5 equiv) to an acetonitrile solution containing **ML** (1 equiv), a mixture was obtained. Characterisation of the reaction mixture indicated it was comprised of a $[Fe_2Ag_3\mathbf{L}_6T_2]^{7+}$ trigonal bipyramid (**C1**$\subset BF_4$) with a BF_4^- counterion bound within its central cavity, and a secondary species we have assigned as the $[FeAg\mathbf{L}_3T]^{3+}$ helicate **C3** (scheme 2; ESI *S*1.3.3). The same result was obtained when the reaction was carried out in one-step, with both iron(II) and silver (I) being added from the outset. The assignment of this mixture was supported by 2D NMR spectroscopy, mass spectral analysis, and DOSY NMR which indicated the presence of two species varying significantly in size. Exclusive formation of trigonal bipyramid **C1**$\subset BF_4$ was observed when the reaction mixture was heated at 65°C for 24 hours, following either a stepwise or one-pot self-assembly strategy. Single crystals of **C1**$\subset BF_4$ were grown through slow diffusion of diethyl ether into an acetonitrile solution containing the construct. The single-crystal X-ray structure of **C1**$\subset BF_4$ (fig. *S*23) highlights the *facial* iron(II) coordination geometry at the *tris*(pyridylimine) binding site. This is reflected in the ^{1}H NMR spectrum by the presence of a single set of resonances per ligand proton.[31] The three silver(I) ions were observed to adopt a four-coordinate see-saw geometry, which has previously been reported for metals with a d^{10} electron configuration.[38]

Additional experiments with potassium hexafluorophosphate and sodium hexafluoroantimonate indicated that these larger anions could displace the tetrafluoroborate counterion from the interior cavity of the trigonal bipyramid. The ^{19}F NMR spectrum of the reaction mixture following PF_6^- addition to **C1**$\subset BF_4$ clearly indicated two sets of peaks for PF_6^- corresponding to free and encapsulated PF_6^- anion (fig. *S*10). Similarly, a change in the ^{19}F NMR profile of SbF_6^- was also recorded following addition of this anion to a solution of **C1**$\subset BF_4$ (fig. *S*8).

In contrast to results set out with tetrafluoroborate, when silver triflate or triflimide were used in self-assembly reactions alongside the corresponding iron(II) salts, smaller bimetallic helical structures were obtained (scheme *S*4, *S*5). These results indicate the requirement for a suitable templating anion during the self-assembly process.

Single-crystal X-ray data for **C1** encapsulating BF_4^-, PF_6^- and SbF_6^- anions were collected following growth of crystals by slow diffusion of diethyl ether into acetonitrile solutions. Comparison of the structures revealed subtle changes in the M-M distances, with shorter Fe-Fe distances corresponding to longer Ag-Ag distances (table *S*3) within one structure. Measurement of the internal void space using VOIDOO revealed a gradual increase in cavity volume as the encapsulated anion increased in size. Fill occupancies were calculated at 49% for BF_4^-, 61% for PF_6^- and 64% for SbF_6^- host-guest complexes; each of these values lies close to the optimal percentage fill volume of 55 % proposed by Rebek.[39] Another feature unveiled by VOIDOO was the better enclosure of the cavity in **C1** compared with classical tetrahedral structures. In particular, it is noteworthy that a probe radius significantly smaller than water was used to map the cavity, indicating that molecules larger than water, including the anions included in this study, could not fit through the windows without significant structural rearrangement (ESI *S*3).

Scheme 2. Subcomponent self-assembly of a mixture containing **C1**$\subset BF_4$ and **C3** from ligand **L**, TREN, Fe(II) and Ag(I) tetrafluoroborate salts. Upon heating at 65°C for 24 hours, the exclusive formation of **C1**$\subset BF_4$ was observed, its τ_4 parameter was calculated as 0.637. The silver-nitrogen bonds in **C3** exist in dynamic equilibrium.

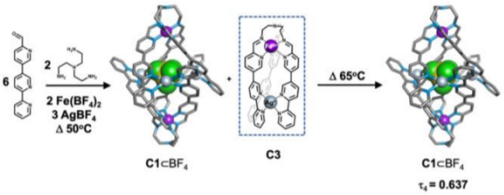

In addition to **C1**$\subset BF_4$, slow diffusion of diethyl ether into an acetonitrile solution containing **C1**$\subset BF_4^-$ over the course of five days resulted in the isolation of a minor impurity that we hypothesised was formed when the silver scavenged a chloride anion. The resulting structure, **C1**(Cl), was an elongated trigonal bipyramid with a μ_3-Cl ion bound in the centre of the complex (fig. 1). Compared with **C1**$\subset BF_4$, this structure had a 2.7 Å longer Fe-Fe distance and a 3.35 Å shorter average Ag-Ag distance, highlighting the adaptability of this architecture. The silver-chloride bonds exist in dynamic equilibrium alongside the silver-nitrogen bonds, and the capability of the

equatorial silver ions to bind an additional atom and change their coordination number opens up potential catalytic capabilities for this class of compound.

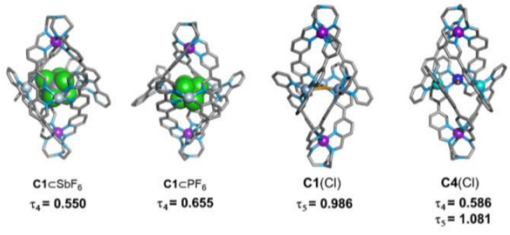

Figure 1. Single-crystal X-ray structures of trigonal bipyramidal complexes **C1**⊂SbF_6, **C1**⊂PF_6, **C1**(Cl), **C4**(Cl) and their corresponding τ_4/τ_5 parameters. Purple spheres: iron(II); grey spheres: silver(I), cyan spheres: copper(I), dark blue spheres: copper(II) green: fluorine; orange: chlorine, blue: nitrogen; grey: carbon.

Bimetallic Trigonal Bipyramid Formation with Copper Salts

Having observed that the coordination number for silver could vary between four and five (**C1** to **C1**(Cl), respectively) without negatively impacting the overall supramolecular assembly, we were interested to see if redox active copper could be accommodating within the equatorial binding site of the trigonal bipyramidal architecture. Moreover, careful measurement of the $\tau_{4/5}$ parameters for the silver complexes revealed their similarity to reported parameters for catalytically active copper centres.[2,43] Specifically, τ_4 for complexes **C1**⊂BF_4 and **C1**⊂PF_6 revealed the Ag(I) ions were bound in a see-saw geometry, whilst τ_4 for **C1**⊂SbF_6 revealed the Ag(I) ions were square planar (table *S*3).[40] For **C1**(Cl), the τ_5 parameter was calculated to be 0.986, indicative of the trigonal bipyramidal geometry around the three Ag(I) centres,[41] and similar to that of previously reported Cu(II) examples.[42,43] Based on these observations we proposed inclusion of copper(I) in the equatorial binding sites, with potential for these metal centres to undergo oxidation to copper(II) with concomitant increase in the coordination number of the metal ion. Such redox changes are well documented in small molecule catalysts.[38]

Copper catalysis has been researched extensively,[38] with pyridine-based Cu(I) complexes being shown to catalyse azide-alkyne cycloaddition,[44] and cyclopropanation reactions.[45] Complexes containing copper have also been shown to catalyse atom transfer radical polymerisation (ATRP) reactions effectively through subsequent oxidations and reductions of the copper centre.[46,47]

Preliminary studies indicated that isostructural copper(I) complexes to **C1** were obtained following the reaction of ligand **L** (6 equiv) with $Fe(BF_4)_2$ (2 equiv), $Cu(MeCN)_4BF_4$ (3 equiv) and TREN (2 equiv) in acetonitrile. Formation of the desired structure, a $[Fe_2Cu_3\mathbf{L}_6T_2]^{7+}$ trigonal bipyramid (**C4**), was supported by ^{1}H NMR spectroscopy which indicated a single symmetric species was present in solution. DOSY NMR also supported the formation of a large discrete structure with a diameter of 19.29 Å, which is comparable with the diameter recorded for **C1**⊂BF_4 in both the solid and solution state. Evidence for formation of the heterometallic construct **C4** could also be found in the mass spectrum (fig. *S*13).

Next, in a bid to emulate the chloride binding behaviour of the silver(I) system (**C1**(Cl)), we evaluated the effect of chloride addition to a solution containing **C4**. Following addition of 3 equivalents of sodium chloride to an acetonitrile solution of **C4** significant broadening of the ^{1}H NMR resonances was observed. When an excess of chloride was added (5 equiv), peaks up to 12.5 ppm were observed (figure *S*13) which is consistent with the presence of a paramagnetic copper(II) species. Diffusion of diethyl ether into an acetonitrile solution containing **C4** and NaCl resulted in the formation of purple crystals. The X-ray structure of this compound was an $[Fe_2Cu_3\mathbf{L}_6T_2(Cl)]^{7+}$ complex (**C4**(Cl)) with one chloride ion bound to one of the copper centres. Analysis of CCDC data supported the assignment of two four-coordinate Cu(I) centres within the equatorial binding sites. Comparisons between fifteen X-ray crystal structures of mononuclear $[Cu(II)NR_4Cl]^{2+}$ complexes and **C4**(Cl) revealed similarities in the Cu(II)-N bond lengths (2.05 and 2.03 Å, respectively). The Cu(II)-Cl bond length in **C4**(Cl) was slightly longer than the average calculated from the CCDC examples (2.47 and 2.30 Å, respectively), which could be attributed to favourable interactions between the central Cl^- anion and the adjacent Cu^+ cations due to their close proximity. Oxidation of Cu(I) to Cu(II) occurred upon binding of the chloride ion,[48,49] whilst the other two copper sites remained as Cu(I). Copper oxidation following halide binding is a key step in Cu(I)/Cu(II) catalytic systems.[47,50]

When tetrabutylammonium bromide (3 equiv) was used in place of the chloride salt, the reaction solution was observed to precipitate rapidly yielding a blue powder, which following dissolution in DMF gave a ^{1}H NMR spectrum corresponding to the metalloligand **ML** (fig. *S*17). Similarly, introduction of three equivalents of tetrabutylammonium nitrate[51] to a solution of **C4** resulted in a purple solid which, following dissolution in d^7-DMF, indicated the presence of a singular symmetric product by ^{1}H NMR spectroscopy (fig. *S*18). Potential binding of triphenylphosphine (PPh_3) to the copper metal centres was also investigated. Formation of the mononuclear species, **ML** was observed by ^{1}H NMR spectroscopy following addition of one equivalent of PPh_3 to an acetonitrile solution of **C4**. We conclude from this result that preferential binding of phosphine to the copper centres makes them unavailable for incorporation within the trigonal bipyramidal structure, the bulky aromatic groups may play a role in this and future work will investigate less sterically hindered phosphines.

We also attempted the direct formation of a trigonal bipyramid incorporating copper(II) ions in the equatorial positions from a copper(II) tetrafluoroborate precursor. Combining stoichiometric equivalents of **L**, $Fe(BF_4)_2$, $Cu(BF_4)_2$, NaCl and TREN in acetonitrile and heating at 65°C for 24 hours generated a purple solution. Chloride anions were included within the subcomponent mixture to saturate the Cu(II) coordination sites. The broadened ^{1}H NMR spectrum obtained following this reaction is consistent with formation of a paramagnetic Cu(II) structure and comparable with the spectrum obtained following addition of chloride to **C4**(Cl) (fig. *S*20). Moreover high-resolution mass spectral analysis (fig. *S*21) supported the inclusion of chloride ions within a trigonal bipyramidal structure of the form $[Fe_2Cu_3\mathbf{L}_6T_2(Cl)_3]^{7+}$ (**C5**). The possibility of incorporating both Cu(I) and Cu(II) into this flexible system is attractive for catalytic applications.

Conclusions

The synthesis and characterisation of a series of self-assembled bimetallic trigonal bipyramidal architectures from a heteroditopic ligand are reported. Trigonal bipyramidal architectures are much less explored than other three-dimensional container molecules, such as tetrahedra, despite the good degree of enclosure and potential structural flexibility of this architecture. Here we report a series of bimetallic iron(II) and silver(I) trigonal bipyramidal cages incorporating spherical polyatomic anions including BF_4^-, PF_6^- and

SbF_6^-. The same components were also shown to bind chloride anions through direct coordination with the equatorial metal centres. Upon binding of chloride the coordination number of the silver and copper centres were shown to increase by one. In the case of copper this increased coordination number corresponded with oxidation of copper(I) to copper(II). The resultant mixed-valence $[Fe_2Cu^{I}_2Cu^{II}\mathbf{L}_6T_2(Cl)]^{7+}$ (**C4**(Cl)) complex was characterised by X-ray crystallography and mass spectral analysis. The binding of halide ions to copper centres is a key step often seen in Cu(I)/Cu(II) catalytic systems,[47,50] and introduces the exciting possibility of generating supramolecular catalysts in which the metal centres are not limited to acting as structural components but also may directly act in a catalytic capacity.

This research was supported by a Royal Society University Research Fellowship (IAR), the Engineering and Physical Sciences Research Council (grants EP/K039547/1 and EP/R00482X/1), and the Diamond Light Source for the allocated time on the beamline I19 (Mt17379).

Data availability

Data associated with this article, including experimental procedures, compound characterisation, X-ray crystallography and VOIDOO calculations are available in the ESI.†

Author contributions

I. A. R. conceived and supervised the project; L. L. K. T. designed and performed the experiments and characterised all compounds; A. C. Y. S. synthesized novel ligand **L**; I. J. Y. R. performed all crystallographic characterisation.

Conflicts of interest

There are no conflicts to declare.

Notes and references

1 J. L. Bolliger, A. M. Belenguer and J. R. Nitschke, *Angew. Chem. Int. Ed.*, 2013, **52**, 7958–7962.

2 T. Kusukawa, T. Nakai, T. Okano and M. Fujita, *Chem. Lett.*, 2003, **32**, 284–285.

3 Y. Fang, J. A. Powell, E. Li, Q. Wang, Z. Perry, A. Kirchon, X. Yang, Z. Xiao, C. Zhu, L. Zhang, F. Huang and H. C. Zhou, *Chem. Soc. Rev.*, 2019, **48**, 4707–4730.

4 M. B. Duriska, S. M. Neville, J. Lu, S. S. Iremonger, J. F. Boas, C. J. Kepert and S. R. Batten, *Angew. Chem. Int. Ed.*, 2009, **48**, 8919–8922.

5 G. R. Lorzing, E. J. Gosselin, B. A. Trump, A. H. P. York, A. Sturluson, C. A. Rowland, G. P. A. Yap, C. M. Brown, C. M. Simon and E. D. Bloch, *J. Am. Chem. Soc.*, 2019, **141**, 12128–12138.

6 I. A. Riddell, M. M. J. Smulders, J. K. Clegg and J. R. Nitschke, *Chem. Commun.*, 2011, **47**, 457–459.

7 P. Mal, B. Breiner, K. Rissanen and J. R. Nitschke, *Science*, 2009, **324**, 1697–1699.

8 M. Yoshizawa, T. Kusukawa, M. Fujita and K. Yamaguchi, *J. Am. Chem. Soc.*, 2000, **122**, 6311–6312.

9 D. Zhang, T. K. Ronson, J. Mosquera, A. Martinez, L. Guy and J. R. Nitschke, *J. Am. Chem. Soc.*, 2017, **139**, 6574–6577.

10 J. L. Bolliger, T. K. Ronson, M. Ogawa and J. R. Nitschke, *J. Am. Chem. Soc.*, 2014, **136**, 14545–14553.

11 R. Custelcean, *Chem. Soc. Rev.*, 2014, **43**, 1813–1824.

12 C. He, X. Chen, C. Sun, L. Zhang, W. Xu, S. Zhang, Z. Wang and F. Dai, *ACS Appl. Mater. Interfaces,* 2021, **13**(29), 33812-33820

13 C. García-Simón, M. Garcia-Borràs, L. Gómez, T. Parella, S. Osuna, J. Juanhuix, I. Imaz, D. Maspoch, M. Costas and X. Ribas, *Nat. Commun.*, 2014, **5**, 2–10.

14 V. Martínez-Agramunt, D. G. Gusev and E. Peris, *Chem. Eur. J.*, 2018, **24**, 14802–14807.

15 A. E. Martín Díaz and J. E. M. Lewis, *Front. Chem.*, 2021, **9**, 1–11.

16 G. Y. Wu, X. Shi, H. Phan, H. Qu, Y. X. Hu, G. Q. Yin, X. L. Zhao, X. Li, L. Xu, Q. Yu and H. B. Yang, *Nat. Commun.*, 2020, **11**, 1–11.

17 R. Saha, D. Samanta, A. J. Bhattacharyya and P. S. Mukherjee, *Chem. Eur. J.*, 2017, **23**, 8980–8986.

18 M. Hardy, J. Tessarolo, J. J. Holstein, N. Struch, N. Wagner, R. Weisbarth, M. Engeser, J. Beck, S. Horiuchi, G. H. Clever and A. Lützen, *Angew. Chem. Int. Ed.*, 2021, **8521**, 22562–22569.

19 S. Mishra, B. Paital, H. S. Sahoo, S. G. Pati, D. Tripathy and N. B. Debata, *Dalt. Trans.*, 2020, **49**, 8850–8854.

20 S. Xu, J. J. Shi, B. Ding, Z. Y. Liu, X. G. Wang, X. J. Zhao and E. C. Yang, *Dalt. Trans.*, 2019, **48**, 1823–1834.

21 L. Li, Y. Zhang, M. Avdeev, L. F. Lindoy, D. G. Harman, R. Zheng, Z. Cheng, J. R. Aldrich-Wright and F. Li, *Dalt. Trans.*, 2016, **45**, 9407–9411.

22 W. J. Ramsay, F. T. Szczypiński, H. Weissman, T. K. Ronson, M. M. J. Smulders, B. Rybtchinski and J. R. Nitschke, *Angew. Chem. Int. Ed.*, 2015, **54**, 5636–5640.

23 K. Li, L. Y. Zhang, C. Yan, S. C. Wei, M. Pan, L. Zhang and C. Y. Su, *J. Am. Chem. Soc.*, 2014, **136**, 4456–4459.

24 Y. Zhang, M. R. Crawley, C. E. Hauke, A. E. Friedman and T. R. Cook, *Inorg. Chem.*, 2017, **56**, 4258–4262.

25 E. T. Luis, H. Iranmanesh, K. S. A. Arachchige, W. A. Donald, G. Quach, E. G. Moore and J. E. Beves, *Inorg. Chem.*, 2018, **57**, 8476–8486.

26 T. K. Ronson, W. Meng and J. R. Nitschke, *J. Am. Chem. Soc.*, 2017, **139**, 9698–9707.

27 M. Maity, P. Howlader and P. S. Mukherjee, *Cryst. Growth Des.*, 2018, **18**, 6956–6964.

28 S. Cardona-Serra, E. Coronado, P. Gaviña, J. Ponce and S. Tatay, *Chem. Commun.*, 2011, **47**, 8235–8237.

29 L. L. K. Taylor, I. J. Vitorica-Yrezabal, I. Borilovic, F. Tuna and I. A. Riddell, *Chem. Commun.,* 2021, *accepted.*

30 S. Sanz, H. M. O'Connor, V. Martí-Centelles, P. Comar, M. B. Pitak, S. J. Coles, G. Lorusso, E. Palacios, M. Evangelisti, A. Baldansuren, N. F. Chilton, H. Weihe, E. J. L. McInnes, P. J. Lusby, S. Piligkos and E. K. Brechin, *Chem. Sci.*, 2017, **8**, 5526–5535.

31 M. Hardy, N. Struch, F. Topić, G. Schnakenburg, K. Rissanen and A. Lützen, *Inorg. Chem.*, 2018, **57**, 3507–3515.

32 X. Sun, D. W. Johnson, K. N. Raymond and E. H. Wong, *Inorg. Chem.*, 2001, **40**, 4504–4506.

33 C. Browne, W. J. Ramsay, T. K. Ronson, J. Medley-Hallam and J. R. Nitschke, *Angew. Chem. Int. Ed.*, 2015, **54**, 11122–11127.

34 W. X. Gao, H. N. Zhang and G. X. Jin, *Coord. Chem. Rev.*, 2019, **386**, 69–84.

35 G. Olivo, G. Capocasa, D. Del Giudice, O. Lanzalunga and S. Di Stefano, *Chem. Soc. Rev.*, 2021, **50**, 7681–7724.

36 L. L. K. Taylor, A. Sung, I. J. Vitorica-Yrezabal and I. A. Riddell, 2021, *unpublished*.

37 A. Sung, *MChem Thesis*, The University of Manchester, 2019.

38 T. J. Zerk and P. V. Bernhardt, *Coord. Chem. Rev.*, 2018, **375**, 173–190.

39 S. Mecozzi and J. Rebek, *Chem. Eur. J.*, 1998, **4**, 1016–1022.

40 L. Yang, D. R. Powell and R. P. Houser, *J. Chem. Soc. Dalt. Trans.*, 2007, 955–964.

41 A. G. Blackman, E. B. Schenk, R. E. Jelley, E. H. Krenske and L. R. Gahan, *Dalt. Trans.*, 2020, **49**, 14798–14806.

42 B. S. Lim and R. H. Holm, *Inorg. Chem.*, 1998, **37**, 4898–4908.

43 L. Chu, K. I. Hardcastle and C. E. MacBeth, *Inorg. Chem.*, 2010, **49**, 7521–7529.

44 C. L. Luo, C. X. Hu, P. Shang, G. Z. Wen, J. J. Zhu, Y. H. Xuan, B. L. Xia, Y. C. Liu, Z. H. Jiang, G. Dong, W. Zhang, L. C. Gui and X. F. Jiang, *New J. Chem.*, 2021, **45**, 8910–8917.

45 C. T. Yeung, H. L. Yeung, C. S. Tsang, W. Y. Wong and H. L. Kwong, *Chem. Commun.*, 2007, 5203–5205.

46 K. Schroder, R. T. Mathers, J. Buback, D. Konkolewicz, A. J. D. Magenau and K. Matyjaszewski, *ACS Macro Lett.*, 2012, **1**, 1037–1040.

47 T. J. Zerk and P. V. Bernhardt, *Inorg. Chem.*, 2017, **56**, 5784–5792.

48 W. T. Eckenhoff and T. Pintauer, *Inorg. Chem.*, 2007, **46**, 5844–5846.

49 C. M. Moore, D. A. Quist, J. W. Kampf and N. K. Szymczak, *Inorg. Chem.*, 2014, **53**, 3278–3280.

50 S. Zhang and L. Zhao, *Nat. Commun.*, 2019, **10**, 1–10.

51 M. Leschke, M. Melter, B. Walfort, A. Driess, G. Huttner and H. Lang, *Zeitschrift fur Anorg. und Allg. Chemie*, 2004, **630**, 2022–2030.

Supporting Information for

Mixed Metal Trigonal Bipyramidal Metal-Organic Cages with Adaptable Metal Coordination Centres

Lauren L. K. Taylor,[a] April C. Y. Sung, Iñigo J. Vitorica-Yrezabal,[a] Imogen A. Riddell*[a]

[a] Department of Chemistry, University of Manchester, Oxford Road, Manchester, M13 9PL (UK)

*Email: imogen.riddell@manchester.ac.uk

Contents

S1 Synthesis and Characterisation

S1.1 General Experimental Details

Unless stated otherwise, all chemicals were supplied from Sigma-Aldrich, Fluorochem, Fisher Scientific, Alfa Aesar or Scientific Laboratory Supplies Ltd and used without further purification. Deuterated NMR solvents were supplied from Sigma-Aldrich and NMR spectra were recorded on a B500 Bruker Advance II+ 500 MHz spectrometer. Chemical shifts are reported in parts per million (ppm). Coupling constants (*J*) are reported in hertz (Hz). Standard abbreviations indicating multiplicity were used as follows: s = singlet, d = doublet, t = triplet, dd = doublet of doublets, m = multiplet. ^{1}H and ^{13}C assignments were made using 2D NMR methods (COSY, NOESY, HSQC, HMBC). High resolution mass spectra were obtained using a Thermo Orbitrap Exactive Plus Extended Mass Range mass spectrometer. Elemental analyses were performed by the microanalytical services of The University of Manchester with a CFlash 2000 elemental analyser for the analyses of carbon, hydrogen and nitrogen.

S1.2 Ligand Synthesis

[2,2':5',3''-Terpyridine]-6''-carbaldehyde (**L**) ligand synthesis was adapted from a previously reported protocol.[1]

Scheme S1. Synthesis of heteroditopic ligand **L** *via* a convergent synthesis strategy starting from 5-bromo-2-pyridinecarboxaldehyde. i) *p*-TsOH, ii) $Pd(dppf)Cl_2.CH_2Cl_2$, KOAc, iii) $Pd(PPh_3)_4$, Na_2CO_3, iv) HCl (2 M).

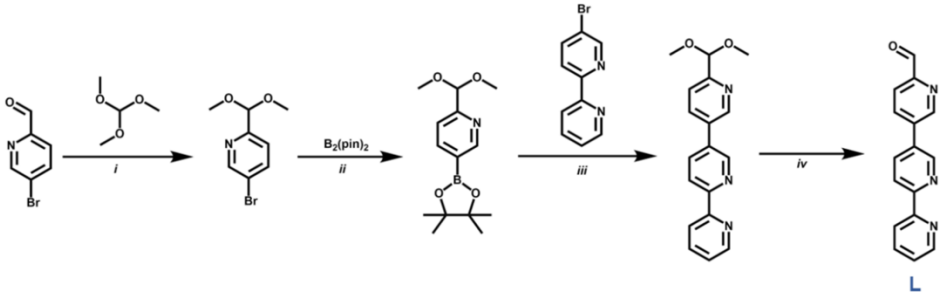

S1.3 Complexation Reactions with Iron(II) and Silver(I)

Scheme S2. General reaction conditions for the self-assembly of an $[Fe_2Ag_3\mathbf{L}_6T_2]^{7+}$ trigonal bipyramid from ligand **L**, TREN, iron(II) and silver(I) salts.

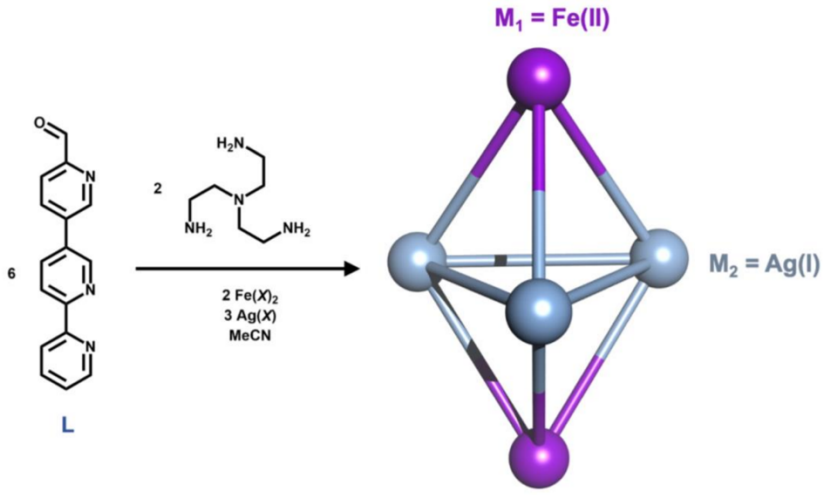

S1.3.1 Reactions with Iron(II) and Silver(I) Tetrafluoroborate

Scheme S3. Reaction scheme for the self-assembly of $[Fe_2Ag_3\mathbf{L}_6T_2](BF_4)_7$ trigonal bipyramid **C1**⊂BF_4 from ligand **L**, TREN, $Fe(BF_4)_2$ and $AgBF_4$.

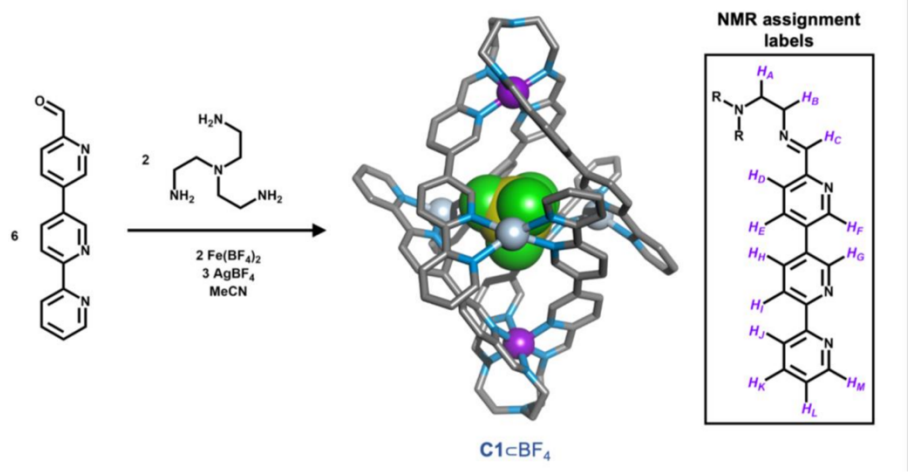

Complex 1⊂BF_4 **(C1**⊂BF_4**)**

L (20.3 mg, 77 mmol, 6 equiv), $Fe(BF_4)_2.6H_2O$ (8.6 mg, 25.5 mmol, 2 equiv), $AgBF_4$ (7.5 mg, 38.3 mmol, 3 equiv) and TREN (3.84 mL, 26.2 mmol, 2 equiv) were dissolved in acetonitrile (2 mL) giving a purple solution. This was heated (50°C, 24 hr) and the purple solution was layered with diethyl ether. The resulting purple solid was filtered and washed with chloroform to give a purple solid (12.2 mg, 5.6 μmol, 22%). ^{1}H (500 MHz, 298 K, CD_3CN): 9.49 (s, 1H, H_C,), 8.53 – 8.57 (m, 2H, H_F, H_D), 8.27 (d, 2H, J = 7.60 Hz, H_E, H_H), 8.07 (d, 1H, J = 8.15 Hz, H_M), 8.03 (td, 1H, J = 7.63, 1.65 Hz, H_L), 7.82 (d, 1H, J = 8.35 Hz, H_I), 7.70 (d, 1H, J = 4.15 Hz, H_J), 7.65 (dd, 1H, J = 8.40, 2.24 Hz, H_G), 7.52 (t, 1H, J = 6.18 Hz, H_K), 3.95 (s, 1H, H_B), 3.80 (s, 1H, H_A), 3.28 (t, 1H, J = 12.14 Hz, H_A). DOSY diffusion coefficient: 5.88 x 10^{-10} m^2 s^{-1}. [Accurate mass, *m/z*]: $\{Fe_2Ag_3\mathbf{L}_6T_2(BF_4)_4\}^{3+}$ = 884.7950, $\{Fe_2Ag_3\mathbf{L}_6T_2(BF_4)_5\}^{2+}$ = 1310.6953, $\{Fe_2Ag_2\mathbf{L}_6T_2(BF_4)_2\}^{6+}$ = 563.6169, $\{Fe_2Ag_2\mathbf{L}_6T_2(BF_4)_3\}^{3+}$ = 779.8252, $\{Fe_2Ag_2\mathbf{L}_6T_2(BF_4)_4\}^{2+}$ = 1214.2403, $\{FeAg_2\mathbf{L}_3T(H_2O)Cl(BF_4)\}^{2+}$ = 643.5553, $\{FeAg_2\mathbf{L}_3T(BF_4)_2\}^{2+}$ = 660.5716.

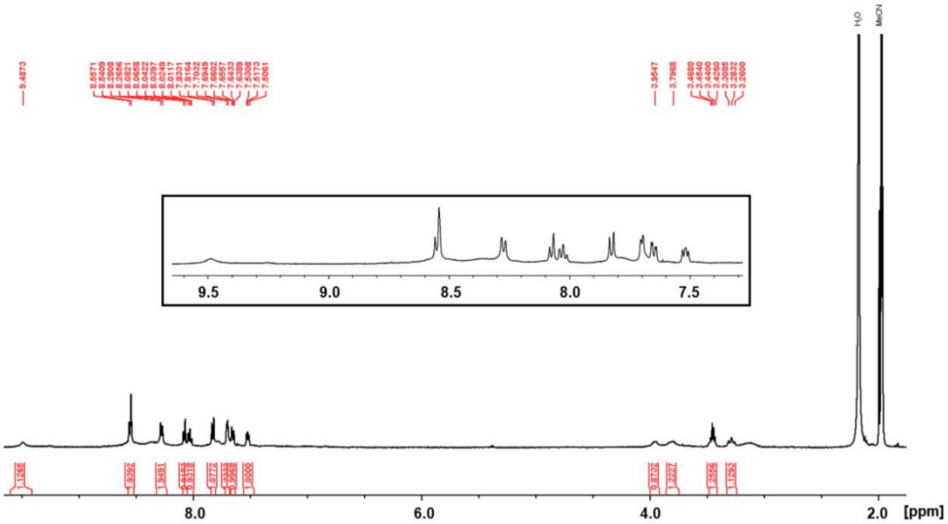

Figure S1. ^{1}H NMR (500 MHz, CD_3CN, 298 K) spectrum of **C1**⊂BF_4. Insert highlights the multiplicity of peaks in the aromatic region.

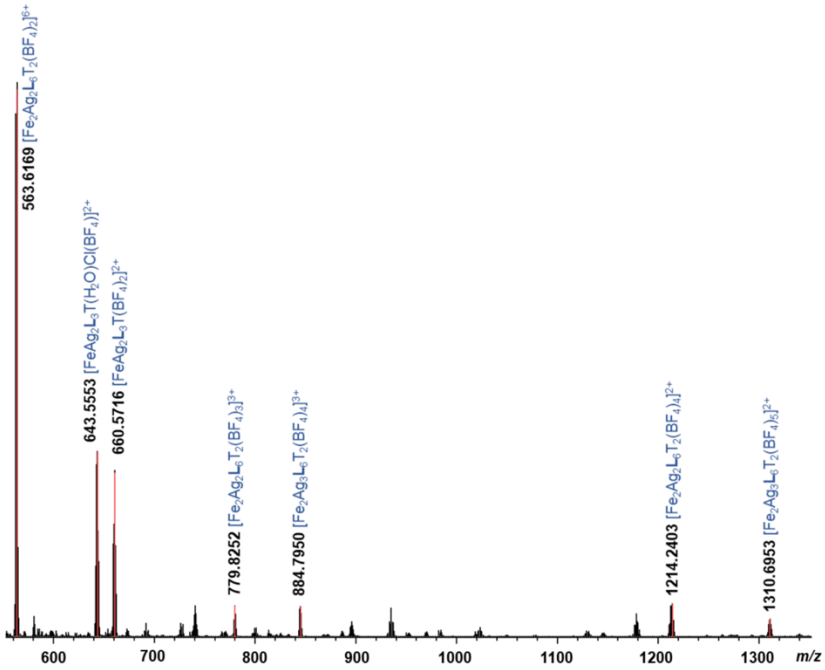

Figure S2. High-resolution mass spectrum for an acetonitrile solution of **C1**⊂BF_4.

S1.3.2 Reactions with Iron(II) and Silver(I) Triflate

Scheme S4. Reaction scheme for the self-assembly of [FeAg**L**$_3$T](OTf)$_3$ dinuclear helicate **C2** from ligand **L**, TREN, Fe(OTf)$_2$ and AgOTf.

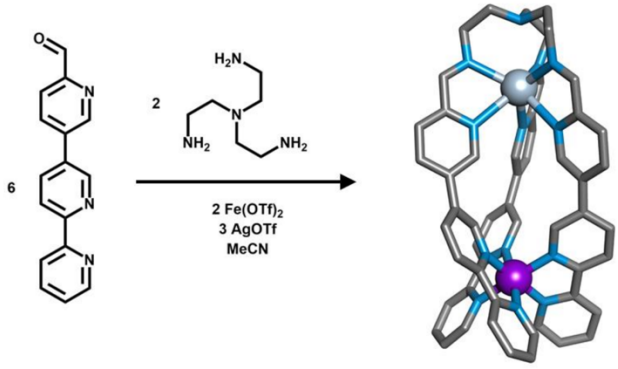

C2

Complex 2 (C2)

L (19.8 mg, 75.9 mmol, 6 equiv), Fe(OTf)$_2$ (10.0 mg, 28.2 mmol, 2 equiv), AgOTf (9.8 mg, 38.3 mmol, 3 equiv) and TREN (3.84 mL, 26.2 mmol, 2 equiv) were dissolved in acetonitrile (2 mL) giving a purple solution. This was heated (65°C, 24 hr) and the purple solution was layered with diethyl ether. The resulting purple solid was filtered and washed with chloroform to give a purple crystalline solid (20.1 mg, 19.4 μmol, 69%). *NMR assignment labels based on those in scheme S3.* ^{1}H (500 MHz, 298 K, CD_3CN): 8.49 – 8.55 (m, 3H, H_F, H_M, H_G), 8.50 (s, 1H, H_C), 8.13 (td, 2H, J = 7.98, 2.34 Hz, H_H, H_I), 8.08 – 8.10 (m, 1H, H_L), 8.06 (dd, 1H, J = 7.85, 2.20 Hz, H_E), 7.66 (d, 1H, J = 7.90 Hz, H_D), 7.46 (t, 1H, J = 6.65 Hz, H_K), 7.14 (d, 1H, J = 7.14 Hz, H_J), 4.06 (t, 1H, J = 13.67 Hz, H_B), 3.64 (dd, 1H, J = 13.72, 2.20 Hz, H_B), 3.28 (dt, 1H, J = 19.82, 3.32 Hz, H_A), 2.69 (d, 1H, J = 13.05 Hz, H_A). DOSY diffusion coefficient: 7.72 x 10^{-10} m^2 s^{-1}. [Accurate mass, *m/z*]: {FeAg**L**$_3$T}$^{3+}$ = 346.7414, {FeAg**L**$_3$T(OTf)}$^{2+}$ = 594.5874, {FeAg**L**$_3$T(OTf)$_2$}$^+$ = 1338.1263, {Fe$_2$**L**$_3$T(H$_2$O)$_2$Cl$_2$(OTf)}$^{2+}$ = 674.5244, {FeAg**L**$_3$T(H$_2$O)Cl}$^{2+}$ = 594.5971.

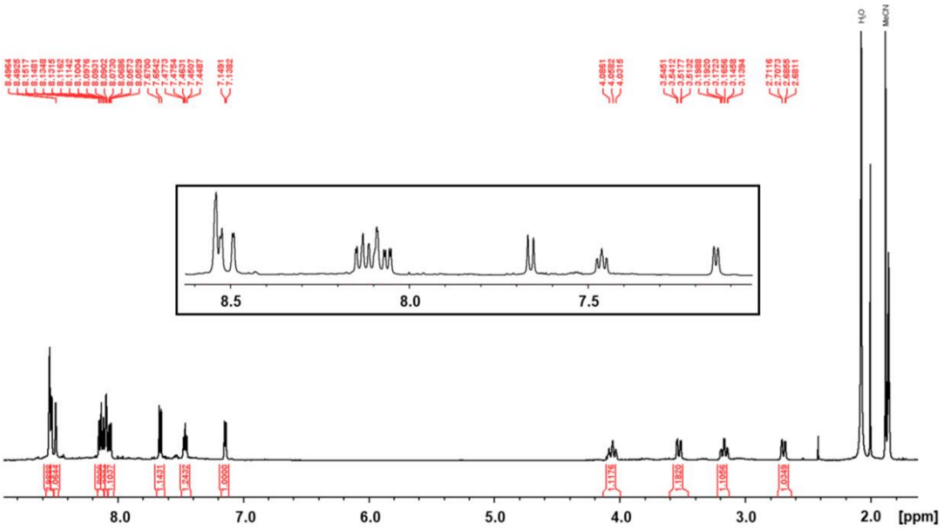

Figure S3. ^{1}H NMR (500 MHz, CD_3CN, 298 K) spectrum of **C2**. Insert highlights the multiplicity of peaks in the aromatic region.

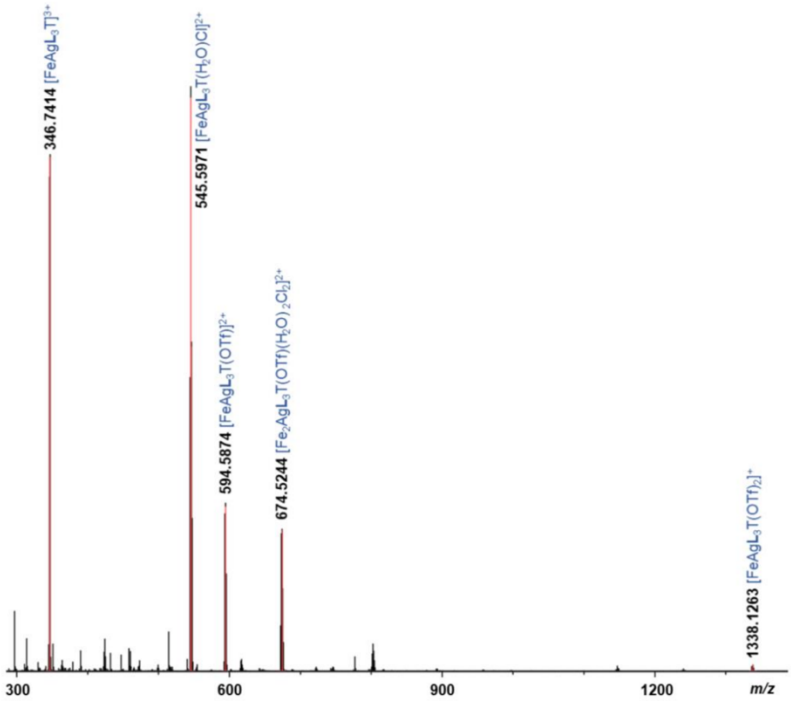

Figure S4. High-resolution mass spectrum for an acetonitrile solution of **C2**.

S1.3.3 Reactions with Iron(II) and Silver(I) Triflimide

Scheme S5. Reaction scheme for the self-assembly of predicted product [FeAg**L**$_3$T](NTf$_2$)$_3$ dinuclear helicate **C3** from ligand **L**, TREN, Fe(NTf$_2$)$_2$ and AgNTf$_2$, where the Ag(I) ion was bound by three bipyridine motifs[2] and the iron(II) was bound in the *tris*pyridylimine site. The ^{1}H NMR of **C3** was similar to that of **C2**, and DOSY NMR spectroscopy highlighted that **C3** was a similar size to **C2**. The positions of iron(II) and silver(I) in **C2** were characterised by X-ray crystallography, and it was anticipated that the slight difference in NMR spectrum between **C2** and **C3** was due to the switched positions of the metal ions. Mass spectrometry of **C3** also indicated the sole presence of a dinuclear helicate in solution.

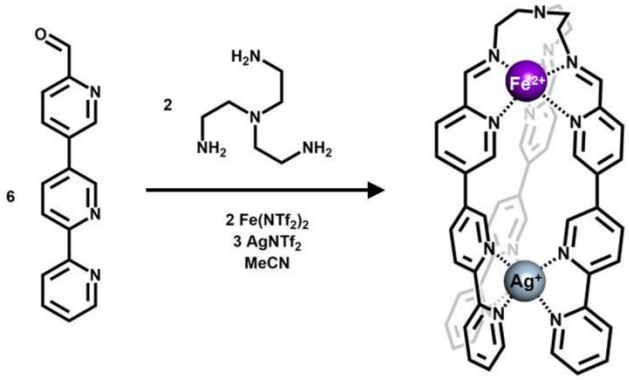

C3

Complex 3 (C3)

L (20.1 mg, 77.0 mmol, 6 equiv), Fe(NTf$_2$)$_2$.7H$_2$O (15.6 mg, 21.0 mmol, 2 equiv), AgNTf$_2$ (14.9 mg, 38.4 mmol, 3 equiv) and TREN (3.84 mL, 26.2 mmol, 2 equiv) were dissolved in acetonitrile (2 mL) giving a pink solution. This was heated (65°C, 24 hr) and the pink solution was layered with diethyl ether. The resulting purple solid was filtered and washed with chloroform to give a purple crystalline solid (20.2 mg, 19.4 μmol, 93%). *NMR assignment labels based on those in scheme S3.* ^{1}H (500 MHz, 298 K, CD$_3$CN): 8.71 (s, 1H, H_C), 8.63 (dd, 2H, J = 8.10, 3.75 Hz, H_M, H_G), 8.59 (s, 1H, H_F), 8.19 – 8.26 (m, 3H, H_L, H_I, H_H), 8.16 (dd, 1H, J = 7.90, 2.04 Hz, H_E), 7.76 (d, 1H, J = 7.90 Hz, H_D), 7.57 (t, 1H, J = 6.36 Hz, H_K), 7.24 (d, 1H, J = 5.49 Hz, H_J), 4.16 (t, 1H, J = 13.41 Hz, H_B), 3.63 (d, 1H, J = 12.46 Hz, H_B), 3.28 (td, 2H, J = 13.16, 3.10 Hz, H_A, H_A), 2.69 (d, 1H, J = 13.05 Hz, H_A). DOSY diffusion coefficient: 7.57 x 10^{-10} m^2 s^{-1}. [Accurate mass, *m/z*]: {FeAg**L**$_3$T}$^{3+}$ = 346.7415, {FeAg**L**$_3$T(NTf$_2$)}$^{2+}$ = 660.0734, {FeAg**L**$_3$T(NTf$_2$)$_2$}$^+$ = 1600.0651.

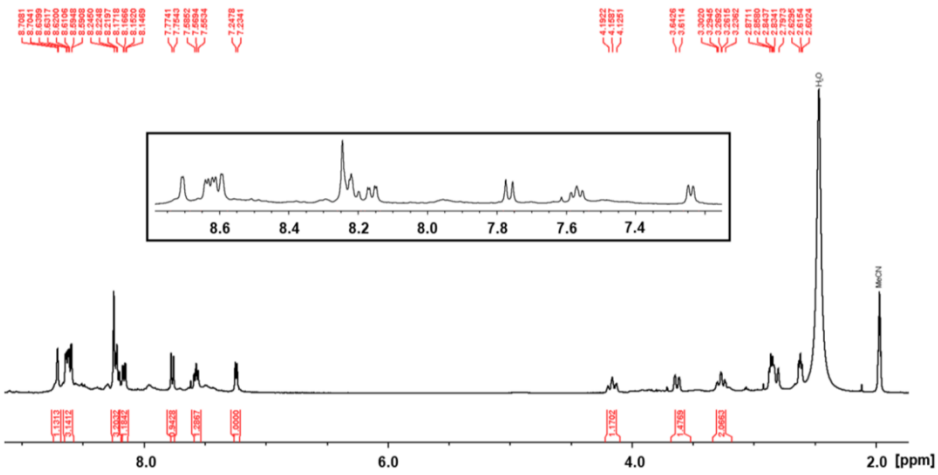

Figure S5. ^{1}H NMR (500 MHz, CD_3CN, 298 K) spectrum of **C3**. Insert highlights the multiplicity of peaks in the aromatic region.

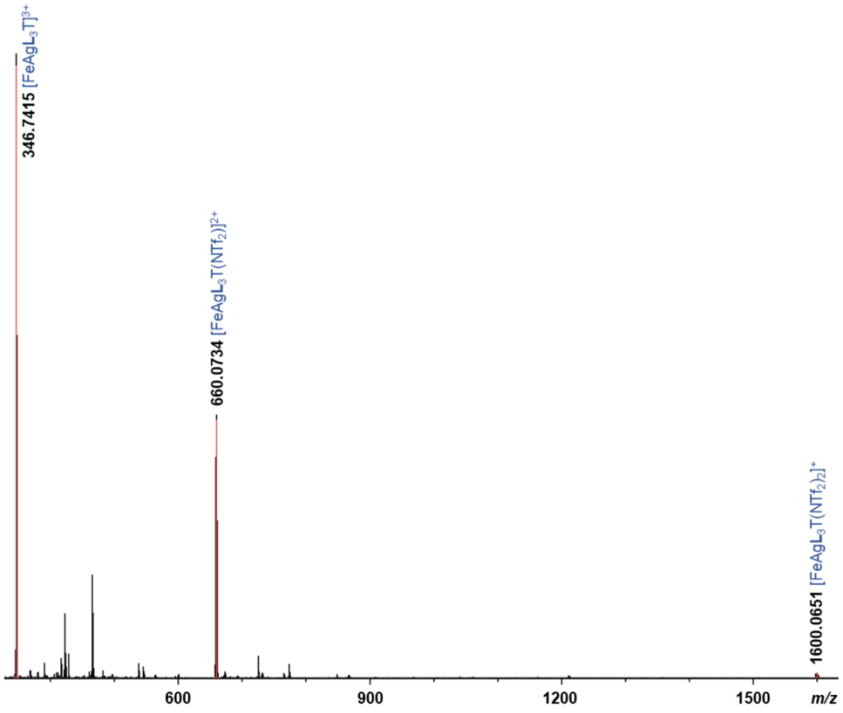

Figure S6. High-resolution mass spectrum for an acetonitrile solution of **C3**.

S1.4 Anion Encapsulation

S1.4.1 Hexafluoroantimonate Encapsulation

Scheme S6. Reaction scheme for the self-assembly of $[Fe_2Ag_3\mathbf{L}_6T_2](BF_4)_7$ trigonal bipyramid **C1**⊂BF_4 followed by the addition of $NaSbF_6$ resulting in the formation of trigonal bipyramid **C1**⊂SbF_6 with an SbF_6^- anion encapsulated within the central cavity.

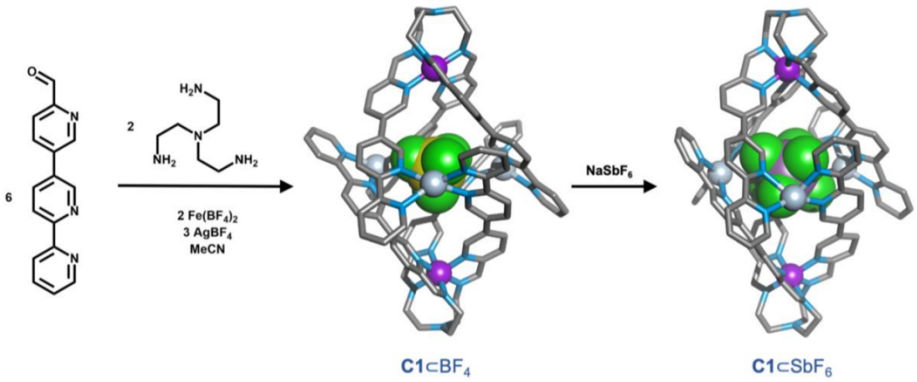

Complex 1⊂SbF_6 **(C1**⊂SbF_6**)**

$NaSbF_6$ (1.3 mg, 5.04 umol, 2.2 equiv) was added to a solution containing complex **C1**⊂BF_4 (5 mg, 2.29 mmol, 1 equiv). The resulting purple solution was added to a J-Young NMR tube. The tube was sealed, and the solution was degassed by three vacuum/N_2 fill cycles before being heated (65°C, 24 hr). Single crystals of **C1**⊂SbF_6 were grown by diffusion of diethyl ether into an acetonitrile solution containing **C1**⊂SbF_6.

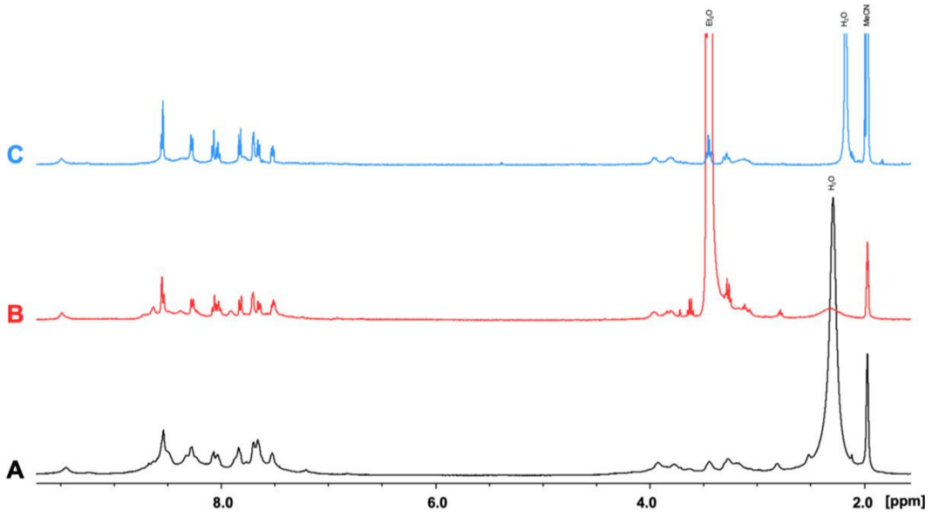

Figure S7. ^{1}H NMR (500 MHz, CD_3CN, 298 K) stacked plot of **A:** one-pot reaction forming **C1**⊂BF_4, **B**: the formation of **C1**⊂SbF_6 after the addition of $NaSbF_6$ (2.2 equiv) into the spectrum **A** solution, **C:** reference spectrum for **C1**⊂BF_4. Addition of SbF_6^- into spectrum **A** resulted in significant sharpening of the ^{1}H NMR spectrum.

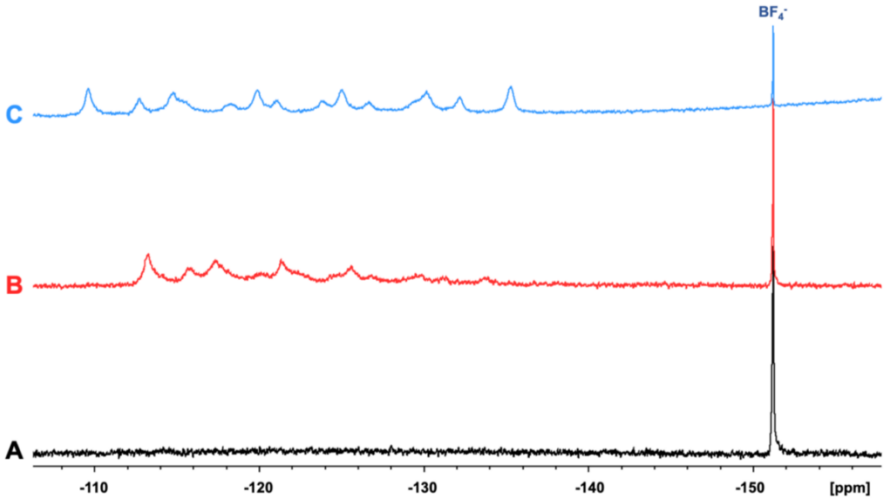

Figure S8. ^{19}F NMR (376 MHz, CD_3CN, 298 K) stacked plot of **A:** one-pot reaction forming **C1**⊂BF_4, **B**: after the addition of $NaSbF_6$ (2.2 equiv) into the spectrum **A** solution, **C:** reference spectrum of $NaSbF_6$ and KBF_4 in an acetonitrile solution. The shift of SbF_6^- peaks in spectrum **B** can be attributed to encapsulation of the SbF_6^- anion within the trigonal bipyramidal cage.

S1.4.2 Hexafluorophosphate Encapsulation

Scheme S7. Reaction scheme for the addition of KPF_6 into a solution containing a mixture of **C1**⊂BF_4 and **C3** to promote the formation of trigonal bipyramid **C1**⊂PF_6 which has a PF_6^- anion encapsulated within the central cavity.

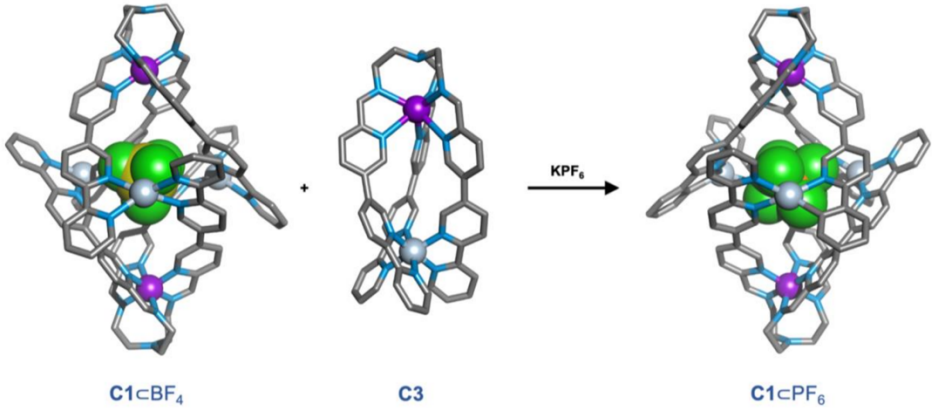

Complex 1⊂PF_6 **(C1**⊂PF_6**)**

KPF_6 (1.4 mg, 7.61 μmol, 2.5 equiv) was added to a solution containing a mixture of complexes **C1**⊂BF_4 and **C3** (5 mg, 2.29 mmol, 1 equiv). The resulting purple solution was added to a J-Young NMR tube. The tube was sealed, and the solution was degassed by three vacuum/N_2 fill cycles before being heated (65ºC, 24 hr). Single crystals of **C1**⊂PF_4 were grown by diffusion of diethyl ether into an acetonitrile solution containing **C1**⊂PF_4.

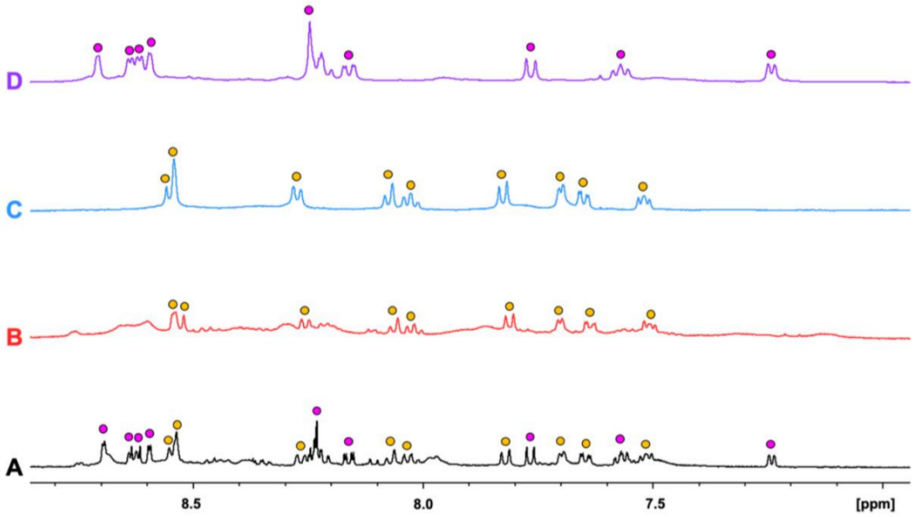

Figure S9. ^{1}H NMR (500 MHz, CD_3CN, 298 K) stacked plot of **A:** reaction mixture containing both **C1**⊂BF_4 and **C3**, **B**: after the addition of PF_6 (1.4 mg) into the spectrum **A** solution, **C:** reference spectrum of **C1**⊂BF_4, **D:** reference spectrum of **C3**. Upon addition of PF_6^- into the mixed system, the amount of **C3** in the system observable by ^{1}H NMR decreases.

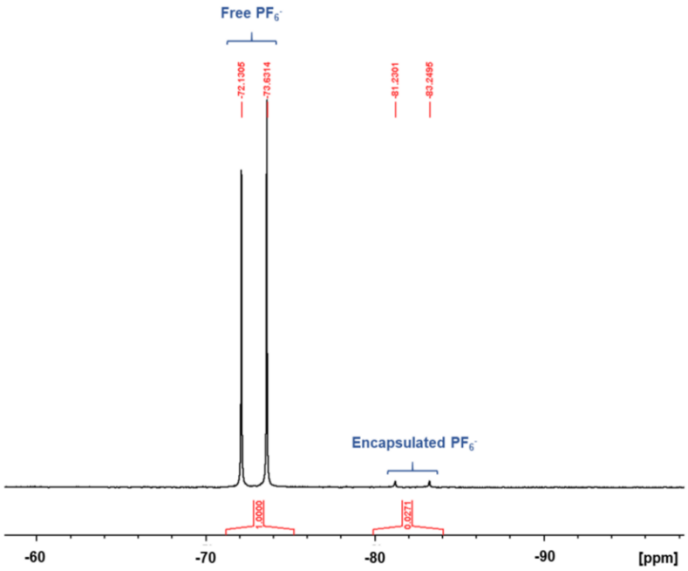

Figure S10. ^{19}F NMR (376 MHz, CD_3CN, 298 K) spectrum of **C1**⊂PF_6, highlighting two sets of peaks for both free PF_6^- and PF_6^- encapsulated within the trigonal bipyramid.

S1.4.3 Chloride Bridged Trigonal Bipyramid

During the crystallisation process, two different crystals formed from the solution containing trigonal bipyramidal complex **C1**⊂BF_4. One of these was **C1**⊂BF_4, whilst the other was a minor impurity formed when the silver centres in the system scavenged a chloride anion. The resulting structure, **C1**(Cl), was an elongated trigonal bipyramid with a μ_3-Cl ion in the centre of the complex.

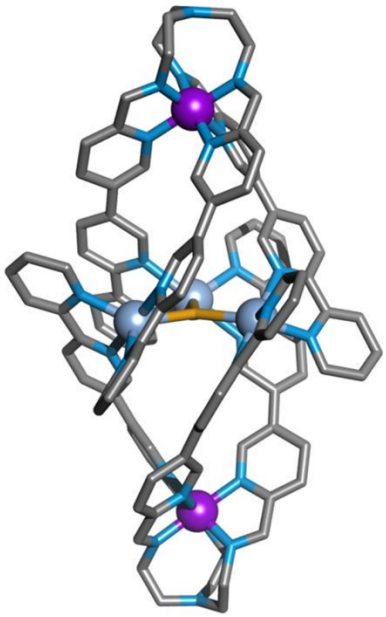

C1(Cl)

Figure S11. Single-crystal X-ray structure of chloride bridged structure **C1**(Cl). The Fe-Fe distance in **C1**(Cl) was significantly longer than in **C1**⊂BF_4, **C1**⊂SbF_6 and **C1**⊂PF_6, highlighting the adaptability of the trigonal bipyramidal architecture.

S1.5 Variations of Metal Ions within Trigonal Bipyramidal Structures

S1.5.1 Complexation Reactions with Iron(II) and Copper(I)

Scheme S8. Reaction scheme for the self-assembly of predicted product $[Fe_2Cu_3\mathbf{L}_3T](BF_4)_7$ trigonal bipyramid **C4** from ligand **L**, TREN, $Fe(BF_4)_2$ and $Cu(MeCN)_4BF_4$.

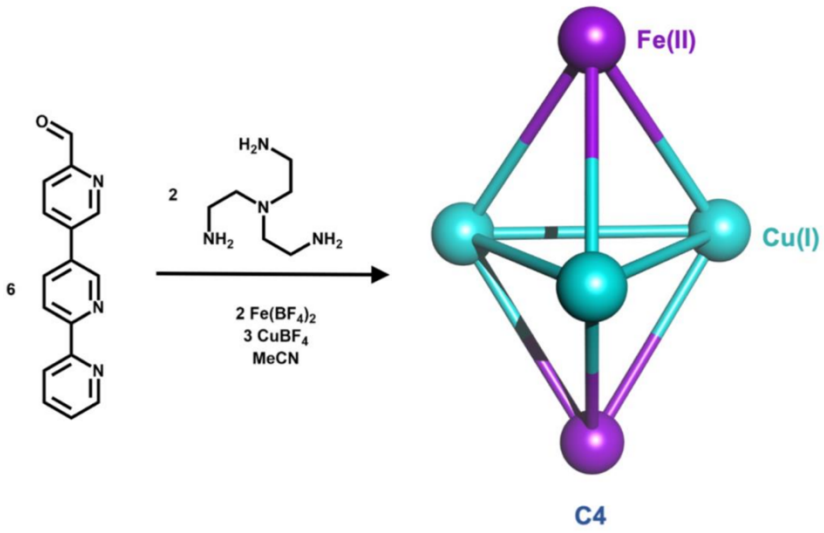

Complex 4 (C4)

L (3.0 mg mg, 11.5 mmol, 6 equiv), $Fe(BF_4)_2$ (1.3 mg, 3.8 mmol, 2 equiv), $Cu(MeCN)_4BF_4$ (1.8 mg, 7.59 mmol, 3 equiv) and TREN (0.56 mL, 3.82 mmol, 2 equiv) were dissolved in deuterated acetonitrile (0.35 mL) and the resulting light purple solution was added to a J-Young NMR tube. The tube was sealed, and the solution was degassed by three vacuum/N_2 fill cycles before being heated (65°C, 24 hr). *NMR assignment labels based on those in scheme S3.* ^{1}H (500 MHz, 298 K, CD_3CN): 9.39 (broad s, 1H, H_C), 8.59 (d, 1H, J = 8.01 Hz, H_D), 8.31 (d, 1H, J = 8.40 Hz, H_H), 8.27 (t, 1H, J = 7.7 Hz, H_E), 8.08 (d, 1H, J = 4.15 Hz, H_F), 7.90 (s, 1H, H_G), 7.87 (d, 1H, J = 8.30 Hz, H_I), 7.68 (d, 1H, J = 7.95 Hz, H_J), 7.60 (t, 1H, J = 6.25 Hz, H_L), 7.15 (s, 1H, H_M), 6.85 (d, 1H, J = 7.70 Hz, H_K), 3.86 (s, 2H, H_A), 2.96 (t, 2H, J = 11.98 Hz, H_B). DOSY diffusion coefficient: 6.63 x 10^{-10} m^2 s^{-1}. [Accurate mass, *m/z*]: $\{Fe_2Cu_3\mathbf{L}_6T_2(BF_4)_2\}^{5+}$ = 447.1065, $\{Fe_2Cu_3\mathbf{L}_6T_2(BF_4)_3\}^{4+}$ = 580.6332, $\{Fe_2Cu_3\mathbf{L}_6T_2(BF_4)_4\}^{3+}$ = 800.4848, $\{Fe_2Cu_3\mathbf{L}_6T_2(BF_4)_5\}^{2+}$ = 1224.2292, $\{Fe_2Cu_2\mathbf{L}_6T_2(BF_4)_3\}^{3+}$ = 750.5074, $\{Fe_2Cu_2\mathbf{L}_6T_2(BF_4)_4\}^{2+}$ = 1168.2625, $\{FeCu\mathbf{L}_3T\}^{3+}$ = 331.4178, $\{FeCu\mathbf{L}_3T(BF_4)\}^{2+}$ = 540.6287, $\{Fe\mathbf{L}_3T\}^{2+}$ = 465.6625, $\{Fe\mathbf{L}_3T(BF_4)\}^{+}$ = 1018.3288.

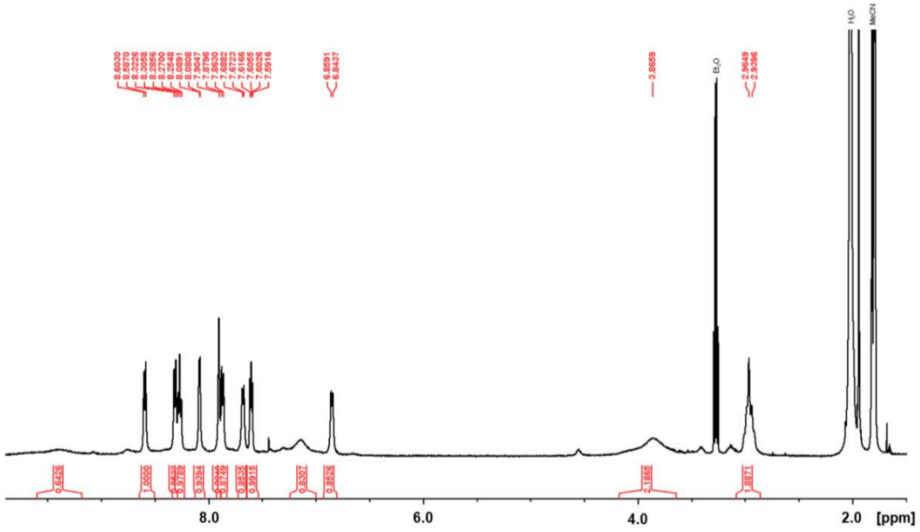

Figure S12. ^{1}H NMR (500 MHz, CD_3CN, 298 K) spectrum of **C4**.

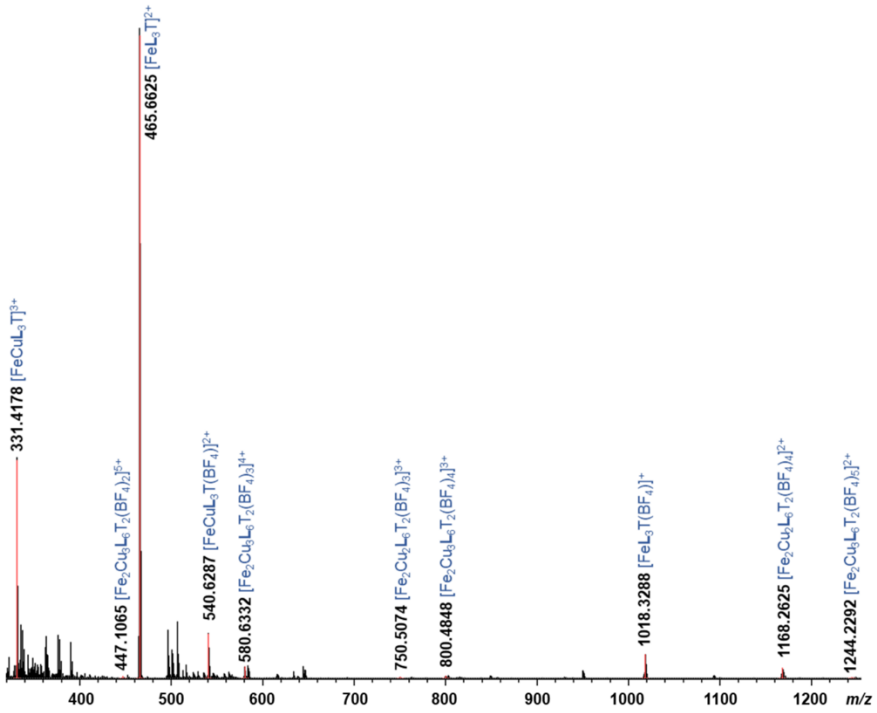

Figure S13. High-resolution mass spectrum for an acetonitrile solution of **C4**.

S1.5.2 Additions into **C4**

Scheme S9. The addition of NaCl (1.5 equiv) into an acetonitrile solution containing Fe**L**$_3$T (1 equiv) and Cu(MeCN)$_4$BF$_4$ (1.5 equiv) resulted in the formation of solution A. Addition of excess NaCl into solution A resulted in the formation of solution B.

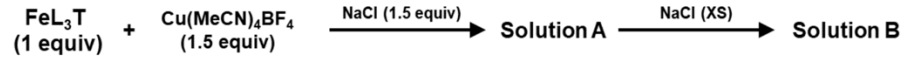

Solution A

Fe**L**$_3$T (3.1 mg, 3.33 mmol, 1 equiv), Cu(MeCN)$_4$BF$_4$ (1.5 mg, 4.77 mmol, 1.5 equiv) and NaCl (0.29 mg, 4.96 mmol, 1.5 equiv) were dissolved in deuterated acetonitrile (0.35 mL) and the resulting purple solution was added to a J-Young NMR tube. The tube was sealed, and the solution was degassed by three vacuum/N_2 fill cycles before being heated (65°C, 24 hr).

Solution B

NaCl (2 mg, 34.22 mmol, 5 equiv, excess) was dissolved into solution A and the resulting purple solution was added to a J-Young NMR tube. The tube was sealed, and the solution was degassed by three vacuum/N_2 fill cycles before being heated (65°C, 24 hr).

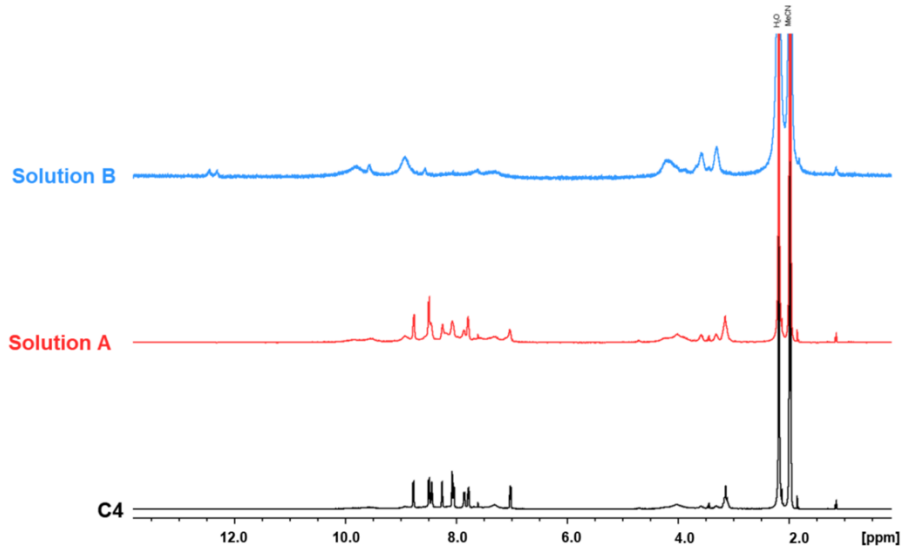

Figure S14. ^{1}H NMR (500 MHz, CD_3CN, 298 K) stacked plot of black: **C4**, red: solution A and blue: solution B.

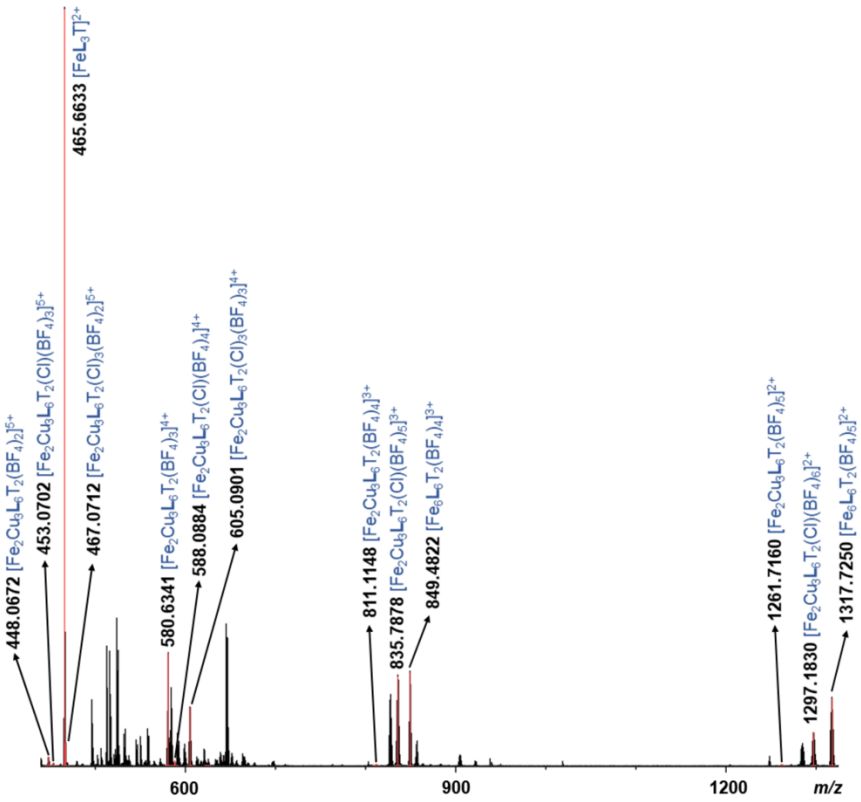

Figure S15. High-resolution mass spectrum for solution B.

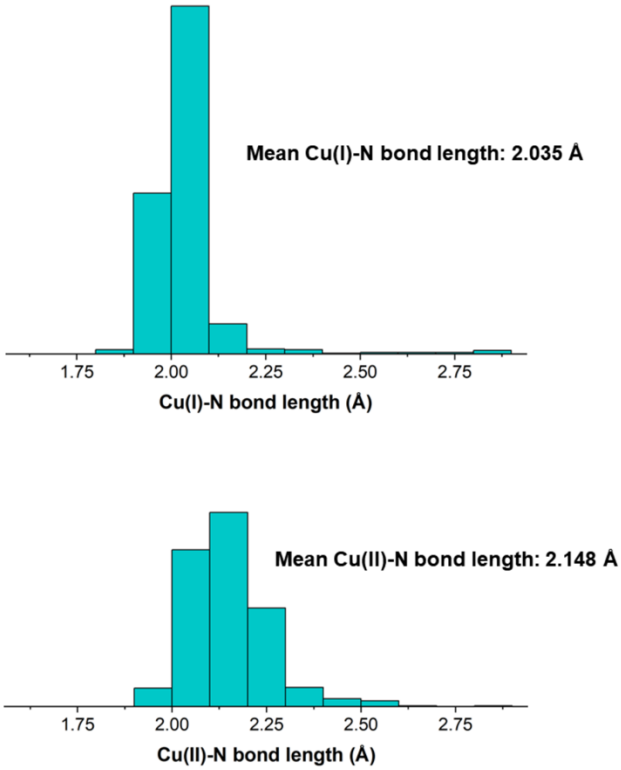

Figure S16. CCDC data on crystal structures containing top: [Cu(I)-N_4] and bottom: [Cu(II)-N_6]. Data for **C4**(Cl) is consistent with assignment of two Cu(I) ions within the equatorial sites.

Scheme S10. The addition of $^{t}BuNH_4Br$ into an acetonitrile solution containing Fe**L**$_3$T (1 equiv) and $Cu(MeCN)_4BF_4$ (1.5 equiv) resulted in the formation of solution C.

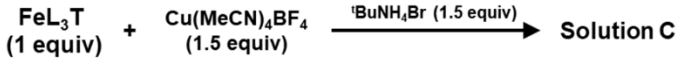

Solution C

Fe**L**$_3$T (2.9 mg, 3.11 mmol, 1 equiv), $Cu(MeCN)_4BF_4$ (1.5 mg, 4.77 mmol, 1.5 equiv) and $^{t}BuNH_4Br$ (1.5 mg, 4.65 mmol, 1.5 equiv) were dissolved in deuterated acetonitrile (0.35 mL) and the resulting purple solution was added to a J-Young NMR tube. The tube was sealed, and the solution was degassed by three vacuum/N_2 fill cycles before being heated (65°C, 24 hr). After 24 hours, the resulting complex crashed out of solution completely. The solvent was removed, and the resulting purple solid was redissolved in DMF. This solution was added to a J-Young NMR tube. The tube was sealed, and the solution was degassed by three vacuum/N_2 fill cycles before being heated (65°C, 24 hr).

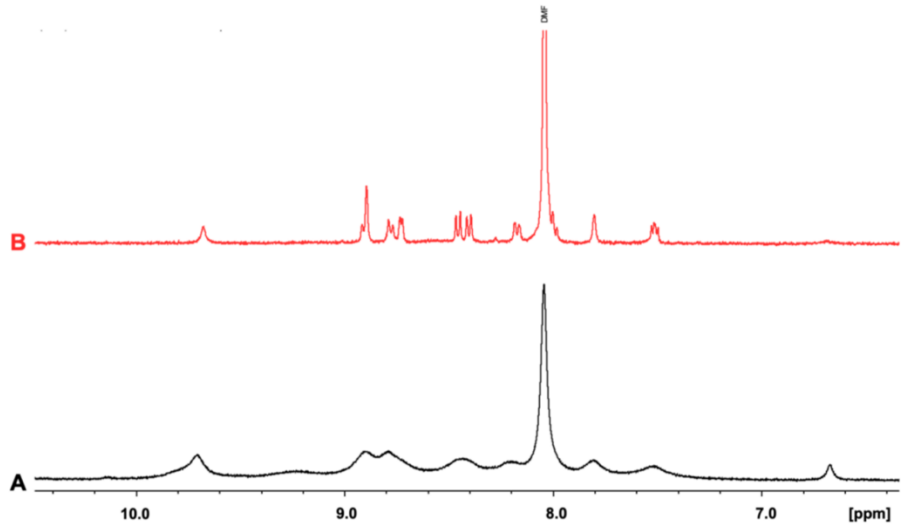

Figure S17: ^{1}H NMR (500 MHz, C_3D_7NO, 298 K) stacked plot spectrum of **A**: solution C and **B:** metalloligand **ML** in DMF.

Scheme S11. The addition of $^{t}BuNH_4NO_3$ (3 equiv) into an acetonitrile solution containing Fe**L**$_3$T (1 equiv) and $Cu(MeCN)_4BF_4$ (1.5 equiv) resulted in the formation of solution D.

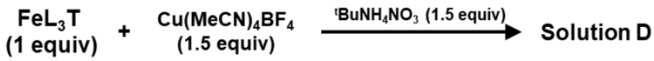

Solution D

Fe**L**$_3$T (3.0 mg, 3.22 mmol, 1 equiv), $Cu(BF_4)_2$ (1.5 mg, 4.77 mmol, 1.5 equiv) and $^{t}BuNH_4NO_3$ (1.5 mg, 4.93 mmol, 1.5 equiv) were dissolved in deuterated acetonitrile (0.35 mL) and the resulting purple solution was added to a J-Young NMR tube. The tube was sealed, and the solution was degassed by three vacuum/N_2 fill cycles before being heated (65°C, 24 hr). After 24 hours, the resulting complex crashed out of solution completely. The solvent was removed, and the resulting purple solid was redissolved in DMF. This solution was added to a J-Young NMR tube. The tube was sealed, and the solution was degassed by three vacuum/N_2 fill cycles before being heated (65°C, 24 hr).

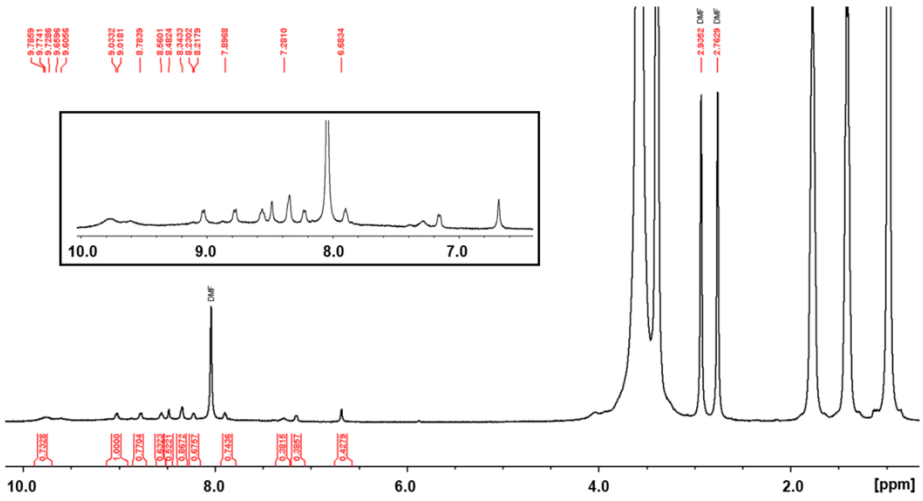

Figure S18: ^{1}H NMR (500 MHz, C_3D_7NO, 298 K) spectrum of solution D.

Scheme S12. The addition of PPh_3 (3 equiv) into an acetonitrile solution containing Fe**L**$_3$T (1 equiv) and $Cu(MeCN)_4BF_4$ (1.5 equiv) resulted in the formation of solution E which contained a mixture of Fe**L**$_3$T and PPh_3.

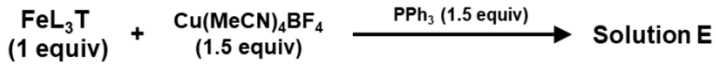

Solution E

Fe**L**$_3$T (3.0 mg, 3.22 mmol, 1 equiv), $Cu(BF_4)_2$ (1.5 mg, 4.77 mmol, 1.5 equiv) and PPh_3 (1.3 mg, 4.96 mmol, 1.5 equiv) were dissolved in deuterated acetonitrile (0.35 mL) and the resulting purple solution was added to a J-Young NMR tube. The tube was sealed, and the solution was degassed by three vacuum/N_2 fill cycles before being heated (65°C, 24 hr).

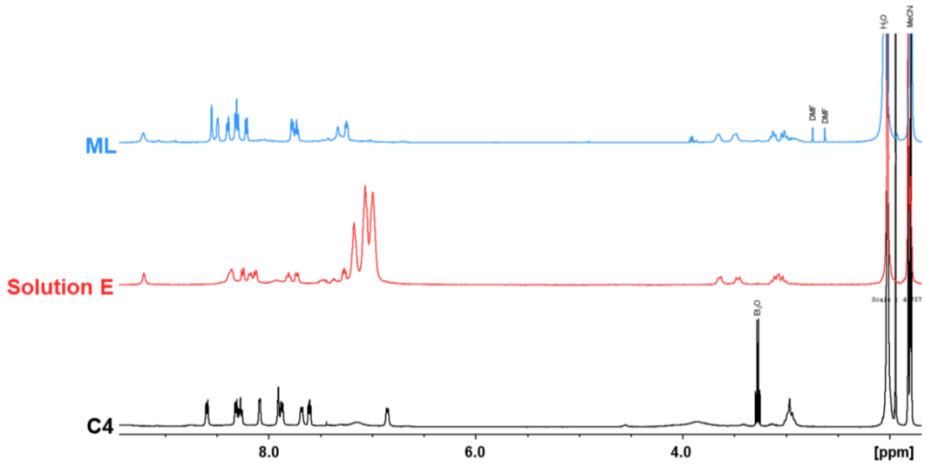

Figure S19: ^{1}H NMR (500 MHz, CD_3CN, 298 K) stacked plot of black: **C4**, red: solution E and blue: mononuclear Fe**L**$_3$T (**ML**).

S1.5.3 Complexation Reactions with Iron(II) and Copper(II)

Scheme S13. Reaction scheme for the self-assembly of predicted product $[Fe_2Cu_3\mathbf{L}_3T](BF_4)_{10}$ trigonal bipyramid **C5** from ligand **L**, TREN, NaCl, $Fe(BF_4)_2$ and $Cu(BF_4)_2$. Additional predicted products with different numbers of chloride ions bound to the Cu(II) centres are also depicted.

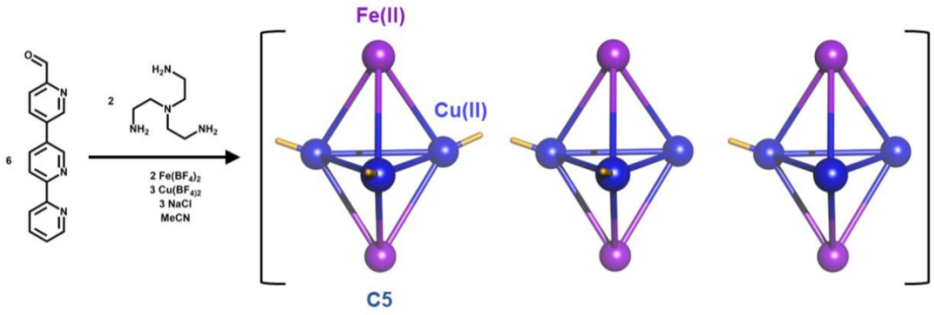

Complex 5 (C5)

L (5.0 mg, 19.12 μmol, 6 equiv), $Fe(BF_4)_2$ (2.2 mg, 6.52 μmol, 2 equiv), $Cu(BF_4)_2$ (2.3 mg, 9.58 μmol, 3 equiv), TREN (0.93 μL, 6.37 μmol, 2 equiv) and NaCl (0.56, 9.58 μmol, 3 equiv) were dissolved in deuterated acetonitrile (0.35 mL) and the purple solution was added to a J-Young NMR tube. The tube was sealed, and the solution was degassed by three vacuum/N_2 fill cycles before being heated (65°C, 24 hr). [Accurate mass, *m/z*]: $\{Fe_2Cu_3\mathbf{L}_6T_2(Cl)_3\}^{7+}$ = 311.7539, $\{Fe_2Cu_3\mathbf{L}_6T_2(Cl)_3(BF_4)\}^{6+}$ = 373.0616, $\{Fe_2Cu_3\mathbf{L}_6T_2(Cl)_3(BF_4)_2\}^{5+}$ = 466.8695, $\{Fe_2Cu_3\mathbf{L}_6T_2(Cl)_3(BF_4)_3\}^{4+}$ = 605.0882, $\{Fe_2Cu_2\mathbf{L}_6T_2(Cl)_3(BF_4)_4\}^{3+}$ = 835.7856, $\{Fe_2Cu_2\mathbf{L}_6T_2(Cl)_3(BF_4)_5\}^{2+}$ = 1297.1810, $\{Fe_2Cu_3\mathbf{L}_6T_2(Cl)_2(BF_4)_4\}^{4+}$ = 617.5599, $\{Fe_2Cu_2\mathbf{L}_6T_2(Cl)_2(BF_4)_5\}^{3+}$ = 852.7975, $\{Fe_2Cu_2\mathbf{L}_6T_2(Cl)_2(BF_4)_6\}^{2+}$ = 1322.6977, $\{Fe\mathbf{L}_3T\}^{2+}$ = 465.6617.

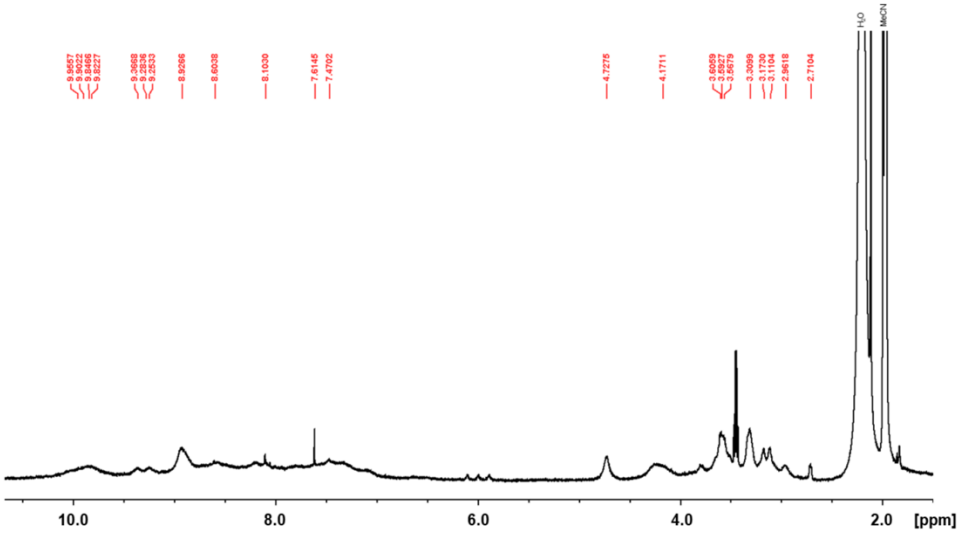

Figure S20: ^{1}H NMR (500 MHz, CD_3CN, 298 K) spectrum of **C5**.

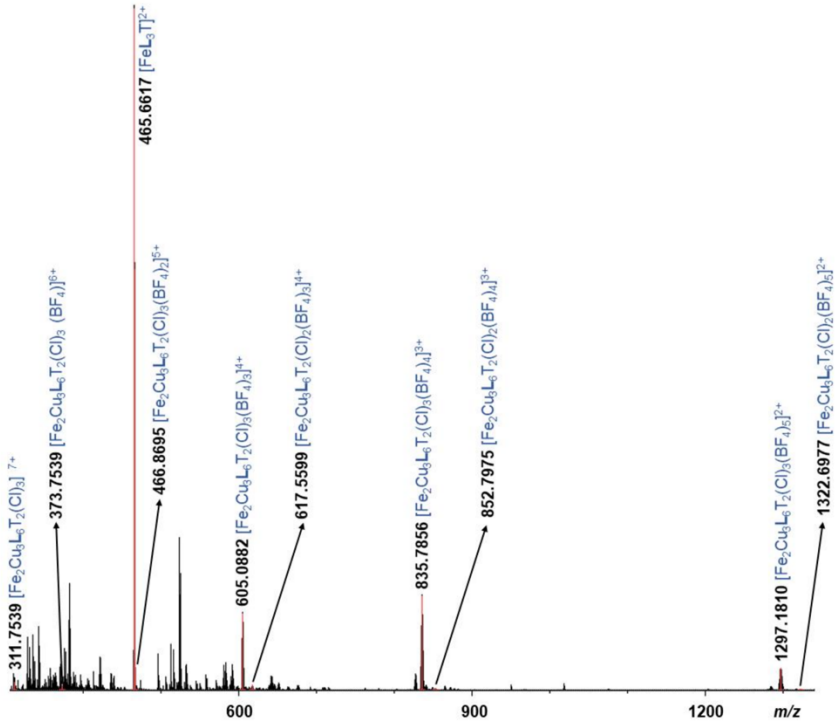

Figure S21. High-resolution mass spectrum for an acetonitrile solution of **C5**.

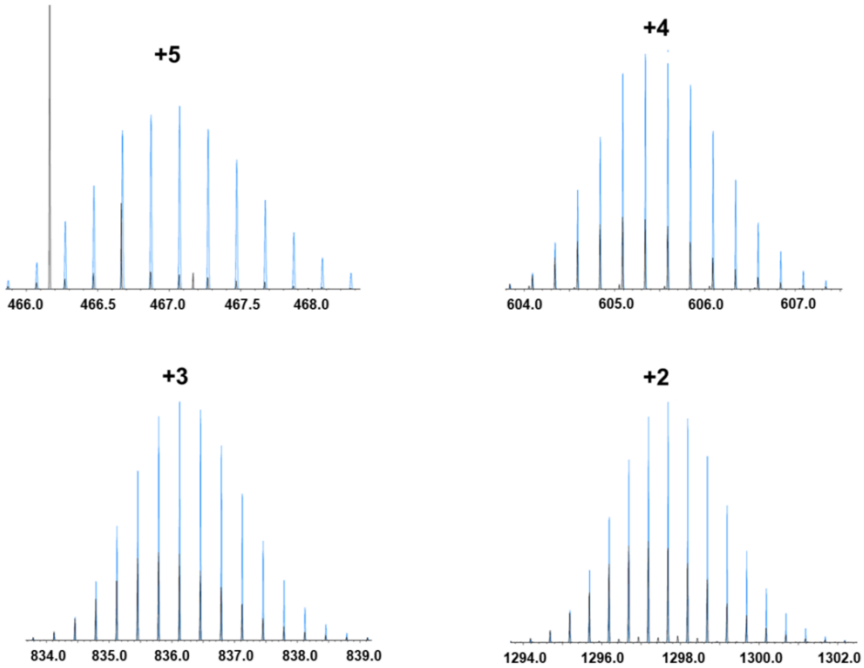

Figure S22. High-resolution mass spectra of **C5** and the corresponding calculated isotopic patterns for the +5, +4, +3 and +2 peaks. Black: recorded spectral pattern and blue: calculated spectral pattern.

S2 X-Ray Crystallography

Data αCollection. X-Ray data for compounds **C1**⊂BF_4**, C1**⊂SbF_6**, C1**⊂PF_6**, C1**(Cl), **C2** and **C4**(Cl) were collected at a temperature of 100 K using a Rigaku FR-X with Cu-Kα radiation equipped with a HypixHE6000 detector, equipped with an Ox0ford Cryosystems nitrogen flow gas system. Data was measured using CrysAlisPro and GDA suite of programs.

Crystal structure determinations and refinements. X-Ray data were processed and reduced using CrysAlisPro suite of programmes. Absorption correction was performed using empirical methods (SCALE3 ABSPACK) based upon symmetry-equivalent reflections combined with measurements at different azimuthal angles.[3–5] The crystal structure was solved and refined against all F^2 values using the SHELXL and Olex 2 suite of programmes.[6,7]

Data has not been processed to publication standard.

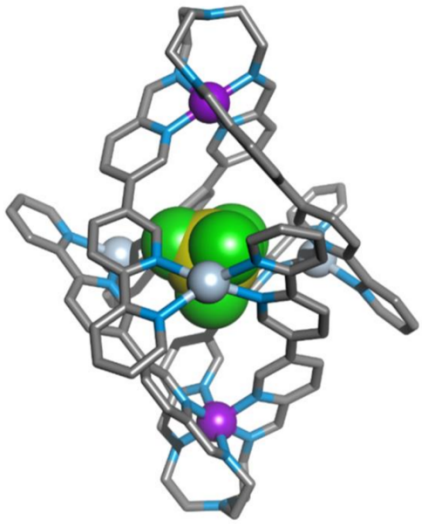

Figure S23. Single-crystal X-ray structure of complex **C1**⊂BF_4 where purple spheres: iron(II); grey spheres: silver(I), yellow: boron, green: fluorine; blue: nitrogen; grey: carbon. The counterions and hydrogen atoms were omitted for clarity, except the central space-filled BF_4^- anion.

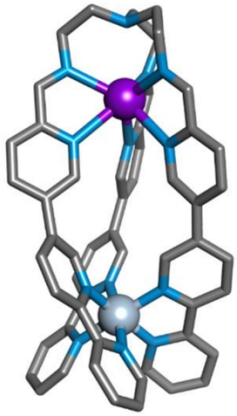

Figure S24. Single-crystal X-ray structure of complex **C2** where purple spheres: iron(II); grey spheres: silver(I), blue: nitrogen; grey: carbon. The counterions and hydrogen atoms were omitted for clarity.

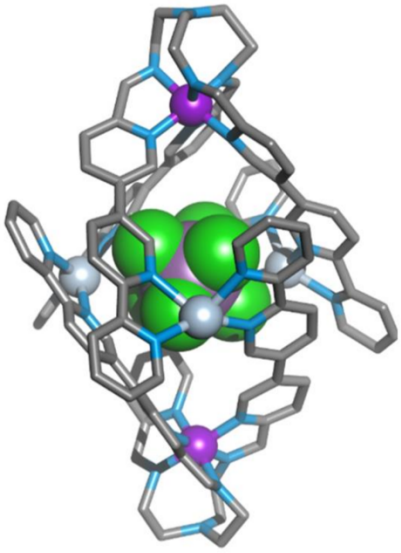

Figure S25. Single-crystal X-ray structure of complex **C1**⊂SbF_6 where purple spheres: iron(II); grey spheres: silver(I), mauve: antimony, green: fluorine; blue: nitrogen; grey: carbon. The counterions and hydrogen atoms were omitted for clarity, except the central space-filled SbF_6^- anion.

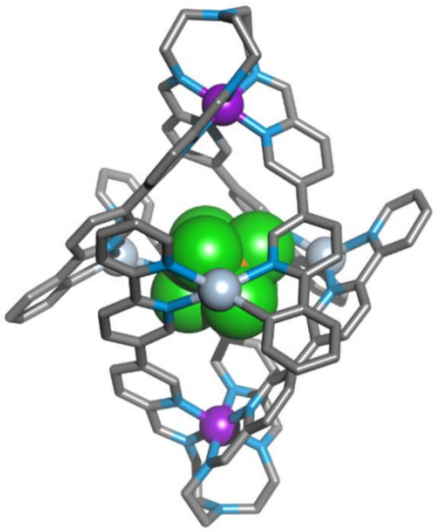

Figure S26. Single-crystal X-ray structure of complex **C1**⊂PF_6 where purple spheres: iron(II); grey spheres: silver(I), orange: phosphorus, green: fluorine; blue: nitrogen; grey: carbon. The counterions and hydrogen atoms were omitted for clarity, except the central space-filled PF_6^- anion.

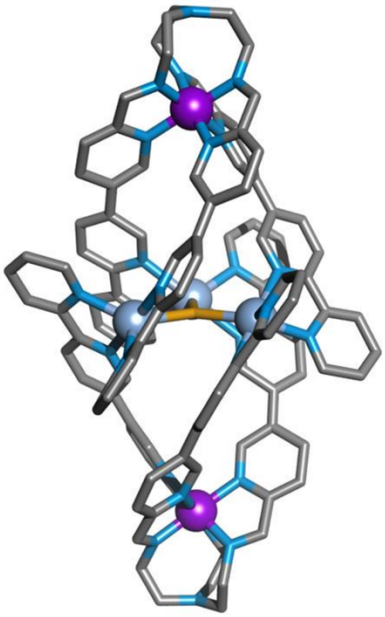

Figure S27. Single-crystal X-ray structure of complex **C1**(Cl) where purple spheres: iron(II); grey spheres: silver(I), orange: chlorine; blue: nitrogen; grey: carbon. The counterions and hydrogen atoms were omitted for clarity.

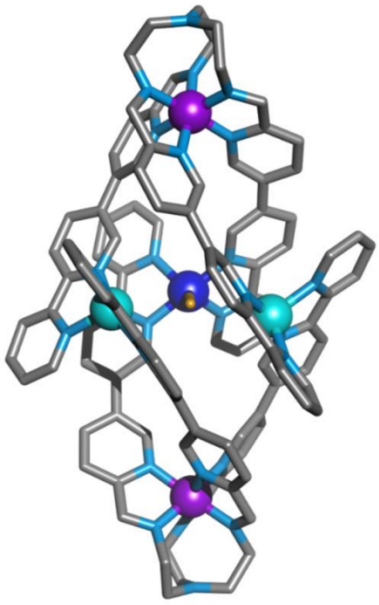

Figure S28. Single-crystal X-ray structure of complex **C4**(Cl) where purple spheres: iron(II); cyan spheres: copper(I), dark blue spheres: copper(II) orange: chlorine; blue: nitrogen; grey: carbon. The counterions and hydrogen atoms were omitted for clarity.

Table S1. Crystallographic information for **C1**⊂BF_4, **C2** and **C1**⊂SbF_6.

Identification code	**C1**⊂BF_4	**C2**	**C1**⊂SbF6
Empirical formula	$C_{108}H_{88}Ag_3B_7F_{28}Fe_2N_{26}$	$C_{60.6}H_{45.5}Ag_1B_3F_{12}Fe_1N_{14}$	$C_{108}H_{90}Ag_3B_2F_{27.41}Fe_2N_{26}Sb_{3.81}$
Formula weight	2793.02	1400.25	3193.16
Temperature/K	104(7)	100.01(10)	99.9(4)
Crystal system	triclinic	trigonal	monoclinic
Space group	P-1	R3	C2/c
a/Å	14.4298(6)	12.8505(2)	41.223(3)
b/Å	17.5476(9)	12.8505(2)	21.7598(16)
c/Å	25.9093(13)	30.2658(4)	31.8946(11)
α/°	84.476(4)	90	90
β/°	85.628(4)	90	94.820(5)
γ/°	66.198(4)	120	90
Volume/$Å^3$	5969.5(5)	4328.35(15)	28508(3)
Z	2	2.97	8
$\rho_{calc}g/cm^3$	1.554	1.595	1.488
μ/mm^{-1}	6.671	5.555	11.181
F(000)	2796.0	2097.0	12510.0
Crystal size/mm^3	0.1 × 0.1 × 0.1	0.1 × 0.1 × 0.1	0.15 × 0.15 × 0.015
Radiation	Cu Kα (λ = 1.54184)	Cu Kα (λ = 1.54184)	Cu Kα (λ = 1.54184)
2Θ range for data collection/°	5.518 to 152.238	8.466 to 152.036	4.302 to 154.618
Index ranges	-18 ≤ h ≤ 16, -22 ≤ k ≤ 18, -29 ≤ l ≤ 32	-16 ≤ h ≤ 16, -11 ≤ k ≤ 15, -37 ≤ l ≤ 37	-48 ≤ h ≤ 51, -26 ≤ k ≤ 18, -39 ≤ l ≤ 32
Reflections collected	55124	8636	64384
Independent reflections	23462 [R_{int} = 0.0569, R_{sigma} = 0.0708]	3701 [R_{int} = 0.0291, R_{sigma} = 0.0374]	28320 [R_{int} = 0.0869, R_{sigma} = 0.1778]
Data/restraints/parameters	23462/0/1576	3701/1/274	28320/171/1427
Goodness-of-fit on F^2	1.024	1.231	1.767
Final R indexes [I>=2σ (I)]	R_1 = 0.0864, wR_2 = 0.2503	R_1 = 0.0932, wR_2 = 0.2522	R_1 = 0.2940, wR_2 = 0.5438
Final R indexes [all data]	R_1 = 0.1255, wR_2 = 0.2846	R_1 = 0.0947, wR_2 = 0.2550	R_1 = 0.3798, wR_2 = 0.5918
Largest diff. peak/hole / e $Å^{-3}$	3.45/-1.07	3.32/-0.72	4.10/-0.82

Table S2. Crystallographic information for **C1**⊂PF_6, **C1**(Cl) and **C4**(Cl).

Identification code	**C1**⊂PF_6	**C1**(Cl)	**C4**(Cl)
Empirical formula	$C_{108}H_{90}Ag_3B_2F_{37.87}Fe_2N_{26}P_5$	$C_{108}H_{89}Ag_3B_6ClF_{24}Fe_2N_{26}$	$C_{116}H_{98}Cu_3B_7F_{31}Fe_2N_{30}Cl$
Formula weight	3079.98	2742.67	2826.96
Temperature/K	99.9(3)	100(10)	99.97(10)
Crystal system	triclinic	monoclinic	monoclinic
Space group	P-1	$P2_1/n$	C2/c
a/Å	14.7304(5)	15.3475(6)	15.0980(6)
b/Å	17.6910(7)	26.7954(16)	28.8076(11)
c/Å	26.0614(6)	30.4943(10)	30.5304(13)
α/°	83.873(3)	90	90
β/°	85.536(3)	93.296(3)	93.255(4)
γ/°	65.831(4)	90	90
Volume/$Å^3$	6156.4(4)	12519.8(10)	13257.4(9)
Z	2	4	4
$\rho_{calc}g/cm^3$	1.662	1.455	1.416
μ/mm^{-1}	7.248	6.496	3.320
F(000)	3073.0	5500.0	5525.0
Crystal size/mm^3	0.1 × 0.1 × 0.1	0.1 × 0.1 × 0.1	0.1 × 0.1 × 0.01
Radiation	Cu Kα (λ = 1.54184)	Cu Kα (λ = 1.54184)	Cu Kα (λ = 1.54184)
2Θ range for data collection/°	5.494 to 152.944	4.394 to 153.98	5.798 to 90.696
Index ranges	-17 ≤ h ≤ 14, -22 ≤ k ≤ 21, -31 ≤ l ≤ 32	-15 ≤ h ≤ 18, -30 ≤ k ≤ 33, -28 ≤ l ≤ 38	-13 ≤ h ≤ 10, -26 ≤ k ≤ 24, -27 ≤ l ≤ 28
Reflections collected	67032	81514	16335
Independent reflections	23848 [R_{int} = 0.0693, R_{sigma} = 0.0761]	24760 [R_{int} = 0.1403, R_{sigma} = 0.1617]	5425 [R_{int} = 0.0607, R_{sigma} = 0.0782]
Data/restraints/parameters	23848/136/1664	24760/34/1532	5425/73/861
Goodness-of-fit on F^2	1.100	1.851	2.405
Final R indexes [I>=2σ (I)]	R_1 = 0.1001, wR_2 = 0.2798	R_1 = 0.1878, wR_2 = 0.4059	R_1 = 0.1342, wR_2 = 0.3496
Final R indexes [all data]	R_1 = 0.1356, wR_2 = 0.3125	R_1 = 0.3148, wR_2 = 0.4459	R_1 = 0.1763, wR_2 = 0.3642
Largest diff. peak/hole / e $Å^{-3}$	4.35/-1.42	4.07/-2.07	2.12/-0.73

S2.1 Structural Comparison

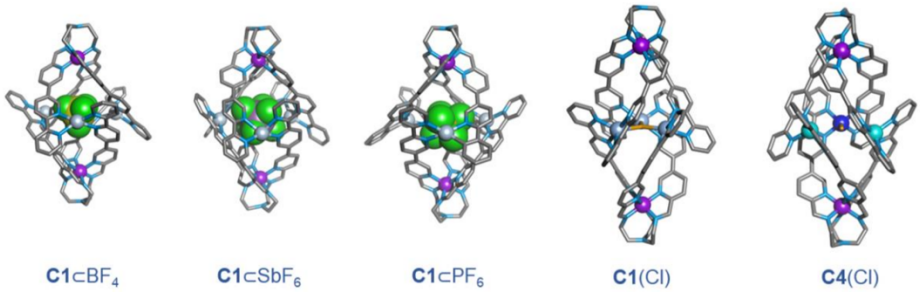

Figure S29. Single-crystal X-ray structures of complexes **C1**⊂BF_4 with an encapsulated BF_4^- anion**,** **C1**⊂SbF_6 with an encapsulated SbF_6^- anion**,** **C1**⊂SbF_6 with an encapsulated PF_6^- anion, **C1**(Cl) with a central Cl^- anion and **C4**(Cl) with a bound Cl^- anion**.**

Table S3. Tabulated metal-metal distances obtained from single-crystal X-ray structures for complexes **C1**⊂BF_4, **C1**⊂SbF_6, **C1**⊂PF_6, **C1**(Cl) and **C4**(Cl), and their corresponding τ_4 or τ_5 parameters.

	Fe – Fe distance (Å)	**Ag – Ag average distance (Å)**	**Cu – Cu average distance (Å)**	**τ_4 parameter[8]**	**τ_5 parameter[9]**
C1⊂BF_4	12.559	8.006	-	0.637	-
C1⊂SbF_6	13.095	7.819	-	0.550	-
C1⊂PF_6	12.549	8.189	-	0.655	-
C1(Cl)	15.233	4.475	-	-	0.986
C4(Cl)	14.481	-	5.279	0.586	1.082

S3 VOIDOO Calculations

Following removal of counterions and solvent from the single crystal X-ray structures of complexes **C1** cavity calculations were run using Voidoo.[10] The volume of the internal binding pocket within each structure was calculated using a probe of radius 1.0 Å, this is a smaller probe radius than the default setting for water of 1.4 Å. The decreased probe was chosen to better map the internal space, as we observed the trigonal bipyramid has some tight angles which were not accounted for with a larger probe.

The decreased probe radius highlights the improved degree of enclosure of these architectures relative to their tetrahedral analogues. This indicates that encapsulated species are better protected from the external environment, and may also benefit from an increased number of non-covalent interactions between the host and guest species. We also note that as a 1.0 Å radius is contained within the capsule with no need to block to the windows calculation of the internal void pocket of trigonal bipyramidal architectures is less subjective than comparable calculations for tetrahedra, which often rely on manually blocking the face of the tetrahedron.[11]

The following parameters were used in the calculation:

Primary grid spacing	0.1
Number of detection cycles	10
Growth factor van der Waals radii	1.1
Min size of real cavities	1
Number of refinement cycles	10
Grid shrink factor	0.9
Convergence criterion ($Å^3$)	0.1

Cavities were mapped as ccp4 files and visualised using Pymol v1.4.

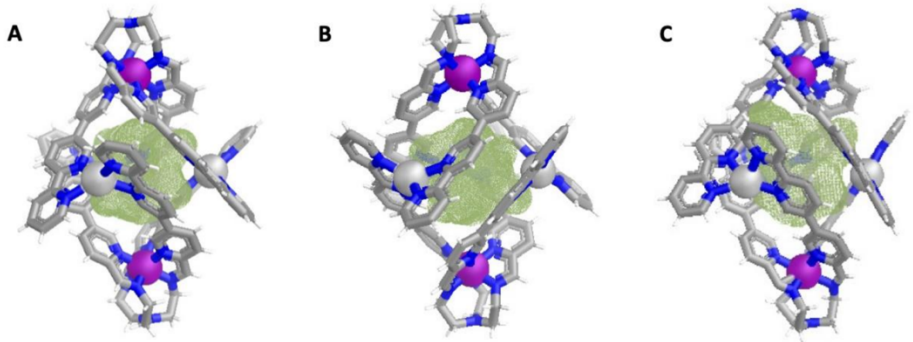

Figure S30. Calculated void spaces using VOIDOO and the single-crystal X-ray structures of **C1** encapsulating A: BF_4^- (108 Å^3), B: PF_6^- (123 Å^3) and C: SbF_6^- (132 Å^3). A gradual increase in volume of the cavity is observed as the size of anion increases.

Utilising the same settings as outlined above we also calculated void cavities in the crystal structures of **C1**(Cl) and **C4**(Cl). Calculations were run both in the presence and absence of the bound chloride anion to highlight how the internal space in the trigonal bipyramid changes following inclusion of chloride in the structure. All structures showed limited void volumes. When the chloride anions were deleted multiple cavities were observed highlighting the constriction at the centre of the architecture where the three metal ions converge.

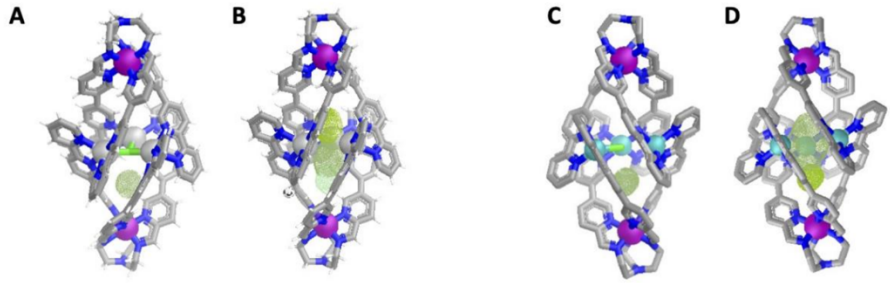

Figure S31. Calculated void cavities for **C1**(Cl) in the presence (A) and absence (B) of a centrally bound chloride ion, and **C4** in the presence (C) and absence (D) of a centrally bound chloride ion.

S4 References

1 L. L. K. Taylor, I. J. Vitorica-Yrezabal, I. Borilovic, F. Tuna and I. A. Riddell, *Chem. Commun.* 2021, *accepted.*

2 J. de Mendoza, E. Mesa, J.-C. Rodríguez-Ubis, P. Vázquez, F. Vögtle, P.-M. Windscheif, K. Rissanen, J.-M. Lehn, D. Lilienbaum and R. Ziessel, *Angew. Chem.*, 1991, **103**, 1365–1367.

3 G. M. Sheldrick, SADABS.

4 R. H. Blessing, *Acta Crystallogr. Sect. A*, 1995, **51**, 33–38.

5 L. Krause, R. Herbst-Irmer, G. M. Sheldrick and D. Stalke, *J. Appl. Crystallogr.*, 2015, **48**, 3–10.

6 G. M. Sheldrick, *Acta Crystallogr. Sect. C Struct. Chem.*, 2015, **71**, 3–8.

7 O. V. Dolomanov, L. J. Bourhis, R. J. Gildea, J. A. K. Howard and H. Puschmann, *J. Appl. Crystallogr.*, 2009, **42**, 339–341.

8 L. Yang, D. R. Powell and R. P. Houser, *J. Chem. Soc. Dalt. Trans.*, 2007, 955–964.

9 A. G. Blackman, E. B. Schenk, R. E. Jelley, E. H. Krenske and L. R. Gahan, *Dalt. Trans.*, 2020, **49**, 14798–14806.

10 G. J. Kleywegt and T. Alwyn Jones, *Acta Crystallogr. Sect. D Biol. Crystallogr.*, 1994, **50**, 178–185.

11 Y. R. Hristova, M. M. J. Smulders, J. K. Clegg, B. Breiner and J. R. Nitschke, *Chem. Sci.*, 2011, **2**, 638–641.

10. Chapter Four: Paper Three - Integrative Self-Sorting of an $[Fe_4L_6]^{8+}$ Tetrahedron Governed by Anion Templation and Chelation

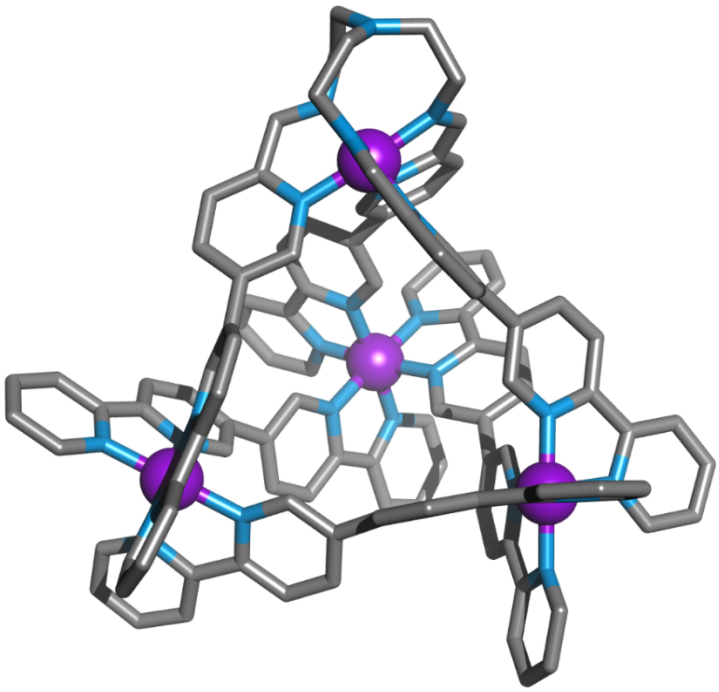

Chemical Science

EDGE ARTICLE

Integrative self-sorting of an $[Fe_4L_6]^{8+}$ tetrahedron governed by anion templation and chelation

Received 00th January 20xx,
Accepted 00th January 20xx

DOI: 10.1039/x0xx00000x

Lauren L. K. Taylor[a], April C. Y. Sung, Iñigo J. Vitorica-Yrezabal,[a] and Imogen A. Riddell[a*]

Diversification of metal-organic tetrahedra is essential if we are to realise their full potential. Here we report the first example of a self-assembled, integratively sorted $[Fe_4L_6]^{8+}$ tetrahedron. Exclusive formation of the tetrahedron, which incorporates one unique metal vertex, is governed by the choice of amine and metal salt counterion. Inclusion of a triamine, that generated a hexadentate chelating group, is required to orientate the heteroditopic ligand employed, while the perchlorate counterion from the metal salt templates an intermediate mononuclear complex directing the final stages of the tetrahedron self-assembly. The C_3-symmetric structure is characterised by HR-MS, NMR spectroscopy and X-ray crystallography, and provides the proof of principle for use of heteroditopic ligands in classical M_4L_6 supramolecular structures.

Within a subcomponent mixture, self-sorting principles can control the spontaneous self-assembly process and promote the formation of specific products.[1,2] This phenomenon is prevalent throughout Nature, governing processes such as base pairing in DNA,[3] the self-fractioning of white blood cells in human blood[4] and the highly-ordered, spontaneous grouping of alike neurons during foetal brain development.[5]

Recently there has been a growing interest in understanding and controlling complex self-sorting phenomenon in synthetic systems.[6–11] In the field of metallo-supramolecular architectures the desire to controllably generate complex structures with unusual and useful functionality has led researchers to explore incorporation of reduced symmetry ligands[12–14] as well as the formation of heteroleptic structures.[15–19] Generation of discrete structures from these components requires that ligands are controllably orientated through sorting phenomena.

Self-sorting processes have been defined as either narcissistic or integrative,[20,21] where narcissistic self-sorting describes the phenomenon of self-association[2,22] and integrative self-sorting describes the combination of multiple different structural components within a single system.[11,22] Most commonly these terms are applied to the self-assembly of complexes from more than one homoditopic ligand. However, the self-assembly of reduced symmetry heteroditopic ligands can also be defined using these descriptors. In the latter case it is the coordination environment around the metal ion that is considered.[7,11]

[a] Department of Chemistry, University of Manchester, Oxford Road, Manchester, M13 9PL (UK). E-mail: imogen.riddell@manchester.ac.uk

For systems where neither sorting regime dominates it is also possible to generate equilibrium mixtures containing several thermodynamic products of similar energies; this socially sorted mixture is termed a dynamic library.[23]

Heteroleptic systems capable of integrative self-sorting produce assemblies with increased structural complexity through incorporation of different ligands each with individual functionalities, and is a valuable way to access new, useful architectures.[8,24,25] Gaining control over sorting to enable inclusion of more than one ligand within a metal-organic structure can however be challenging as narcissistic associations often dominate.[22,26] Even systems with extremely similar ligands, where you might expect the energies of all products to be indistinguishable, have a tendency to generate a mixture of homocomplexes where the ligands segregate.[23,27] For heteroditopic ligands orientation of the ligand with respect to the metal centre can be governed using steric and electronic arguments to bias either narcissistic or integrative sorting.[11,28]

Scheme 1. *Left:* Self-assembly of a heteroleptic tetrahedral cage **C1** by integrative sorting. *Right:* Formation of a homoleptic cage **C2** and the mononuclear complex **C3.** Both outcomes are possible when using **L1**, **L2**, TREN and Fe(II) starting materials.

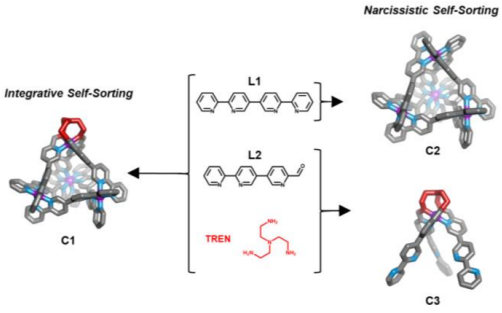

Herein we detail self-assembly reactions incorporating two very similar ligands (scheme 1; **L1** and **L2**) with a choice of amine and a range of iron(II) salts. Based on the anion and amine employed in the reaction, the system can display integrative sorting to generate **C1** exclusively or socially sort to form a mixture of two tetrahedral cages **C1** and **C2**, and the mononuclear complex **C3.**

The *bis*bidentate ligands, **L1** and **L2,** can both bind octahedral metal ions through their bidentate N^N binding sites. Ligand 1 (**L1**) contains two bipyridine binding sites and was previously reported to form $[M^{n+}_4\mathbf{L1}_6]^{n+}$ tetrahedral architectures in the presence of octahedrally coordinating metal ions including Fe(II)[29] and Co(III).[30] Ligand 2 (**L2**) features a bidentate bipyridyl binding site at one end and a pyridine aldehyde moiety capable of reacting with a range of amines to generate a bidentate pyridylimine at the other.[31] The relative orientation of the bidentate binding sites in these ligands is comparable, leading us to hypothesis the ligands could be interchanged within $[M_4L_6]^{8+}$ tetrahedra.

To the best of our knowledge the Fe_4L_6 tetrahedron (**C1**), which incorporates both **L1** and **L2**, is the only example of an M_4L_6 tetrahedron formed through integrative sorting behaviour. Incorporation of **L1** and **L2** generates a structure which has overall C_3-symmetry and incorporates one unique vertex which may allow for introduction of functionality not possible at the *tris*bipy sites,[32] or affect host guest binding through alteration of guest access and egress.[33]

Role of Amine in Directing Sorting Behaviour

In initial studies **L1**, **L2**, $Fe(ClO_4)_2$ and *p*-toluidine were combined in CD_3CN to determine if the system displayed any self-sorting behaviour. Analysis of the ^{1}H NMR from this reaction showed major peaks corresponding to the homoleptic cage (**C2**) alongside a broad baseline. Employing an internal standard we were able to quantitate that 67% of **L1** had been incorporated into **C2**. Since no peaks corresponding to free **L1** could be observed we hypothesised that the remaining 33% of **L1** had been incorporated into M_4L_6 tetrahedral complexes alongside **L2** and *p*-toluidine. Mass spectrometric analysis supported the formation of a dynamic library of M_4L_6 complexes with between three and six **L1** ligands incorporated (Fig *S*5). No evidence for formation of cages with greater than three equivalents of **L2** was found suggesting that under the conditions of ionisation cages incorporating significant numbers of this component are less stable.

We next added one equivalent of TREN per four metal centres to the dynamic library (DL), hypothesising that the triamine would displace three equivalents of *p*-toluidine and orientate three pyridyl imines around one metal centre (Fig 1). Critically, incorporation of a triamine within this system prevents formation of a mixture of tetrahedral complexes with varying ligand composition. In the presence of TREN and octahedrally coordinating metal ions, **L2** does not have the capability to form a tetrahedral assembly in the absence of **L1**. Instead, the formation of mononuclear $[M\mathbf{L1}_3T]^{n2+}$ and helical $[M_2\mathbf{L1}_3T]^{n4+}$ structures have been observed.[34] We therefore proposed that in order to saturate all the metal and ligand binding sites, the iron(II) ions and ligands liberated upon disruption of the dynamic library could recombine to generate a single tetrahedral species with the formula $[Fe_4(\mathbf{L1})_3(\mathbf{L2})_3T]^{8+}$ (**C1**). Following addition of TREN, displacement of *p*-toluidine occurred rapidly revealing a sharp ^{1}H NMR spectrum consistent with formation of a single supramolecular complex. Formation of the predicted C_3-symmetric complex was confirmed by HR-MS, 2D NMR analysis and single crystal X-ray diffraction.

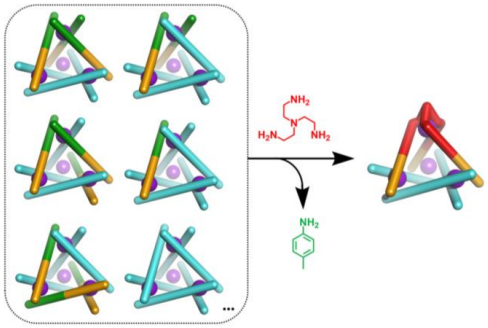

Figure 1. Displacement of *p*-toluidine by TREN to generate **C1** exclusively from a dynamic library (DL) of cages. The initial DL includes a mixture of cages with varying numbers and orientations of **L1** and **L2**.

Single crystals of **C1** were grown through slow diffusion of diethyl ether into acetonitrile over the course of seven days. Measurement of the Fe(II) to N bond lengths in the crystal structure of **C1** did not indicate any significant bond strain. All bond lengths were consistent with coordination of low spin Fe(II) within a N^6 coordination environment. Moreover, these values were comparable with those obtained from the single crystal structure of homoleptic tetrahedron **C2**. Assignment of the ^{1}H NMR spectrum revealed that upon incorporation in **C1**, the two adjacent bipyridine units of **L1** became inequivalent, consistent with formation of the C_3-symmetric tetrahedral architecture (Fig 2). Refinement of the single crystal X-ray data did not provide definitive evidence for encapsulation of the perchlorate counterion, however, structurally related M_4L_6 tetrahedra have been reported to bind perchlorate anions with good affinity.[30,35]

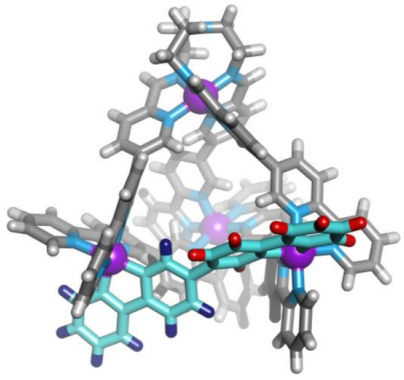

Figure 2. Single crystal X-ray structure of the cationic portion of **C1**. The two different bipyridine environments on **L1** are coloured blue and red. Counterions and solvent removed for clarity.

To try and better understand the factors governing the *p*-toluidine to TREN amine exchange process we next added three equivalents of 2-pyridinecarboxaldehyde and one equivalent of TREN per iron(II) ion to a solution of purified **C2**. After heating the mixture at 65°C for 24 hours the ^{1}H NMR spectrum contained no evidence of **C2** (Fig *S*6). Analysis of the reaction mixture confirmed exclusive formation of a mononuclear *tris*pyridylimine complex, and the displaced **L1** ligand precipitated from solution following decomplexation. We therefore propose that displacement of *p*-toluidine from complexes within the DL is not the sole driving force for the structural rearrangement observed upon addition of TREN. Demetallation of the M_4L_6 structures, driven by the addition of TREN, also plays a significant role in the structural rearrangement of the mixture. This is consistent with previously reported mechanistic studies.[27]

Role of Anionic Template in Directing Sorting Behaviour

Next we compared the effect different iron(II) salts had on the ^{1}H NMR profile of the self-assembled reaction mixture. When iron(II) triflimide (4 equiv.) was used in the self-assembly reaction alongside three equivalents of **L1** and **L2** and one equivalent of TREN, a complex ^{1}H NMR spectrum was recorded which could not be simplified through common purification techniques. Analysis of the spectrum identified two distinct sets of peaks corresponding to the heteroleptic and homoleptic tetrahedra (**C1** and **C2**, Fig *S*22). Mass spectroscopic analysis of the reaction mixture also indicated the presence of the mononuclear species **C3**. The large size of the triflimide anion[35] ensures it cannot act as an internal template anion for either **C1** or **C2** and thus enabled the formation of a mixture of cages in a 1:2 **C1:C2** ratio.

We next attempted analogous reactions using $Fe(OTf)_2$ and $Fe(BF_4)_2$ salts in place of $Fe(ClO_4)_2$. ^{1}H NMR and mass spectrometric analyses of the reaction mixtures revealed that neither metal salt promoted exclusive integrative self-sorting but instead generated mixtures of **C1**, **C2** and **C3**. ^{19}F NMR spectra of the reaction mixture generated using $Fe(OTf)_2$ revealed three distinct fluorine environments which were assigned to triflate encapsulated within **C1** and **C2**, and unbound triflate (Fig. *S*18).

Comparison of the reaction mixtures generated using one of the four metal salts revealed that while iron perchlorate exclusively resulted in the formation of **C1**, in its absence formation of **C2** was preferred, but did not form exclusively (Fig 3).

To better understand the role of perchlorate we investigated addition of this anion as a potassium perchlorate salt to self-assembly reactions containing stoichiometric amounts of **L1**, **L2**, TREN and $Fe(NTf_2)_2$. Addition of potassium perchlorate to a solution containing a crude mixture of **C1**, **C2** and **C3** synthesised with $Fe(NTf_2)_2$ salt resulted in changes in the spectrum consistent with perchlorate encapsulation within both cages, but did not alter the ratio of **C1:C2**. Moreover, the ratio of **C1:C2** remained unchanged after heating the reaction mixture at 90°C for 7 days indicating that once formed the composition of the DL did not change.

The observation that **C1** and **C2** are both capable of binding perchlorate anions is not unexpected given their structural similarities. Both structures have comparable average Fe-Fe distances (9.36 Å and 9.44 Å, respectively) and enclose similarly shaped void cavities of comparable volume (ESI *S*3). Exclusive formation of **C1** may be achieved by either promoting formation of **C1** (*i*), or impeding formation of **C2** (*ii*) which consumes subcomponent **L1** that would otherwise be incorporated within **C1** (Scheme 2).

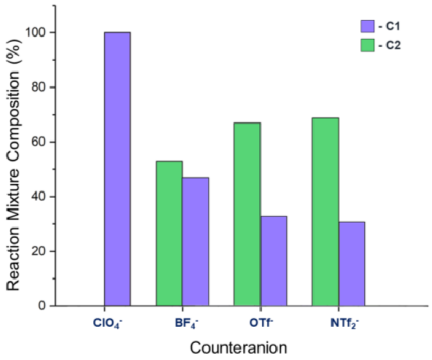

Figure 3. Composition of reaction mixture generated following self-assembly reactions with stoichiometric equivalents of **L1**, **L2**, TREN and Fe(II) salts with ClO_4^-, BF_4^-, OTf^- and NTf_2^- counterions.

The self-assembly of the mononuclear complex **C3**, which is a precursor to **C1**, is inconsequential as this subunit will be included within the final reaction mixture either as the mononuclear structure or within cage **C1**.

Scheme 2. Self-assembly pathways to cage **C1** and **C2**.

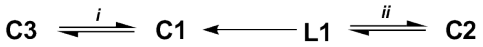

To rationalise the preferential formation of **C1** we looked to X-ray diffraction and ^{1}H NMR data of **C3**(*X*)$_2$. Single crystals of **C3** with each anion (ClO_4^-, BF_4^-, OTf^- and NTf_2^-) revealed that the ClO_4^- anion was uniquely positioned between the three arms of the tripod (Fig 4). We also observed a lengthening of the average Fe- N bond lengths in the presence of the perchlorate (1.976 Å relative to 1.967 Å observed with BF_4^-) which we hypothesised may aid the incorporation of **L1** within the structure. In contrast, the single crystal structures collected with BF_4^-, OTf^- and NTf_2^- counterions indicated the anion was clearly separated from the cation and did not bind in the three-fold axis. Examination of the solution state ^{1}H NMR data also revealed significant changes in the chemical shift of **C3** resonances when perchlorate was the counterion versus BF_4^-, OTf^- and NTf_2^- (Fig *S*24). These results support our hypothesis that perchlorate acts to preorganise **C3** for the insertion of **L1** making formation of **C1** the preferred product.

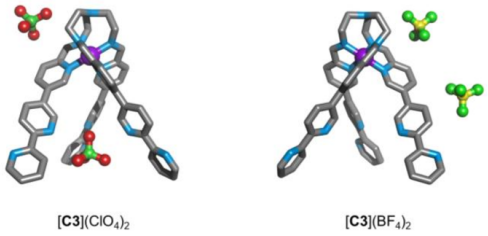

Figure 4. Single crystal X-ray structures of [**C3**]$(ClO_4)_2$ and [**C3**]$(BF_4)_2$, showing the corresponding positions of the counterions in the solid state. Hydrogens and solvent removed for clarity.

Conclusions

The formation and structural characterisation of an integratively sorted $M_4L(L^x)_3(L^y)_3$ metal-organic tetrahedral architecture is reported. M_4L_6 complexes are well documented to have desirable functional properties but, to date, examples of reduced-symmetry tetrahedra are rare. Moreover, formation of M_4L_6 tetrahedra which incorporate more than one ligand or metal ion have all previously been reported as components of statistical dynamic libraries. Here we demonstrate how the choice of amine and metal salt counterion can direct the exclusive formation of the integratively sorted species, **C1**. Exclusive formation of heteroleptic tetrahedron **C1** was achieved through incorporation of $Fe(ClO_4)_2$ into a system containing subcomponents **L1**, **L2** and TREN. Utilising alternative iron(II) salts generated a statistical mixture of heteroleptic cage **C1**, homoleptic cage **C2** and mononuclear species **C3**. X-ray crystallographic analysis of **C3**$(X)_2$, where $X = BF_4^-$, ClO_4^-, OTf^- and NTf_2^-, revealed that unique to the perchlorate example, a ClO_4^- anion was positioned between the three ligands on the three-fold rotation axis of the complex. It was hypothesised that incorporation of the anion in this position preorganises the structure for the formation of **C1** in the presence of **L1**. Increasing the structural diversity of tetrahedra through incorporation of dissimilar metal coordination sites is an appealing strategy to increase the functionality of metal-organic structures. Understanding the parameters that govern formation of **C1** is essential if the full potential of integratively self-sorted tetrahedra are to be explored for potential applications such as separation and catalysis.

This research was supported by a Royal Society University Research Fellowship (IAR), the Engineering and Physical Sciences Research Council (grants EP/K039547/1 and EP/R00482X/1), and the Diamond Light Source for the allocated time on the beamline I19 (Mt17379).

Data availability

Data associated with this article, including experimental procedures, compound characterisation, X-ray crystallography and VOIDOO calculations are available in the ESI.†

Author contributions

I. A. R. conceived and supervised the project; L. L. K. T. designed and performed the experiments and characterised all compounds; A. C. Y. S. synthesized novel ligand **L**; I. J. Y. R. performed all crystallographic characterisation.

Conflicts of interest

There are no conflicts to declare

Notes and references

1 M. Frank, L. Krause, R. Herbst-Irmer, D. Stalke and G. H. Clever, *Dalt. Trans.*, 2014, **43**, 4587–4592.
2 M. Lal Saha and M. Schmittel, *Org. Biomol. Chem.*, 2012, **10**, 4651–4684.
3 F. Crick and J. Watson, *Nature*, 1953, **171**, 737–738.
4 R. H. Carlson, C. V. Gabel, S. S. Chan, R. H. Austin, J. P. Brody and J. W. Winkelman, *Phys. Rev. Lett.*, 1997, **79**, 2149–2152.
5 S. Ackerman, *Discovering the Brain*, Washington (DC): National Academies Press (US), 1992.
6 M. M. Safont-Sempere, G. Fernández and F. Würthner, *Chem. Rev.*, 2011, **111**, 5784–5814.
7 Z. He, W. Jiang and C. A. Schalley, *Chem. Soc. Rev.*, 2015, **44**, 779–789.
8 W. M. Bloch and G. H. Clever, *Chem. Commun.*, 2017, **53**, 8506–8516.
9 S. Pullen, J. Tessarolo and G. H. Clever, *Chem. Sci.*, 2021, **12**, 7269–7293.
10 M. Konopka, P. Cecot, J. M. Harrowfield and A. R. Stefankiewicz, *J. Mater. Chem. C*, 2021, **9**, 7607–7614.
11 M. M. J. Smulders, A. Jiménez and J. R. Nitschke, *Angew. Chemie - Int. Ed.*, 2012, **51**, 6681–6685.
12 S. Cardona-Serra, E. Coronado, P. Gaviña, J. Ponce and S. Tatay, *Chem. Commun.*, 2011, **47**, 8235–8237.
13 J. E. M. Lewis, A. Tarzia, A. J. P. White and K. E. Jelfs, *Chem. Sci.*, 2020, **11**, 677–683.
14 A. D. Faulkner, R. A. Kaner, Q. M. A. Abdallah, G. Clarkson, D. J. Fox, P. Gurnani, S. E. Howson, R. M. Phillips, D. I. Roper, D. H. Simpson and P. Scott, *Nat. Chem.*, 2014, **6**, 797–803.
15 Y. Q. Zou, D. Zhang, T. K. Ronson, A. Tarzia, Z. Lu, K. E. Jelfs and J. R. Nitschke, *J. Am. Chem. Soc.*, 2021, **143**, 9009–9015.
16 J. Tessarolo, H. Lee, E. Sakuda, K. Umakoshi and G. H. Clever, *J. Am. Chem. Soc.*, 2021, **143**, 6339–6344.
17 A. W. Markwell-Heys, M. L. Schneider, J. M. L. Madridejos, G. F. Metha and W. M. Bloch, *Chem. Commun.*, 2021, **57**, 2915–2918.
18 T. K. Ronson, D. A. Roberts, S. P. Black and J. R. Nitschke, *J. Am. Chem. Soc.*, 2015, **137**, 14502–14512.
19 M. M. J. Smulders, I. A. Riddell, C. Browne and J. R. Nitschke, *Chem. Soc. Rev.*, 2013, **42**, 1728–1754.
20 A. Wu and L. Isaacs, *J. Am. Chem. Soc.*, 2003, **125**, 4831–4835.
21 F. J. Rizzuto and J. R. Nitschke, *J. Am. Chem. Soc.*, 2020, **142**, 7749–7753.
22 L. R. Holloway, P. M. Bogie and R. J. Hooley, *Dalt. Trans.*, 2017, **46**, 14719–14723.
23 L. R. Holloway, 2018.
24 A. J. Metherell and M. D. Ward, *Chem. Sci.*, 2016, **7**, 910–915.
25 Q. F. Sun, S. Sato and M. Fujita, *Angew. Chemie - Int. Ed.*, 2014, **53**, 13510–13513.
26 X. Zhao, H. Wang, B. Li, B. Zheng, D. Yang, W. Xu, X. Li, X. J. Yang and B. Wu, *Chem. Commun.*, 2021, **57**, 6078–6081.
27 L. R. Holloway, M. C. Young, G. J. O. Beran and R. J. Hooley, *Chem. Sci.*, 2015, **6**, 4801–4806.
28 K. Mahata, M. L. Saha and M. Schmittel, *J. Am. Chem. Soc.*, 2010, **132**, 15933–15935.
29 C. R. K. Glasson, J. K. Clegg, J. C. McMurtrie, G. V. Meehan,

L. F. Lindoy, C. A. Motti, B. Moubaraki, K. S. Murray and J. D. Cashion, *Chem. Sci.*, 2011, **2**, 540–543.
30 B. P. Burke, W. Grantham, M. J. Burke, G. S. Nichol, D. Roberts, I. Renard, R. Hargreaves, C. Cawthorne, S. J. Archibald and P. J. Lusby, *J. Am. Chem. Soc.*, 2018, **140**, 16877–16881.
31 M. L. Saha, S. Neogi and M. Schmittel, *Dalt. Trans.*, 2014, **43**, 3815–3834.
32 S. L. Han, J. Yang, D. Tripathy, X. Q. Guo, S. J. Hu, X. Z. Li, L. X. Cai, L. P. Zhou and Q. F. Sun, *Inorg. Chem.*, 2020, **59**, 14023–14030.
33 L. Zhang, Y. Jin, G. H. Tao, Y. Gong, Y. Hu, L. He and W. Zhang, *Angew. Chemie - Int. Ed.*, 2020, **59**, 20846–20851.
34 A. Sung, *MChem Thesis*, The University of Manchester, 2019.
35 I. A. Riddell, Y. R. Hristova, J. K. Clegg, C. S. Wood, B. Breiner and J. R. Nitschke, *J. Am. Chem. Soc.*, 2013, **135**, 2723–2733.

Supporting Information for

Integrative self-sorting of an $[Fe_4L_6]^{8+}$ tetrahedron governed by anion templation and chelation

Lauren L. K. Taylor, April C. Y. Sung, Iñigo J. Vitorica-Yrezabal, Imogen A. Riddell*

Department of Chemistry, University of Manchester, Oxford Road, Manchester, M13 9PL (UK)

*Email: imogen.riddell@manchester.ac.uk

Table of Contents

S1 Synthesis and Characterisation

S1.1 General Experimental Details

Unless stated otherwise, all chemicals were supplied from Sigma-Aldrich, Fluorochem, Fisher Scientific, Alfa Aesar or Scientific Laboratory Supplies Ltd and used without further purification. Deuterated NMR solvents were supplied from Sigma-Aldrich and NMR spectra were recorded on a B500 Bruker Advance II+ 500 MHz spectrometer. Chemical shifts are reported in parts per million (ppm). Coupling constants (*J*) are reported in hertz (Hz). Standard abbreviations indicating multiplicity were used as follows: s = singlet, d = doublet, t = triplet, dd = doublet of doublets, m = multiplet. ^{1}H and ^{13}C assignments were made using 2D NMR methods (COSY, NOESY, HSQC, HMBC). High-resolution mass spectra were obtained using a Thermo Orbitrap Exactive Plus Extended Mass Range mass spectrometer. Elemental analyses were performed by the microanalytical services of The University of Manchester with a CFlash 2000 elemental analyser for the analyses of carbon, hydrogen and nitrogen.

S1.2 Ligand Synthesis

2,2':5',3'':6'',2'''-quaterpyridine (L1): Synthesis was adapted from Cerfontaine *et al.*[1]

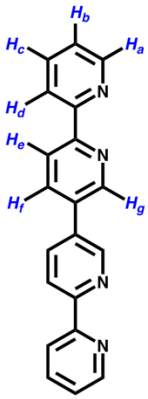

$Ni(PPh_3)_2Cl_2$ (0.56 g, 0.86 mmol) was added to anhydrous DMF (10 mL) and the mixture was stirred until it turned blue (rt, 5 min). Zinc dust (0.065 g, 0.99 mmol) was added and the mixture was stirred under N_2 until it turned brown (rt, 45 min). 5-Bromo-2,2'-bipyridine (0.20 g, 0.85 mmol) was added and the solution was stirred (rt, 24 hr). NH_4OH (2 M, 150 mL) was added and the resulting grey solution was extracted with ethyl acetate (3 x 50 mL). The combined organic layers were dried over $MgSO_4$ and the solvent was removed under reduced pressure to give the crude white solid. The crude product was added to ethyl acetate and the mixture was centrifuged (5 min). The supernatant was removed and the resultant white solid was washed with diethyl ether, diisopropyl ether and hexane, before being dissolved in DMSO and precipitated out with diethyl ether leaving a white solid (43 mg, 0.14 mmol, 16%). ^{1}H NMR (400 MHz, 298 K, DMSO-d_6): 9.18 (s, 2H, H_g), 8.74 (s, 2H, H_a), 8.54 (d, 2H, J = 8.28 Hz, H_e), 8.47 (d, 2H, J = 7.91 Hz, H_d), 8.43 (d, 2H, J = 8.25 Hz, H_f), 8.00 (t, 2H, J = 7.68 Hz, H_c), 7.50 (t, 2H, J = 6.07 Hz, H_b). ^{13}C (400 MHz, 298 K, DMSO-d_6): 155.2, 149.9, 147.9, 144.5, 141.7 137.9, 135.9, 135.6, 132.9, 121.0. [Accurate mass, *m/z*]: expected: 310.1218, found: 333.1097 $[M + Na]^+$. Elemental analysis (%) calculated for $C_{20}H_{14}N_4$: C 77.40, H 4.55, N 18.05; found: C 77.03, H 4.49, N 17.77.

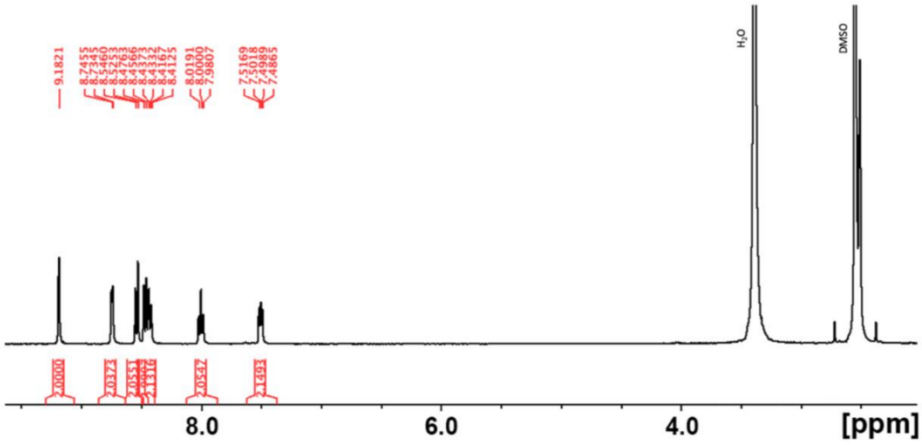

Figure S1. ^{1}H NMR (400 MHz, DMSO-d_6, 298 K) spectrum of **L1**.

The following synthesis was adapted from a previously reported protocol.[2]

6''-(dimethoxymethyl)-2,2':5',3''-terpyridine (L2'): 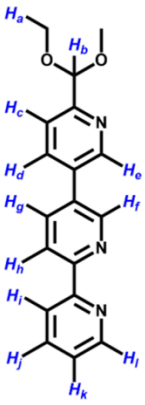

2-(Dimethoxymethyl)-5-(4,4,5,5-tetramethyl-1,3,2-dioxaborolan-2-yl)pyridine (1.2 g, 4.27 mmol), 5-bromo-2,2'-bipyridine (0.53 g, 2.25 mmol), Na_2CO_3 (0.76 g, 7.17 mmol) and $Pd(PPh_3)_4$ (0.29 g, 0.25 mmol) were dissolved in a 10:1 mixture of DMF:H_2O (22 mL). The yellow solution was degassed by three vacuum/N_2 fill cycles before being stirred under a flow of N_2 (70°C, 24 hr). The resulting brown solution was cooled and diluted in water before being extracted with dichloromethane (3 x 20 mL). The combined organic layers were then washed with water (3 x 10 mL) and dried over Na_2SO_4 before the solvent was removed to give the crude product as a brown solid (0.61 g, 1.98 mmol, 88%), this was sufficiently pure for the next step. ^{1}H NMR (500 MHz, 298 K, $CDCl_3$): 8.85 (t, 2H, H_f, H_e), 8.64 (s, 1H, H_i), 8.46 (d, J = 8.24 Hz, 1H, H_h) 8.38 (d, J = 7.96 Hz, 1H, H_c), 7.97 (dd, J = 8.25, 2.36 Hz, H_d), 7.93 (dd, J = 8.11, 2.32 Hz, H_g), 7.71 (td, 1H, J = 11.62, 1.74 Hz, H_j), 7.60 (TPPO), 7.47 (td, 1H, J = 7.60, 1.36 Hz, H_l), 7.39 (TPPO), 7.27 (ddd, 1H, J = 7.44, 4.80, 1.03 Hz, H_k), 5.39 (s, 1H, H_b), 3.39 (s, 6H, H_a). [ESI, m/z]: expected: 307.1, found: 330.1 $[M + Na]^+$.

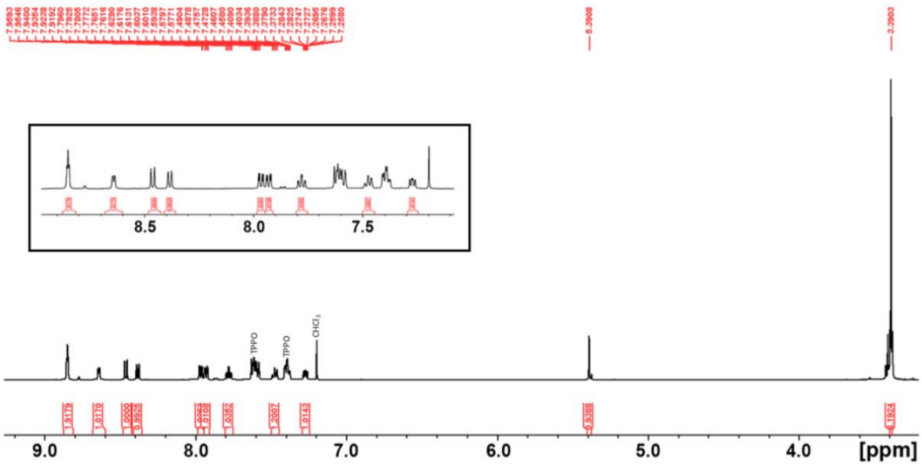

Figure S2. ^{1}H NMR (400 MHz, DMSO-d_6, 298 K) spectrum of **L2'**. Insert highlights the aromatic region splitting.

[2,2':5',3''-Terpyridine]-6''-carbaldehyde (L2) : 6''-(dimethoxymethyl)-2,2':5',3''-terpyridine

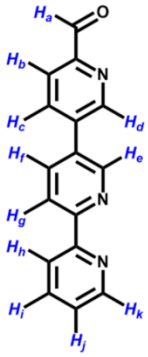

(2.3 g, 7.49 mmol) was dissolved in THF (7.3 mL) and HCl (2 M, 14.2 mL) was added. The yellow solution was sealed under N_2 and heated (40°C, 22 hr) before being neutralised by the addition of saturated $NaHCO_3$, resulting in the formation of a white precipitate. The white solid was dissolved in a 3:1 mixture of $CHCl_3$:2-propanol and the aqueous layer was washed with $CHCl_3$ (3 x 5 mL) before being dried over $MgSO_4$ and filtered to give a grey solid (1.4 g, 0.52 mmol, 72%). ^{1}H HMR (500 MHz, 298 K, $CDCl_3$): 10.09 (s, 1H, H_a), 9.03 (s, 1H, H_d), 8.91 (s, 1H, H_e) 8.66 (d, J = 3.98 Hz, 1H, H_h), 8.52 (d, J = 8.27 Hz, H_g), 8.41 (d, J = 7.98 Hz, H_b), 8.02 – 8.10 (m, 3H, H_f, H_c, H_k), 7.79 (td, 1H, J = 11.59, 1.76 Hz, H_i), 7.29 (ddd, 1H, J = 7.48, 4.79, 1.09 Hz, H_j). ^{13}C (126 MHz, 298 K, CD_3CN): δ 194.1, 157.1, 156.1, 153.1, 150.4, 149.6, 148.9, 138.1, 138.1, 136.8, 136.5, 133.2, 125.3, 122.6, 121.8, 121.7. [Accurate mass, *m/z*]: expected: 261.0902, found: 262.0969 $[M + H]^+$.

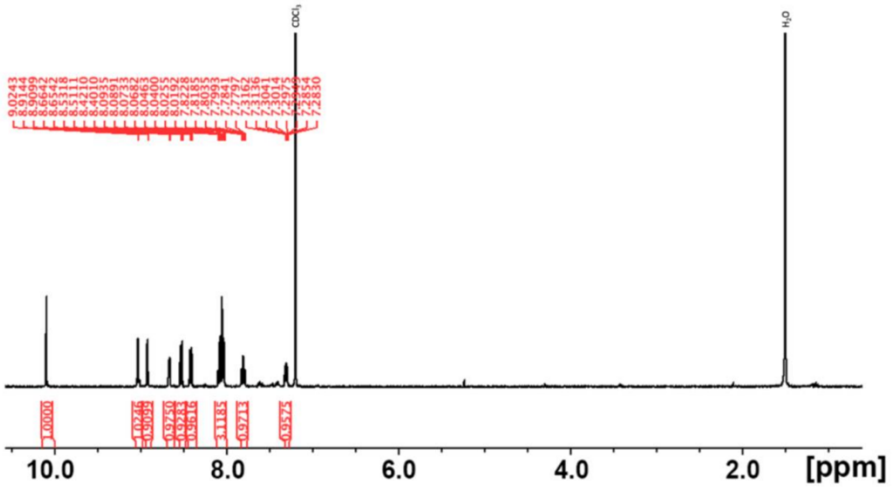

Figure S3. ^{1}H NMR (500 MHz, $CDCl_3$, 298 K) spectrum of **L2**.

S1.3 Complexation Reactions

S1.3.1 Reactions with *p*-Toluidine

Scheme S1. General reaction scheme for the formation of tetrahedral architectures with general formula $[Fe_4(\mathbf{L1})_x(\mathbf{L2})_y(p\text{-tol})_y](ClO_4)_8$ from ligands **L1**, **L2**, $Fe(ClO_4)_2$ and *p*-toluidine.

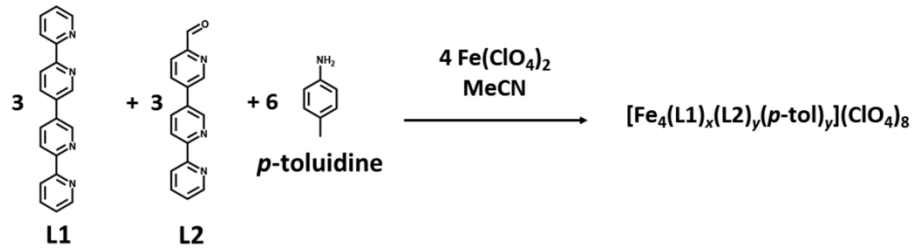

$[Fe_4(L1)_x(L2)_y(p\text{-tol})_y](ClO_4)_8$

L1 (3.6 mg, 11.6 μmol, 3 equiv), **L2** (3.0 mg, 11.6 μmol, 3 equiv), $Fe(ClO_4)_2.xH_2O$ (3.9 mg, 15.3 μmol, 4 equiv) and *p*-toluidine (1.2 mg, 11.5 μmol, 3 equiv) were dissolved in deuterated acetonitrile (0.35 mL) and the resulting pink solution was added to a J-Young NMR tube. The tube was sealed, and the solution was degassed by three vacuum/N_2 fill cycles before being heated (50°C, 24 hr). Diethyl ether was added to the solution causing precipitation and the mixture was centrifuged (5 min). The supernatant was removed leaving the product as a pink solid. [Accurate mass, *m/z*]: $\{Fe_4(\mathbf{L1})_3(\mathbf{L2})_3(p\text{-tol})_3(ClO_4)\}^{7+}$ = 329.3581, $\{Fe_4(\mathbf{L1})_3(\mathbf{L2})_3(p\text{-tol})_3(ClO_4)_2\}^{6+}$ = 400.7427, $\{Fe_4(\mathbf{L1})_3(\mathbf{L2})_3(p\text{-tol})_3(ClO_4)_3\}^{5+}$ = 500.6807, $\{Fe_4(\mathbf{L1})_3(\mathbf{L2})_3(p\text{-tol})_3(ClO_4)_4\}^{4+}$ = 650.8379, $\{Fe_4(\mathbf{L1})_3(\mathbf{L2})_3(p\text{-tol})_3(ClO_4)_5\}^{3+}$ = 900.7668, $\{Fe_4(\mathbf{L1})_3(\mathbf{L2})_3(p\text{-tol})_3(ClO_4)_6\}^{2+}$ = 1401.1227. $\{Fe_4(\mathbf{L1})_4(\mathbf{L2})_2(p\text{-tol})_2(ClO_4)\}^{7+}$ = 323.4965, $\{Fe_4(\mathbf{L1})_4(\mathbf{L2})_2(p\text{-tol})_2(ClO_4)_2\}^{6+}$ = 393.9042, $\{Fe_4(\mathbf{L1})_4(\mathbf{L2})_2(p\text{-tol})_2(ClO_4)_3\}^{5+}$ = 492.6746, $\{Fe_4(\mathbf{L1})_4(\mathbf{L2})_2(p\text{-tol})_2(ClO_4)_4\}^{4+}$ = 640.5803, $\{Fe_4(\mathbf{L1})_4(\mathbf{L2})_2(p\text{-tol})_2(ClO_4)_5\}^{3+}$ = 887.4231, $\{Fe_4(\mathbf{L1})_4(\mathbf{L2})_2(p\text{-tol})_2(ClO_4)_6\}^{2+}$ = 1381.1086. $\{Fe_4(\mathbf{L1})_5(\mathbf{L2})(p\text{-tol})(ClO_4)\}^{7+}$ = 317.7777, $\{Fe_4(\mathbf{L1})_5(\mathbf{L2})(p\text{-tol})(ClO_4)_2\}^{6+}$ = 387.2322, $\{Fe_4(\mathbf{L1})_5(\mathbf{L2})(p\text{-tol})(ClO_4)_3\}^{5+}$ = 484.6684, $\{Fe_4(\mathbf{L1})_5(\mathbf{L2})(p\text{-tol})(ClO_4)_4\}^{4+}$ = 630.8224, $\{Fe_4(\mathbf{L1})_5(\mathbf{L2})(p\text{-tol})(ClO_4)_5\}^{3+}$ = 874.0794, $\{Fe_4(\mathbf{L1})_5(\mathbf{L2})(p\text{-tol})(ClO_4)_6\}^{2+}$ = 1361.0936. $\{Fe_4(\mathbf{L1})_6(ClO_4)\}^{7+}$ = 312.0593, $\{Fe_4(\mathbf{L1})_6(ClO_4)_2\}^{6+}$ = 380.7264, $\{Fe_4(\mathbf{L1})_6(ClO_4)_3\}^{5+}$ = 476.6622, $\{Fe_4(\mathbf{L1})_6(ClO_4)_4\}^{4+}$ = 620.5644, $\{Fe_4(\mathbf{L1})_6(ClO_4)_5\}^{3+}$ = 860.7353, $\{Fe_4(\mathbf{L1})_6(ClO_4)_6\}^{2+}$ = 1341.0775.

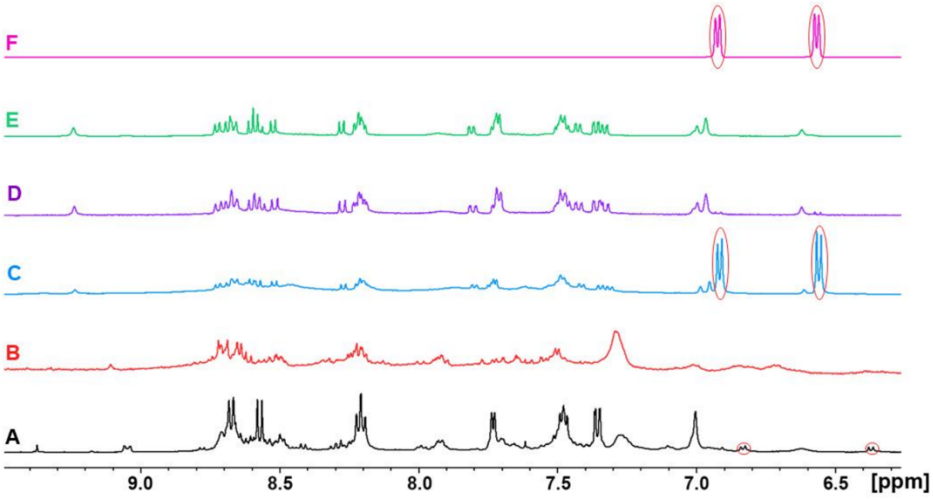

Figure S4. Stacked ^{1}H NMR (500 MHz, CD_3CN, 298 K) spectra of the aromatic region of **A**: system containing $[Fe_4(\mathbf{L1})_x(\mathbf{L2})_y(p\text{-tol})_y](ClO_4)_8$, where the dominant species (incorporating 67% of **L1**) observed by NMR is $[Fe_4(\mathbf{L1})_6](ClO_4)_8$, with minor peaks for *p*-toluidine in red circles. **B**: control reaction of **L2** (6 equiv), *p*-toluidine (6 equiv) and $Fe(ClO_4)_2$ (4 equiv), **C**: addition of TREN (1 equiv) into solution **A**, highlighting the ejection of free *p*-toluidine into solution (red circles) and the formation of the mixed-ligand tetrahedron [**C1**]$(ClO_4)_8$, **D**: precipitation of solution **C** with diethyl ether, removing the free *p*-toluidine from the solution and leaving [**C2**]$(ClO_4)_8$ exclusively, **E**: reference spectrum of [**C1**]$(ClO_4)_8$, **F:** *p*-toluidine in solution.

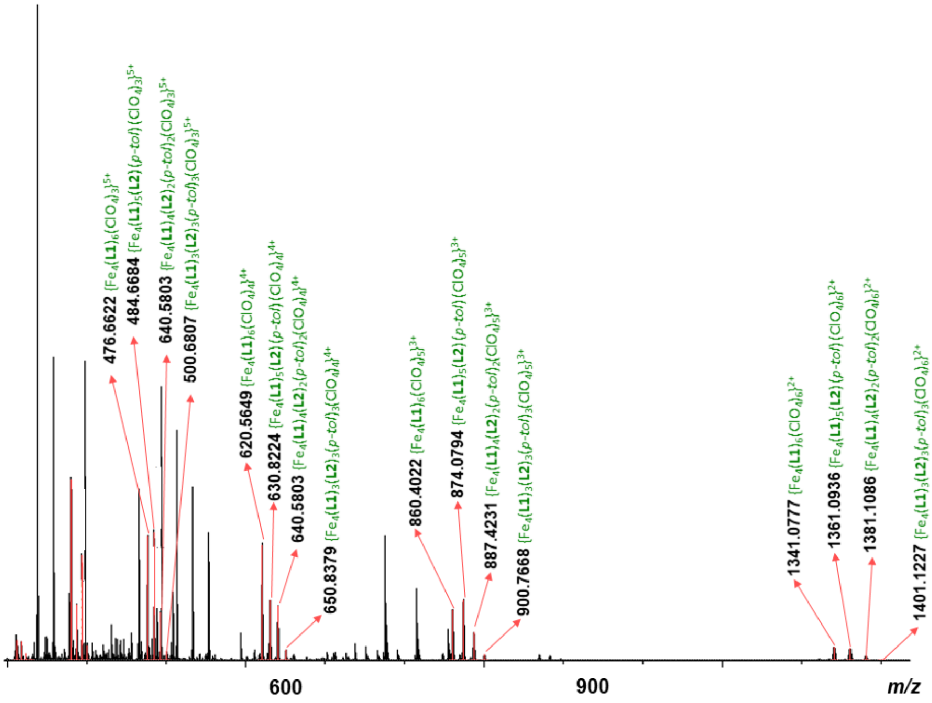

Figure S5. High-resolution mass spectrum for an acetonitrile solution of $[Fe_4(\mathbf{L1})_x(\mathbf{L2})_y(p\text{-tol})_y](ClO_4)_8$ (green). Patterns for the +2 to +5 peaks are annotated, whilst the +6 and +7 peaks are highlighted in red.

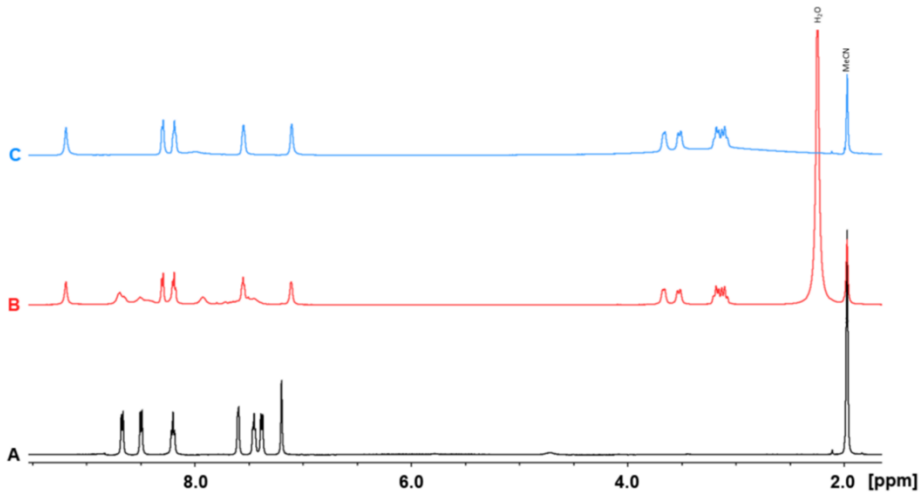

Figure S6. Stacked ^{1}H NMR (500 MHz, CD_3CN, 298 K) spectra of **A**: homotetrahedron [**C2**]$(BF_4)8$, **B**: reaction mixture following addition of TREN (1 equiv) and 2-pyridinecarboxaldehyde (3 equiv) into a solution of homotetrahedron [**C2**]$(BF_4)_8$, **C**: standard for the reaction of TREN (1 equiv), 2-pyridinecarboxaldehyde (3 equiv) and $Fe(BF_4)_2$ (1 equiv).

S1.3.2 Reactions with TREN

Scheme S2. General reaction scheme for the formation of **C1** and/or **C2**. All hydrogen atoms are labelled for NMR assignment.

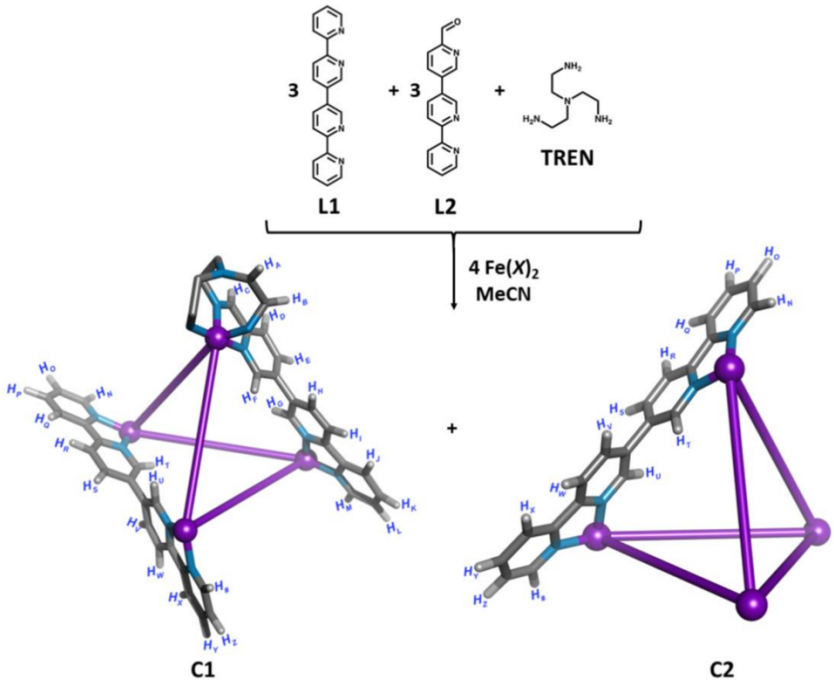

$[Fe_4(L1)_6](ClO_4)_8$.

L1 (2.8 mg, 9.0 μmol, 6 equiv) and $Fe(ClO_4)_2.xH_2O$ (1.5 mg, 5.9 μmol, 4 equiv) were dissolved in deuterated acetonitrile (0.35 mL) and the resulting pink solution was added to a J-Young NMR tube. The tube was sealed, and the solution was degassed by three vacuum/N_2 fill cycles before being heated (50°C, 24 hr). Diethyl ether was added to the solution causing precipitation and the mixture was centrifuged (5 min). The supernatant was removed leaving the product as a pink solid. ^{1}H NMR (500 MHz, 298 K, CD_3CN): 8.67 (d, 2H, J = 8.09 Hz, H_Q, H_X), 8.56 (d, 2H, J = 8.30 Hz, H_R, H_W), 8.21 (t, 2H, J = 7.89 Hz, H_P, H_Y), 7.71 (d, 2H, J = 5.25 Hz, H_S, H_V), 7.36 (t, 2H, J = 6.67 Hz, H_O, H_Z), 7.36 (dd, 2H, J = 8.23 Hz, H_N, $H_\#$), 7.01 (s, 2H, H_T, H_U). [Accurate mass, *m/z*]: $\{Fe_4(\mathbf{L1})_6(ClO_4)\}^{7+}$ = 312.0593, $\{Fe_4(\mathbf{L1})_6(ClO_4)_2\}^{6+}$ = 380.7264, $\{Fe_4(\mathbf{L1})_6(ClO_4)_3\}^{5+}$ = 476.6622, $\{Fe_4(\mathbf{L1})_6(ClO_4)_4\}^{4+}$ = 620.5644, $\{Fe_4(\mathbf{L1})_6(ClO_4)_5\}^{3+}$ = 860.7353, $\{Fe_4(\mathbf{L1})_6(ClO_4)_6\}^{2+}$ = 1341.0775.

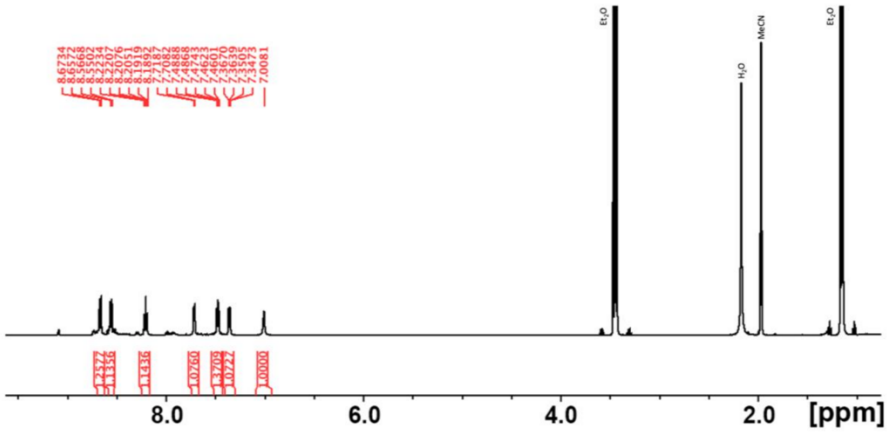

Figure S7. ^{1}H NMR (500 MHz, CD_3CN, 298 K) spectrum of homotetrahedron [**C2**]$(ClO_4)_8$.

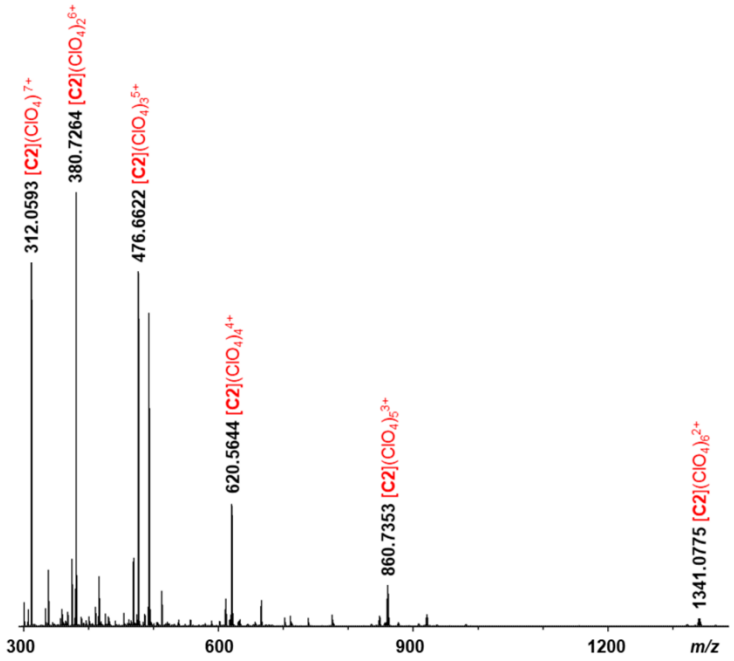

Figure S8. High-resolution mass spectrum for an acetonitrile solution of homotetrahedron [**C2**]$(ClO_4)_8$ (red).

[Fe_4(L1)$_3$(L2)$_3$T](ClO$_4$)$_8$.

L1 (3.7 mg, 11.9 μmol, 3 equiv), **L2** (2.6 mg, 10.0 μmol, 3 equiv), $Fe(ClO_4)_2.xH_2O$ (3.7 mg, 14.5 μmol, 4 equiv) and *tris*(2-aminoethyl)amine (0.50 μL, 3.3 μmol, 1 equiv) were dissolved in deuterated acetonitrile (0.35 mL) and the resulting pink solution was added to a J-Young NMR tube. The tube was sealed, and the solution was degassed by three vacuum/N_2 fill cycles before being heated (50°C, 24 hr). Diethyl ether was added to the solution causing precipitation and the mixture was centrifuged (5 min). The supernatant was removed leaving the product as a pink solid. ^{1}H NMR(500 MHz, 298 K, CD_3CN): 9.24 (s, 1H, H_C), 8.72 (d, 1H, J = 8.11 Hz, H_Q), 8.65 – 8.70 (m, 3H, H_X, H_R, H_W), 8.60 (d, 1H, J = 8.27 Hz, H_F), 8.57 (d, 1H, J = 8.33 Hz, H_G), 8.52 (d, 1H, J = 8.33 Hz, H_H) 8.28 (d, 1H, J = 7.92 Hz, H_E), 8.18 – 8.24 (m, 3H, J = 6.56 Hz, H_P, H_Y, H_S), 7.81 (d, 1H, J = 8.39 Hz, H_D), 7.69 – 7.75 (m, 3H, J = 7.08 Hz, H_V, H_O, H_Z), 7.45 – 7.52 (m, 3H, J = 7.73 Hz, H_N, H_T, H_U), 7.42 (d, 1H, J = 7.96, $H_\#$), 7.36 (d, 1H, J = 8.24 Hz, H_I), 7.33 (d, 1H, J = 8.24 Hz, H_M), 6.99 (s, 1H, H_K), 6.96 (s, 1H, H_L), 6.62 (s, 1H, H_J). [Accurate mass, *m/z*]: {Fe_4(**L1**)$_3$(**L2**)$_3$T(ClO$_4$)}$^{7+}$ = 304.2057, {Fe_4(**L1**)$_3$(**L2**)$_3$T(ClO$_4$)$_2$}$^{6+}$ = 371.5649, {Fe_4(**L1**)$_3$(**L2**)$_3$T(ClO$_4$)$_3$}$^{5+}$ = 465.6632, {Fe_4(**L1**)$_3$(**L2**)$_3$T(ClO$_4$)$_4$}$^{4+}$ = 606.8213, {Fe_4(**L1**)$_3$(**L2**)$_3$T(ClO$_4$)$_5$}$^{3+}$ = 842.0778, {Fe_4(**L1**)$_3$(**L2**)$_3$T(ClO$_4$)$_6$}$^{2+}$ = 1313.0922.

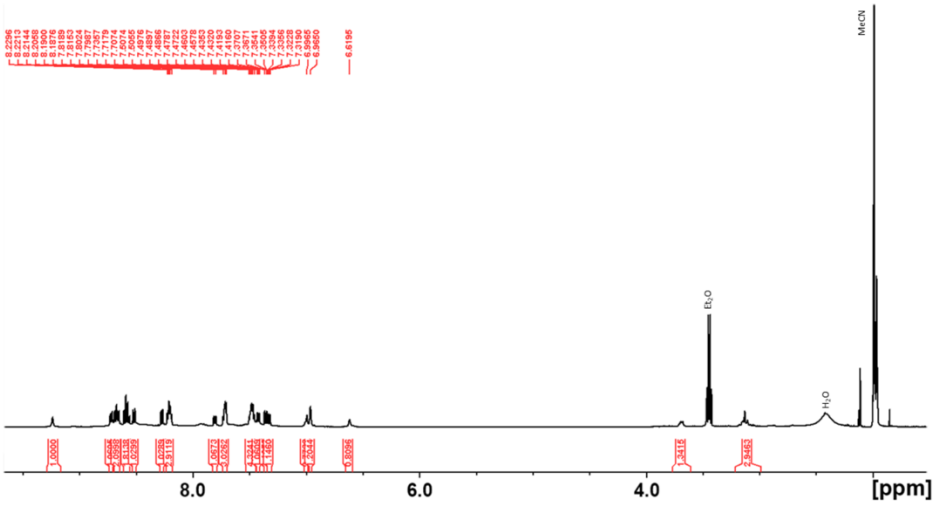

Figure S9. ^{1}H NMR (500 MHz, CD_3CN, 298 K) spectrum of iron perchlorate mixed ligand tetrahedron [**C1**](ClO$_4$)$_8$.

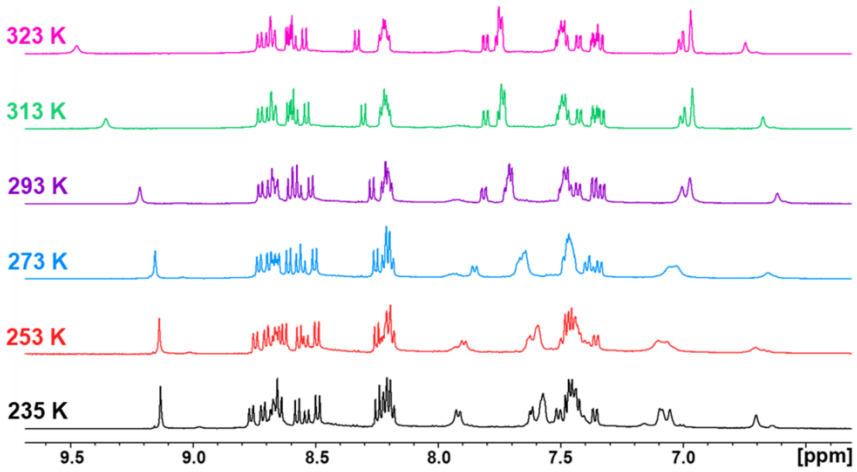

Figure S10. Variable temperature ^{1}H NMR (500 MHz, CD_3CN, 298 K) stack plot of mixed ligand tetrahedron [**C1**]$(ClO_4)_8$.

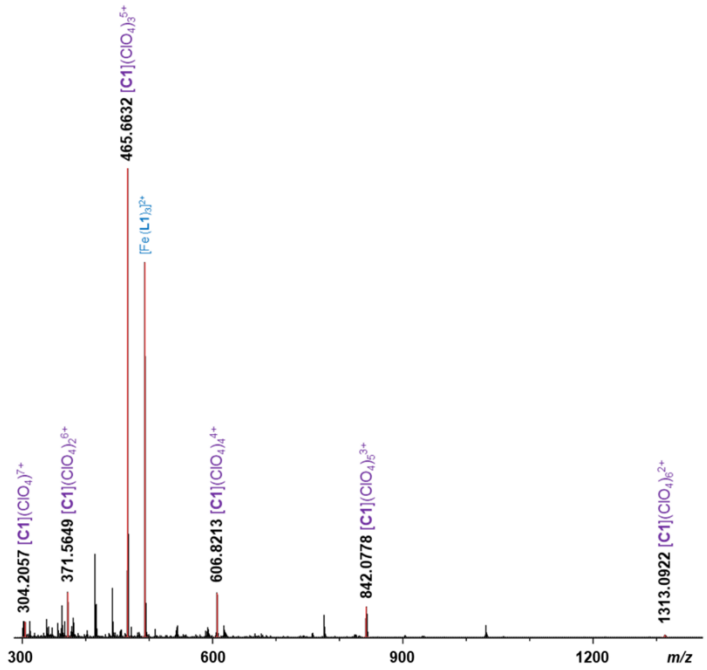

Figure S11. High-resolution mass spectrum for an acetonitrile solution of heterotetrahedral complex [**C2**]$(ClO_4)_8$ (purple).

$[Fe_4(L1)_6](BF_4)_8$

L1 (1.9 mg, 6.12 μmol, 6 equiv) and $Fe(BF_4)_2.6H_2O$ (1.8 mg, 5.33 μmol, 4 equiv) were dissolved in deuterated acetonitrile (0.35 mL) and the resulting red solution was added to a J-Young NMR tube. The tube was sealed, and the solution was degassed by three vacuum/N_2 fill cycles before being heated (50°C, 24 hr). Diethyl ether was added to the solution causing precipitation and the mixture was centrifuged (5 min). The supernatant was removed leaving the product as a red solid. ^{1}H NMR(500 MHz, 298 K, CD_3CN): 8.67 (d, 2H, J = 7.92 Hz, H_Q, H_X), 8.49 (d, 2H, J = 8.22 Hz, H_R, H_W), 8.19 (t, 2H, J = 7.58 Hz, H_P, H_Y), 7.59 (s, 2H, H_S, H_V), 7.45 (t, 2H, J = 6.28 Hz, H_O, H_Z), 7.38 (d, 2H, J = 7.99 Hz, H_N, $H_\#$), 7.19 (s, 2H, H_T, H_U). [Accurate mass, m/z]: $\{Fe_4(\mathbf{L1})_6(BF_4)\}^{7+}$ = 310.3528, $\{Fe_4(\mathbf{L1})_6(BF_4)_2\}^{6+}$ = 376.5791, $\{Fe_4(\mathbf{L1})_6(BF_4)_3\}^{5+}$ = 469.0956, $\{Fe_4(\mathbf{L1})_6(BF_4)_4\}^{4+}$ = 608.1202, $\{Fe_4(\mathbf{L1})_6(BF_4)_5\}^{3+}$ = 839.8284, $\{Fe_4(\mathbf{L1})_6(BF_4)_6\}^{2+}$ = 1303.2453.

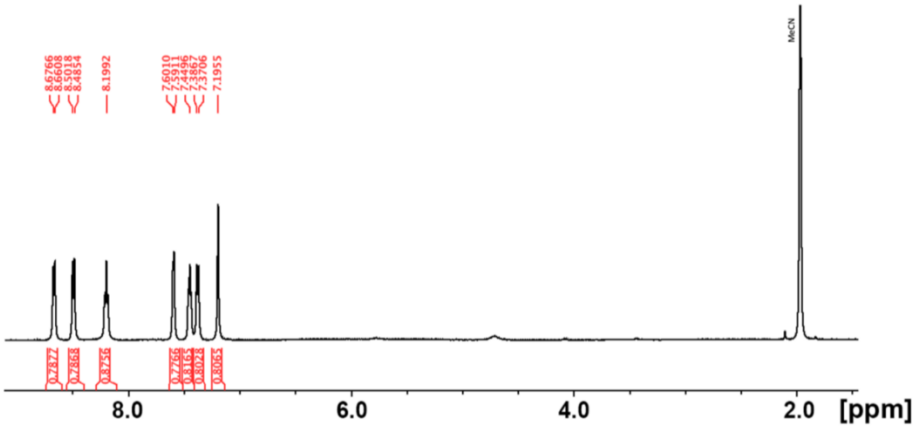

Figure S12. ^{1}H NMR (500 MHz, CD_3CN, 298 K) spectrum of homotetrahedron [**C2**]$(BF_4)_8$.

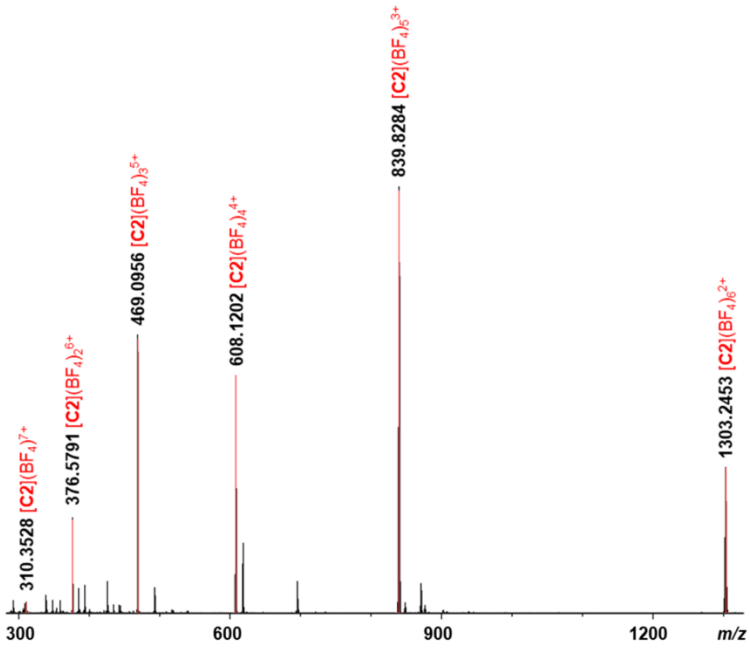

Figure S13. High-resolution mass spectrum for an acetonitrile solution of homotetrahedron [**C2**]$(BF_4)_8$ (red).

$[Fe_4(L1)_6](BF_4)_8$ / $[Fe_4(L1)_3(L2)_3](BF_4)_8$

L1 (1.8 mg, 5.8 μmol, 3 equiv), **L2** (1.7 mg, 6.5 μmol, 3 equiv), $Fe(BF_4)_2.6H_2O$ (2.9 mg, 8.6 μmol, 4 equiv) and *tris*(2-aminoethyl)amine (0.32 μL, 2.1 μmol, 1 equiv) were dissolved in deuterated acetonitrile (0.35 mL) and the resulting dark blue solution was added to a J-Young NMR tube. The tube was sealed, and the solution was degassed by three vacuum/N_2 fill cycles before being heated (50°C, 24 hr). Diethyl ether was added to the solution causing precipitation and the mixture was centrifuged (5 min). The supernatant was removed leaving the product as a blue/black solid. [Accurate mass, *m/z*]: $\{Fe_4(\mathbf{L1})_3(\mathbf{L2})_3T(BF_4)\}^{7+}$ = 302.5004, $\{Fe_4(\mathbf{L1})_3(\mathbf{L2})_3T(BF_4)_2\}^{6+}$ = 367.4180, $\{Fe_4(\mathbf{L1})_3(\mathbf{L2})_3T(BF_4)_3\}^{5+}$ = 458.1028, $\{Fe_4(\mathbf{L1})_3(\mathbf{L2})_3T(BF_4)_4\}^{4+}$ = 594.3785, $\{Fe_4(\mathbf{L1})_3(\mathbf{L2})_3T(BF_4)_5\}^{3+}$ = 821.5061, $\{Fe_4(\mathbf{L1})_3(\mathbf{L2})_3T(BF_4)_6\}^{2+}$ = 1275.7621. $\{Fe_4(\mathbf{L2})_6(BF_4)\}^{7+}$ = 310.3536, $\{Fe_4(\mathbf{L2})_6(BF_4)_2\}^{6+}$ = 376.4131, $\{Fe_4(\mathbf{L2})_6(BF_4)_3\}^{5+}$ = 469.0961, $\{Fe_4(\mathbf{L2})_6(BF_4)_4\}^{4+}$ = 608.1215, $\{Fe_4(\mathbf{L2})_6(BF_4)_5\}^{3+}$ = 839.8301, $\{Fe_4(\mathbf{L2})_6(BF_4)_6\}^{2+}$ = 1303.2486.

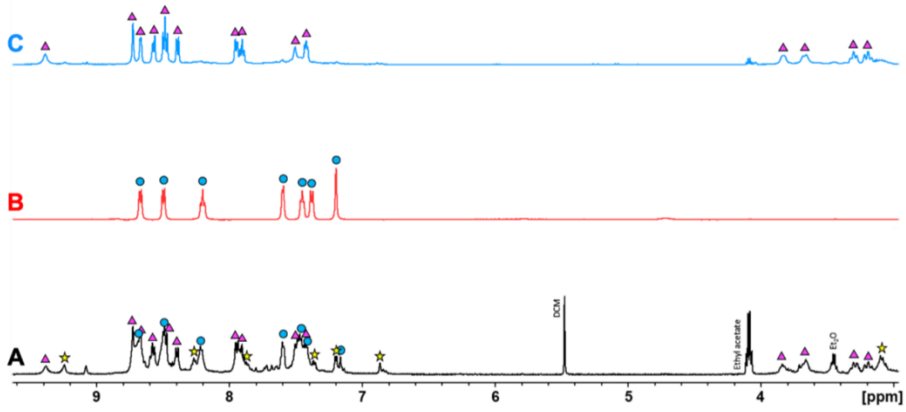

Figure S14. Stacked ^{1}H NMR (500 MHz, CD_3CN, 298 K) spectra of **A**: iron tetrafluoroborate mixed ligand system, **B**: iron tetrafluoroborate homotetrahedron [**C2**]$(ClO_4)_8$ *(blue circles)*. **C:** mononuclear complex [**C3**]$(BF_4)_2$ *(pink triangles).* Peaks assigned to [**C1**]$(BF_4)_8$ through comparison with the heterotetrahedron [**C1**]$(ClO_4)_8$ are denoted by yellow stars.

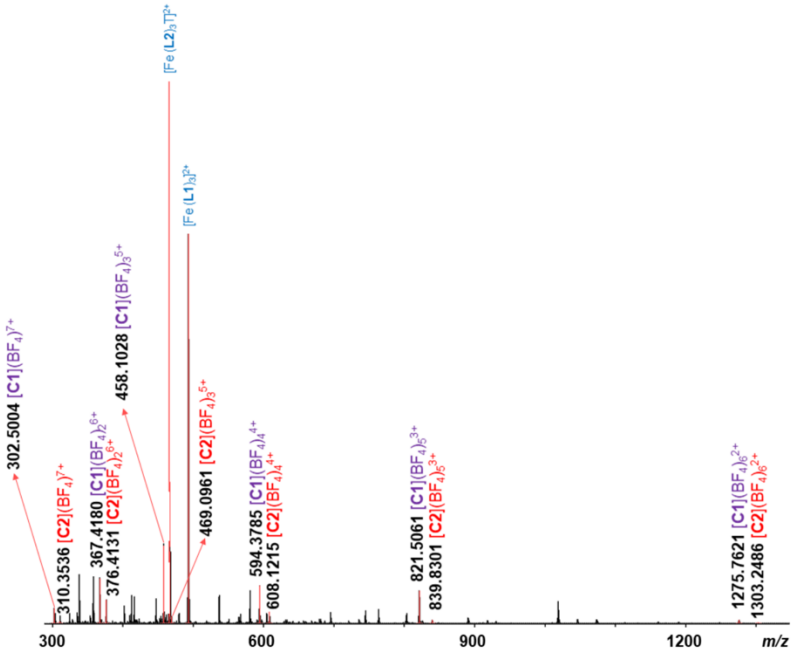

Figure S15. High-resolution mass spectrum for an acetonitrile solution of the tetrahedral mixture of complex **C1**$(BF_4)_8$ (purple) and **C2**$(BF_4)_8$ (red). Additional isotopic patterns are highlighted in blue.

$[Fe_4(L1)_6](OTf)_8$

L1 (2.4 mg, 7.7 μmol, 6 equiv) and $Fe(OTf)_2$ (1.8 mg, 5.1 μmol, 4 equiv) were dissolved in deuterated acetonitrile (0.35 mL) and the resulting purple solution was added to a J-Young NMR tube. The tube was sealed, and the solution was degassed by three vacuum/N_2 fill cycles before being heated (50°C, 24 hr). Diethyl ether was added to the solution causing precipitation and the mixture was centrifuged (5 min). The supernatant was removed leaving the product as a purple solid. ^{1}H NMR(500 MHz, 298 K, CD_3CN): 8.60 (d, 2H, J = 8.04 Hz, H_Q, H_X), 8.48 (d, 2H, J = 8.32 Hz, H_R, H_W), 8.09 (td, 2H, J = 11.70, 1.28 Hz, H_P, H_Y), 7.69 (d, 2H, J = 5.00 Hz, H_S, H_V), 7.37 (t, 2H, J = 6.26 Hz, H_O, H_Z), 7.28 (dd, 2H, J = 8.36, 1.86 Hz, H_N, $H_\#$), 6.89 (s, 2H, H_T, H_U). [Accurate mass, m/z]: $\{Fe_4(\mathbf{L1})_6(OTf)_3\}^{5+}$ = 506.4666, $\{Fe_4(\mathbf{L1})_6(OTf)_4\}^{4+}$ = 670.5705, $\{Fe_4(\mathbf{L1})_6(OTf)_5\}^{3+}$ = 943.4110, $\{Fe_4(\mathbf{L1})_6(OTf)_6\}^{2+}$ = 1489.5942.

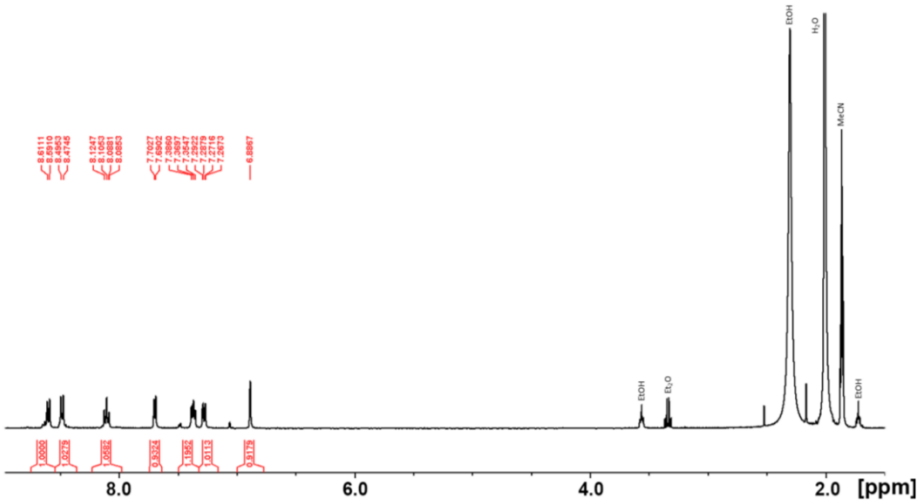

Figure S16. ^{1}H NMR (500 MHz, CD_3CN, 298 K) spectrum of homotetrahedron [**C2**]$(OTf)_8$.

$[Fe_4(L1)_6](OTf)_8$ / $[Fe_4(L1)_3(L2)_3](OTf)_8$

L1 (3.6 mg, 11.6 μmol, 3 equiv), **L2** (3.0 mg, 11.5 μmol, 3 equiv), $Fe(OTf)_2$ (5.4 mg, 15.2 μmol, 4 equiv) and *tris*(2-aminoethyl)amine (0.56 μL, 3.9 μmol, 1 equiv) were dissolved in deuterated acetonitrile (0.35 mL) and the resulting pink solution was added to a J-Young NMR tube. The tube was sealed, and the solution was degassed by three vacuum/N_2 fill cycles before being heated (50°C, 24 hr). Diethyl ether was added to the solution causing precipitation and the mixture was centrifuged (5 min). The supernatant was removed leaving the product as a pink solid. [Accurate mass, *m/z*]: $\{Fe_4(\mathbf{L1})_3(\mathbf{L2})_3T(OTf)_4\}^{4+}$ = 642.5834, $\{Fe_4(\mathbf{L1})_3(\mathbf{L2})_3T(OTf)_5\}^{3+}$ = 925.0872, $\{Fe_4(\mathbf{L1})_3(\mathbf{L2})_3T(OTf)_6\}^{2+}$ = 1462.1077. $\{Fe_4(\mathbf{L1})_6(OTf)_4\}^{4+}$ = 670.0698, $\{Fe_4(\mathbf{L1})_6(OTf)_5\}^{3+}$ = 943.4112, $\{Fe_4(\mathbf{L1})_6(OTf)_6\}^{2+}$ = 1490.0951.

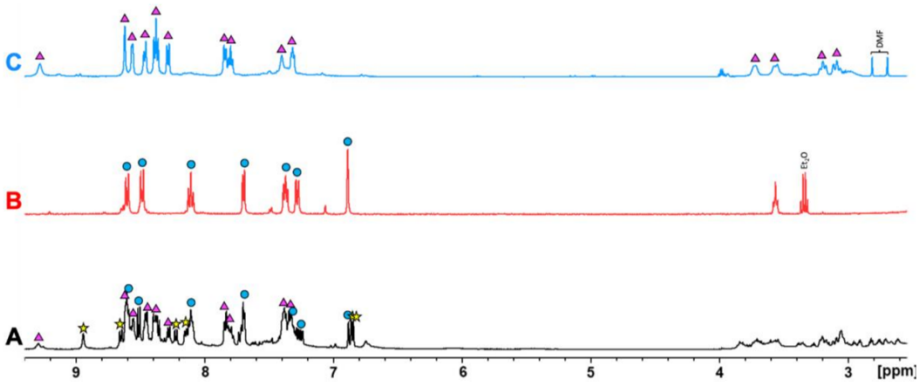

Figure S17. Stacked ^1H NMR (500 MHz, CD_3CN, 298 K) spectra of **A**: iron triflate mixed ligand system, **B**: iron triflate homotetrahedron [**C2**]$(OTf)_8$ *(blue circles)*. **C:** mononuclear complex [**C3**]$(OTf)_2$ *(pink triangles).* Peaks assigned to [**C1**]$(OTf)_8$ through comparison with the heterotetrahedron [**C1**]$(ClO_4)_8$ are denoted by yellow stars.

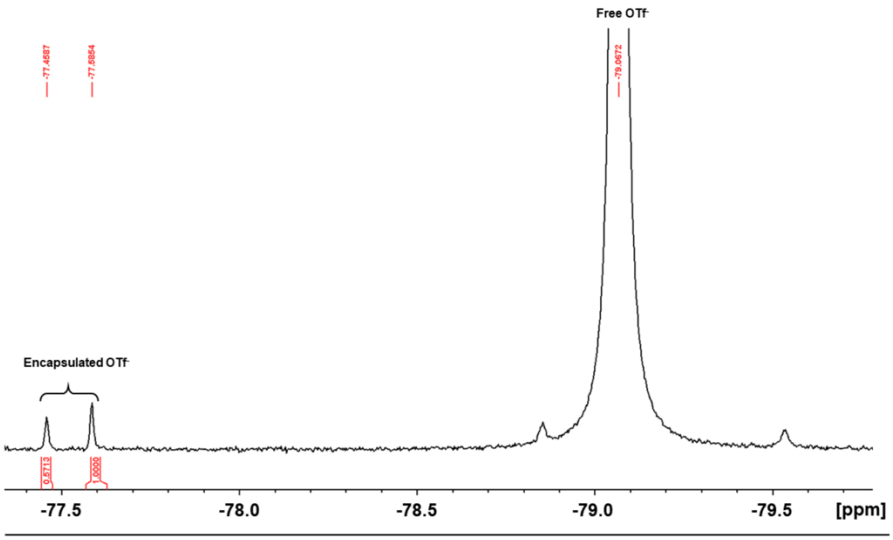

Figure S18. ^{19}F NMR (471 MHz, CD_3CN, 298 K) spectrum of the iron triflate mixed ligand system [**C1**](OTf)$_8$, highlighting the peak for free triflate anions as well as two additional peaks for triflate encapsulation in homotetrahedron **C2** (-77.46 ppm) and heterotetrahedron **C1** (-77.59 ppm).

[Fe_4(L1)$_6$](NTf_2)$_8$

L1 (4.3 mg, 13.9 μmol, 6 equiv) and Fe(NTf_2)$_2$.7H_2O (6.7 mg, 9.0 μmol, 4 equiv) were dissolved in deuterated acetonitrile (0.35 mL) and the resulting red solution was added to a J-Young NMR tube. The tube was sealed, and the solution was degassed by three vacuum/N_2 fill cycles before being heated (50°C, 24 hr). Diethyl ether was added to the red solution, causing a red precipitate to appear. Diethyl ether was added to the solution causing precipitation and the mixture was centrifuged (5 min). The supernatant was removed leaving the product as a red solid. ^1H NMR(500 MHz, 298 K, CD_3CN): 8.73 (d, 2H, J = 7.88 Hz, H_Q, H_X), 8.52 (d, 2H, J = 8.30 Hz, H_R, H_W), 8.08 – 8.17 (m, 2H, H_P, H_Y), 7.53 (t, 2H, J = 4.47 Hz H_S, H_V), 7.48 (dd, 2H, J = 8.29, 2.76 Hz, H_O, H_Z), 7.40 (d, 2H, J = 5.30 Hz, H_N, $H_\#$), 7.09 (s, 2H, H_T, H_U). [Accurate mass, *m/z*]: {Fe_4(**L1**)$_6$(NTf_2)}$^{7+}$ = 338.0867, {Fe_4(**L1**)$_6$(NTf_2)$_2$}$^{6+}$ = 440.7159, {Fe_4(**L1**)$_6$(NTf_2)$_3$}$^{5+}$ = 585.0429, {Fe_4(**L1**)$_6$(NTf_2)$_4$}$^{4+}$ = 801.0327, {Fe_4(**L1**)$_6$(NTf_2)$_5$}$^{3+}$ = 1162.0928, {Fe_4(**L1**)$_6$(NTf_2)$_6$}$^{2+}$ = 1882.9839.

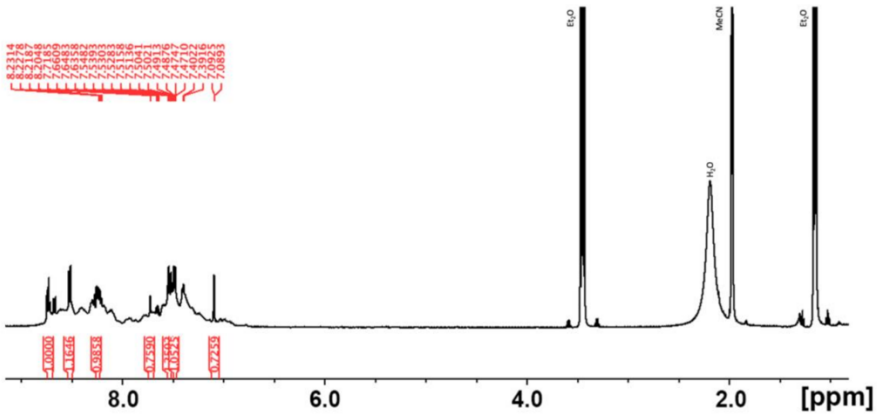

Figure S19. ^{1}H NMR (400 MHz, CD_3CN, 298 K) spectrum of homotetrahedron [**C2**]$(NTf_2)_8$. The broadened baseline is the result of incomplete self-assembly with the triflimide anion being too large to act as an internal template.

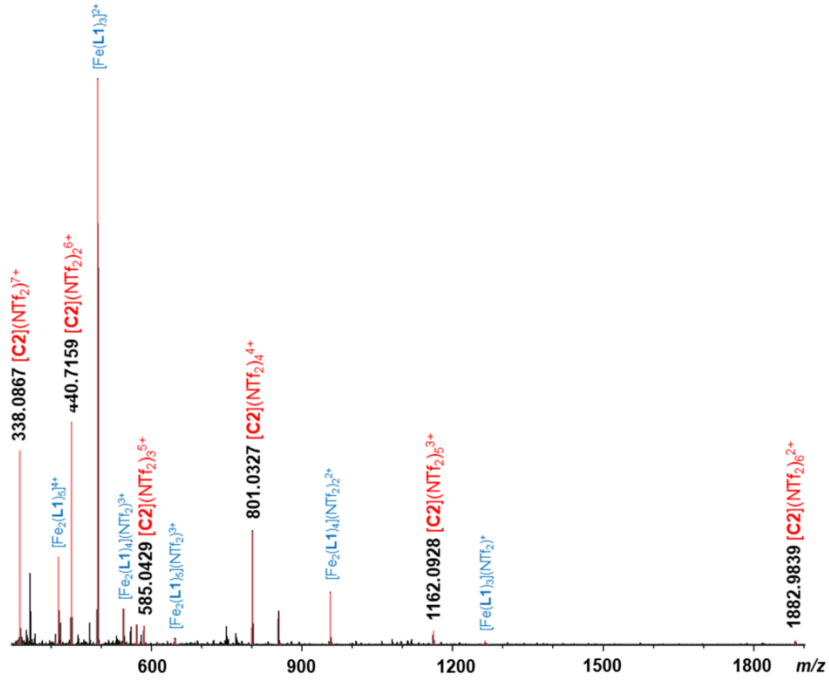

Figure S20. High-resolution mass spectrum for an acetonitrile solution of homotetrahedral complex [**C2**]$(NTf_2)_8$ (red). Additional isotopic patterns are highlighted in blue.

$[Fe_4(L1)_6](NTf_2)_8$ / $[Fe_4(L1)_3(L2)_3](NTf_2)_8$

L1 (2.5 mg, 8.1 μmol, 3 equiv), **L2** (2.1 mg, 8.0 μmol, 3 equiv), $Fe(NTf_2)_2.7H_2O$ (8.0 mg, 10.8 μmol, 4 equiv) and *tris*(2-aminoethyl)amine (0.32 μL, 2.1 μmol, 1 equiv) were dissolved in deuterated acetonitrile (0.35 mL) and the resulting dark purple solution was added to a J-Young NMR tube. The tube was sealed, and the solution was degassed by three vacuum/N_2 fill cycles before being heated (50°C, 24 hr). Diethyl ether was added to the solution causing precipitation and the mixture was centrifuged (5 min). The supernatant was removed leaving the product as a purple solid. [Accurate mass, *m/z*]: $\{Fe_4(\mathbf{L1})_3(\mathbf{L2})_3T(NTf_2)_2\}^{6+}$ = 431.0713, $\{Fe_4(\mathbf{L1})_3(\mathbf{L2})_3T(NTf_2)_3\}^{5+}$ = 574.0482, $\{Fe_4(\mathbf{L1})_3(\mathbf{L2})_3T(NTf_2)_4\}^{4+}$ = 787.5388, $\{Fe_4(\mathbf{L1})_3(\mathbf{L2})_3T(NTf_2)_5\}^{3+}$ = 1143.6910, $\{Fe_4(\mathbf{L1})_3(\mathbf{L2})_3T(NTf_2)_6\}^{2+}$ = 1855.4942. $\{Fe_4(\mathbf{L1})_6(NTf_2)_4\}^{4+}$ = 801.0315, $\{Fe_4(\mathbf{L1})_6(NTf_2)_5\}^{3+}$ = 1161.6829, $\{Fe_4(\mathbf{L1})_6(NTf_2)_6\}^{2+}$ = 1882.9613.

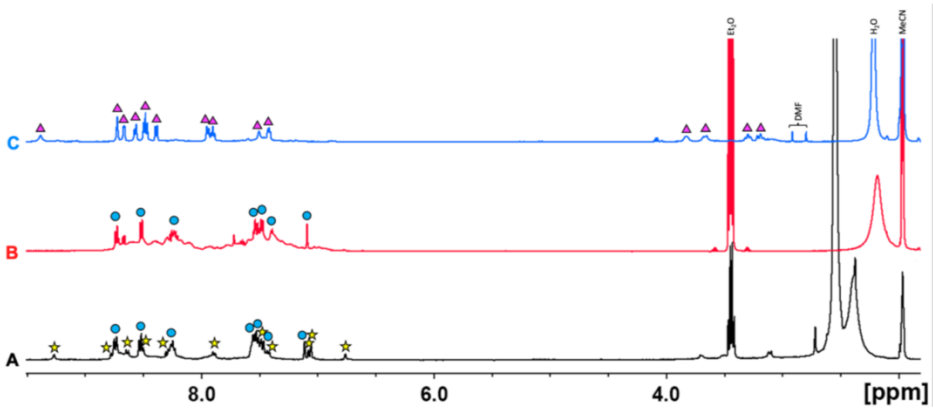

Figure S21. Stacked ^{1}H NMR (500 MHz, CD_3CN, 298 K) spectra of **A**: iron triflimide mixed ligand system, **B**: iron triflimide homotetrahedron [**C2**]$(NTf_2)_8$ *(blue circles)*. **C:** mononuclear complex [**C3**]$(NTf_2)_2$ *(pink triangles).* Peaks assigned to [**C1**]$(NTf_2)_8$ through comparison with the heterotetrahedron [**C1**]$(ClO_4)_8$ are denoted by yellow stars.

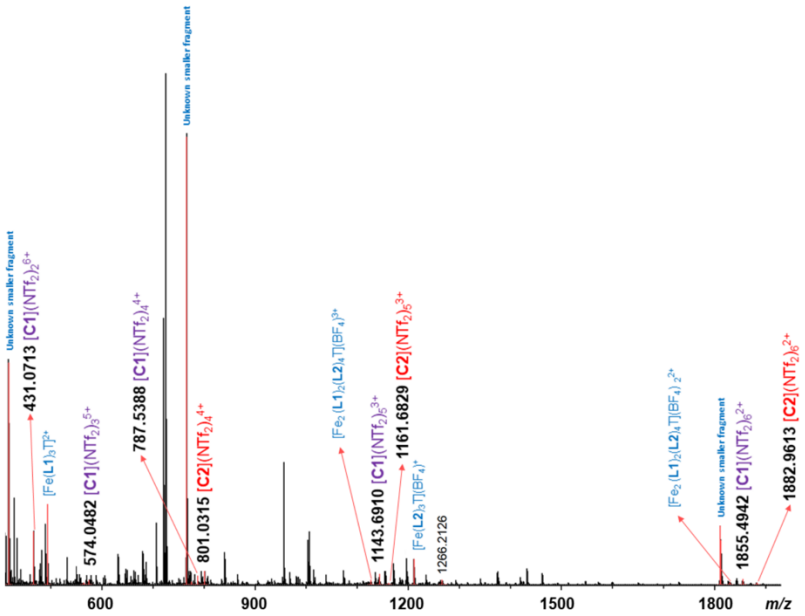

Figure S22. High-resolution mass spectrum for an acetonitrile solution of the tetrahedral mixture of complex [**C1**]$(NTf_2)_8$ (purple) and [**C2**]$(NTf_2)_8$ (red). Additional isotopic patterns are highlighted in blue.

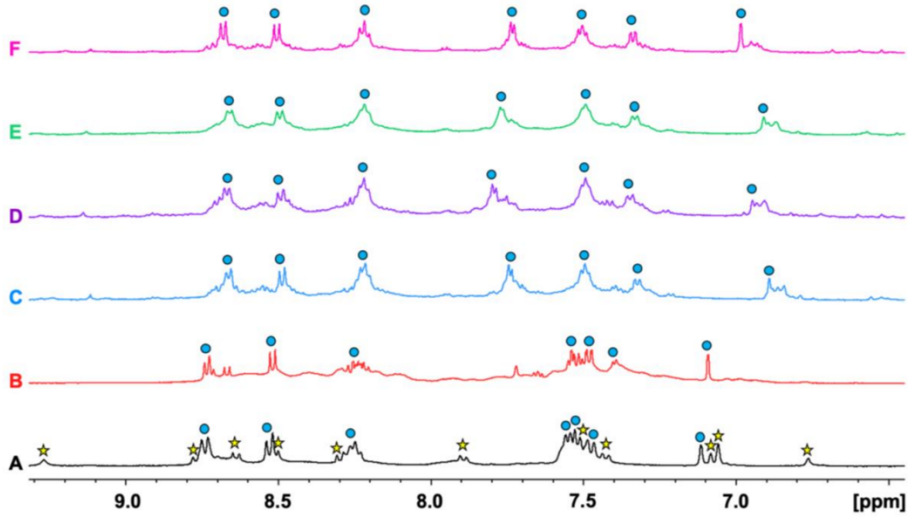

Figure S23. Stacked ^{1}H NMR (500 MHz, CD_3CN, 298 K) spectra of **A**: iron triflimide mixed ligand system, **B**: iron triflimide homotetrahedron *(blue circles)*, **C**: addition of PF_6^- to a solution of **A**, **D**: addition of SbF_6^- to a solution of **A**, **E**: addition of AsF_6^- to a solution of **A, F**: addition of ReO_4^- to a solution of **A.** Peaks for heterotetrahedron [**C1**]$(NTf_2)_8$ are denoted by yellow stars. In addition to perchlorate, the addition of anions into DL **A** were investigated. In all four reactions (**C, D, E** and **F)** the homotetrahedron is the dominant complex in observed in solution.

S1.3.3 Comparison of Mononuclear $[C3]^{2+}$ Complexes with Different Counterions

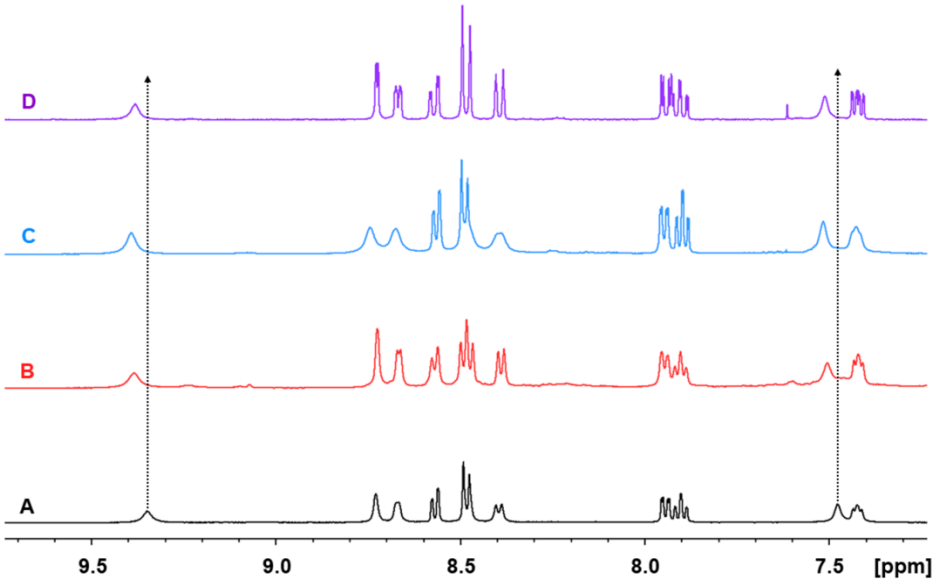

Figure S24. Stacked ^{1}H NMR (500 MHz, CD_3CN, 298 K) spectra of **A**: [**C3**]$(ClO_4)_2$, **B**: [**C3**]$(BF_4)_2$, **C**: [**C3**]$(OTf)_2$, **D**: [**C3**]$(NTf_2)_2$. Dashed arrows highlight the shift relative to the perchlorate spectrum of peaks at 9.35 ppm and 7.48 ppm.

S2 X-Ray Crystallography

Data αCollection. X-Ray data for compound **C2** were collected at a temperature of 100 K using a Rigaku Supernova with Mo-Kα radiation equipped with a CCD-Eos detector and an Oxford Cryosystems nitrogen flow gas system. X-Ray data for compound [**C3**]$(BF_4)_2$, [**C3**]$(ClO_4)_2$ and [**C3**]$(OTf)_2$ were collected at a temperature of 100 K using a Rigaku FR-X with Cu-Kα radiation equipped with a HypixHE6000 detector, equipped with an Oxford Cryosystems nitrogen flow gas system. X-Ray data for compounds **C1** and [**C3**]$(NTf_2)_2$ were collected at a temperature of 100 K using a synchrotron radiation (λ= 0.6889 Å) at Diamond Light Source,[3] equipped with a Pilatus 2M detector and an Oxford Cryosystems nitrogen flow gas system. Data was measured using CrysAlisPro and GDA suite of programs.

Crystal structure determinations and refinements. X-Ray data were processed and reduced using CrysAlisPro suite of programmes. Absorption correction was performed using empirical methods (SCALE3 ABSPACK) based upon symmetry-equivalent reflections combined with measurements at different azimuthal angles.[4–6] The crystal structure were solved and refined against all F^2 values using the SHELXL and Olex 2 suite of programmes.[7,8] Despite the highly intense X-ray source, crystals of **C2** present a diffraction limit of 1 Å.

All atoms in crystal structures were refined anisotropically with the exception of the hydrogens atoms. Hydrogen atoms were placed in the calculated idealized positions for all crystal structures. BF_4^-, $SO_3CF_3^-$ and ClO_4^- anions in crystal structures were disordered and modelled over two positions. The anions structure were constrained to have idealize structure. The atomic displacement parameters (adp) of the ligands have been restrained using similar Ueq and rigid bond (RIGU) and Similar Ueq (SIMU) restraints.

Compounds [**C3**]$(OTf)_2$**, C1** and **C2** present large voids filled with featureless electron density. Solvent mask software implemented in Olex2 shows an electron count of 154, 2074 and 357 electrons, which correspond to 7, 94 and 16 molecules of acetonitrile in the unit cell, respectively.

A number of A and B alerts were found, especially for structure **C2** and [**C3**](OTf)$_2$ due to the poor resolution obtained for **C2** and the large disorder found in both the [**C3**](OTf)$_2$ and **C2** crystal structures.

CCDC 2112326-2112330 and 2112640 contain the supplementary crystallographic data for this paper. These data can be obtained free of charge *via* www.ccdc.cam.ac.uk/conts/retrieving.html (or from the Cambridge Crystallographic Data Centre, 12 Union Road, Cambridge CB21EZ, UK; fax: (+44)1223-336-033; or deposit@ccdc.cam.ac.uk).

Table S1. Crystallographic information for **C1** and **C2.**

Identification code	**C1**	**C2**
Empirical formula	$C_{120.39}H_{94.58}Cl_8Fe_4N_{28.19}O_{32.99}$	$C_{132}H_{90}F_{24}Fe_4N_{26}O_{24}S_8$
Formula weight	2971.07	3360.17
Temperature/K	100(2)	150.00(10)
Crystal system	trigonal	monoclinic
Space group	R-3	I2/a
a/Å	21.1400(7)	31.990(3)
b/Å	21.1400(7)	18.5196(12)
c/Å	67.0247(16)	28.075(2)
α/°	90	90
β/°	90	114.492(11)
γ/°	120	90
Volume/Å^3	25940.3(18)	15136(2)
Z	6	4
ρ_{calc}g/cm^3	1.141	1.475
μ/mm^{-1}	0.480	0.590
F(000)	9109.0	6816.0
Crystal size/mm^3	0.16 × 0.1 × 0.02	0.34 × 0.13 × 0.03
Radiation	Synchrotron (λ = 0.6889)	Mo Kα (λ = 0.71073)
2Θ range for data collection/°	3.194 to 49.034	5.434 to 41.628
Index ranges	-25 ≤ h ≤ 21, -25 ≤ k ≤ 23, -80 ≤ l ≤ 78	-31 ≤ h ≤ 25, -17 ≤ k ≤ 18, -27 ≤ l ≤ 28
Reflections collected	60877	27222
Independent reflections	10558 [R_{int} = 0.0722, R_{sigma} = 0.0487]	7890 [R_{int} = 0.1191, R_{sigma} = 0.1327]
Data/restraints/parameters	10558/283/605	7890/586/944
Goodness-of-fit on F^2	1.244	1.280
Final R indexes [I>=2σ (I)]	R_1 = 0.1384, wR_2 = 0.3692	R_1 = 0.1348, wR_2 = 0.3475
Final R indexes [all data]	R_1 = 0.1947, wR_2 = 0.4153	R_1 = 0.2015, wR_2 = 0.3981
Largest diff. peak/hole / e Å^{-3}	0.95/-0.43	1.20/-0.91

Table S2. Crystallographic information for [**C3**]$(ClO_4)_2$ and [**C3**]$(BF_4)_2$

Identification code	**[C3]$(ClO_4)_2$**	**[C3]$(BF_4)_2$**
Empirical formula	$C_{60}H_{54}Cl_2FeN_{16}O_8$	$C_{60}H_{54}B_2F_8FeN_{16}$
Formula weight	1253.94	1228.66
Temperature/K	99.96(10)	100.0(3)
Crystal system	trigonal	trigonal
Space group	R-3c	R-3c
a/Å	14.7047(2)	14.55050(10)
b/Å	14.7047(2)	14.55050(10)
c/Å	99.8911(10)	100.1119(5)
α/°	90	90
β/°	90	90
γ/°	120	120
Volume/Å^3	18705.5(5)	18355.7(3)
Z	12	12
ρ_{calc}g/cm^3	1.336	1.334
μ/mm^{-1}	3.279	2.632
F(000)	7800.0	7608.0
Crystal size/mm^3	0.1 × 0.1 × 0.1	0.1 × 0.1 × 0.1
Radiation	Cu Kα (λ = 1.54184)	Cu Kα (λ = 1.54184)
2Θ range for data collection/°	5.308 to 152.36	5.296 to 152.424
Index ranges	-15 ≤ h ≤ 17, -18 ≤ k ≤ 12, -122 ≤ l ≤ 123	-18 ≤ h ≤ 18, -17 ≤ k ≤ 17, -126 ≤ l ≤ 123
Reflections collected	41454	40183
Independent reflections	4330 [R_{int} = 0.0385, R_{sigma} = 0.0221]	4239 [R_{int} = 0.0234, R_{sigma} = 0.0133]
Data/restraints/parameters	4330/110/318	4239/0/271
Goodness-of-fit on F^2	1.611	1.077
Final R indexes [I>=2σ (I)]	R_1 = 0.1052, wR_2 = 0.3256	R_1 = 0.0808, wR_2 = 0.2593
Final R indexes [all data]	R_1 = 0.1108, wR_2 = 0.3372	R_1 = 0.0819, wR_2 = 0.2606
Largest diff. peak/hole / e Å^{-3}	2.20/-2.21	1.36/-0.86

Table S3. Crystallographic information for [**C3**](OTf)$_2$ and [**C3**](NTf$_2$)$_2$.

Identification code	**[C3](OTf)$_2$**	**[C3](NTf$_2$)$_2$**
Empirical formula	$C_{62}H_{54}F_6FeN_{16}O_6S_2$	$C_{65.86}H_{56.79}F_{12}FeN_{18.93}O_8S_4$
Formula weight	1353.18	1653.52
Temperature/K	99.9(4)	100
Crystal system	trigonal	trigonal
Space group	R-3c	P-1
a/Å	15.2040(8)	12.5031(2)
b/Å	15.2040(8)	15.5665(3)
c/Å	100.275(2)	19.8576(4)
α/°	90	80.413(2)
β/°	90	72.158(2)
γ/°	120	77.821(2)
Volume/Å^3	20074(2)	3574.56(13)
Z	12	2
ρ_{calc}g/cm^3	1.343	1.536
μ/mm^{-1}	3.056	0.396
F(000)	8376.0	1693.0
Crystal size/mm^3	0.15 × 0.15 × 0.03	0.05 × 0.03 × 0.01
Radiation	Cu Kα (λ = 1.54184)	Synchrotron (λ = 0.6889)
2Θ range for data collection/°	5.288 to 153.252	3.366 to 72.534
Index ranges	-19 ≤ h ≤ 19, -17 ≤ k ≤ 18, -125 ≤ l ≤ 124	-20 ≤ h ≤ 21, -26 ≤ k ≤ 26, -33 ≤ l ≤ 33
Reflections collected	45638	77550
Independent reflections	4685 [R_{int} = 0.0350, R_{sigma} = 0.0170]	32879 [R_{int} = 0.0387, R_{sigma} = 0.0411]
Data/restraints/parameters	4685/734/419	32879/724/1168
Goodness-of-fit on F^2	1.697	1.082
Final R indexes [I>=2σ (I)]	R_1 = 0.1322, wR_2 = 0.3989	R_1 = 0.0422, wR_2 = 0.1232
Final R indexes [all data]	R_1 = 0.1626, wR_2 = 0.4480	R_1 = 0.0492, wR_2 = 0.1277
Largest diff. peak/hole / e Å^{-3}	0.82/-0.48	0.78/-0.96

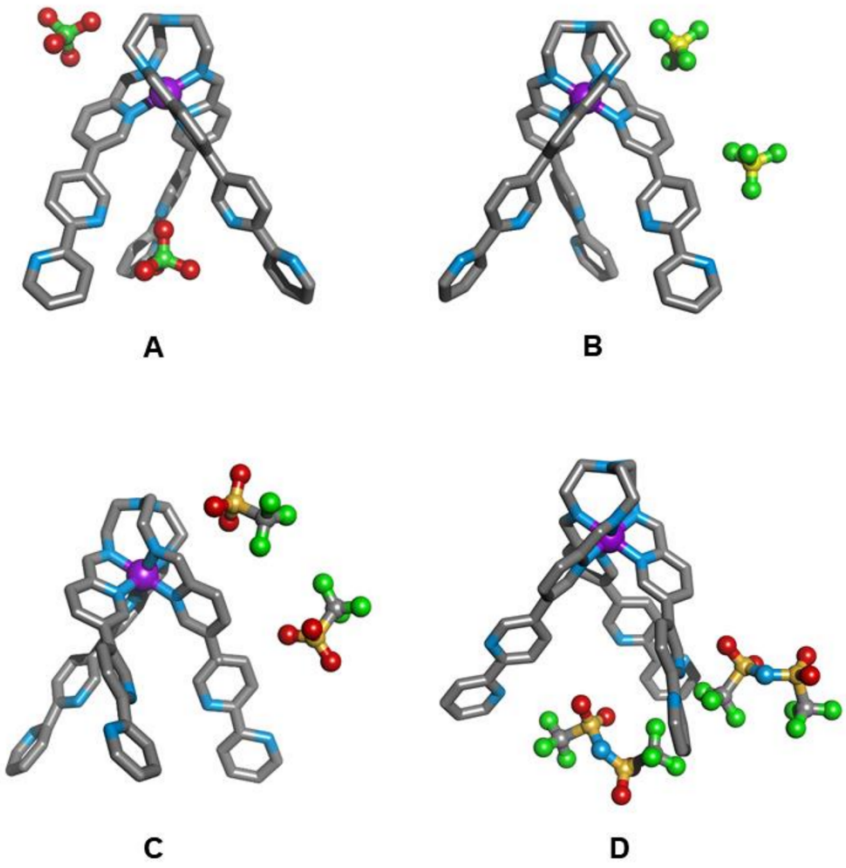

***Figure S25*. A:** Single-crystal X-ray structures of mononuclear iron species **A:** [**C3**]$(ClO_4)_2$, where one ClO_4^- counteranion sits on the three-fold rotation axis of the complex, confined between the three ligands, **B:** [**C3**]$(BF_4)_2$, where both BF_4 counterions sits on the periphery of the complex, **C**: [**C3**]$(OTf)_2$, where both counterions sit on the periphery of the complex, and **C**: [**C3**]$(NTf_2)_2$, where both counterions sit on the periphery of the complex.

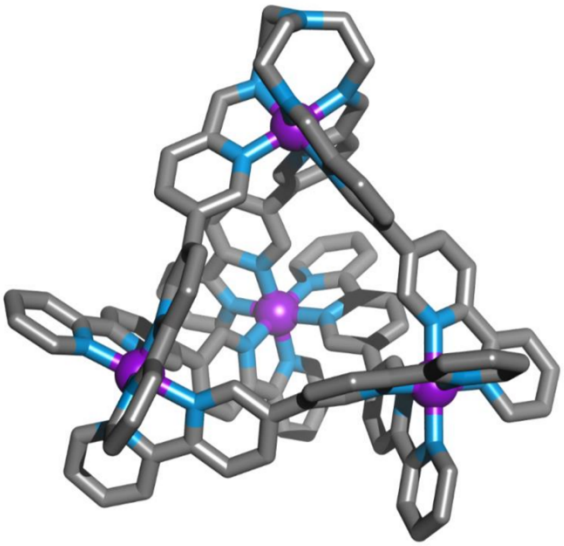

Figure S26. Single-crystal X-ray structures of heterotetrahedron [**C1**]$(ClO_4)_8$. Counterions and hydrogens were omitted for clarity.

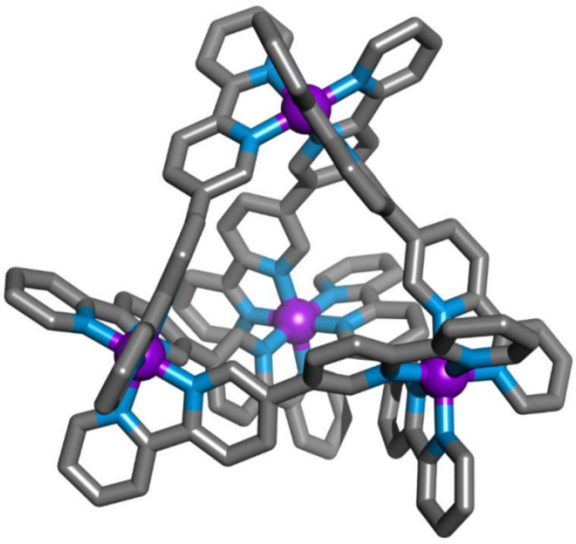

Figure S27. Single-crystal X-ray structures of homotetrahedron [**C2**]$(OTf)_8$. The central OTf^- counterion, additional counterions and hydrogens were omitted for clarity.

S3 VOIDOO Calculations

Following removal of counterions and solvent from the single crystal X-ray structures of complexes **C1** and **C2** cavity calculations were run using VOIDOO.[9,10] The volume of the internal binding pocket within each structure was calculated using a probe of radius 1.6 Å, this was the minimum probe radius that allowed detection of discrete void spaces. Calculations run with smaller probe radii (1.4 and 1.5 Å) allowed the probe to roll out of the cavity and map space external to the cage.

The following parameters were used in the calculation:

Primary grid spacing	0.1
Number of detection cycles	10
Growth factor van der Waals radii	1.1
Min size of real cavities	1
Number of refinement cycles	30
Grid shrink factor	0.9
Convergence criterion (Å^3)	0.1

Cavities were mapped as ccp4 files and visualised using Pymol v1.4.

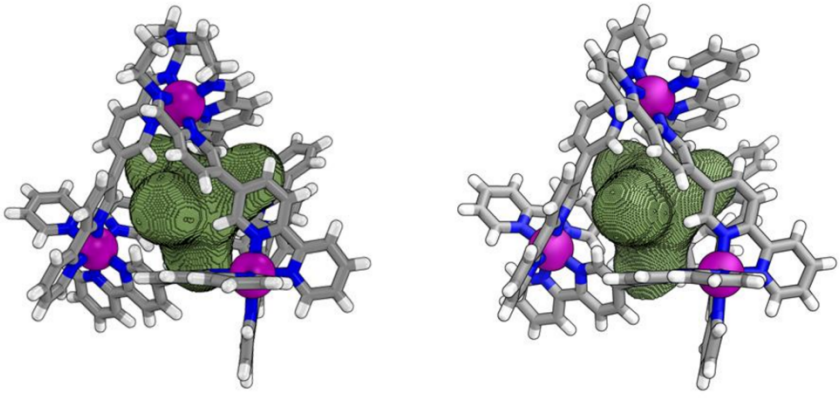

C1
Volume: 162 Å^3

C2
Volume: 161 Å^3

Figure S28. VOIDOO structures of heteroleptic tetrahedron **C1** and homoleptic tetrahedron **C2** with calculated cavity volumes of 162 Å^3 and 161 Å^3, respectively.

S4 References

1 B. Elias, S. Cerfontaine, L. Troian-Gautier, L. Troian-Gautier, S. A. M. Wehlin, F. Loiseau and E. Cauët, *Dalt. Trans.*, 2020, **49**, 8096–8106.

2 L. L. K. Taylor, I. J. Vitorica-Yrezabal, I. Borilovic, F. Tuna and I. A. Riddell, *Chem. Commun.*

3 H. Nowell, S. A. Barnett, K. E. Christensen, S. J. Teat and D. R. Allan, *J. Synchrotron Radiat.*, 2012, **19**, 435–441.

4 G. M. Sheldrick, SADABS.

5 R. H. Blessing, *Acta Crystallogr. Sect. A*, 1995, **51**, 33–38.

6 L. Krause, R. Herbst-Irmer, G. M. Sheldrick and D. Stalke, *J. Appl. Crystallogr.*, 2015, **48**, 3–10.

7 G. M. Sheldrick, *Acta Crystallogr. Sect. C Struct. Chem.*, 2015, **71**, 3–8.

8 O. V. Dolomanov, L. J. Bourhis, R. J. Gildea, J. A. K. Howard and H. Puschmann, *J. Appl. Crystallogr.*, 2009, **42**, 339–341.

9 G. J. Kleywegt and T. A. Jones, *Acta Crystallogr. D. Biol. Crystallogr.*, 1994, **50**, 178–185.

10 Y. R. Hristova, M. M. J. Smulders, J. K. Clegg, B. Breiner and J. R. Nitschke, *Chem. Sci.*, 2011, **2**, 638-641.

11. Miscellaneous Complexes

The following work was carried out by LLKT, including all syntheses and characterisation. All complexes are either fully or partially characterised.

11.1. General Methods

Unless stated otherwise, all chemicals were supplied from Sigma-Aldrich, Fluorochem, Fisher Scientific, Alfa Aesar or Scientific Laboratory Supplies Ltd and used without further purification. Deuterated NMR solvents were supplied from Sigma-Aldrich and NMR spectra were recorded on a B500 Bruker Advance II+ 500 MHz spectrometer or a B400 Bruker AVIII 400**.** Chemical shifts are reported in parts per million (ppm). Coupling constants (*J*) are reported in hertz (Hz). Standard abbreviations indicating multiplicity were used as follows: s = singlet, d = doublet, t = triplet, dd = doublet of doublets, td = triplet of doublets m = multiplet. ^{1}H assignments were made using 2D NMR methods (COSY, NOESY). High resolution mass spectra were obtained using a Thermo Orbitrap Exactive Plus Extended Mass Range mass spectrometer. X-ray data were processed and reduced using CrysAlisPro.[1] Absorption correction was performed using empirical methods (SCALE3 ABSPACK) based upon symmetry-equivalent reflections combined with measurements at different azimuthal angles. The crystal structure was solved and refined against all F^2 values using the SHELX and Olex2 suite of programmes.[2–4] All atoms were refined anisotropically. Hydrogen atoms were placed in calculated positions and refined using idealised geometries and assigned fixed isotropic displacement parameters.

11.2. Fluoride Bridged Analogues

Chapter two reports the formation of a mixed spin-state trigonal bipyramidal complex with ligand **L**[1], TREN and iron(II) tetrafluoroborate. The following results are attempts to synthesize analogous fluoride-bridged structures with alternative triamine molecules. Two triamine molecules were investigated in place of TREN: carbon based triamine 1,1,1-tris(aminoethyl)ethane (TAME) and nitrogen based tris(3-aminopropyl)amine (TRPN).

11.2.1. Synthesis of $[Fe_6F_6L_6(TAME)_2](BF_4)_7$

To the best of our knowledge, the largest self-assembled complexes containing TAME are simple mononuclear species formed with a variety of metals.[5,6] We hypothesised that the reduced size of TAME compared with TREN could alter the coordination angles around the iron(II) in the *tris*pyridylimine binding site, causing distortion of the resulting trigonal bipyramidal structure, or even formation of an alternative architecture. Formation of a TAME-incorporated multimetallic trigonal bipyramidal cage would be the first of its kind containing the triamine, and distortion of the cage could bring the metals closer in space, potentially increasing the F-mediated antiferromagnetic exchange between the peripheral high-spin Fe(II) ions and the central Fe(III) ion.

The route followed was analogous to that of the $[Fe_6F_6L_6(TREN)_2](BF_4)_7$ (**38**) synthesis (scheme 1), but was carried out in a 1:1 acetonitrile:methanol mixture due to the solubility of the TAME hydrochloride salt. The reaction was a one-pot self-assembly reaction and a dark blue solid was isolated in a 15% yield. No crystals suitable for X-ray diffraction were grown and the complex was characterised by ^{1}H NMR and mass spectroscopy.

The corresponding ^{1}H NMR spectrum was paramagnetic in nature with peaks as high as 70.04 ppm (figure 1). The paramagnetic region was similar to that of $[Fe_6F_6L_6(TREN)_2](BF_4)_7$, with three singlets between 23 – 71 ppm. The mass spectrum supported the formation of a singular fluoride bridged complex containing TAME in solution, with the +2 to +7 peaks being clearly resolved.

Scheme 1. Subcomponent self-assembly of $\mathbf{L}^1$, TAME and iron(II) tetrafluoroborate to generate fluoride bridged complex **38**.

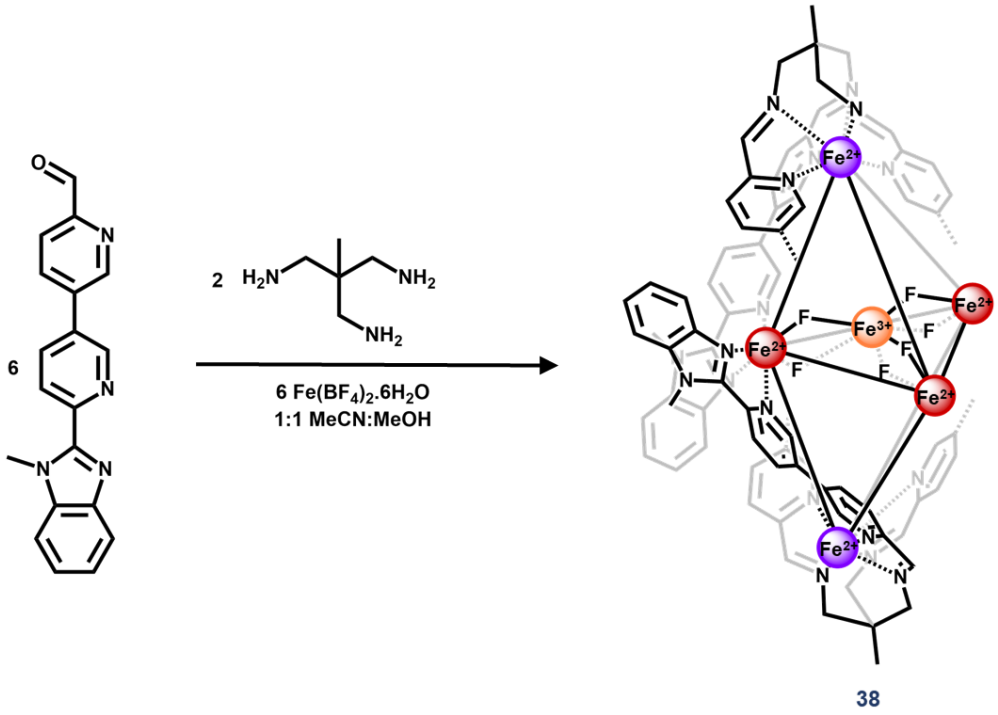

Experimental data

Ligand $\mathbf{L}^1$ (15.1 mg, 94.78 μmol, 6 equiv), $Fe(BF_4)_2.6H_2O$ (16.2 mg, 47.9 μmol, 6 equiv) and TAME (3.6 mg, 30.8 μmol, 2 equiv) were dissolved in a 1:1 acetonitrile:methanol mixture (3 mL) giving a blue solution. This was heated (50°C, 24 hr) and the blue solution was layered with diethyl ether. The resulting blue precipitate was filtered and washed with chloroform to give a dark blue crystalline solid (11.4 mg, 4.63 μmol, 15%). [Accurate mass, *m/z*]: $\{Fe_6\mathbf{L}^1{}_6F_6(TAME)_2\}^{7+}$ = 351.6434 $\{Fe_6\mathbf{L}_6F_6(TAME)_2(BF_4)\}^{6+}$ = 424.7514, $\{Fe_6\mathbf{L}_6F_6(TAME)_2(BF_4)_2\}^{5+}$ = 527.1027, $\{Fe_6\mathbf{L}_6F_6(TAME)_2(BF_4)_3\}^{4+}$ = 680.3794, $\{Fe_6\mathbf{L}_6F_6(TAME)_2(BF_4)_4\}^{3+}$ = 936.1734, $\{Fe_6\mathbf{L}_6F_6(TAME)_2(BF_4)_5\}^{2+}$ = 1447.7629.

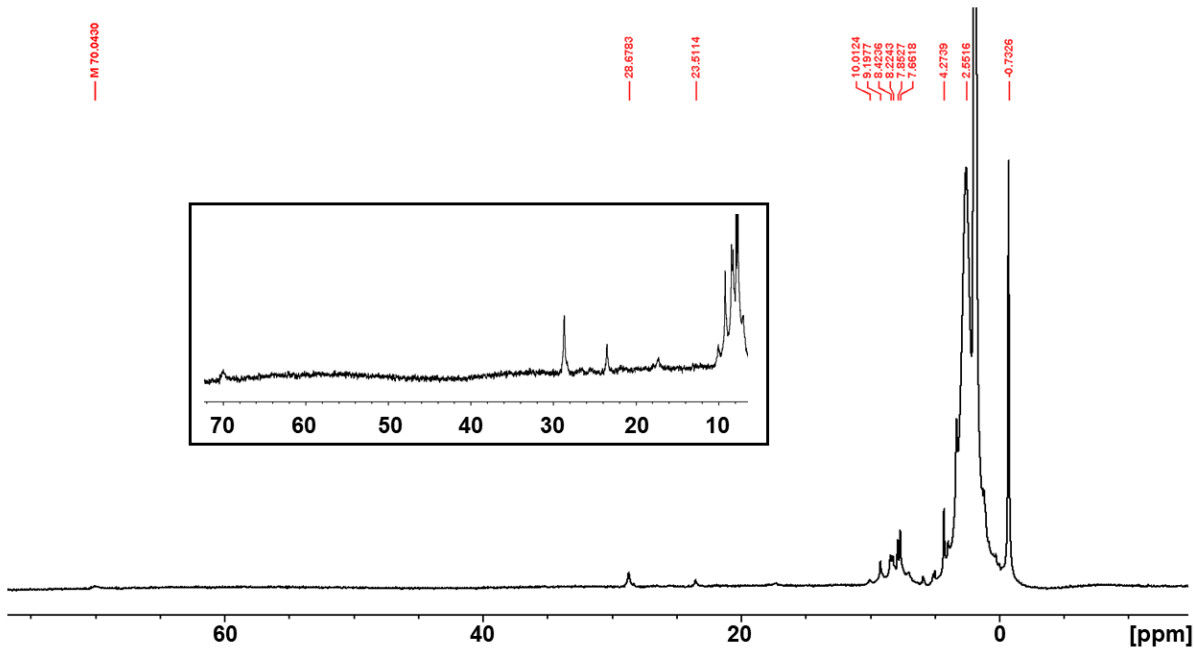

Figure 1. ^{1}H NMR (500 MHz, 1:1 CD_3CN:MeOD, 298 K) spectrum of complex **38**. Insert highlights the region between 5 – 75 ppm.

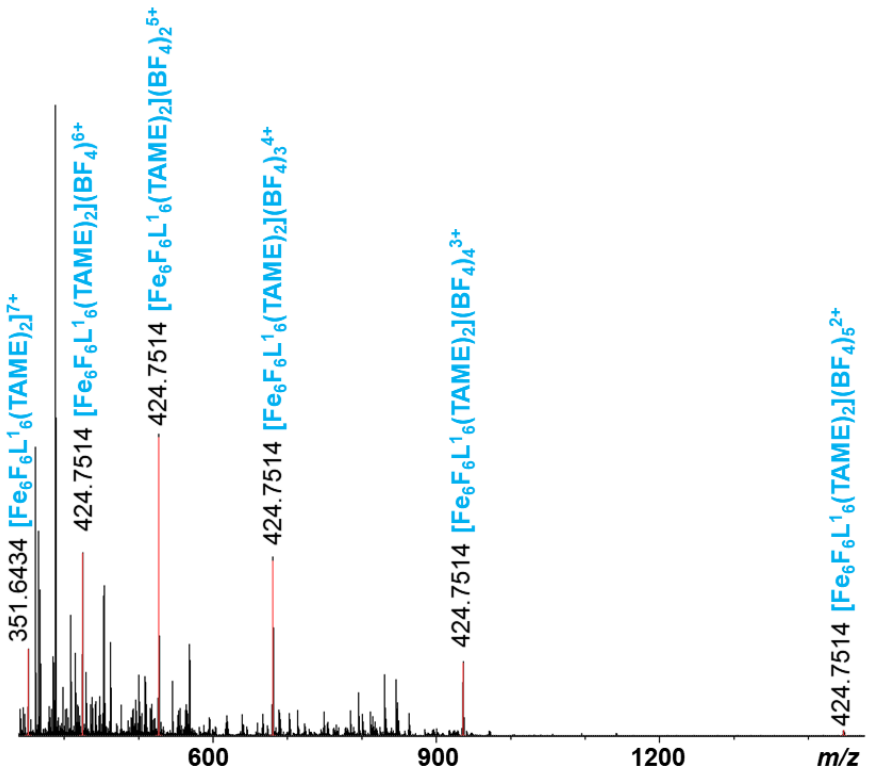

Figure 2. High-resolution mass spectrum for a 1:1 acetonitrile:methanol solution of $[Fe_6F_6\mathbf{L^1}_6(TAME)_2]^{7+}$. Isotopic patterns corresponding to complex **38** are represented by red lines.

11.2.2. Attempted Synthesis of $[Fe_6F_6L_6(TRPN)_2](BF_4)_7$

Self-assembled systems containing *bis*bidentate ligands have previously been shown to form larger structures with TRPN compared with TREN in the presence of d^{10} metal ions.[7] We theorised that in the presence of TRPN, our system could form a larger, more flexible fluoride-bridged species in the presence of iron(II). The route followed was analogous to that of the $[Fe_6F_6L_6(TREN)_2](BF_4)_7$ synthesis (scheme 3). The reaction was a one-pot self-assembly reaction carried out on an NMR scale which yielded a purple solution. No crystals suitable for X-ray diffraction were grown and the resulting complex was characterised by ^{1}H NMR and mass spectroscopy.

The corresponding ^{1}H NMR spectrum showed a broad set of peaks between 0.6 – 9.7 ppm and was indicative of a diamagnetic complex (figure 2). The system was inherently insoluble, suggesting the formation of a polymeric system, and began to precipitate out of solution after a period of 24 hours. The mass spectrum showed no evidence of complexation beyond the formation of a mononuclear $[Fe\mathbf{L^1}_3(TRPN)]^{2+}$ architecture.

Scheme 2. Subcomponent self-assembly of $\mathbf{L^1}$, TRPN and iron(II) tetrafluoroborate to generate an intractable mixture.

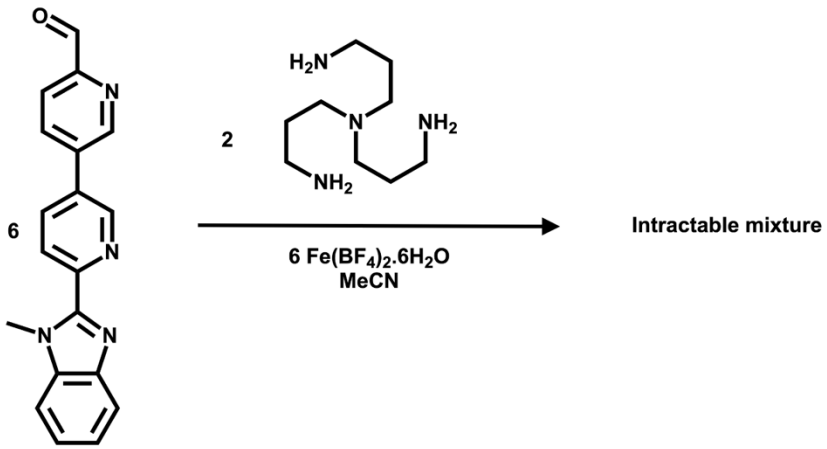

Experimental data

Ligand $\mathbf{L^1}$ (2.5 mg, 7.96 μmol, 6 equiv), $Fe(BF_4)_2.6H_2O$ (2.8 mg, 8.29 μmol, 6 equiv) and TRPN (0.53 μL, 2.73 μmol, 2 equiv) were dissolved in deuterated acetonitrile (0.35 mL) and the resulting purple solution was added to a J-Young tube. The tube was sealed, and the solution was degassed by three vacuum/N_2 fill cycles before being heated (50°C, 24 hr). [Accurate mass, *m/z*]: $\{Fe\mathbf{L^1}_3(TRPN)\}^{2+}$ = 566.2328.

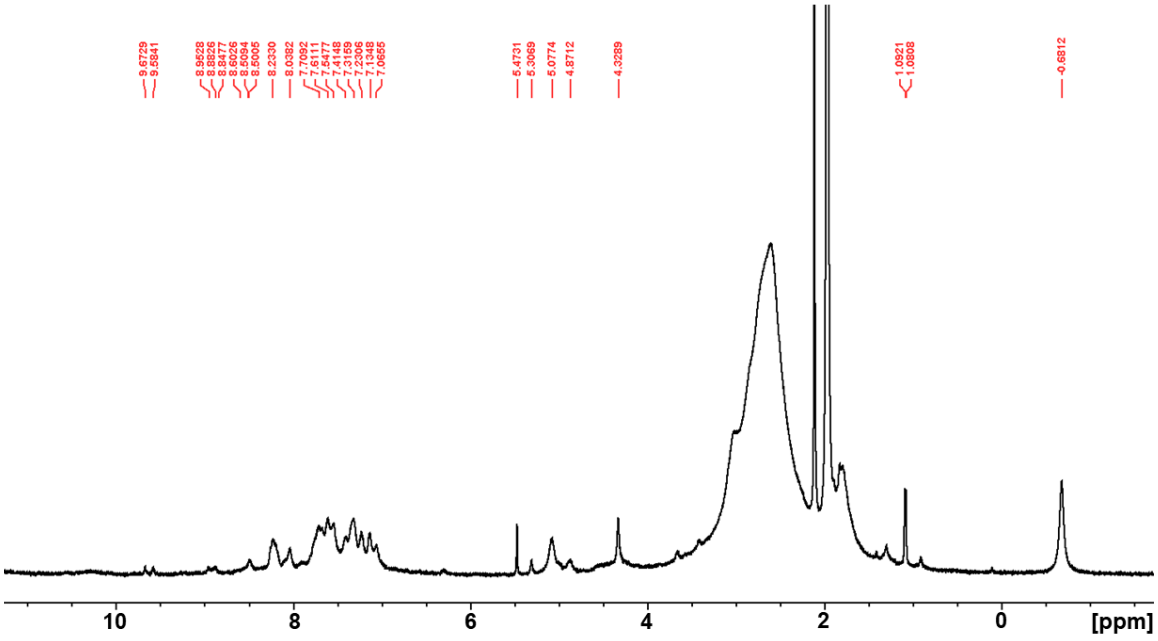

Figure 3. ^{1}H NMR (500 MHz, CD_3CN, 298 K) spectrum of a mixture containing **L^{1}**, TRPN and iron(II) tetrafluoroborate.

11.3. Additional Complexes with Ligand 1 (**L^{1}**)

The following complexes were the result of initial reactions with **L^{1}**, TREN and varying metal salts. It was hypothesised that **L^{1}** would be capable of forming cubic $[M_6L_{12}T_4]^{12+}$ complexes in the presence of TREN and appropriate metal ions. The formation of smaller self-assembled architectures proved to be more favourable in solution compared with a larger cubic structure, an outcome often seen in supramolecular self-assembled systems.[8]

11.3.1. Complexation with Zinc(II)

The attempted synthesis of a zinc(II) cubic structure resulted in the formation of a smaller $[Zn_4L_6T_2]^{8+}$ complex (**39**). This architecture was then purposefully formed by reacting four equivalents of zinc(II) perchlorate with six equivalents of ligand **L^{1}** and two equivalents of TREN in acetonitrile at 60ºC (scheme 3). The ^{1}H NMR spectrum of the yellow solution showed complete consumption of the aldehyde peak of the ligand (10.01 ppm) and formation of a new imine peak (8.76 ppm) indicating successful imine formation. The spectrum was indicative of a single symmetric species in solution and the mass spectrum reflected this finding. No crystals suitable for X-ray diffraction were grown for the complex.

Scheme 3. Subcomponent self-assembly of $\mathbf{L^1}$, TREN and zinc(II) perchlorate to generate proposed complex **39**.

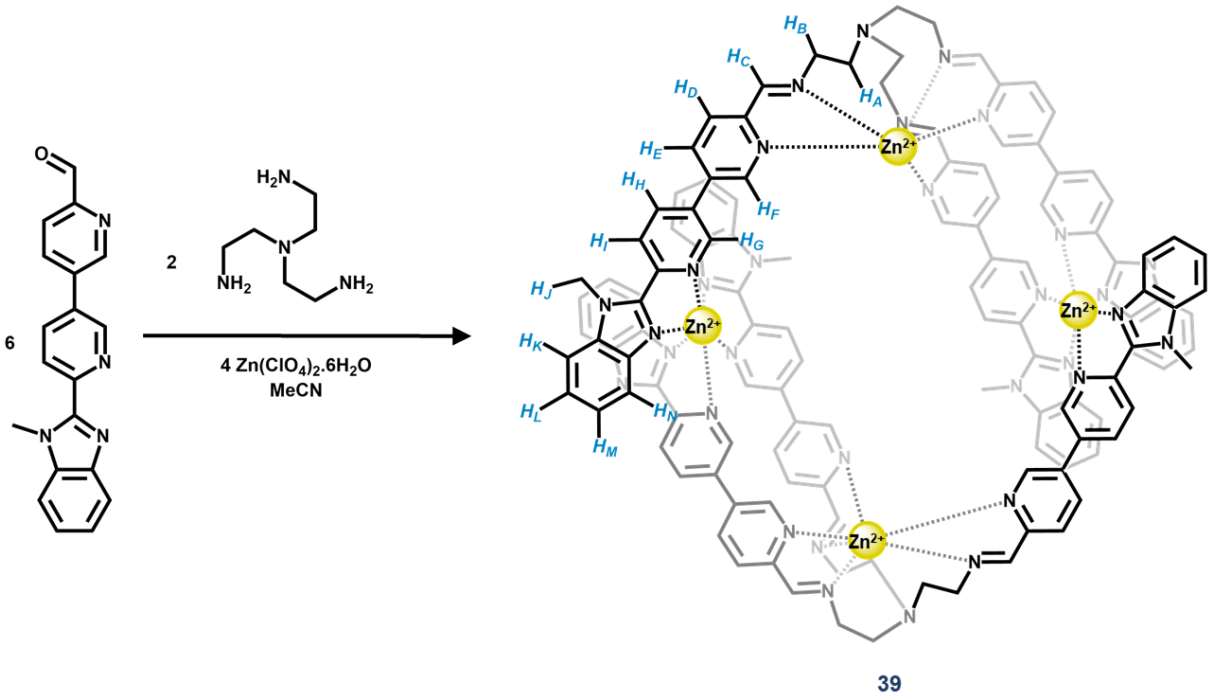

Experimental data

Ligand $\mathbf{L^1}$ (19.8 mg, 63.06 μmol, 6 equiv), $Zn(ClO_4)_2.6H_2O$ (15.7 mg, 42.16 μmol, 4 equiv) and TREN (3.14 μL, 21.45 μmol, 2 equiv) were dissolved in acetonitrile (0.35 mL) giving a yellow solution. This was heated (50°C, 24 hr) and the yellow solution was layered with diethyl ether. The resulting yellow precipitate was filtered and washed with chloroform to give a pale yellow solid (15.6 mg, 6.71 μmol, 31%). ^{1}H (500 MHz, 298 K, CD_3CN): δ = 8.76 (s, 1H, H_C), 8.46 (d, 1H, H_N, J = 8.32 Hz), 8.22 (dd, 2H, H_I, H_H, J = 8.11, 2.06 Hz), 8.03 (d, 1H, H_D, J = 7.85 Hz), 7.74 (d, 1H, H_K, J = 8.46 Hz), 7.45 (t, 2H, H_M, J = 8.28 Hz), 7.25 (s, 1H, H_G), 7.02 (t, 1H, H_L, J = 7.35 Hz), 6.69 (dd, 2H, H_E, H_F, J = 5.08, 1.22 Hz), 4.19 (s, 3H, H_J), 3.94 (t, 1H, H_B, J = 11.60 Hz), 3.67 (dd, 1H, H_B, J = 12.01, 3.35 Hz), 3.20 (dd, 1H, H_A, J = 13.60, 3.62 Hz), 2.98 (td, 1H, H_A, J = 20.33, 3.72 Hz). [Accurate mass, *m/z*]: $\{Zn_4\mathbf{L^1}_6T_2\}^{8+}$ = 291.5807, $\{Zn_4\mathbf{L^1}_6T_2(BF_4)\}^{7+}$ = 348.0623, $\{Zn_4\mathbf{L^1}_6T_2(BF_4)_2\}^{6+}$ = 421.7573, $\{Zn_4\mathbf{L^1}_6T_2(BF_4)_3\}^{5+}$ = 525.0804, $\{Zn_4\mathbf{L^1}_6T_2(BF_4)_4\}^{4+}$ = 682.1102, $\{Zn_4\mathbf{L^1}_6T_2(BF_4)_5\}^{3+}$ = 943.1300, $\{Zn_4\mathbf{L^1}_6T_2(BF_4)_6\}^{8+}$ = 1464.1701.

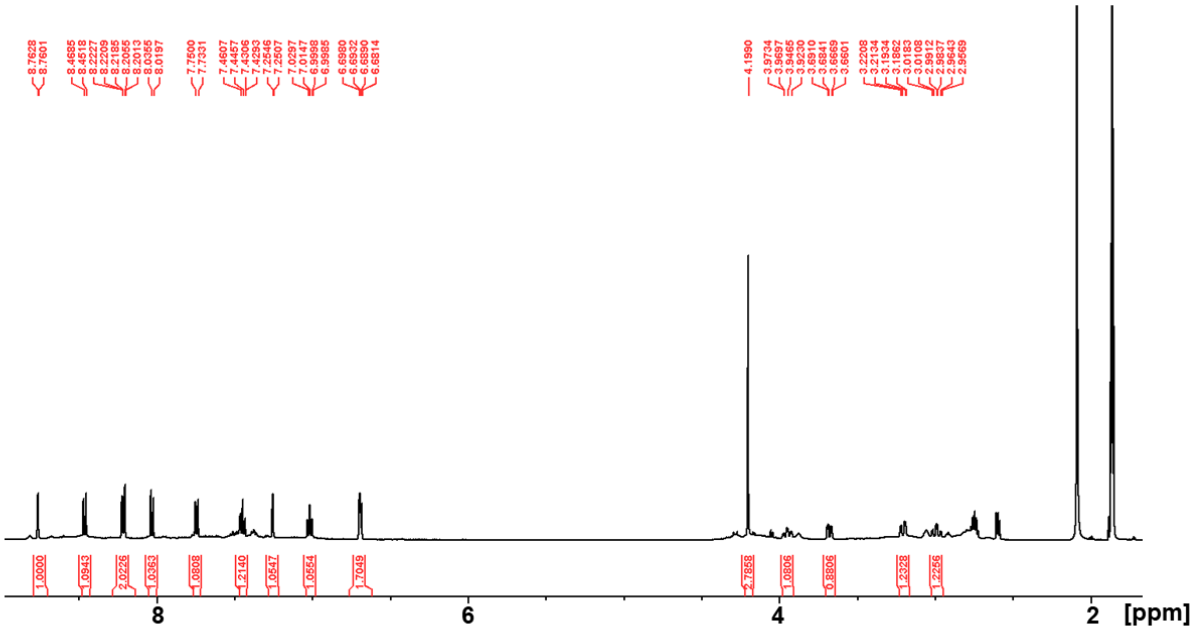

Figure 4. ^{1}H NMR (500 MHz, CD_3CN, 298 K) spectrum of complex **39**.

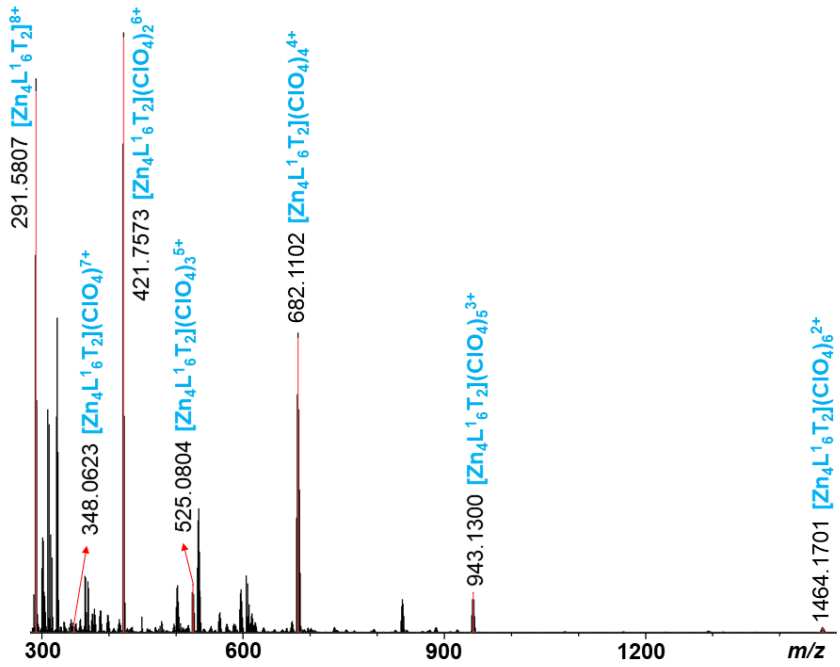

Figure 5. High-resolution mass spectrum for an acetonitrile solution of complex **39**. Isotopic patterns corresponding to **39** are represented by red lines.

11.3.2. Complexation with Cadmium(II)

Cadmium(II) has a larger ionic radius than zinc(II)[9] and it was theorised that in the presence of Cd(II) the formation of a cubic architecture would be more feasible due to the alleviation of any potential strain that could be present at the vertices of the structure. The attempted synthesis of a $[Cd_6\mathbf{L^1}_{12}T_4]^{12+}$ cubic assembly resulted in the formation of a dinuclear $[Cd_2\mathbf{L^1}_3T]^{4+}$ helicate (scheme 4, **40**). The increased ionic radius of cadmium(II) allows the $\mathbf{L^1}_3T$ moiety to favourably wrap around two metal cations, forming an entropically favourable helical structure in solution. Single crystals of **40** were grown through diffusion of diethyl ether into an acetonitrile solution containing the complex.

The ^{1}H NMR spectrum was indicative of a single symmetric species in solution with evidence of imine peak formation at 8.73 ppm following complexation of cadmium(II) within the *tris*pyridylimine site.

Compared with iron(II), cadmium(II)-nitrogen bond lengths are relatively long (1.968 Å and 2.366 Å respectively).[10,11] Mass spectral evidence for **40** demonstrated a high degree of fragmentation and we postulate the longer Cd-N bonds decrease the stability of the overall structure.

Scheme 4. Subcomponent self-assembly of $\mathbf{L^1}$, TREN and cadmium(II) perchlorate to generate helicate **40**.

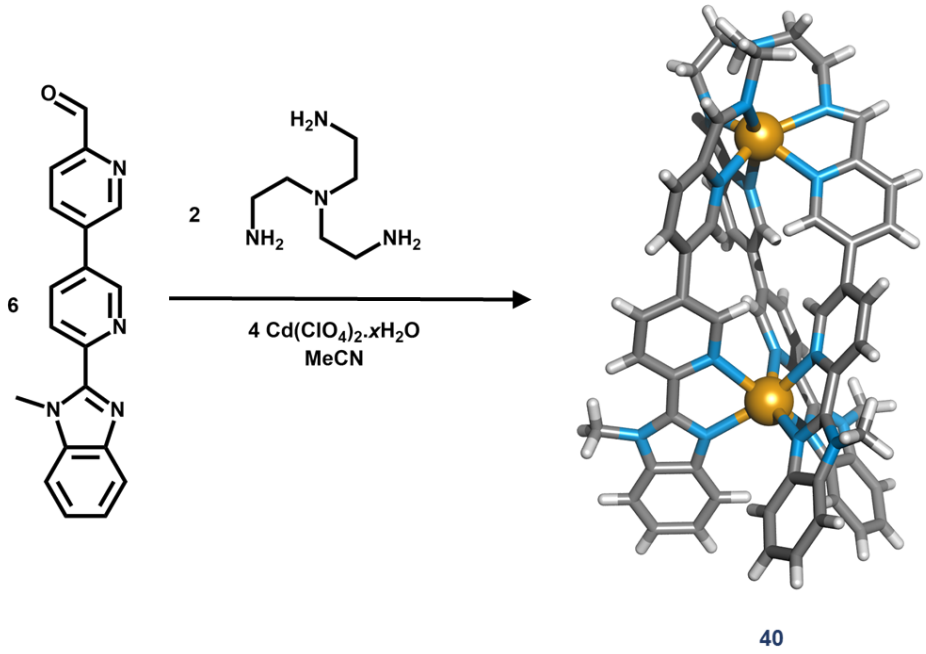

40

Experimental data

Ligand **L**[1] (5.3 mg, 16.88 μmol, 3 equiv), $Cd(ClO_4)_2.xH_2O$ (3.5 mg, 11.24 μmol, 2 equiv) and TREN (0.82 μL, 5.63 μmol, 2 equiv) were dissolved in deuterated acetonitrile (0.35 mL) and the resulting orange solution was added to a J-Young NMR tube. The tube was sealed, and the solution was degassed by three vacuum/N_2 fill cycles before being heated (50°C, 24 hr). *NMR assignment is based on the labels in scheme 3.* ^{1}H (400 MHz, 298 K, CD_3CN): δ = 8.94 (s, 1H, H_F), 8.73 (s, 1H, H_C), 8.46 (d, 1H, H_G, J = 7.08 Hz), 8.38 (d, 1H, H_H, J = 7.72 Hz), 8.18 (d, 1H, H_E, J = 5.40 Hz), 7.90 (d, 1H, H_I, J = 7.24 Hz), 7.72 (broad singlet, 1H, H_D), 7.62 (d, 2H, H_N, H_K, J = 7.28 Hz), 7.44 (t, 1H, H_M, J = 7.30 Hz), 7.39 (t, 1H, H_L, J = 7.10 Hz), 4.14 (s, 3H, H_J).

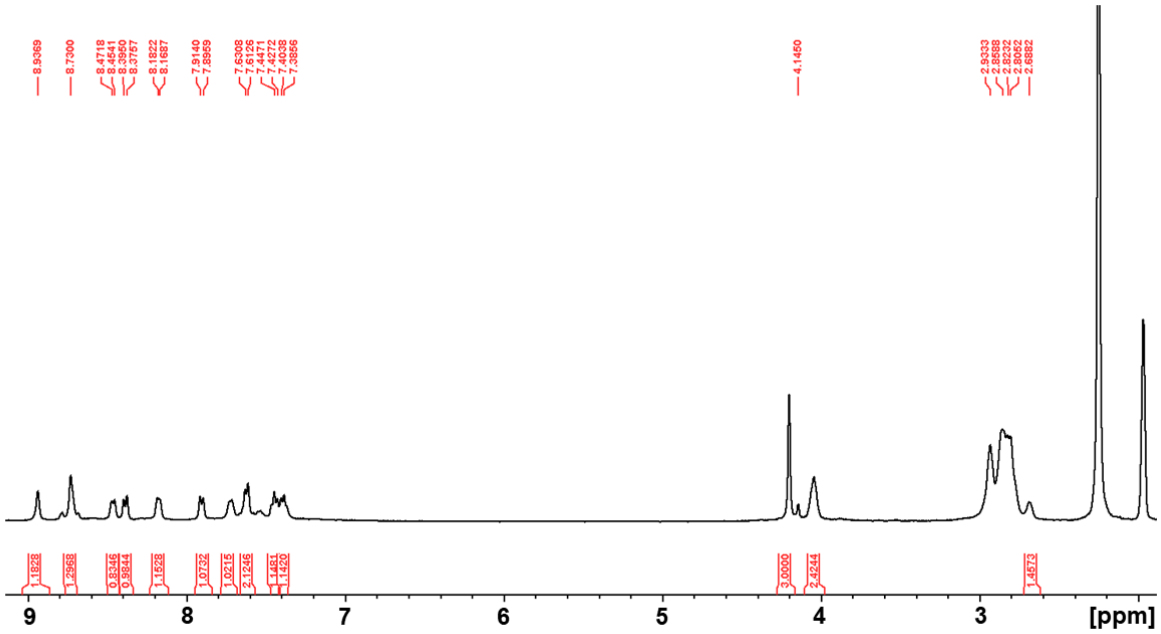

Figure 6. ^{1}H NMR (400 MHz, CD_3CN, 298 K) spectrum of complex **40**.

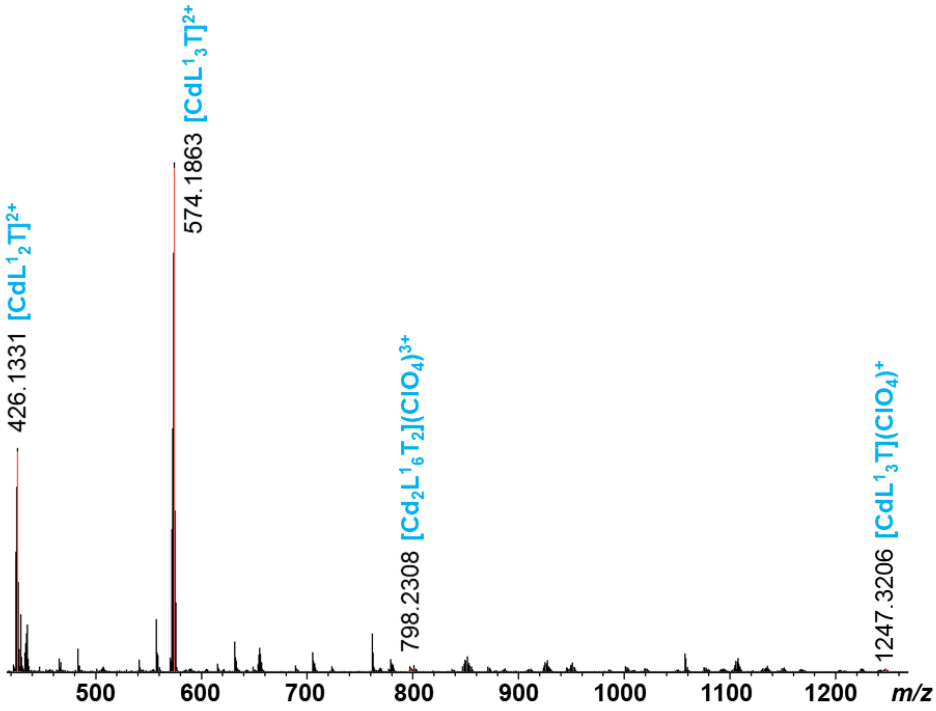

Figure 7. High-resolution mass spectrum for an acetonitrile solution containing $\mathbf{L^1}$, TREN and cadmium(II) perchlorate. Isotopic patterns corresponding to complexes are represented by red lines.

11.3.3. Formation of a Mixed-Ligand Tetrahedron Containing $\mathbf{L^1}$

The formation of ligand $\mathbf{L^1}$ is achieved through a five step synthetic route which includes two Suzuki coupling reactions. The reaction conditions in scheme 5 facilitated an Ullmann-type cross coupling reaction resulting in the formation of *bis*benzimidazole molecule 6,6'-bis(1-methyl-1H-benzo[d]imidazol-2-yl)-3,3'-bipyridine ($\mathbf{L^2}$) in an amount too small to be quantified by NMR or mass spectrometry.

Scheme 5. Suzuki coupling reaction of 2-(dimethoxymethyl)-5-(4,4,5,5-tetramethyl-1,3,2-dioxaborolan-2-yl)pyridine and 2-(5-bromopyridin-2-yl)-1-methyl-1H-benzo[d]imidazole, forming the protected version of $\mathbf{L^1}$ as the major product, and $\mathbf{L^2}$ as the minor product.

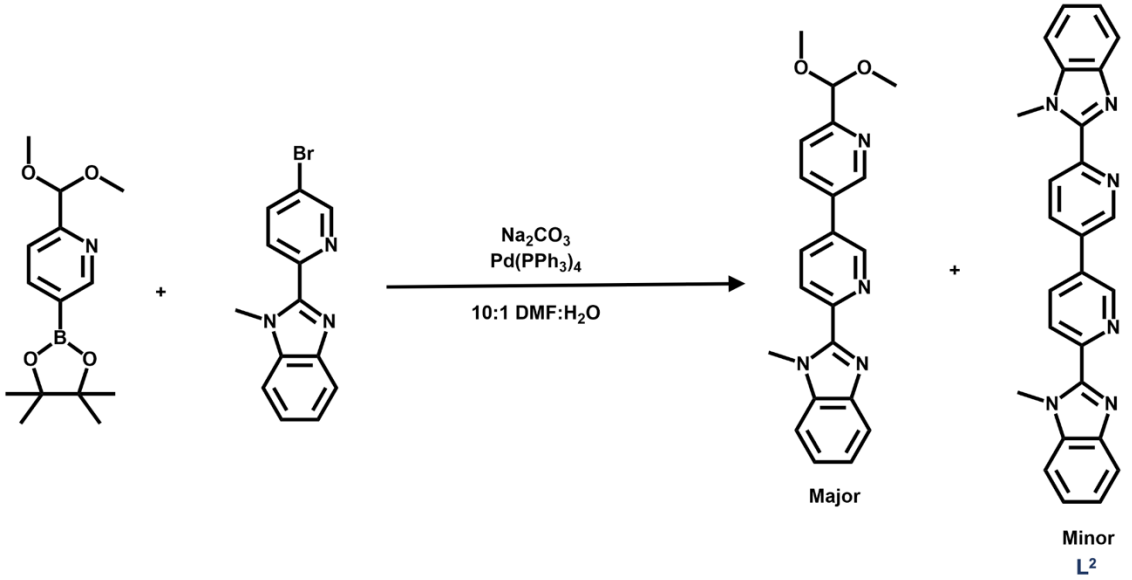

Without further purification, the major product in scheme 5 was deprotected and reacted with TREN in the presence of $Fe(BF_4)_2$ to form the fluoride-bridged complex described in chapter two. One batch of crystals grown from a solution containing this reaction mixture were identified as a mixed-ligand tetrahedron containing both $\mathbf{L^1}$ and the *bis*benzimidazole ligand $\mathbf{L^2}$ (scheme 6). Similar to the mixed-ligand tetrahedron reported in chapter four, the structure contained four equivalents of iron(II) bound by three equivalents of each ligand, and incorporated one TREN molecule. Ligands similar to $\mathbf{L^2}$ have previously been synthesized and used in combination with ruthenium(II) to form dinuclear complexes capable of catalysing the reduction of CO_2.[12]

Scheme 6. Subcomponent self-assembly of $\mathbf{L^1}$, $\mathbf{L^2}$, TREN and iron(II) tetrafluoroborate to generate tetrahedral architecture $[Fe_4\mathbf{L^1}_3\mathbf{L^2}_3T_2]^{8+}$ (**41**).

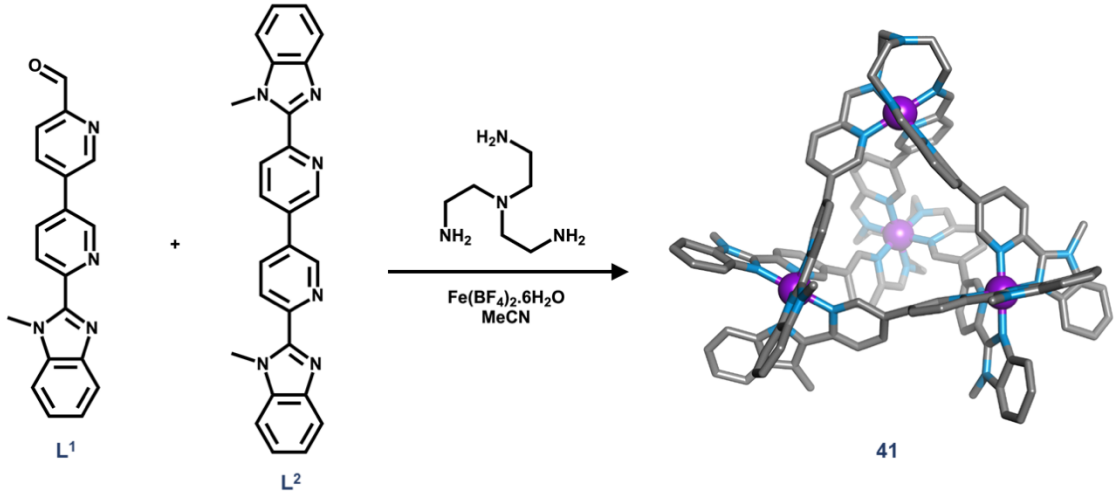

The tetrahedral architecture contains three equivalents of each ligand, $\mathbf{L^1}$ and $\mathbf{L^2}$, as well as four Fe(II) centres at the vertices and two TREN molecules. Two of the iron centres are bound in a *tris*pyridylimine binding site and two are bound by three benzimidazole motifs. The bond valence sum analysis carried out in chapter two (ESI) was used here to characterise all four metal centres in this mixed-tetrahedron as low-spin iron(II).

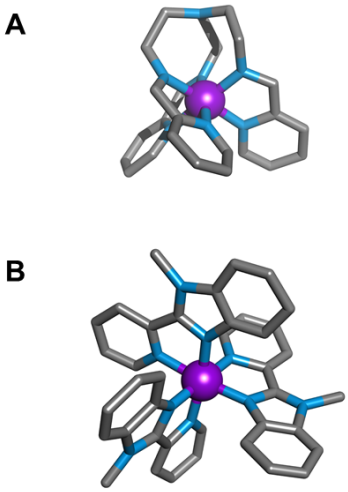

Figure 8. The two binding sites identified in this mixed-ligand tetrahedron are A: the *tris*pyridylimine binding site and B: the *tris*benzimidazole binding site, both of which bind iron(II) in the low-spin state in this complex. Figures were obtained from the single-crystal X-ray structure where purple: low-spin iron(II); blue: nitrogen; grey: carbon, and the extended ligand structure was omitted for clarity.

The direct formation of ligand $\mathbf{L^2}$ and subsequently the self-assembly of **41** could allow the self-sorting phenomenon described in chapter four to be explored more extensively.

11.4. Introductory Self-Assembly Reactions

A number of commercial diamino ligands were investigated early in the project to determine if interesting or useful species could be self-assembled. Ligand $\mathbf{L^3}$ is a dianiline molecule containing a flexible ethyl spacer between two phenyl rings (scheme 7). This ligand has previously been shown to form metal-organic frameworks in the presence of 2-pyridine carboxaldehyde (PyA) and zinc(II) nitrate.[13,14] The incorporation of ligands containing aliphatic linkers is rare in the formation of discrete architectures, as systems frequently contain highly conjugated ligands with rigidity.

Structurally similar ligands with more rigid spacers have been shown to form discrete tetrahedral architectures with iron(II) tetrafluoroborate in acetonitrile,[15] but these structures showed no evidence of anion encapsulation. Subcomponent self-assembly reactions with ligand $\mathbf{L^3}$, 2-pyridine carboxaldehyde and iron(II) tetrafluoroborate were investigated and the subsequent tetrahedron formed was shown to bind a hexafluoroantimonate anion in the solid state.

Scheme 7. Subcomponent self-assembly of $\mathbf{L^3}$, 2-pyridine carboxaldehyde and iron(II) tetrafluoroborate to generate tetrahedral complex $[Fe_4\mathbf{L^3}_6(PyA)_{12}]^{8+}$ (**42**). The addition of sodium hexafluoroantimonate (1 equiv) resulted in the encapsulation of an SbF_6^- anion within the central cavity of the architecture.

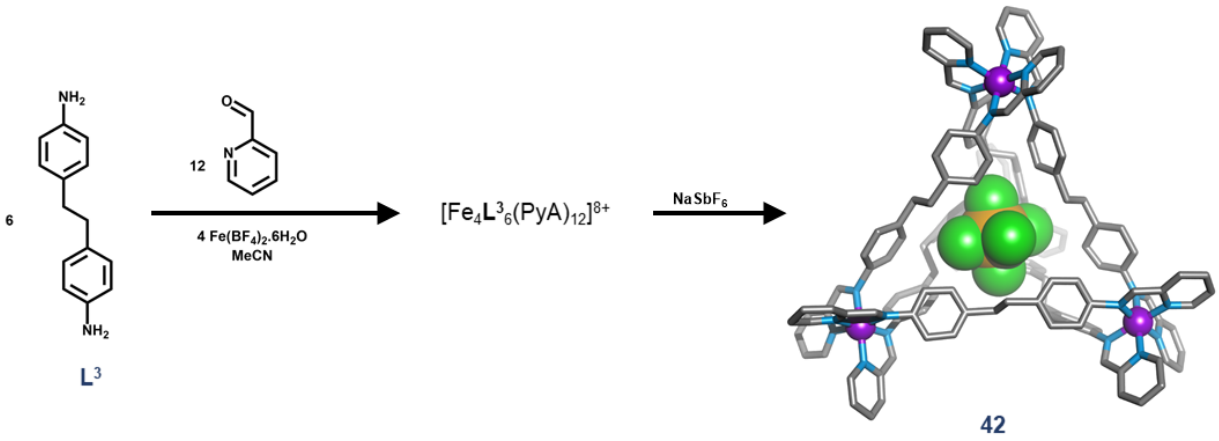

The ^{1}H NMR spectrum is deceptively simple but proved unassignable due to more than one structure existing in solution. Mass spectral data supports the existence of a dynamic mixture of $[Fe_4\mathbf{L^3}_6(PyA)_{12}]^{8+}$ tetrahedron and $[Fe_2\mathbf{L^3}_3(PyA)_6]^{4+}$ helicate.

Experimental data

Ligand $\mathbf{L^3}$ (202 mg, 0.95 mmol, 6 equiv), $Fe(BF_4)_2.6H_2O$ (218 mg, 0.64 mmol, 4 equiv) and 2-pyridine carboxaldehyde (0.18 mL, 1.9 mmol, 12 equiv) were dissolved in acetonitrile (10 mL) giving a purple solution. This was heated (50°C, 24 hr) and the yellow solution was layered with diethyl ether. The resulting purple precipitate was filtered and washed with chloroform to give a purple solid (470 mg, 0.20 mmol, 31%). SbF_6^- was introduced as $NaSbF_6$ into a solution containing tetrahedral architecture $[Fe_4\mathbf{L^3}_6(PyA)_{12}]^{8+}$. [Accurate mass, *m/z*]: $\{Fe_4\mathbf{L^3}_6(PyA)_{12}\}^{8+}$ = 320.6056, $\{Fe_4\mathbf{L^3}_6(PyA)_{12}(BF_4)\}^{7+}$ = 378.6056, $\{Fe_4\mathbf{L^3}_6(PyA)_{12}(BF_4)_2\}^{6+}$ = 456.4761, $\{Fe_4\mathbf{L^3}_6(PyA)_{12}(BF_4)_3\}^{5+}$ = 565.3724, $\{Fe\mathbf{L^3}_3(PyA)_6\}^{2+}$ = 613.2441, $\{Fe_4\mathbf{L^3}_6(PyA)_{12}(BF_4)_4\}^{4+}$ = 728.2157, $\{Fe_4\mathbf{L^3}_6(PyA)_{12}(BF_4)_5\}^{3+}$ = 999.9564, $\{Fe_4\mathbf{L^3}_6(PyA)_{12}(BF_4)_6\}^{8+}$ = 1543.4366.

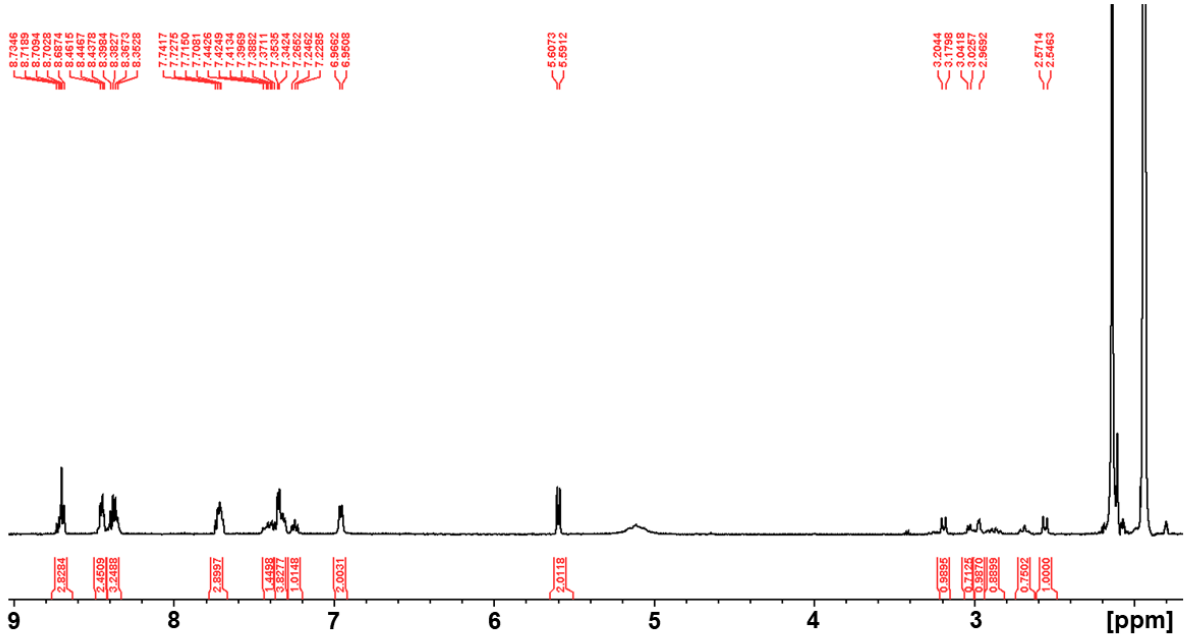

Figure 9. ^{1}H NMR (500 MHz, CD_3CN, 298 K) spectrum of subcomponent self-assembly reaction containing of $\mathbf{L^3}$, 2-pyridine carboxaldehyde and iron(II) tetrafluoroborate.

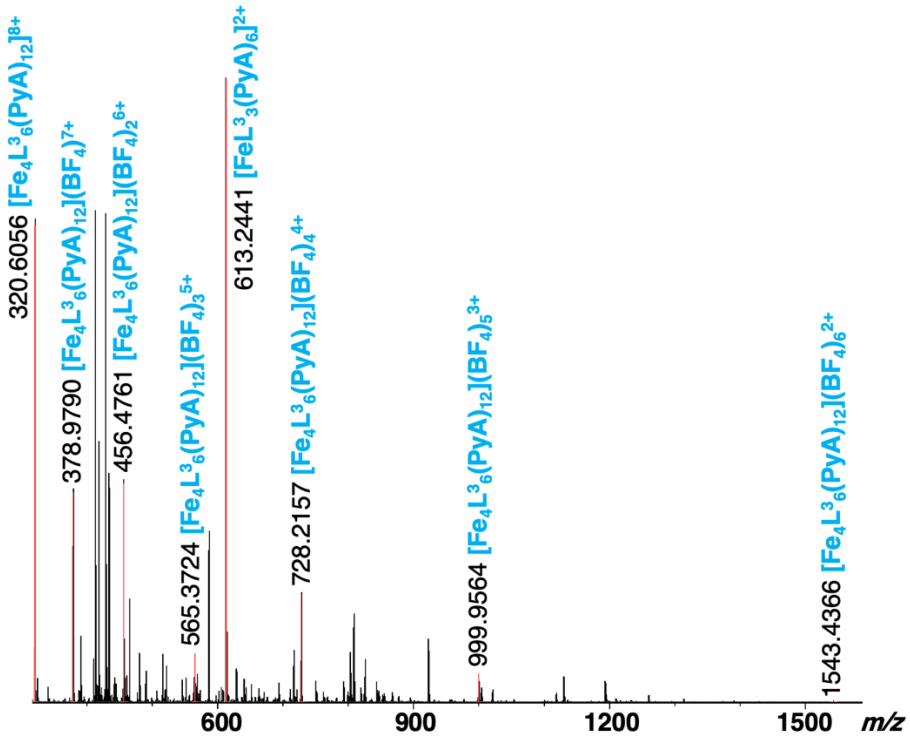

Figure 10. High-resolution mass spectrum for an acetonitrile solution of **42**. Isotopic patterns corresponding to complex **42** are represented by red lines.

11.5. X-Ray Crystallography

The X-ray crystallography data for **40, 41** and **42** were collected by IVY either at Diamond Light Source or in house. All data was refined by LT. Data is not processed to publication standard.

Data αCollection. X-Ray data for compounds **40** and **42** were collected at a temperature of 100 K using a synchrotron radiation at the single crystal X-ray diffraction beamline I19 in Diamond Light Source,[16] equipped with a Pilatus 2M detector and an Oxford Cryosystems nitrogen flow gas system. Data were measured using GDA suite of programs. X-Ray data for compound **41** was collected at 150(2) K using a Rigaku FR-X four circle diffractometer with a Hypix-6000HE HPC detector and FR-X microfocused rotating anode Cu K_α radiation source ($\lambda = 1.54146$).

Crystal Structure Determinations and Refinements. X-Ray data were processed and reduced using CrysAlisPro suite of programmes. Absorption correction was performed using empirical methods (SCALE3 ABSPACK) based upon symmetry-equivalent reflections combined with measurements at different azimuthal angles.[17–19] The crystal structure was solved and refined against all F2 values using the SHELXL and Olex 2 suite of programmes.[3,4]

Table 1. Crystallographic information for **40**.

Identification code	40
Empirical formula	$C_{63}H_{41}Cd_2Cl_{3.7}N_{16}O_{12.66}$
Formula weight	1580.69
Temperature/K	293(2)
Crystal system	monoclinic
Space group	$P2_1/c$
a/Å	15.227(3)
b/Å	17.805(2)
c/Å	27.372(6)
α/°	90
β/°	98.025(17)
γ/°	90
Volume/Å^3	7348(2)
Z	4
ρ_{calc}g/cm^3	1.429
μ/mm^{-1}	0.723
F(000)	3165.0
Crystal size/mm^3	0.1 × 0.1 × 0.1
Radiation	Synchrotron (λ = 0.6889)
2Θ range for data collection/°	2.618 to 49.92
Index ranges	-16 ≤ h ≤ 16, -17 ≤ k ≤ 19, -28 ≤ l ≤ 30
Reflections collected	28500
Independent reflections	10707 [R_{int} = 0.1756, R_{sigma} = 0.2614]
Data/restraints/parameters	10707/796/773
Goodness-of-fit on F^2	1.168
Final R indexes [I>=2σ (I)]	R_1 = 0.2443, wR_2 = 0.5471
Final R indexes [all data]	R_1 = 0.3895, wR_2 = 0.5877
Largest diff. peak/hole / e Å^{-3}	1.80/-0.83

Table 2. Crystallographic information for **41**.

Identification code	**41**
Empirical formula	$C_{137}H_{108}B_7F_{28}Fe_4N_{36}$
Formula weight	3089.66
Temperature/K	100.01(10)
Crystal system	triclinic
Space group	P-1
a/Å	21.1326(7)
b/Å	21.5618(11)
c/Å	22.7778(10)
α/°	91.570(4)
β/°	106.649(3)
γ/°	106.297(4)
Volume/Å^3	9478.4(7)
Z	2
ρ_{calc}g/cm^3	1.083
μ/mm^{-1}	3.056
F(000)	3146.0
Crystal size/mm^3	0.1 × 0.1 × 0.1
Radiation	Cu Kα (λ = 1.54184)
2Θ range for data collection/°	4.078 to 90.92
Index ranges	-19 ≤ h ≤ 19, -19 ≤ k ≤ 19, -19 ≤ l ≤ 21
Reflections collected	58483
Independent reflections	15546 [R_{int} = 0.0634, R_{sigma} = 0.0677]
Data/restraints/parameters	15546/1505/1960
Goodness-of-fit on F^2	2.153
Final R indexes [I>=2σ (I)]	R_1 = 0.2127, wR_2 = 0.5117
Final R indexes [all data]	R_1 = 0.2548, wR_2 = 0.5329
Largest diff. peak/hole / e Å^{-3}	2.21/-0.58

Table 3. Crystallographic information for **42**.

Identification code	**42**
Empirical formula	$C_{30}H_{20}N_4ClFe_4ISb_{0.25}F_{0.25}O_{0.25}$
Formula weight	734.54
Temperature/K	293(2)
Crystal system	monoclinic
Space group	Cc
a/Å	31.0550(6)
b/Å	21.1585(5)
c/Å	31.6300(7)
α/°	90
β/°	95.176(2)
γ/°	90
Volume/Å^3	20698.6(8)
Z	4
ρ_{calc}g/cm^3	0.236
μ/mm^{-1}	0.301
F(000)	1464.0
Crystal size/mm^3	0.1 × 0.1 × 0.1
Radiation	Synchrotron (λ = 0.6889)
2Θ range for data collection/°	3.288 to 72.348
Index ranges	-51 ≤ h ≤ 50, -35 ≤ k ≤ 34, -53 ≤ l ≤ 52
Reflections collected	212853
Independent reflections	94321 [R_{int} = 0.0824, R_{sigma} = 0.1172]
Data/restraints/parameters	94321/2/953
Goodness-of-fit on F^2	1.884
Final R indexes [I>=2σ (I)]	R_1 = 0.1956, wR_2 = 0.4323
Final R indexes [all data]	R_1 = 0.3148, wR_2 = 0.4610
Largest diff. peak/hole / e Å^{-3}	5.05/-2.92
Flack parameter	0.490(9)

11.6. References

1 Oxford Diffractions, A. T. U. L. Oxford Diffractions.

2 G. M. Sheldrick, *Acta Crystallogr. Sect. A Found. Crystallogr.*, 2015, **71**, 3–8.

3 G. M. Sheldrick, *Acta Crystallogr. Sect. C Struct. Chem.*, 2015, **71**, 3–8.

4 O. V. Dolomanov, L. J. Bourhis, R. J. Gildea, J. A. K. Howard and H. Puschmann, *J. Appl. Crystallogr.*, 2009, **42**, 339–341.

5 E. B. Fleischer, A. E. Gebala, D. R. Swift and P. A. Tasker, *Inorg. Chem.*, 1972, **11**, 2775–2784.

6 M. Seredyuk, A. B. Gaspar, V. Ksenofontov, Y. Galyametdinov, J. Kusz and P. Gütlich, *Adv. Funct. Mater.*, 2008, **18**, 2089–2101.

7 J. Mosquera, S. Zarra and J. R. Nitschke, *Angew. Chem. Int. Ed.*, 2014, **53**, 1556–1559.

8 F. J. Rizzuto, J. P. Carpenter and J. R. Nitschke, *J. Am. Chem. Soc.*, 2019, **141**, 9087–9095.

9 D. C. Ghosh and R. Biswas, *Int. J. Mol. Sci.*, 2003, **4**, 379–407.

10 N. Ousaka, J. K. Clegg and J. R. Nitschke, *Angew. Chem. Int. Ed.*, 2012, **51**, 1464–1468.

11 W. Meng, T. K. Ronson, J. K. Clegg and J. R. Nitschke, *Angew. Chem. Ed.*, 2013, **52**, 1017–1021.

12 H. Sato, *Chem. Commun.*, 1998, **2**, 249–250.

13 B. Manna, B. Joarder, A. V. Desai, A. Karmakar and S. K. Ghosh, *Chem. Eur. J.*, 2014, **20**, 12399–12404.

14 B. Manna, A. K. Chaudhari, B. Joarder, A. Karmakar and S. K. Ghosh, *Angew. Chem. Ed.*, 2013, **52**, 998–1002.

15 W. Meng, J. K. Clegg, J. D. Thoburn and J. R. Nitschke, *J. Am. Chem. Soc.*, 2011, **133**, 13652–13660.

16 H. Nowell, S. A. Barnett, K. E. Christensen, S. J. Teat and D. R. Allan, *J. Synchrotron Radiat.*, 2012, **19**, 435–441.

17 R. H. Blessing, *Acta Crystallogr. Sect. A*, 1995, **51**, 33–38.

18 L. Krause, R. Herbst-Irmer, G. M. Sheldrick and D. Stalke, *J. Appl. Crystallogr.*, 2015, **48**, 3–10.

19 G. M. Sheldrick, SADABS.

12. Conclusion and Outlook

The work presented in this thesis has explored the design, synthesis and characterisation of three-dimensional architectures formed through subcomponent self-assembly reactions between heteroditopic ligands and transition-metal ions. This contribution is significant given the relatively scant literature that currently contributes to this area of self-assembly, and it opens up opportunities to develop metal-organic structures incorporating heteroditopic ligands and metal ions with inequivalent coordination environments. The results discussed have investigated complex architectures using a number of characterisation techniques including NMR spectroscopy, mass spectrometry, magnetic measurements and X-ray crystallography.

Chapter two discusses the formation of a mixed spin-state trigonal bipyramidal architecture formed through the self-assembly of a benzimidazole-based heteroditopic ligand, TREN and iron(II) tetrafluoroborate. From a self-assembly perspective the design of this system is interesting as it allows a remarkable number of fluoride ions to be abstracted from the tetrafluoroborate counterions, whilst simultaneously oxidising one of the iron(II) centres to iron(III). The central $[Fe^{III}(\mu_2\text{-}F)_6(Fe^{II})_3]^{3+}$ star motif incorporates three high-spin iron(II) centres which are stabilised in this spin-state by the benzimidazole motifs present in the ligand structure, and a central high-spin iron(III) ion bound through the six bridging fluorides. The paramagnetic nature of high-spin iron(II) and iron(III) also make this compound interesting for magnetic applications. An analogous fluoride bridged structure in which the TREN molecules were replaced with TAME is discussed in Chapter five, highlighting how subtle changes in the subcomponent mixture still permits the formation of mixed-valence fluoride-bridged complexes. The synthesis of such compounds opens up the potential for structurally and electronically similar trigonal bipyramidal complexes to be synthesised for possible applications in molecular magnetism. This work utilised NMR spectroscopy during the characterisation process, and included a rare example of DOSY NMR spectroscopy of a paramagnetic complex.

In Chapter three, the formation of bimetallic trigonal bipyramidal architectures from a bipyridine-based heteroditopic ligand were reported. A series of structurally analogous complexes with general formula $[Fe_2Ag_3\mathbf{L}_6T_2]^{7+}$ were synthesised and crystallographically characterised, where two iron(II) centres were bound at the apex of the structure, and three silver(I) ions were bound in the equatorial plane. The X-ray crystal structures of these complexes highlighted the ability of the complex to encapsulate the polyatomic spherical anions BF_4^-, PF_6^- and SbF_6^- within the architecture's central cavity. The structure was able to elongate in order to facilitate the binding of a μ_3-Cl ion to the three silver(I) centres, subsequently changing each silver(I) ions coordination number from four to five. This observation was characterised crystallographically and opened up the possibility for catalytically active metals, such as copper, to be incorporated within the structure. This idea was investigated and two bimetallic iron-copper architectures with formulas $[Fe_2Cu^+_3\mathbf{L}_6T_2]^{7+}$ and $[Fe_2Cu^+_3\mathbf{L}_6T_2(Cl)_3]^{7+}$ were

synthesised. The ability for both copper(I) and copper(II) to be incorporated in the equatorial sites of the structure is promising for potential redox switching at each of the copper centres.

Self-assembly of the copper(II)-containing trigonal bipyramid proceeded in the presence of NaCl to allow complete saturation of the copper(II) coordination sites, and mass spectral analysis supported the formation of an iron(II)/copper(II) trigonal bipyramid with three chloride ions incorporated. The position of the chloride atoms could not be determined by mass spectrometry, and efforts to grow single crystals of the complex are ongoing.

Interestingly, when NaCl was introduced into a solution containing the copper(I) analogue $[Fe_2Cu^{+}_3\mathbf{L}_6T_2]^{7+}$, one chloride ion bound to one of the copper centres, oxidising it to copper(II) and changing the coordination number from four to five. This observation is a key feature of catalytic copper(I)/copper(II) complexes, and the mixed-valence structure was characterised by X-ray crystallography. We envisage that further investigation into catalysis at the copper sites within this structure could result in the formation of a new class of supramolecular catalysts.

Chapter four investigates the self-sorting phenomena of heteroleptic tetrahedra and reports the first example of an integratively self-sorted $[M_4\mathbf{L}_6]^{8+}$ tetrahedron. Careful selection of amine and metal salt counterion allowed control over a system containing two very similar ligands to be obtained, resulting in the exclusive formation of an iron(II) tetrahedron with one unique vertex. When the counterion in the system was BF_4^-, OTf^- or NTf_2^-, a dynamic mixture of homo- and heteroleptic tetrahedra, as well as mononuclear $[Fe\mathbf{L}_3T]^{2+}$ were observed. Contrastingly, when the counterion was ClO_4^-, the heteroleptic tetrahedron was obtained solely. Characterisation of crystallographic data for $[Fe\mathbf{L}_3T](X)_2$ (where X= BF_4^-, OTf^-, NTf_2^- or ClO_4^-) highlighted the unique incorporation of a central ClO_4^- anion within the three arms of the structure. This feature was only observed for the mononuclear perchlorate system, highlighting preorganisation in the $[Fe\mathbf{L}_3T](ClO_4)_2$ structure as a driving force for the exclusive formation of the heteroleptic tetrahedron from a mixture of ligands. Understanding the anion-induced integrative self-sorting observed within this system is crucial for further exploration of heteroleptic systems and their potential for applications in areas such as separation and catalysis.

Throughout this thesis, the self-assembly of heteroditopic ligands in combination with transition metal ions are investigated. The design, formation and characterisation of complex three-dimensional architectures are reported, and both homo- and heterometallic systems are investigated. Chapters two and three highlight the site-specific binding of metal ions due to the incorporation of different binding sites within the same ligand. We have utilised X-ray crystallography to characterise such structures and the subsequent binding of different anions within their central cavity space.

Further investigations into the connectivity and coordination environments present in the iron(II)/copper(I/II) systems is key to determine the potential catalytic activity of the compounds. Additional experiments will explore the potential for the copper centres to bind phosphines and

additional anions, and will determine the redox potentials of the copper ions in order to determine the compounds capability as a transition metal catalysis. Incorporation of different metal ions into this structure will also be explored to determine the effect that both metal ion radii and alternation in the coordination sphere has on the resulting architectures.

The formation of a TAME-based fluoride bridged compound is discussed in Chapter five. This compound was analogous to the mixed spin-state complex discussed in Chapter two, but was formed in a 1:1 mixture of acetonitrile:methanol. Chapters three and four report the formation of architectures which incorporate TREN, and further studies will investigate how the substitution of TREN for TAME in these examples, and thus the change from acetonitrile to a 1:1 acetonitrile:methanol mixture, will affect the self-assembly and the subsequent structures that form. For the heteroleptic system discussed in Chapter four, a change in solvent could affect the parameters that govern the sorting of the system.

This thesis details the self-assembly of transition metal ions with two different heteroditopic ligands, one benzimidazole-based ligand and one bipyridine-based ligand. Modification of these to include additional functionality will further expand the scope of this underreported area. Addition of solubilising groups to heteroditopic ligands has already been explored by the group and has allowed the formation of water-soluble three-dimensional constructs, which opens up potential for these compounds to have biological applications. Increasing the length of the ligand will also be investigated in order to synthesize larger, more complex constructs which are expected to expand the encapsulation abilities of this class of compound.